Developing a Progressive Damage and Failure Model for Hybrid 3D Woven Textile Composites using NCYL Multiscale Method

by

Deepak Kumar Patel

A dissertation submitted in partial fulfillment
of the requirements for the degree of
Doctor of Philosophy
(Aerospace Engineering)
in the University of Michigan
2017

Doctoral Committee:

Professor Anthony M. Waas, Chair
Professor Krishnakumar R. Garikipati
Associate Professor Veera Sundararaghavan
Dr. Chian-Fong Yen, Army Research Laboratory

Deepak Kumar Patel

pateldkp@umich.edu

ORCID iD: 0000-0002-2018-2783

To my family and in loving memory of my grandmother, Sumitra Naik, who has been a constant source of love and caring, and will be forever in my heart.

ACKNOWLEDGMENTS

I express the deepest gratitude to my advisor, Professor Anthony Waas, who has guided me throughout this project with his brilliant ideas whilst allowing me the freedom to work in my own way. His energy and enthusiasm always motivated me whenever I found myself in difficult situations. It was his inspiration that motivated me to advance my career to this level and finally become the author of this dissertation. Without his guidance and encouragement the thesis would not have been completed.

I would like to thank Professor Veera Sundararaghavan and Professor Krishna Garikipati as dissertation committee members, for their insightful comments and suggestions during the preparation of this dissertation. Dr. Chian-Fong Yen also provided me with numerous ideas and advice in my research, and I owe him my great gratitude. I would like to thank Prof. Daniel J. Inman, Chairman, Department of Aerospace Engineering at the University of Michigan for providing me excellent work environment. I also thank the faculty members of the Aerospace department and other departments at the University of Michigan from whom I had the privilege to learn many concepts and fundamentals which proved to be very valuable during this project.

I would like to thank my classmates, labmates and friends and particularly Armanj Hasanyan who have been a great help whenever I got snagged in some conceptual problem or other difficulties. In addition I would like to thank, Dr. Jiawen Xie and Dr. Ashith Joseph, for constantly providing support whenever needed. It was a great pleasure to work with my colleagues in the Composite Structures Laboratory. Experimental work done by Professor Mark Pankow are greatly helpful for developing and validating the analysis in this dissertation. Special thanks go to my officemates, Dr. Dianyun Zhang, Dr. Marianna Maiaru and Dr. Solver Thorsson. I have received generous help from Dr. Paul Davidson and Dr. Royan J. DMello on numerical simulations and brilliant suggestions on extending my analysis. I will never forget the days spent with Dr. Wooseok Ji, Dr. Nhung Nguyen, Dr. Pascal Meyer, Dr. Akinori Yoshimura, Dr. Cyrus Kosztowny, David Singer, Alastair Croxford, Avinkrishnan

Vijayachandran, Shiyao Lin, and Tian Kuo.

I sincerely thank the staff of the Department of Aerospace Engineering at the University of Michigan and the Department of Aeronautics & Astronautics at the University of Washington for their tremendous support for the students. Special thanks go to Ms. Denise Phelps and Ms. Julie Power who provided me with countless help on academic program coordination. Special thanks goes to Dzung Tran, Research Scientist and Machine shop manager at the University of Washington for his dedicated help and support to finish my experimental work for this project. The research of this dissertation was supported in part through computational resources and services provided by Advanced Research Computing at the University of Michigan and the Hyak supercomputer system at the University of Washington. I gratefully acknowledge the HYAK and FLUX high-performance computing clusters at the University of Washington and University of Michigan, respectively, for enabling this study.

The author is grateful for financial sponsorship from the Army Research Office (Drs. Larry Russel and Asher Rubinstein, as Program Managers) and the encouragement and support of Dr. Chian Yen at the Army Research Laboratory, Aberdeen Proving Ground, MD. Thanks to Dr. Asher Rubeinstein for the helpful discussions in past review meetings. The author would also like to acknowledge Dr Steve Engelstad, Principle Investigator, Lockheed Martin and Dr Stephen B Clay, AFRL, Program manager, for the encouragement and support and sharing the experimental results.

I would also like to thank my beloved parents and close friends who have always taught me to follow my heart no matter what obstacles I might encounter. I am greatly indebted to them for their unconditional support and encouragement all through my life. This journey would not have been possible without you.

TABLE OF CONTENTS

LIST OF FIGURES

LIST OF TABLES

LIST OF APPENDICES

ABSTRACT

Results from a research study concerned with developing an experimentally validated computational tool for predicting the progressive damage and failure response of 3D woven textile composites (3DWTCs) in a multiscale framework are presented. There are different constituents within the textile composite; fiber tows, including carbon, glass and kevlar. The dry fiber tows are infused with SC-15 polymer matrix into a single composite material. The 3DWTCs are made through a 3D textile weaving process. Three different versions of hybridized architectures are examined to determine the progression of failure under tensile and compressive loading. The different types of 3DWTCs are compared against one another to understand the benefits of hybridization and the resulting performance enhancements. The scope of the project also includes conducting a micro-CT analysis to study the effect of microstructure imperfections on predicting the progressive damage and failure response, using a two-scale computational mechanics framework. The micro-CT analysis delivers information on the size of a representative unit cell (RUC), the fiber tows cross sectional details and the porosity (if any) within the composite. These microstructure scale inputs are the building blocks for 3D geometric modeling and finite element (FE) analysis of unit cell (or a collection of these) at a global scale. The objective of this work is to perform a multiscale investigation to study the progressive damage and failure at different length scales. In the computational modeling, the macroscale finite element analysis (FEA) is carried out at the representative volume element (RVE) and coupon level, while the micromechanics analysis is implemented simultaneously at the subscale level using material properties of the constituents (fiber and matrix) as input. The subscale micromechanics analysis uses the N-layers concentric cylinder model (NCYL) to compute the local fields in the fiber and matrix cylinders. The influence of matrix microdamage at the subscale leads to progressive degradation of fiber tow stiffness at the macroscale, modeled using a secant moduli approach, resulting in the pre-peak nonlinear response. The post-peak strain softening response

resulting from different failure modes like fiber tow rupture, tow splitting and matrix cracking in fiber tow, as well as inside the volume of textile, are modeled using a mesh-objective smeared crack approach (SCA). The FE models, in addition to being generated using nominally perfect geometry, are also generated directly from Micro-CT data using the software tool SIMPLEWARE. The FE mesh generated using this tool is a replication of real in-situ imperfection in the structure. A study on modeling the geometric imperfections and its effect on global stress-strain response of the structure is carried out both at RVE and Coupon level as a part of this research. The use of analytical solutions at the fiber-matrix scale in a multiscale framework delivers a distinct computational advantage in the damage and failure analysis, where high fidelity and computational efficiency are both gained at the same time.

CHAPTER 1

Introduction

1.1 Motivation

Textile composites have widespread use in aerospace, automobile, civil and defense industries due to their better structural properties tailoring capability and superior mechanical performance, along with high damage tolerance, high impact resistance and low fabrication cost. In the large family of textile composites, three dimensional woven textile composites (3DWTCs) are recognized as a potential high performance composite material and possess a great advantage of high resistance to delamination, as the latter is a common mode of failure in conventional laminated composites. The mechanical performance can be enhanced due to reinforcement in the thickness direction and the in-plane properties are significantly improved due to attempts at aligning the in-plane fiber tows. This unique signature is a characteristic of the 3D textile weaving process but at significantly reduced manufacturing cost and time, compared to traditional pre-preg based materials. The design methods adopted for 3DWTC structures are still based on testing and therefore a high fidelity but computationally efficient model is much needed. Such a model should be based on the physics of material response and failure, using constitutive model properties that can be measured independently through a set of coupon level tests. However, the hierarchical nature of composites makes the characterization and modeling of such materials a great challenge. Most of the damage and failure events evolve at the constituent material scale with little knowledge on the in-situ constituent properties. Predictions from computational models, therefore, may encompass a high level of uncertainty. For large-scale structural analysis, homogenization at the macroscale is essential to achieve computational efficiency, whereas the model also needs to consider the influence of the underlying microstructure.

The progressive damage and failure analysis of composites has proven to be a

challenging problem over the years, and reliable computational tools are indispensable to accurately predict the strength and the major failure modes, simultaneously. The mechanics of composite materials can be described well in a multiscale framework as most of the failure phenomena at the global scale are dependent on constituent level properties at the sub-scale. The available mean field theories for failure analysis can be used for the prediction of homogenized elastic properties, but they are not able to capture the local stress and strain gradients in the matrix layers or the fiber-matrix interface. As a result, these models yield an overestimate of the composite nonlinear behavior. Because damage and failure are governed by extreme properties of the fields and not necessarily by the average properties, these methods find limited applications to progressive damage development and failure analysis of composite structures.

Multiscale modeling is a suitable and efficient methodology for progressive damage and failure analysis of 3DWTC, where information is shared across different length scales. The proposed computational scheme should be able to bridge the gap between micro and macro scale in a cost effective way. In the literature, a number of micromechanics models have been developed. Zhang and Waas [1] proposed a micromechanics-based two-scale model which is able to predict the nonlinear response of unidirectional composites. Their proposed micromechanics analysis uses the analytical solutions derived from the concentric cylinder model along with the generalized self-consistent model to find the effective properties of the unidirectional fiber reinforced composite and also the stress and strain fields within the fiber and matrix. The composite material is represented by an inner fiber core and an outer matrix annulus. In this research, the 2-CYL fiber-matrix concentric cylinder model is extended into a concentric fiber and any number of (N-1) matrix layers in general, keeping the volume fraction constant, referred to as the N-layer concentric cylinder micromechanics model (NCYL), which can analytically calculate the strain and stress field within the fiber and matrix cylinders for a given applied remote composite strain field, acting on the outer boundary of the matrix cylinder. The spatial variation of strain and stress fields within the cylinder are the key determinants for progressive damage and failure analysis of composite structures and hence, these fields need to be predicted with high accuracy. The advantage of the NCYL model is that the matrix strain and stress fields can be found in a discrete manner for each layer and the evolution of damage can be localized at a particular layer of the matrix. These results are used at the sub-scale in a 2-scale analysis to calculate the effective nonlinear composite response at the macro-scale. Because the sub-scale computation relies on an analytical solution, a distinct computational advantage in composite progressive

damage and failure analysis is evident, compared against a fully computational model at each scale.

1.2 Research objective and thesis outline

Three dimensional, orthogonal woven composites are a class of 3DWTC composite structures containing a set of fiber tows spreading in all three mutually perpendicular directions (x, y and z-axes). Mechanical properties are highly dependent on the geometry of reinforcements and their complex architectures. 3DWTC is manufactured by laying up the warp and weft fiber layers and consequently running a Z-fiber in the thickness direction to bind the in-plane layers together. A matrix material is impregnated into these complex woven lay-ups and cured under certain condition to get the woven solid structure. The interlacing fiber tows inside the matrix pocket introduce much complex microstructure in the weaves, which makes the modeling and failure analysis of the woven composites really challenging. The topology and architecture of the weaves need to be modeled precisely to obtain accurate failure predictions, and multiple material length scales should be considered to capture the complex failure mechanisms which initiate at the fiber-matrix scale.

The purpose of this research is to establish a validated multiscale computational framework to predict the progressive damage and failure response of these complex 3DWTC using constitutive property data measured from coupon level tests. The pre-peak nonlinear behavior of the composite is modeled using the NCYL micromechanics model. The detaliled explanation for the NCYL model and the development of the matrix nonlinear constitutive model for N=2, 3 and 4 cylinders are provided in Chapter 2. The post-peak failure response of the composite is modeled using smeared crack approach (SCA), where the stress-strain formulation of the continuum is related to the non-continuum traction-separation law through a characteristic length, henceforth making it mesh objective. Various fiber and matrix failure modes are included in this study and their implementation in the SCA are explained in Chapter 3. The material system (fiber and matrix materials) used in manufacturing these hybrid complex architectures are detailed in Chapter 4. Although, there are many forms of 3D woven composite with the variations of Z-fiber depth in thickness direction, we will focus here mainly on three different configurations. The microstructure characterization studies, details of the modeling strategy including imperfections and construction of the finite element (FE) model directly from the micro-CT data, are presented in Chapter 4. The predictive capability of the proposed method is eval-

uated by comparing the computational results of various hybrid textile configurations with experiment for tensile loading conditions in Chapter 5. The detailed experimental set-up for compression test, effect of hybridization on the compressive response and the coupon level modeling and simulations to validate the experimental results are discussed in Chapter 6, followed by conclusions in Chapter 7.

CHAPTER 2

N-Layer concentric cylinder model (NCYL): an extended micromechanics-based multiscale model for nonlinear composites

2.1 Introduction

A validated multi-scale computational mechanics framework for progressive failure modeling of composite structures is developed. Zhang and Waas [1] proposed a micromechanics based two-scale multiscale model which is able to predict the nonlinear response of a composite. Their proposed micromechanics analysis uses the analytical solutions derived from the concentric cylinder model (CCM) along with the generalized self-consistent model (GSCM) to find the effective properties of the unidirectional fiber reinforced composites, which are dependent on constituent level fiber-matrix mechanical properties and fiber volume fraction. In this model, the composite material is represented by an inner fiber core and an outer matrix annulus. It should be noted that the 2-CYL fiber-matrix concentric cylinder micromechanics model can be extended to a concentric fiber and any number of (N-1) matrix layers in general, keeping the volume fraction constant, hence called the N-cylinder model (NCYL), which can analytically calculate the strain and stress field within the fiber and matrix cylinders for a given applied remote composite strain field, acting on the outer boundary of the matrix cylinder. The spatial variation of strain and stress fields within the cylinder are the key determinants for progressive damage and failure analysis of composite structures and hence, they need to be predicted accurately. The advantage of the NCYL concentric cylinder model is that the matrix strain and stress fields can be found in a discrete manner for each layer and the evolution of damage can be

localized at a particular layer of matrix. These results can be used at the sub-scale in a multi-scale analysis to calculate the effective nonlinear composite response at a global scale. This work is based on a full analytical solution and hence, it delivers a distinct computational advantage in composite failure analysis. That is, high fidelity and computational efficiency are gained at the same time.

Obtaining the analytical elasticity solutions of strain and stress fields of composite structures has been a research area of interest for the last few decades as these materials have received widespread applications in the aerospace industry as lightweight materials with enhanced mechanical properties. The prediction of homogenized mechanical properties of unidirectional (UD) composites has drawn the attention of many researchers for a long time and various well known micromechanics models have been proposed in the literature to evaluate the elastic properties of UD composites. The analysis at the scale of fiber and matrix is referred to as micromechanics, which can be categorized as follows: (1) Phenomenological models such as the Voigt [2] and Reuss [3] models. The Voigt model is also known as the rule of mixture (ROM) which is based on an iso-strain assumption, while the Reuss model is known as the inverse rule of mixture (IROM) model, which is based on an iso-stress assumption. (2) Semi-empirical models are known to correct the ROM model by introducing correction factors. The modified rule of mixture (MROM) models and the Halpin-Tsai model [4] fall under this category. (3) Elasticity approach models include the concentric cylinder model (CCM), proposed by Hashin and Rosen [5], where the composite material is represented by an inner fiber core and an outer matrix annulus. In this model, it is assumed that the entire composite is composed of concentric cylinders, which vary in size, but the ratio of the fiber to the matrix radius is constant for each concentric cylinder in order to maintain the same volume fraction. Christensen and Lo proposed a generalized self-consistent model [6] in order to evaluate the transverse shear modulus G_{23} in closed form. Other homogenization methods like Mori-Tanaka model (M-T), developed by Mori and Tanaka [7] are inclusion models, where fibers are simulated by inclusions embedded in a homogeneous medium. Tandon and Weng [8] studied ellipsoidal inclusions of different aspect ratios and used the M-T model to arrive at expressions for the five independent elastic constants for a fiber reinforced lamina. The self-consistent model (S-C) has been proposed by Hill [9] and Budiansky [10] to predict the elastic properties of composite materials reinforced by isotropic spherical particles, and later this model was applied to UD composites with long fibers. The S-C model leads to an iterative method that gives the stiffness matrix of the homogenized medium. A new micromechanics model has been proposed by

Huang et al. [11, 12] recently to predict the stiffness and strength of UD composites.

Numerical FE modeling is another widely used reliable tool to predict the mechanical properties of composites, but it includes many aspects, such as fiber packing definition, geometrical dimensions, definition of RVE, definition of appropriate boundary conditions, and explicit meshing of fiber and matrix, all of which add to computational time. The computational cost in numerical FE multi-scale models, where each scale is solved numerically, represents a major disadvantage. Studies by Li [13] and Sun and Vaidhya [14] discuss the effects of boundary conditions in the use of different types of representative volume elements used in multi-scale analysis.

A micromechanics based multiscale model for a two-phase fiber and matrix system has been proposed by Zhang and Waas [1], which establishes a multiscale computational framework for nonlinear composites, in which the subscale micromechanical analysis is carried out using an analytical solution that is derived from the CCM in conjunction with the extended GSCM. The full analytical micromechanics model is able to capture the stress and strain gradients in the constituent materials when the composite material is subjected to mechanical loading. The evolution of the composite effective nonlinear stress versus strain response is dictated through two scalar variables that correspond to matrix microdamage determined at the subscale micromechanical analysis. The accuracy of the model is assessed by comparison against a corresponding 3D FEA.

The purpose of this research is to generalize the above mentioned analytical method [1] to any number of matrix layers and resolve the local fields for N-matrix cylinders, so that the development of damage and failure can be captured in a more refined manner, analytically. That is, within a multiscale computational framework for nonlinear composites, the evolution of localized damage is predicted for the discrete layers of matrix and not for the whole volume of matrix, as done earlier in Reference [1]. In this analysis, the number of layers of the concentric cylinder are arbitrary, with each layer having a different thickness. A composite cylinder with multiple number of matrix layers is considered in such a way that, each layer corresponds to a different volume. This approach is unique and novel, and is effective for progressive damage and failure analysis in a multiscale framework. The approach is validated by comparing with previously known solutions for N=2 cylinders and against fully 3D FE solutions.

2.2 Material system

A multi-layered concentric cylinder model can be used to represent the microstructure of a UD lamina in a prepreg tape-based laminated composite or a fiber tow in textile composites. The fiber packing inside the tow can be assumed as (1) Hexagonal array in the transverse plane where the fibers are of identical cross section or (2) Random array where the fibers are of different diameters but the volume fraction is preserved constant. In both the cases, the fibers are assumed to be infinitely long and the effective response of the composite is macroscopically homogeneous and transversely isotropic, requiring five independent constants to form the composite stiffness tensor. Though the choice of these elastic constants are not unique, the axial modulus, E_1^c, the axial Poisson's ratio, ν_{12}^c, the axial shear modulus, G_{12}^c, the plane-strain bulk modulus, K_{23}^c and the transverse shear modulus, G_{23}^c, are used throughout the research. Therefore, the stiffness tensor for a transversely isotropic material can be written in terms of these elastic constants as,

$$\boldsymbol{C}^c = \begin{bmatrix} E_1^c + 4\nu_{12}^{c^2}K_{23}^c & 2\nu_{12}^c K_{23}^c & 2\nu_{12}^c K_{23}^c & 0 & 0 & 0 \\ 2\nu_{12}^c K_{23}^c & K_{23}^c + G_{23}^c & K_{23}^c - G_{23}^c & 0 & 0 & 0 \\ 2\nu_{12}^c K_{23}^c & K_{23}^c - G_{23}^c & K_{23}^c + G_{23}^c & 0 & 0 & 0 \\ 0 & 0 & 0 & G_{23}^c & 0 & 0 \\ 0 & 0 & 0 & 0 & G_{12}^c & 0 \\ 0 & 0 & 0 & 0 & 0 & G_{12}^c \end{bmatrix} \tag{2.1}$$

Other important constants, including the transverse modulus E_2^c and transverse Poisson's ratio, ν_{23}^c can be computed as

$$E_2^c = \frac{4G_{23}^c K_{23}^c}{K_{23}^c + \psi G_{23}^c} \tag{2.2}$$

$$\nu_{23}^c = \frac{K_{23}^c - \psi G_{23}^c}{K_{23}^c + \psi G_{23}^c} \tag{2.3}$$

where ,

$$\psi = 1 + \frac{4K_{23}^c \nu_{12}^{c^2}}{E_1^c}$$

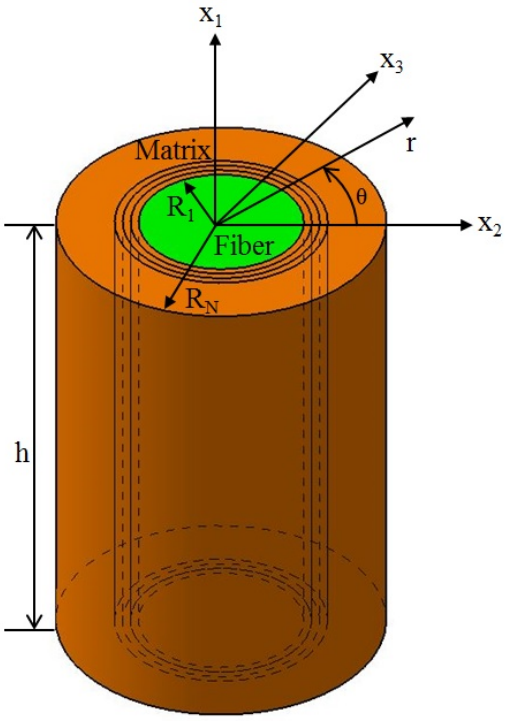

Figure 2.1: Concentric N-cylinders assembly.

A representative multi-layered concentric cylinder unit with fiber radius R_1 and matrix outer radius R_N is shown in Figure 2.1, and the resulting fiber volume fraction is $\nu_f = \frac{R_1^2}{R_N^2}$. We consider a transversely isotropic fiber cylinder surrounded by (N-1) concentric isotropic matrix layers ($R_{k-1} \leq r \leq R_k, k = 2, ..., N$). In this work, we will refer to both Cartesian coordinates (x_1, x_2, x_3) and Polar coordinates (r, θ, x) as shown in Figure 2.1.

In the present study, the fiber is assumed to be linear elastic, transversely isotropic, with "1" designating its longitudinal direction. Its stiffness tensor, $\boldsymbol{C}^f$, can be written in terms of fiber elastic properties as Equation (2.1) by replacing the superscript "c" with "f." In a shorthand notation, the stiffness matrix for the fiber is

$$C^f = \begin{pmatrix} C_{11}^f & C_{12}^f & C_{12}^f & 0 & 0 & 0 \\ C_{12}^f & C_{22}^f & C_{23}^f & 0 & 0 & 0 \\ C_{12}^f & C_{23}^f & C_{22}^f & 0 & 0 & 0 \\ 0 & 0 & 0 & C_{44}^f & 0 & 0 \\ 0 & 0 & 0 & 0 & C_{55}^f & 0 \\ 0 & 0 & 0 & 0 & 0 & C_{55}^f \end{pmatrix} \tag{2.4}$$

where superscript "f" indicates the fiber layer and $C^f_{44} = (C^f_{22} - C^f_{23})/2$.

The matrix material is an isotropic elastic-damaging solid, and its nonlinear response is modeled using a modified J_2 deformation theory of plasticity through a secant moduli approach, as discussed in Section 2.3. As a result, the composite effective stress versus strain curve is extended to the nonlinear regime by substituting secant moduli into Equation (2.1). The stiffness matrix for the matrix layers in a shorthand notation is expressed as,

$$C^k = \begin{pmatrix} C^k_{11} & C^k_{12} & C^k_{12} & 0 & 0 & 0 \\ C^k_{12} & C^k_{11} & C^k_{12} & 0 & 0 & 0 \\ C^k_{12} & C^k_{12} & C^k_{11} & 0 & 0 & 0 \\ 0 & 0 & 0 & C^k_{44} & 0 & 0 \\ 0 & 0 & 0 & 0 & C^k_{44} & 0 \\ 0 & 0 & 0 & 0 & 0 & C^k_{44} \end{pmatrix} \tag{2.5}$$

where superscript $k = 2, ...N$ indicates the matrix layer and $C^k_{44} = (C^k_{11} - C^k_{12})/2$.

2.3 Matrix nonlinear constitutive model

In the present NCYL model, the inner fiber core is surrounded by (N-1) matrix layers. During the process of damage evolution, the damage occurring in the discrete matrix layers are identified based on the calculation of strain and stress field, whereas the undamaged matrix layers retain their virgin properties as shown in Figure 2.1. An assumption in the NCYL model is that the θ-dependence of failure is used to initiate the degradation, but the entire matrix cylinder properties are degraded. It is important to emphasize the fact here that, in the previous study by Zhang and Waas [1], the entire volume of matrix material was degraded by same amount, as there was no way of restricting the local damage zone to a particular region of matrix volume. As a result, it overpredicts the stiffness degradation and the nonlinear stress-strain response governed by stiffness degradation. This limitation is eliminated by NCYL model and the radius of the discrete damage zone can be controlled as an input variable to this model. Now, the homogenized elastic properties of the fiber tow (E^c_1, ν^c_{12}, G^c_{12}, K^c_{23} and G^c_{23}) are functions of the degraded properties of the damaged matrix layers and the virgin properties of the undamaged matrix layers. This is a very significant step to be able to capture the damage locally in the microscale, which is based fully on an analytical solution.

The global (macroscopic and homogenized) behavior of polymer matrix composite

materials exhibits nonlinear stress versus strain response before failure, especially in the matrix dominated directions. Such nonlinear behavior is attributed to matrix microdamage due to the growth of voids and flaws in the polymer matrix. The evolution of such damage accounts for progressive deterioration of the material stiffness; however, the tangent stiffness tensor still remains positive-definite. The coalescence of matrix micro damage finally results in macroscopic matrix cracking, followed by a post-peak strain softening regime. In this instance, the positive definiteness of the matrix stiffness tensor is lost. The matrix constitutive model established in this work is limited to matrix micro damage and progressive degradation of the stiffness tensor only in the pre-peak regime. The post-peak failure response of matrix in the microscale and its effect on the glaobal response of the fiber tow at macroscale is a scope of future research.

It has been shown by Sicking [15] and supported by experimental data from Lamborn and Schapery [16] that a polymer matrix exhibits limited loading path independent behavior, surmised through combined tension-torsion tests. Hence, for such a material, the state of stress can be uniquely determined from the state of strain through a secant modulus. It is further assumed that the evolution of damage is an irreversible process, therefore, once the matrix stiffness tensor is degraded due to microdamage, it cannot be recovered. Such behavior suggests that a modified J_2 deformation theory of plasticity can be employed to model the nonlinear stress-strain response. In the present constitutive model, the degrading secant moduli are utilized to compute the material stiffness tensor during unloading also.

In order to utilize a uniaxial stress-strain response to determine the damaging matrix material response under combined loading, two equivalent variables, the equivalent stress, σ^m_{eq}, and the equivalent strain, ε^m_{eq}, are introduced and related through a secant Young's modulus, E^m_s as $\sigma^m_{eq} = E^m_s \varepsilon^m_{eq}$. According to J_2 deformation theory, the equivalent quantities are related to corresponding stress and strain components as,

$$\sigma^m_{eq} = \sqrt{\frac{1}{2}[(\sigma^m_{11} - \sigma^m_{22})^2 + (\sigma^m_{22} - \sigma^m_{33})^2 + (\sigma^m_{33} - \sigma^m_{11})^2] + 3((\sigma^m_{12})^2 + (\sigma^m_{13})^2 + (\sigma^m_{23})^2)} \tag{2.6}$$

$$\varepsilon^m_{eq} = \frac{1}{1+\nu^m_s}\sqrt{\frac{1}{2}[(\varepsilon^m_{11} - \varepsilon^m_{22})^2 + (\varepsilon^m_{22} - \varepsilon^m_{33})^2 + (\varepsilon^m_{33} - \varepsilon^m_{11})^2] + \frac{3}{4}((\gamma^m_{12})^2 + (\gamma^m_{13})^2 + (\gamma^m_{23})^2)} \tag{2.7}$$

where ν_s^m is the matrix secant Poisson's ratio defined by

$$\nu_s^m = \frac{1}{2} + \frac{E_s^m}{E_e^m}\left(\nu_e^m - \frac{1}{2}\right) \tag{2.8}$$

and E_e^m and ν_e^m are the matrix elastic Young's modulus and elastic Poisson's ratio, respectively. In this research, the matrix nonlinear stress-strain relation is characterized using an exponential representation as,

$$\sigma_{eq}^m = \sigma_y^m - \frac{k_1}{k_2}\left(e^{-k_2\varepsilon_{eq}^m} - e^{-k_2\frac{\sigma_y^m}{E_e^m}}\right) \tag{2.9}$$

where σ_y^m is the yield stress uniaxial tension, and k_1 and k_2 are two material parameters that govern the evaluation of matrix micro damage which can be determined from an experimental stress-strain response [17], which is explained in the flow chart below in Figure 2.2.

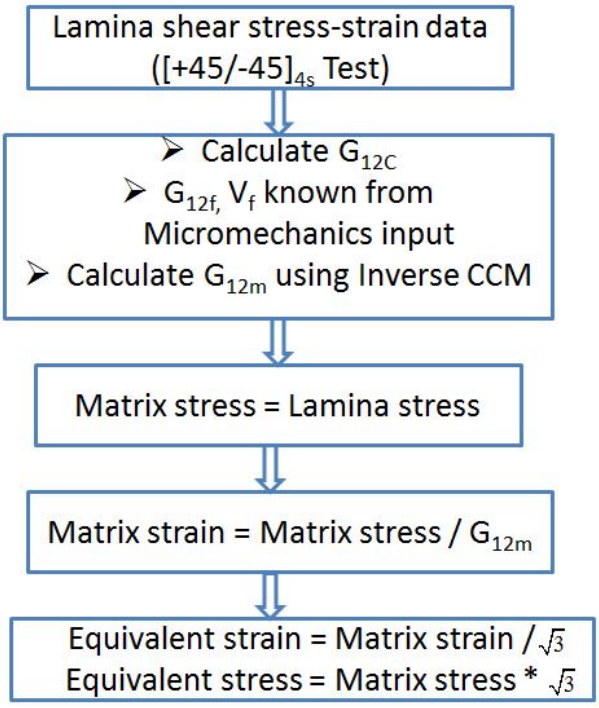

Figure 2.2: Flow chart to calculate the matrix in-situ properties.

The linear part of equivalent stress-strain diagram is used to claculate the yield stress σ_y^m and the nonlinear part of the curve is fitted to Equation (2.9) to calculate the two material parameters k_1 and k_2 respectively. The detailed procedure to compute these curve fitting parameters for each case (N=2, 3 and 4) are explained

in the following sections. The material system SC-15 matrix is considered here to demonstrate the calculation of matrix in-situ properties.

2.3.1 Matrix in-situ properties for NCYL (N=2, 3 and 4)

A schematic diagram of 2-layers fiber-matrix concentric cylinders of a fixed volume fraction is shown in Figure 2.3(a). The total volume of matrix is subdivided into two layers of equal radii (M1 and M2), but the outer boundary of the matrix layers is kept constant to preserve the total volume fraction, as shown in Figure 2.3(b). The radii of M1 and M2 can be defined as any ratio and need not be equal, to be given as inputs to the model N=3. Now, the total volume of matrix is subdivided into three layers of equal radii (M1, M2 and M3), but the outer boundary of the matrix layer is still kept constant to preserve the total volume fraction, as shown in Figure 2.3(c). In general, the radii of M1, M2 and M3 can be defined as any ratio to be given as inputs to the model N=4.

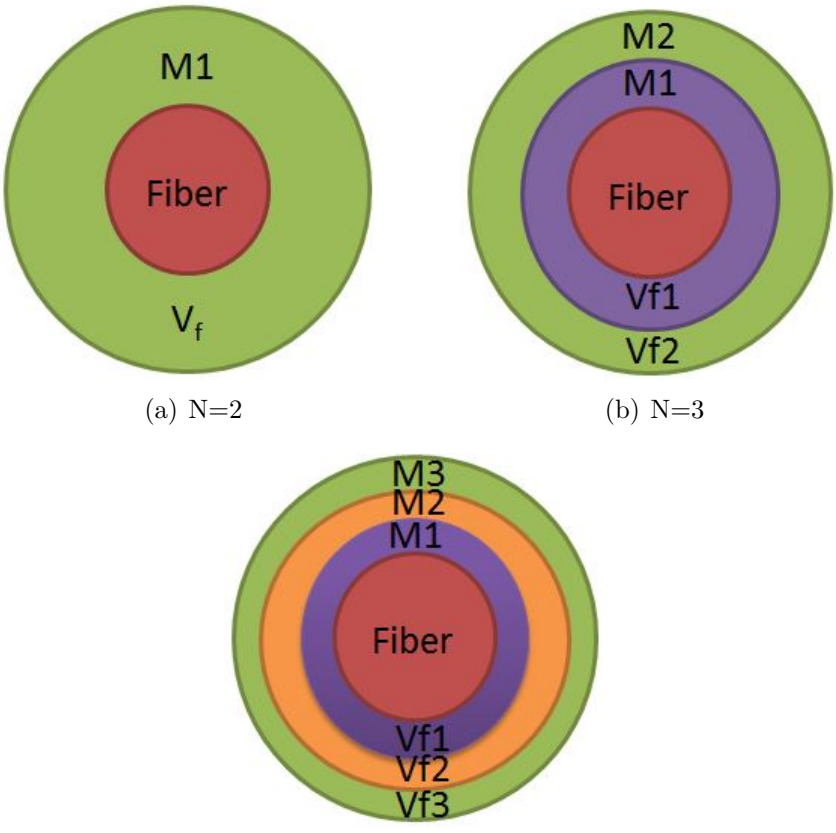

(a) N=2

(b) N=3

(c) N=4

Figure 2.3: Schematic models for NCYL.

The matrix (M1 in Figure 2.3(a)) in-situ properties are calculated from tensile test of $[+45/-45]_{4s}$ laminate as explained in the flow chart above in Figure 2.2. The matrices (M1 and M2 in Figure 2.3(b)) in-situ properties are calculated based on the matrix in-situ properties calculated for N=2. The detailed procedure is explained as a flow chart in Figure 2.4. Again, the in-situ matrices (M1, M2 and M3 in Figure 2.3(c)) properties can be calculated based on the matrix in-situ properties calculated for N=2, as explained in the flow chart in Figure 2.4.

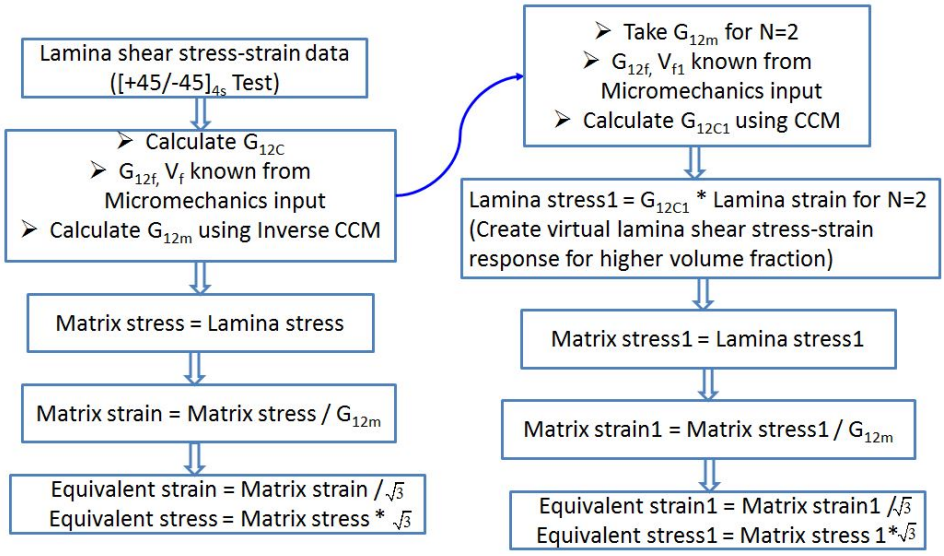

Figure 2.4: Flow chart to calculate the matrix in-situ properties for N=3, 4.

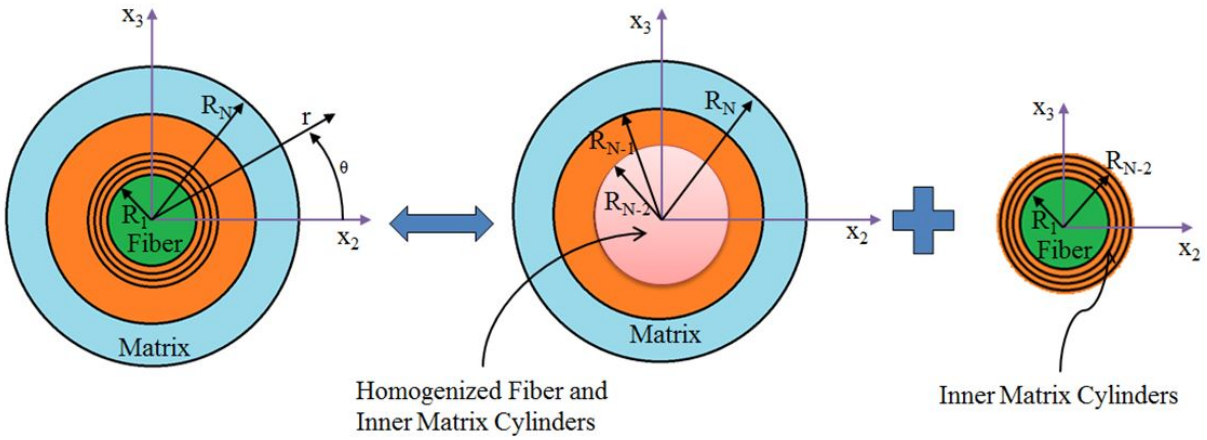

Figure 2.5: Schematic to homogenize the elastic properties for inner layers.

To keep in mind, when calculating the in-situ matrix properties for outer matrix

layer (M2) in Figure 2.3(b), the inner layer of matrix (M1) and the fiber are homogenized, as explained in Figure 2.5. Similar homogenization method is also applicable to N=4 and can be extended to any number of matrix layers in general.

The in-situ nonlinear properties of SC-15 matrix, as computed above are given in Table 2.1. When the damaged matrix layer stiffness is reduced due to microdamage, the nonlinear response of the matrix is modeled through a secant moduli approach, in which the matrix elastic properties are replaced with the corresponding secant moduli. But for undamaged matrix layers, the virgin elastic properties are still retained as explained earlier.

Table 2.1: In-situ nonlinear properties of SC-15 matrix.

	σ_y^m (MPa)	k_1 (MPa)	k_2
M1	30	4500	60

2.4 Analysis procedure

2.4.1 Micromechanics (NCYL model)

In the following analysis, it is assumed that the materials are linearly elastic, so the principle of superposition is applied. As a result, the formulation of the fiber and matrix responses under an arbitrary applied strain is obtained by imposing a single nonzero composite strain and solving the resulting stress and strain fields. From this, the relationship between any applied strain and the response of the stress and strain inside the N-layered composite is obtained. The applied strain in a Cartesian coordinate system is

$$\boldsymbol{\varepsilon}^c = \{\varepsilon_{11}^c \quad \varepsilon_{22}^c \quad \varepsilon_{33}^c \quad \varepsilon_{12}^c \quad \varepsilon_{13}^c \quad \varepsilon_{23}^c\}^T \tag{2.10}$$

where the superscript "c" denotes the applied strain on the composite cylinder, and T denotes the transpose. In order to obtain the stresses and strains inside the N-layered composite, we consider 3 different problems discussed in [5]. First, we consider the problem of an applied axial normal strain, ε_{11}^c. Next, we consider an applied axial shear strain, ε_{12}^c, from which the results for an applied strain ε_{13}^c can also be obtained through a coordinate transformation. The last problem that will be considered is

the Generalized Self-Consistent Method (GSCM) [6], from which the responses of the remaining three applied strains are obtained. In each case the stress and strain fields with the N-layers are solved for in closed form.

2.4.2 Transformation matrix F

The key to the proposed micromechanics model is to relate the applied composite strains to the local matrix strains through a 6 by 6 transformation matrix, $\mathbf{F}$, as

$$\begin{Bmatrix} \varepsilon_{11}^m \\ \varepsilon_{22}^m \\ \varepsilon_{33}^m \\ \gamma_{12}^m \\ \gamma_{13}^m \\ \gamma_{23}^m \end{Bmatrix} = \begin{bmatrix} F_{11} & F_{12} & F_{13} & F_{14} & F_{15} & F_{16} \\ F_{21} & F_{22} & F_{23} & F_{24} & F_{25} & F_{26} \\ F_{31} & F_{32} & F_{33} & F_{34} & F_{35} & F_{36} \\ F_{41} & F_{42} & F_{43} & F_{44} & F_{45} & F_{46} \\ F_{51} & F_{52} & F_{53} & F_{54} & F_{55} & F_{56} \\ F_{61} & F_{62} & F_{63} & F_{64} & F_{65} & F_{66} \end{bmatrix} \begin{Bmatrix} \varepsilon_{11}^c \\ \varepsilon_{22}^c \\ \varepsilon_{33}^c \\ \gamma_{12}^c \\ \gamma_{13}^c \\ \gamma_{23}^c \end{Bmatrix} \tag{2.11}$$

The F_{ij} components can be computed by imposing a single non-zero composite strain at a time on the fiber-matrix N-cylinders and solving the resultant matrix strain fields. It should be noted that the proposed micromechanics model can be extended to any number of matrix layers in general (N arbitrary), but for illustration purposes, in this research, a 4-layered cylinders (N=4) is used for the computation of the axial properties, including the axial tension (E_1^c and ν_{12}^c) and axial shear (G_{12}^c) and this is subsequently used for the computation of the components F_{i1}, F_{i4}, and F_{i5}. The rest of the components in the F matrix are determined via an extended 5-layered GSCM method (N=4 and one outer composite cylinder), which also gives the composite transverse properties, K_{23}^c and G_{23}^c. In each case, the stress and strain fields within the fiber and matrix layers are also obtained in closed-form. The procedures for computing each component in the F matrix as well as the composite effective constants are described in the following section. A Mathematica code is developed to calculate all closed form expressions for the homogenized elastic properties and the F_{ij} components in symbolic form and has been implemented in a multiscale code. So the focus here is to explain the general procedures for any N-cylinders and not to show the explicit lengthy and complex expressions. For reference, the expressions for N=2 are provided in [1] and these are validated by the present Mathematica code.

2.4.3 Computation of E_1^c, ν_{12}^c and F_{i1} components by applying ε_{11}^c

The fiber and $(N-1)$ concentric matrix cylinders are subjected to a constant unidirectional axial strain, ε_{11}^c. We assume axisymmetric response ($\frac{\partial()}{\partial\theta} = 0$) with no shear effects present inside the fiber and the matrices. We will also assume that the displacement fields u_r^i and u_θ^i are independent of the axial coordinate x and u_x^i varies linearly in the axial direction. Therefore, the displacement fields are in the form

$$u_r^i = u_r^i(r) \tag{2.12a}$$

$$u_\theta^i = 0 \tag{2.12b}$$

$$u_x^i = \varepsilon_{11}^c x \tag{2.12c}$$

where u_r, u_θ, and u_x are the radial, circumferential, and axial displacements, respectively, and $i = 1, 2, ...N$. Here $i = 1$ corresponds to the inner fiber layer and $i = 2, 3, ...N$ are the matrix layers. The corresponding nonzero strains are

$$\varepsilon_{rr}^i = \frac{du_r^i}{dr} \tag{2.13a}$$

$$\varepsilon_{\theta\theta}^i = \frac{u_r^i}{r} \tag{2.13b}$$

$$\varepsilon_{xx}^i = \varepsilon_{11}^c \tag{2.13c}$$

The equilibrium equations in each layer in terms of displacement reduces to

$$\frac{d^2u_r^i}{dr^2} + \frac{1}{r}\frac{du_r^i}{dr} - \frac{u_r^i}{r^2} = 0 \tag{2.14}$$

The solution of this second order differential equation is [18]

$$u_r^i = A^i r + \frac{B^i}{r} \tag{2.15}$$

A^i and B^i are unknown constants, which are solved by applying the boundary and continuity conditions. Because the layers are assumed to be perfectly bonded, the displacements and traction are continuous at the interfaces. The continuity conditions at the layer interfaces are,

$$u_r^k(R_k) = u_r^{k+1}(R_k) \tag{2.16a}$$

$$u_x^k(x, R_k) = u_x^{k+1}(x, R_k) \tag{2.16b}$$

$$\sigma_r^k(R_k) = \sigma_r^{k+1}(R_k) \tag{2.16c}$$

where $k = 1, 2, ..., (N-1)$ and R_k is the location of the interface of the layers k and $k+1$. In addition, $B^1 = 0$ in order for u_r^1 to be bounded in the fiber. By also assuming no lateral constraints on the outer matrix layer, we set traction to be zero at the outer matrix layer ($\sigma_r(R_N) = 0$). By applying these boundary conditions, we get $2N$ linear system of equations with $2N$ constants. By solving them, the values of A^i and B^i are obtained, from which the displacement, stress, and strain fields are determined. The composite effective properties are determined by equating the strain energy of the concentric pairs to that of the equivalent homogenized composite material. Following the procedure given in [18], the closed-form expressions for E_1^c and ν_{12}^c are obtained.

Using a Mathematica code, we obtained the closed form expressions for E_1^c, ν_{12}^c for N=4 cylinders in terms of the constituent elastic properties and the fiber volume fraction. The expressions are lengthy and not provided here but the code is verified with the expression for 2-cylinders (N=2) as mentioned in [1]. In order to compute the F_{i1}'s, the only nonzero strain components prescribed on the concentric pair is ϵ_{11}^c. Hence, the lateral surface of the cylinder is constrained, following,

$$u_r(R_N) = 0 \tag{2.17}$$

Solving Equations (2.16) and (2.17) gives all the unknown constants, A^i and B^i, in terms of ϵ_{11}^c. Substituting these constants back in the displacement field, the matrix strain field (ϵ_{xx}^m, ϵ_{rr}^m and $\epsilon_{\theta\theta}^m$) is readily determined from the displacement field, in terms of ϵ_{11}^c. These matrix strains can be further transformed to Cartesian coordinates through the transformation relations provided in Appendix A. Hence, the F_{i1} components are found to be

$$\begin{aligned}
F_{11} &= \epsilon_{11}^m/\epsilon_{11}^c = 1 \\
F_{21} &= \epsilon_{22}^m/\epsilon_{11}^c \\
F_{31} &= \epsilon_{33}^m/\epsilon_{11}^c \\
F_{41} &= \epsilon_{12}^m/\epsilon_{11}^c = 0 \\
F_{51} &= \epsilon_{13}^m/\epsilon_{11}^c = 0 \\
F_{61} &= \epsilon_{23}^m/\epsilon_{11}^c
\end{aligned} \tag{2.18}$$

The expressions for F_{21},F_{31} and F_{61} are obtained using the Mathematica code.

2.4.4 Computation of G_{12}^c and F_{i4} components by applying γ_{12}^c

The outer boundary of the N-layered concentric cylinders is subjected to displacement fields so that an overall axial shear strain of γ_{12}^c is produced. It is convenient to view the representative concentric cylinder units projected onto the $x_1 - x_2$ plane in order to analyze the axial shear response, as shown in Figure 2.6.

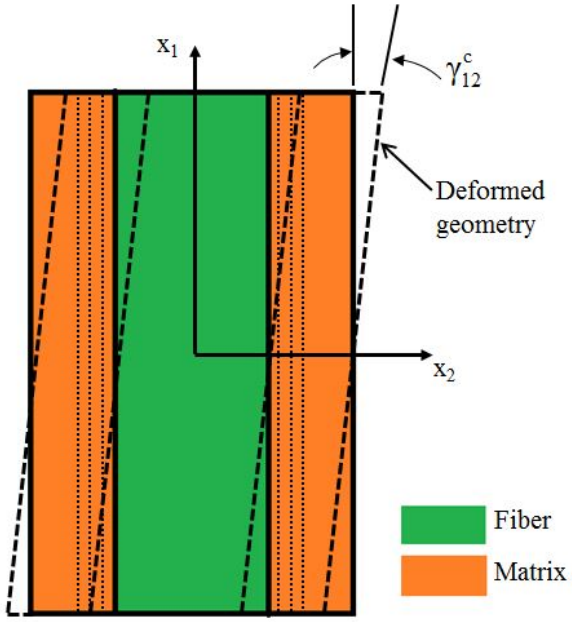

Figure 2.6: Projection of the concentric cylinders onto $x_1 - x_2$ plane when under an axial shear strain, γ_{12}^c.

The resulting displacement fields of the concentric cylinders under an applied shear strain γ_{12}^c are

$$u_x^i = \left(A^i r + \frac{B^i}{r} \right) \cos\theta \tag{2.19a}$$

$$u_\theta^i = -C^i x \sin\theta \tag{2.19b}$$

$$u_r^i = C^i x \cos\theta \tag{2.19c}$$

where $i = 1, ..., N$. The derivation of these equations are further discussed in [1]. Using these displacement fields, we can obtain the strain and stress fields using the strain-displacement relationship and the constitutive equations. We solve for the unknown values A^i, B^i, and C^i $(i = 1, ...N)$ using the displacement and traction

continuity conditions at the fiber-matrix and matrix-matrix interfaces. The continuity conditions are

$$u_x^k(x,\theta,R_k) = u_x^{k+1}(x,\theta,R_k) \tag{2.20a}$$
$$u_\theta^k(x,\theta,R_k) = u_\theta^{k+1}(x,\theta,R_k) \tag{2.20b}$$
$$u_r^k(x,\theta,R_k) = u_r^{k+1}(x,\theta,R_k) \tag{2.20c}$$
$$\tau_{xr}^k(x,\theta,R_k) = \tau_{xr}^{k+1}(x,\theta,R_k) \tag{2.20d}$$

where $k = 1, 2, ..., (N-1)$ and R_k is the location of the interface of the layers k and $k+1$. Note, the second and the third equations in Equation (2.20) result in the same equations. Furthermore, the displacements at the outer boundary of the concentric cylinders must satisfy the imposed boundary conditions so that,

$$u_x^N(x,\theta,R_N) = 0 \tag{2.21a}$$
$$u_\theta^N(x,\theta,R_N) = -\gamma_{12}^c x \sin\theta \tag{2.21b}$$
$$u_r^N(x,\theta,R_N) = \gamma_{12}^c x \cos\theta \tag{2.21c}$$

Similarly, the last two equations in Equation (2.21) provide the same result. Using Equations (2.20) and (2.21), we obtain a linear system of equations, from which the unknown constants A^i, B^i and C^i are solved in terms of γ_{12}^c. By substituting these constants back in the displacement field, matrix shear strain field (γ_{xr}^m and $\gamma_{x\theta}^m$) is readily determined from the displacement field, in terms of γ_{12}^c. The matrix shear stresses are obtained from shear strain fields using the matrix material constitutive law. Since the shear stress at $r = R_N$ and $\theta = 0$ in the cylindrical coordinate system coincides with that in the Cartesian coordinate system, the composite effective axial modulus, G_{12}^c, can be determined by dividing the shear stress by the shear strain. The explicit expressions of G_{12}^c for N=4 cylinders is obtained using the Mathematica code as mentioned earlier. These matrix strains in cylindrical coordinates can be further transformed to Cartesian coordinates through the transformation relations provided

in Appendix A. Hence, the F_{i4} components are found to be,

$$\begin{aligned} F_{14} &= \epsilon_{11}^m/\gamma_{12}^c = 0 \\ F_{24} &= \epsilon_{22}^m/\gamma_{12}^c = 0 \\ F_{34} &= \epsilon_{33}^m/\gamma_{12}^c = 0 \\ F_{44} &= \epsilon_{12}^m/\gamma_{12}^c \\ F_{54} &= \epsilon_{13}^m/\gamma_{12}^c \\ F_{64} &= \epsilon_{23}^m/\gamma_{12}^c = 0 \end{aligned} \tag{2.22}$$

The expressions for F_{44} and F_{54} are obtained using the Mathematica code. In addition, we can obtain the response of the system under γ_{13}^c by replacing θ with $\theta+\frac{\pi}{4}$, following the same procedure as in the case of γ_{12}^c and the corresponding F_{i5} components are found to be,

$$\begin{aligned} F_{15} &= \epsilon_{11}^m/\gamma_{13}^c = 0 \\ F_{25} &= \epsilon_{22}^m/\gamma_{13}^c = 0 \\ F_{35} &= \epsilon_{33}^m/\gamma_{13}^c = 0 \\ F_{45} &= \epsilon_{12}^m/\gamma_{13}^c \\ F_{55} &= \epsilon_{13}^m/\gamma_{13}^c \\ F_{65} &= \epsilon_{23}^m/\gamma_{13}^c = 0 \end{aligned} \tag{2.23}$$

The expressions for F_{45} and F_{55} are obtained using the Mathematica code.

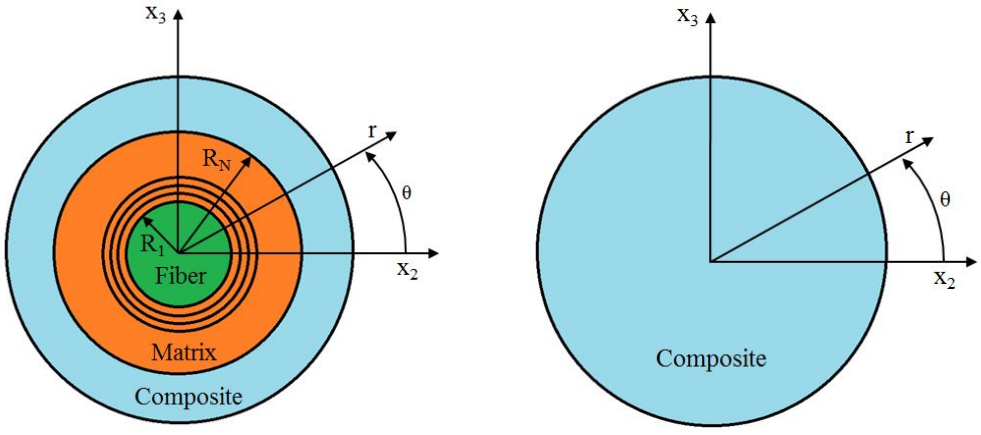

(a) Multilayered concentric cylinders (b) Equivalent composite cylinder

Figure 2.7: Illustration of the NCYL GSCM method (1st Approach).

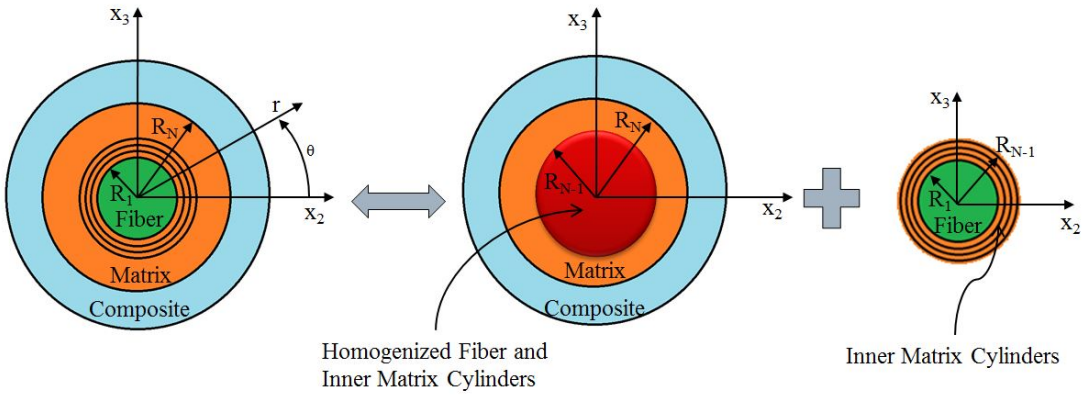

Figure 2.8: Illustration of the NCYL GSCM method (2nd Approach).

2.4.5 Computation of the transverse properties

One of the most challenging problems in composite materials is to predict the exact solution for the effective transverse shear modulus, though there is a considerable amount of literature available on its bounds [5, 19, 20, 21]. It was first proposed by Christensen and Lo [6], that the transverse shear problem can be best solved using the Generalized Self-Consistent Method (GSCM), in which both the fiber and matrix are concentrically embedded in an infinite homogeneous medium with equivalent composite properties. The moduli obtained by this model, although in a somewhat complex format, can be expressed in a closed form and provides a unique approach to interactions among the matrix and fiber reinforcements. However, as used in its eigensolution form, this fiber-matrix-composite model is only applicable to composites with single-phase matrix layer(N=2). The extension of GSCM method from N=2 cylinders to multi cylinders can be approached in two ways: (1) Huang et. al. [22] extended the Christensen and Lo model to multilayered composite cylinders within the general framework of the self-consistent mechanics of composites proposed by Budiansky [10] and Hill [23]. Their method starts with the energy equivalence between summation of individual concentric cylinders and the equivalent composite cylinder, which is considered to be the most fundamental in terms of accommodating multilayered composites. A schematic diagram of NCYL GSCM method for this approach is illustrated in Figure 2.7, with (a) multilayered concentric cylinders embedded in equivalent composite cylinder and (b) the isolated equivalent composite cylinder. It incorporates the Christensen and Lo's configuration into the evaluation of the average strain in each individual cylinder and eventually overcomes all the drawbacks suffered

by the conventional self-consistent method. Their proposed solutions for the effective moduli is to be solved numerically by an iterative method and for N=2, a closed form solution exist which is identical to Christensen and Lo's eigensolution. (2) The second approach can be done by splitting the multilayered cylinders into two parts; one part corresponds to the three-phase model of Christensen and Lo [6], with homogenized cylinder radius R_{N-1}, outer matrix cylinder radius R_N and the equivalent composite cylinder. The other part corresponds to the multi-phase concentric cylinders, with fiber radius R_1, and outer matrix cylinder radius R_{N-1}. The second part is further split in a similar fashion and the process is repeated until it reduces to two-phase concentric cylinder model of Hashin [5], with fiber radius R_1 and matrix cylinder radius R_2. A schematic diagram of NCYL GSCM method for second approach is illustrated in Figure 2.8, where N can vary from 2 to any finite large number and degenerates to the three-phase model of Christensen and Lo [6] for N=2. This latter approach was used by Li et al [24] to evaluate the effective elastic properties of an isotropic elastic medium for four-phases (N=4). The second approach will be used in this work for N-cylinders and anisotropic elastic medium. The computation for the transverse response requires a traction-type boundary condition applied on the outer boundary, rather than the axial problem, in which a strain-type boundary condition is imposed on the outer surface of the concentric cylinders. Since only the transverse response is of interest, the N-layered cylinder model can be reduced into a 2D plane strain problem with the assumption that the fiber is infinitely long in the longitudinal direction. The stress-strain relationships for each layer, including the homogeneous medium are,

$$\begin{pmatrix} \sigma_{22}^i \\ \sigma_{33}^i \\ \tau_{23}^i \end{pmatrix} = \begin{pmatrix} K_{23}^i + G_{23}^i & K_{23}^i - G_{23}^i & 0 \\ K_{23}^i - G_{23}^i & K_{23}^i + G_{23}^i & 0 \\ 0 & 0 & G_{23}^i \end{pmatrix} \begin{pmatrix} \epsilon_{22}^i \\ \epsilon_{33}^i \\ \gamma_{23}^i \end{pmatrix} \tag{2.24}$$

$i = 1, 2, ...N, N+1$, where $N+1^{th}$ layer is the homogenized composite layer. The effective composite properties, K_{23}^{N+1} and G_{23}^{N+1} are determined using the properties of fiber and matrix layers. The Airy's stress function, ϕ, for such a problem in polar coordinates has the form,

$$\phi_i = \frac{M_i}{2} b^2 \ln r + \frac{H_i}{2} r^2 + \left[\frac{A_i}{2} r^2 + \frac{B_i}{2} \frac{r^4}{b^2} + \frac{C_i}{4} \frac{b^4}{r^2} + \frac{D_i}{2} b^2 \right] \cos 2\theta \tag{2.25}$$

where $i = N-1, N, N+1$. The subscripts "N-1", "N" and "N+1" designate the homogenized cylinder, outer matrix cylinder and equivalent composite cylinder respectively as shown in Figure 2.8 and it can vary from N=2 to any finite large num-

ber. For N=2, it degenerates to subscripts "1", "2" and "3" which designate the fiber, matrix and equivalent composite cylinder respectively. The constants M_i, H_i, A_i, B_i, C_i and D_i are to be determined based upon the boundary conditions. The stresses, strains and displacements for the fiber, matrix and equivalent composite material can be computed from the stress function, material constitutive law, and strain-displacement relations, as given in Appendix B.

The key to the N-layered cylinders model for the computation of transverse response is to impose a stress state such that a state of pure shear or transverse tension is achieved in the far field. In particular, the composite effective plane-strain bulk modulus, K^c_{23}, is determined from the biaxial stress state of $\sigma^c_{22} = \sigma^c_{33} = \bar{\sigma}$, while the transverse shear modulus, G^c_{23}, is computed under the far field stress state of $\sigma^c_{22} = -\sigma^c_{33} = \bar{\sigma}$. Though the determination of $F'_{ij}s$ require a single strain to be imposed on the concentric cylinders, the results can be easily deduced from a single stress loading condition.

In order to determine the response of the fiber and the matrices under an applied strain ε^c_{22}, we first consider two problems. The solution of these problems will be superimposed in order to obtain the stress and strain responses under a single applied strain ε^c_{22}.

2.4.5.1 Computation of K^c_{23} by applying biaxial stresses $\sigma^c_{22} = \sigma^c_{33} = \overline{\sigma}$

The solution of an infinite medium under a biaxial state of stress, as shown in Figure 2.9, is well known in the literature.

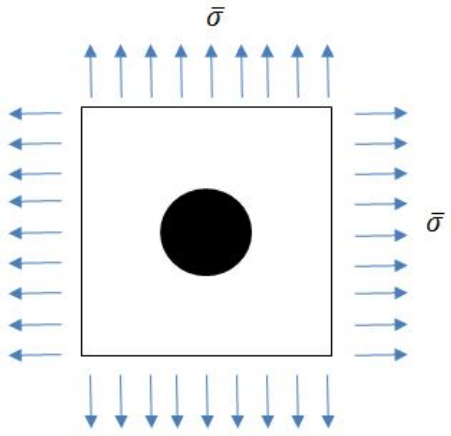

Figure 2.9: Infinite medium with an inclusion subjected to biaxial tensile stress.

This problem is taken to be axisymmetric, resulting in $A_i = B_i = C_i = D_i = 0$ $(i = N-1, N, N+1)$ and $H_{N+1} = \overline{\sigma}$ (state of hydrostatic stress is reached as

$r \to \infty$). The remaining unknowns constants, H_{N-1}, M_N, H_N and M_{N+1} are solved using the traction and displacement continuity conditions as,

$$\sigma_{rr}^{k}(r = R_k) = \sigma_{rr}^{k+1}(r = R_k) \tag{2.26a}$$

$$u_{r}^{k}(r = R_k) = u_{r}^{k+1}(r = R_k) \tag{2.26b}$$

where $k = N-1, N$. This boundary value problem can be written in a matrix form as,

$$\begin{bmatrix} 1 & -\frac{1}{2}\left(\frac{1}{V_f}\right) & -1 & 0 \\ 2\frac{G_{23}^{N-1}}{K_{23}^{N-1}} & \frac{G_{23}^{N-1}}{G_{23}^{N}}\frac{1}{V_f} & -2\frac{G_{23}^{N-1}}{K_{23}^{N}} & 0 \\ 0 & \frac{1}{2} & 1 & -\frac{1}{2} \\ 0 & -\frac{G_{23}^{N+1}}{G_{23}^{N}} & 2\frac{G_{23}^{N+1}}{K_{23}^{N}} & 1 \end{bmatrix} \begin{Bmatrix} H_{N-1} \\ M_N \\ H_N \\ M_{N+1} \end{Bmatrix} = \begin{Bmatrix} 0 \\ 0 \\ \bar{\sigma} \\ 2\frac{G_{23}^{N+1}}{K_{23}^{N+1}}\bar{\sigma} \end{Bmatrix} \tag{2.27}$$

Next, the internal strain energy of the three-phase cylinder model (Figure 2.8) is equated to that of the equivalent composite medium (Figure 2.7(b)) based upon an important finding by Eshelby [25], which states that for a homogeneous medium containing an inclusion, the strain energy, U, under applied displacement conditions, is determined by

$$U = U^o - \frac{1}{2}\int_s \left(T_i^o u_i - T_i u_i^o\right) \mathrm{d}S \tag{2.28}$$

where S is the surface of the inclusion, U^o is the strain energy of the equivalent composite medium without inclusion, T_i^o and u_i^o are the tractions and displacements of the equivalent medium without inclusion, and T_i and u_i are the corresponding quantities for the composite medium with the inclusion. Obviously, the strain energy of the equivalent composite in Figure 2.7(b), U^{equiv}, is identical to that of the composite medium in Figure 2.7(a) if there is no inclusion, which yields $U^{equiv} = U^o$. Based on the strain energy equivalence stated previously, $U^{equiv} = U$. Using the notation for the tractions and corresponding displacements, Equation (2.28) becomes

$$\int_0^{2\pi} \left[\sigma_{rr}^o U_r - \sigma_{rr} U_r^o\right]_{r=b} b \, \mathrm{d}\theta = 0 \tag{2.29}$$

where the stresses and displacements for the equivalent medium without inclusions

are

$$\sigma_{rr}^{o} = \bar{\sigma} \qquad U_r^o = \frac{r}{2K_{23}^{N+1}}\bar{\sigma} \tag{2.30}$$

Substituting the results for the stresses and displacements of the equivalent composites (Equations. (B.6) and (B.12) in Appendix B respectively) as well as Equation (2.30) into Equation (2.29) gives,

$$M_{N+1} = 0 \tag{2.31}$$

Thus, by solving the boundary conditions in Equation (2.27) and setting M_{N+1} to zero, the effective plane-strain bulk modulus, K_{23}^c, can be obtained as

$$K_{23}^c = K_{23}^{N+1} = K_{23}^N + \frac{V_f}{\frac{1}{K_{23}^{N-1} - K_{23}^N} + \frac{1-V_f}{K_{23}^N + G_{23}^N}} \tag{2.32}$$

The explicit expression of K_{23}^c for N=4 cylinders is obtained using the Mathematica code as mentioned earlier. In addition, the stresses, strains and displacement fields for each constituent in the instance that the outer boundary of the equivalent composite material is subjected to biaxial tension are obtained through Equations (B.4)-(B.12) in Appendix B.

2.4.5.2 Computation of G_{23}^c by applying biaxial stresses $\sigma_{22}^c = -\sigma_{33}^c = \overline{\sigma}$

The second problem that we consider is an infinite 2D medium under a tensile stress state, $\sigma_{22}^c = \overline{\sigma}$ and a compressive stress, $\sigma_{33}^c = -\overline{\sigma}$ as shown in Figure 2.10.

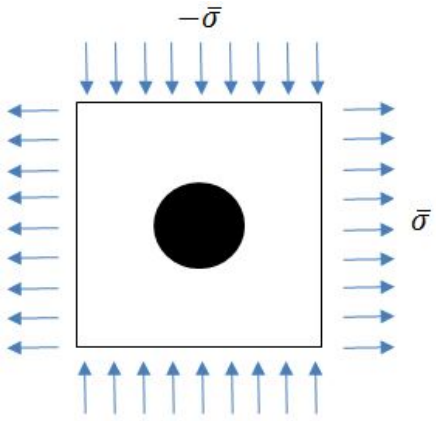

Figure 2.10: Infinite medium with an inclusion under a tension and compression in orthogonal directions.

The state of stress $\sigma_{22}^c = -\sigma_{33}^c = \overline{\sigma}$ is achieved in the far field ($r \to \infty$) by setting $M_i = H_i = 0$ $(i = N-1, N, N+1)$ and $A_{N+1} = -\overline{\sigma}$. The remaining unknowns are obtained using the continuity conditions of traction and displacement at all the layer interfaces as,

$$\sigma_{rr}^k(r = R_k) = \sigma_{rr}^{k+1}(r = R_k) \tag{2.33a}$$
$$\sigma_{r\theta}^k(r = R_k) = \sigma_{r\theta}^{k+1}(r = R_k) \tag{2.33b}$$
$$u_r^k(r = R_k) = u_r^{k+1}(r = R_k) \tag{2.33c}$$
$$u_\theta^k(r = R_k) = u_\theta^{k+1}(r = R_k) \tag{2.33d}$$

where $k = N-1, N$. This boundary value problem can be written in a matrix form as,

$$[b]\,\{d\} = \{f\} \tag{2.34}$$

where,

$$b = \begin{bmatrix}
-1 & 0 & 1 & 0 & \frac{3}{2}\left(\frac{1}{V_f}\right)^2 & 2\frac{1}{V_f} & 0 & 0 \\
1 & 3V_f & -1 & -3V_f & \frac{3}{2}\left(\frac{1}{V_f}\right)^2 & \frac{1}{V_f} & 0 & 0 \\
-2 & 2\left(\frac{G_{23}^{N-1}}{K_{23}^{N-1}} - 1\right)V_f & 2\frac{G_{23}^{N-1}}{G_{23}^{N}} & -2\frac{G_{23}^{N-1}}{G_{23}^{N}}\left(\frac{G_{23}^{N}}{K_{23}^{N}} - 1\right)V_f & -\frac{G_{23}^{N-1}}{G_{23}^{N}}\left(\frac{1}{V_f}\right)^2 & -2\frac{G_{23}^{N-1}}{G_{23}^{N}}\left(\frac{G_{23}^{N}}{K_{23}^{N}} + 1\right)\frac{1}{V_f} & 0 & 0 \\
2 & 2\left(\frac{G_{23}^{N-1}}{K_{23}^{N-1}} + 2\right)V_f & -2\frac{G_{23}^{N-1}}{G_{23}^{N}} & -2\frac{G_{23}^{N-1}}{G_{23}^{N}}\left(\frac{G_{23}^{N}}{K_{23}^{N}} + 2\right)V_f & -\frac{G_{23}^{N-1}}{G_{23}^{N}}\left(\frac{1}{V_f}\right)^2 & 2\frac{G_{23}^{N-1}}{K_{23}^{N}}\frac{1}{V_f} & 0 & 0 \\
0 & 0 & -1 & 0 & -\frac{3}{2} & -2 & \frac{3}{2} & 2 \\
0 & 0 & 1 & 3 & -\frac{3}{2} & -1 & \frac{3}{2} & 1 \\
0 & 0 & -2\frac{G_{23}^{N+1}}{G_{23}^{N}} & 2\frac{G_{23}^{N+1}}{G_{23}^{N}}\left(\frac{G_{23}^{N}}{K_{23}^{N}} - 1\right) & \frac{G_{23}^{N+1}}{G_{23}^{N}} & 2\frac{G_{23}^{N+1}}{G_{23}^{N}}\left(\frac{G_{23}^{N}}{K_{23}^{N}} + 1\right) & -1 & -2\left(\frac{G_{23}^{N+1}}{K_{23}^{N+1}} + 1\right) \\
0 & 0 & 2\frac{G_{23}^{N+1}}{G_{23}^{N}} & 2\frac{G_{23}^{N+1}}{G_{23}^{N}}\left(\frac{G_{23}^{N}}{K_{23}^{N}} + 2\right) & \frac{G_{23}^{N+1}}{G_{23}^{N}} & -2\frac{G_{23}^{N+1}}{K_{23}^{N+1}} & -1 & 2\frac{G_{23}^{N+1}}{K_{23}^{N+1}}
\end{bmatrix}$$

$$d = \begin{bmatrix} A_{N-1} & B_{N-1} & A_N & B_N & C_N & D_N & C_{N+1} & D_{N+1} \end{bmatrix}^T$$

$$f = \begin{bmatrix} 0 & 0 & 0 & 0 & \bar{\sigma} & -\bar{\sigma} & 2\bar{\sigma} & -2\bar{\sigma} \end{bmatrix}^T \tag{2.35}$$

Eshelby's results [25] on the strain energy equivalence gives,

$$\int_0^{2\pi} \left[\sigma_{rr}^o U_r + \sigma_{r\theta}^o U_\theta - \sigma_{rr} U_r^o - \sigma_{r\theta} U_\theta^o\right]_{r=b} b\,\mathrm{d}\theta = 0 \tag{2.36}$$

where the stresses and displacements for the equivalent medium without the inclusions

are,

$$\begin{aligned} \sigma^o_{rr} &= \tau_{23}\cos 2\theta \qquad & \sigma^o_{r\theta} &= -\tau_{23}\sin 2\theta \\ U^o_r &= \frac{r}{2G^{N+1}_{23}}\tau_{23}\cos 2\theta \qquad & U^o_\theta &= -\frac{r}{2G^{N+1}_{23}}\tau_{23}\sin 2\theta \end{aligned} \tag{2.37}$$

Similarly, the substitution of the stresses and displacements of the composite material (Equations (B.6) and (B.12) in Appendix B, respectively) as well as Equation (2.37) into Equation (2.36) results in,

$$D_{N+1} = 0 \tag{2.38}$$

Thus, if the boundary conditions in Equation (2.34) are solved, and we set D_{N+1} to be zero, it gives the results for the composite effective transverse shear modulus through a quadratic equation as,

$$X\left(\frac{G^{N+1}_{23}}{G^N_{23}}\right)^2 + Y\left(\frac{G^{N+1}_{23}}{G^N_{23}}\right) + Z = 0 \tag{2.39}$$

where,

$$\begin{aligned} X &= a_0 + a_1V_f + a_2V_f^2 + a_3V_f^3 + a_4V_f^4 \\ Y &= b_0 + b_1V_f + b_2V_f^2 + b_3V_f^3 + b_4V_f^4 \\ Z &= c_0 + c_1V_f + c_2V_f^2 + c_3V_f^3 + c_4V_f^4 \end{aligned}$$

with,

$$\begin{aligned} a_0 &= -2G^{N^2}_{23}\left(2G^N_{23}+K^N_{23}\right)\left[2G^{N-1}_{23}G^N_{23}+K^{N-1}_{23}(G^{N-1}_{23}+G^N_{23})\right]\left[2G^{N-1}_{23}G^N_{23}+K^N_{23}(G^{N-1}_{23}+G^N_{23})\right] \\ a_1 &= 8G^{N^2}_{23}\left(G^{N-1}_{23}-G^N_{23}\right)\left[2G^{N-1}_{23}G^N_{23}+K^{N-1}_{23}(G^{N-1}_{23}+G^N_{23})\right]\left(G^{N^2}_{23}+G^N_{23}K^N_{23}+K^{N^2}_{23}\right) \\ a_2 &= -12G^{N^2}_{23}K^{N^2}_{23}\left(G^{N-1}_{23}-G^N_{23}\right)\left[2G^{N-1}_{23}G^N_{23}+K^{N-1}_{23}(G^{N-1}_{23}+G^N_{23})\right] \\ a_3 &= 8G^{N^2}_{23}\Big\{G^{N-1^2}_{23}G^{N^2}_{23}K^{N-1}_{23}+G^{N-1^2}_{23}G^N_{23}K^N_{23}(K^{N-1}_{23}-G^N_{23})+K^{N^2}_{23}\Big[G^{N-1}_{23}G^N_{23}(G^{N-1}_{23}-2G^N_{23})+ \\ &\quad K^{N-1}_{23}(G^{N-1}_{23}-G^N_{23})(G^{N-1}_{23}+G^N_{23})\Big]\Big\} \\ a_4 &= 2G^{N^2}_{23}\left(G^{N-1}_{23}-G^N_{23}\right)\left(2G^N+K^N_{23}\right)\left[K^{N-1}_{23}G^N_{23}K^N_{23}-G^{N-1}_{23}\left(2G^N_{23}(K^{N-1}_{23}-K^N_{23})+K^{N-1}_{23}K^N_{23}\right)\right] \\ b_0 &= 4G^{N^3}_{23}\left[2G^{N-1}_{23}G^N_{23}+K^{N-1}_{23}(G^{N-1}_{23}+G^N_{23})\right]\left[2G^{N-1}_{23}G^N_{23}+K^N_{23}(G^{N-1}_{23}+G^N_{23})\right] \\ b_1 &= 8G^{N^2}_{23}K^N_{23}\left(G^{N-1}_{23}-G^N_{23}\right)\left[2G^{N-1}_{23}G^N_{23}+(G^{N-1}_{23}+G^N_{23})K^{N-1}_{23}\right]\left(G^N_{23}-K^N_{23}\right) \\ b_2 &= -2a_2 \\ b_3 &= -2a_3 \end{aligned}$$

$$b_4 = -4G_{23}^{N^3}\left(G_{23}^{N-1} - G_{23}^{N}\right)\left[K_{23}^{N-1}G_{23}^{N}K_{23}^{N} - G_{23}^{N-1}\left(2G_{23}^{N}(K_{23}^{N-1} - K_{23}^{N}) + K_{23}^{N-1}K_{23}^{N}\right)\right]$$

$$c_0 = 2G_{23}^{N^2}K_{23}^{N}\left[2G_{23}^{N-1}G_{23}^{N} + K_{23}^{N-1}(G_{23}^{N-1} + G_{23}^{N})\right]\left[2G_{23}^{N-1}G_{23}^{N} + K_{23}^{N}(G_{23}^{N-1} + G_{23}^{N})\right]$$

$$c_1 = 8G_{23}^{N^2}K_{23}^{N^2}\left(G_{23}^{N-1} - G_{23}^{N}\right)\left[2G_{23}^{N-1}G_{23}^{N} + K_{23}^{N-1}(G_{23}^{N-1} + G_{23}^{N})\right]$$

$$c_2 = a_2$$

$$c_3 = a_3$$

$$c_4 = -2G_{23}^{N^2}K_{23}^{N}\left(G_{23}^{N-1} - G_{23}^{N}\right)\left[K_{23}^{N-1}G_{23}^{N}K_{23}^{N} - G_{23}^{N-1}\left(2G_{23}^{N}(K_{23}^{N-1} - K_{23}^{N}) + K_{23}^{N-1}K_{23}^{N}\right)\right]$$

From this, we can determine the value of the effective transverse shear modulus, G_{23}^{c} or G_{23}^{N+1}, by solving the above quadratic equation. The explicit expression of G_{23}^{c} for N=4 cylinders is obtained using the Mathematica code as mentioned earlier. Finally, a complete set of stresses, strains and displacements for each constituent corresponding to transverse shear is obtained through Equations (B.4)-(B.12) in Appendix B.

2.4.5.3 Computation of F_{i2}, F_{i3}, and F_{i6} components

So far, the stress and strain fields of each constituent in the three-phase cylinder model have been determined for the cases that $\sigma_{22}^{c} = \sigma_{33}^{c} = \bar{\sigma}$ or $\sigma_{22}^{c} = -\sigma_{33}^{c} = \bar{\sigma}$ is imposed, as shown in Figures 2.9 and 2.10 respectively. The matrix strain fields due to a single normal stress, either $\sigma_{22}^{c} = \bar{\sigma}$ or $\sigma_{33}^{c} = \bar{\sigma}$, can be obtained through the superposition of the aforementioned two stress states as shown in Figure 2.11, while the state of pure shear, $\tau_{23}^{c} = \bar{\sigma}$, can be easily deduced from the stress state of $\sigma_{22}^{c} = -\sigma_{33}^{c} = \bar{\sigma}$ by changing θ to $\theta + \pi/4$.

Now, we assume an infinite medium, similar to those in Figures 2.9 and 2.10, under a constant applied single normal strain ε_{22}^{c}. Using the constitutive equations, the resulting stresses are $\sigma_{22}^{c} = (K_{23}^{c} + G_{23}^{c})\varepsilon_{22}^{c}$, $\sigma_{33}^{c} = (K_{23}^{c} - G_{23}^{c})\varepsilon_{22}^{c}$ and $\tau_{23}^{c} = 0$. The stress and strain response of this problem due to a single applied stress (σ_{22}^{c} or σ_{33}^{c}) is obtained by superimposing the stress and strains of the solutions obtained in Section 2.4.5.1 and 2.4.5.2. Since the elasticity problem due to a single applied stress has been solved, the matrix strain fields due to ϵ_{22}^{c} can be easily obtained by superposing the results from the two stresses, σ_{22}^{c} and σ_{33}^{c}. Thus, the matrix strain field (ϵ_{rr}^{m}, $\epsilon_{\theta\theta}^{m}$ and $\gamma_{r\theta}^{m}$) is readily determined in terms of ϵ_{22}^{c}. These matrix strains can be further transformed to Cartesian coordinates through the transformation relations provided

in Appendix A. Hence, the F_{i2} components are found to be

$$\begin{aligned} F_{12} &= \epsilon_{11}^m/\epsilon_{22}^c = 0 \\ F_{22} &= \epsilon_{22}^m/\epsilon_{22}^c \\ F_{32} &= \epsilon_{33}^m/\epsilon_{22}^c \\ F_{42} &= \gamma_{12}^m/\epsilon_{22}^c = 0 \\ F_{52} &= \gamma_{13}^m/\epsilon_{22}^c = 0 \\ F_{62} &= \gamma_{23}^m/\epsilon_{22}^c \end{aligned} \tag{2.40}$$

The expressions for F_{22},F_{32} and F_{62} for N=4 cylinders are obtained using the Mathematica code.

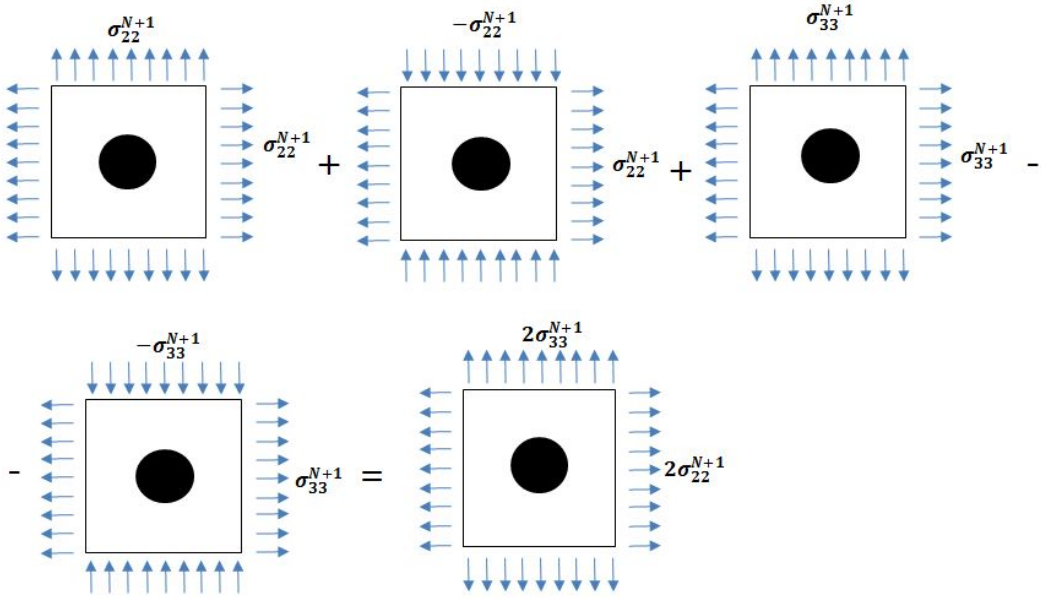

Figure 2.11: Applying superposition.

Similarly, the F_{i3} components can be computed by imposing a single strain ϵ_{33}^c and the resulting non-vanishing components are

$$\begin{aligned} F_{13} &= \epsilon_{11}^m/\epsilon_{33}^c = 0 \\ F_{23} &= \epsilon_{22}^m/\epsilon_{33}^c \\ F_{33} &= \epsilon_{33}^m/\epsilon_{33}^c \\ F_{43} &= \gamma_{12}^m/\epsilon_{33}^c = 0 \\ F_{53} &= \gamma_{13}^m/\epsilon_{33}^c = 0 \\ F_{63} &= \gamma_{23}^m/\epsilon_{33}^c \end{aligned} \tag{2.41}$$

The expressions for F_{23},F_{33} and F_{63} for N=4 cylinders are obtained using the Mathematica code. The matrix strains due to a single composite strain γ_{23}^c can be obtained from the case where a transverse shear stress is imposed in the far field of the N-layered cylinder. The composite transverse stress and strain are simply related by $\tau_{23}^c = G_{23}^c \gamma_{23}^c$, where $\tau_{23}^c = \bar{\sigma}$ is deduced from the stress state $\sigma_{22}^c = -\sigma_{33}^c = \bar{\sigma}$ in Section 2.4.5.2 by changing θ to $\theta + \pi/4$. Thus the F_{i6} components are computed from the matrix strains due to γ_{23}^c as,

$$\begin{aligned} F_{16} &= \epsilon_{11}^m/\gamma_{23}^c = 0 \\ F_{26} &= \epsilon_{22}^m/\gamma_{23}^c \\ F_{36} &= \epsilon_{33}^m/\gamma_{23}^c \\ F_{46} &= \gamma_{12}^m/\gamma_{23}^c = 0 \\ F_{56} &= \gamma_{13}^m/\gamma_{23}^c = 0 \\ F_{66} &= \gamma_{23}^m/\gamma_{23}^c \end{aligned} \tag{2.42}$$

The expressions for F_{26}, F_{36} and F_{66} for N=4 cylinders are obtained using the Mathematica code.

2.4.6 Matrix strain contours under a single applied composite strain

In the previous section, all the columns of **F** matrix are computed by applying the six strain components one at a time. As mentioned earlier, the populated **F** matrix relates the matrix strain components to the applied composite strains as shown in Equation 2.11. In order to validate the proposed micromechanics model, the computed matrix strain fields under a globally prescribed single composite strain using the current analytical solutions are compared against the results from a corresponding 3D FEA. The FEA model utilized to analyze the axial tension and axial shear problem is a 3D 4-layered (1 fiber+3 matrix layers) cylinder model as shown in Figure 2.12. When the cylinder is subjected to axial tensile loading, the problem is axisymmetric, hence, $U_\theta = 0$ is enforced everywhere on the boundary. To ensure a single axial strain is prescribed on the cylinder, one end of the cylinder is fixed ($u_x(x = 0) = 0$), while the other end is subjected to an axial displacement δ. The outer lateral surface is constrained ($u_r(r = R_N) = 0$) such that only a single axial strain is present. The overall axial strain is calculated as δ/L, where L is the length of the cylinder. The boundary conditions for the axial shear problem are given by, Equation (2.21), with

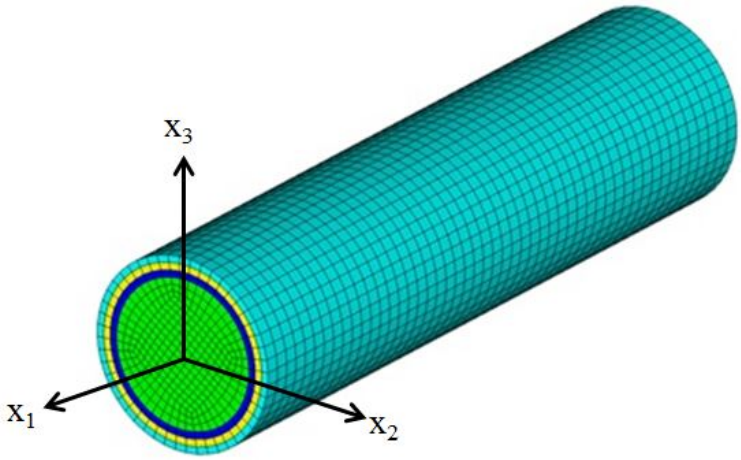

Figure 2.12: FE Model for NCYL Method.

one end fixed. Note that L should be large enough to ignore boundary effects at the ends.

The FEA model used to solve for the transverse tension and transverse shear problem is a 3D 5-layered model, in which one fiber layer and three matrix layers are concentrically embedded in the equivalent composite medium as illustrated in Figure 2.13. Since the equivalent composite medium is assumed to be large enough to produce uniform stress and strain distributions at the boundary, the outer boundary of the composite is modeled as rectangular so that the boundary conditions can be enforced easily. The boundary conditions for transverse normal and transverse shear loading are summarized in Table 2.2.

Table 2.2: Boundary conditions for the transverse normal and transverse shear problem.

	Transverse normal $\epsilon^c_{22} = \bar{\epsilon}$	Transverse shear $\gamma^c_{23} = \bar{\gamma}$
ABCD	$U_1 = 0$	$U_1 = 0$
EFGH	$U_1 = 0$	$U_1 = 0$
AEHD	$U_2 = 0$	$U_2 = 0$, $U_3 = 0$
BFGC	$U_2 = \bar{\epsilon}\, L_2$	$U_2 = 0$, $U_3 = \bar{\gamma}\, L_2$
ABFE	$U_3 = 0$	$U_3 = \bar{\gamma}\, x_2$
DCGH	$U_3 = 0$	$U_3 = \bar{\gamma}\, x_2$

The boundary conditions are prescribed on each outer surface of the rectangle. L_1, L_2 and L_3 are the length of the rectangle along x_1, x_2 and x_3 directions, respectively.

Since the composite is assumed to be transversely isotropic, only four loading conditions are considered, which are axial tension, axial shear, transverse tension

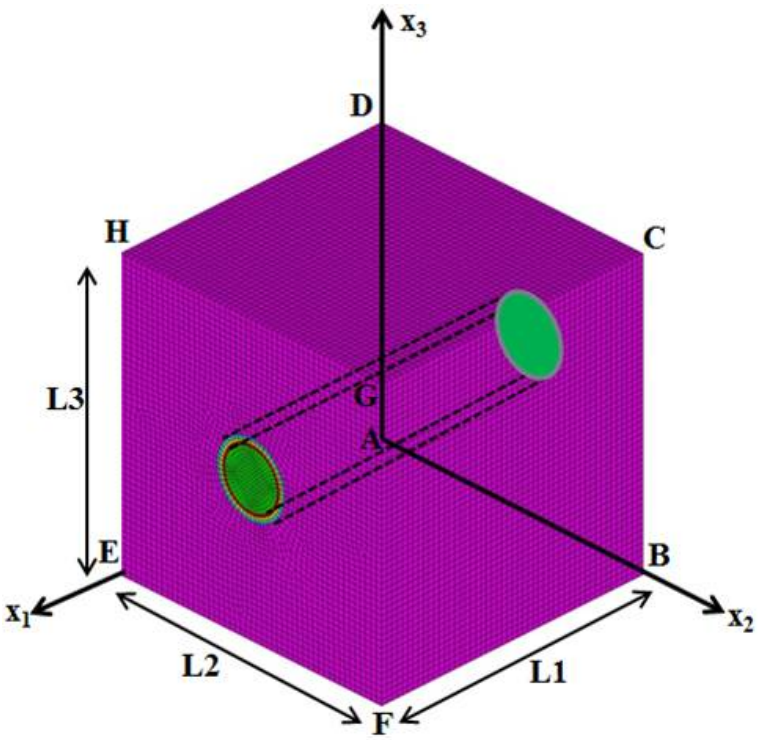

Figure 2.13: FE Model for GSCM Method.

and transverse shear. In each case, a single strain value of 0.1% is prescribed to the relevant component and the remaining strains are enforced to be zero. Since the composite undergoes small deformation, both the fiber and matrix are linear elastic in this regime. The elastic properties of the constituent materials are summarized in Table 2.3, which are taken from various sources [18, 26]. Both S-2 glass fiber and SC-15 epoxy resin are isotropic, while IM-7 carbon fiber is transversely isotropic. The fiber volume fraction is set to 60% in each case.

Table 2.3: The elastic properties for IM-7 carbon fiber, S-2 glass fiber, and SC-15 matrix.

	E_1 GPa	E_2 GPa	ν_{12} -	G_{12} GPa	G_{23} GPa
IM-7 Carbon Fiber	276.0	15.0	0.279	12.0	5.02
S-2 Glass Fiber	114.2	114.2	0.22	46.8	46.8
SC-15 Matrix	2.487	2.487	0.35	0.921	0.921

Figures 2.14-2.17 show the matrix strain contours, for each component, under various applied composite strains as well as the results from the FEA models, in which the constituent fiber is IM-7 carbon fiber. The results for the glass fiber are not shown here. It can be concluded that the proposed micromechanics model provides accurate

prediction of the spatial variation of the matrix fields when the composite is subjected to loading. Capturing the strain and stress concentrations in the matrix material is important to determine the damage and failure characteristics of composites such as nonlinear stress versus strain response, strain to failure, strength and fatigue life. In Section 2.5, a multi-scale computational framework is established to compute the composite nonlinear behavior, in which the proposed analytical method is employed for the subscale micromechanical analysis.

2.5 Multiscale approach for nonlinear homogenized fiber composite

The macroscopic nonlinear response of composite materials is influenced by matrix micro damage at the subscale. The motivation of the current study is to relate the subscale micromechanical analysis to the composite effective response at the macroscale through a multiscale modeling framework. In the proposed model, two scalar variables that characterize the evolution of the matrix microdamage based upon the strain contours computed, are selected. The proposed model is different from previous mean-field methods, in that, the extreme value of the matrix strains are utilized rather than the average value to determine the composite nonlinear damage progression.

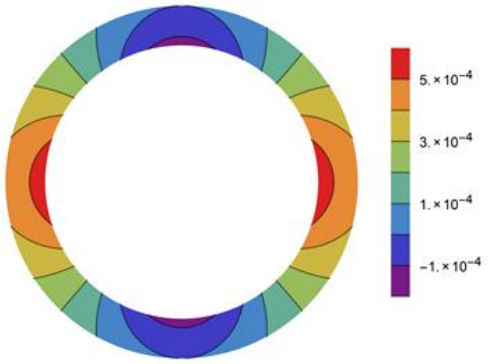

(a) ε_{22}^m from proposed model

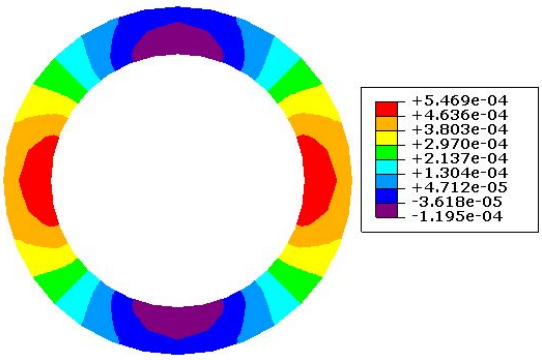

(b) ε_{22}^m from FEA

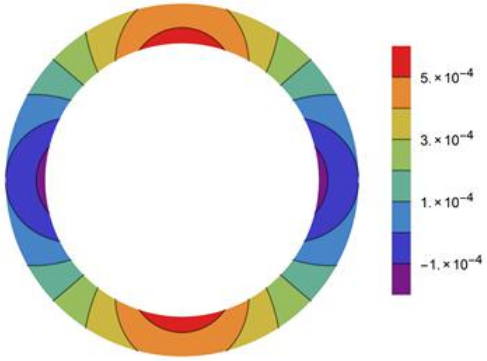

(c) ε_{33}^m from proposed model

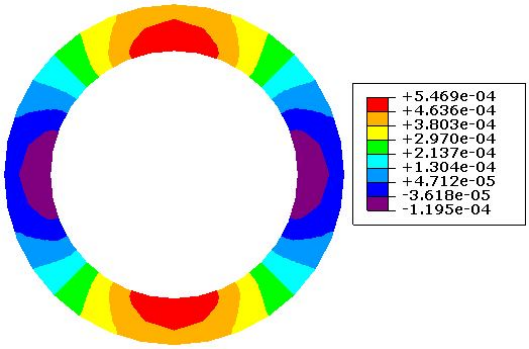

(d) ε_{33}^m from FEA

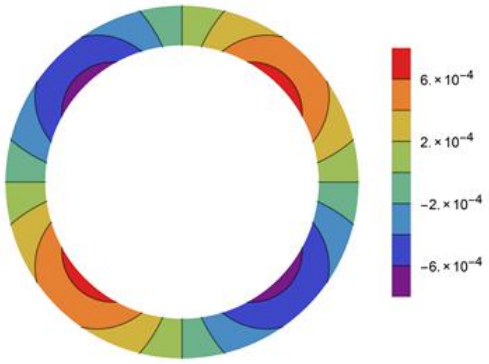

(e) γ_{23}^m from proposed model

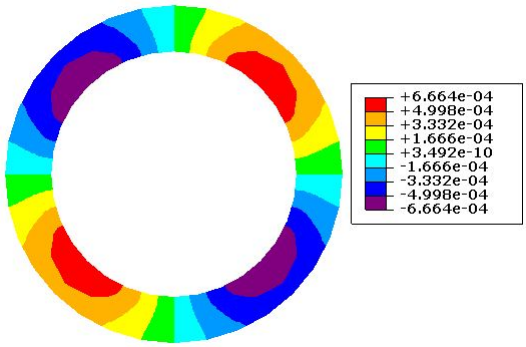

(f) γ_{23}^m from FEA

Figure 2.14: Matrix contours under $\varepsilon_{11}^c = 0.1\%$.

2.5.1 Multiscale computational framework

The multiscale methodology established in this work is based upon two scales. As an example, for the macroscale, tow-level analysis of a unidirectional composite is conducted by utilizing effective homogenized properties to compute stress and strains in the composite. Simultaneously, it is intended to carry out the subscale analysis, at the fiber and matrix level, using the micromechanics model, in which the constituent

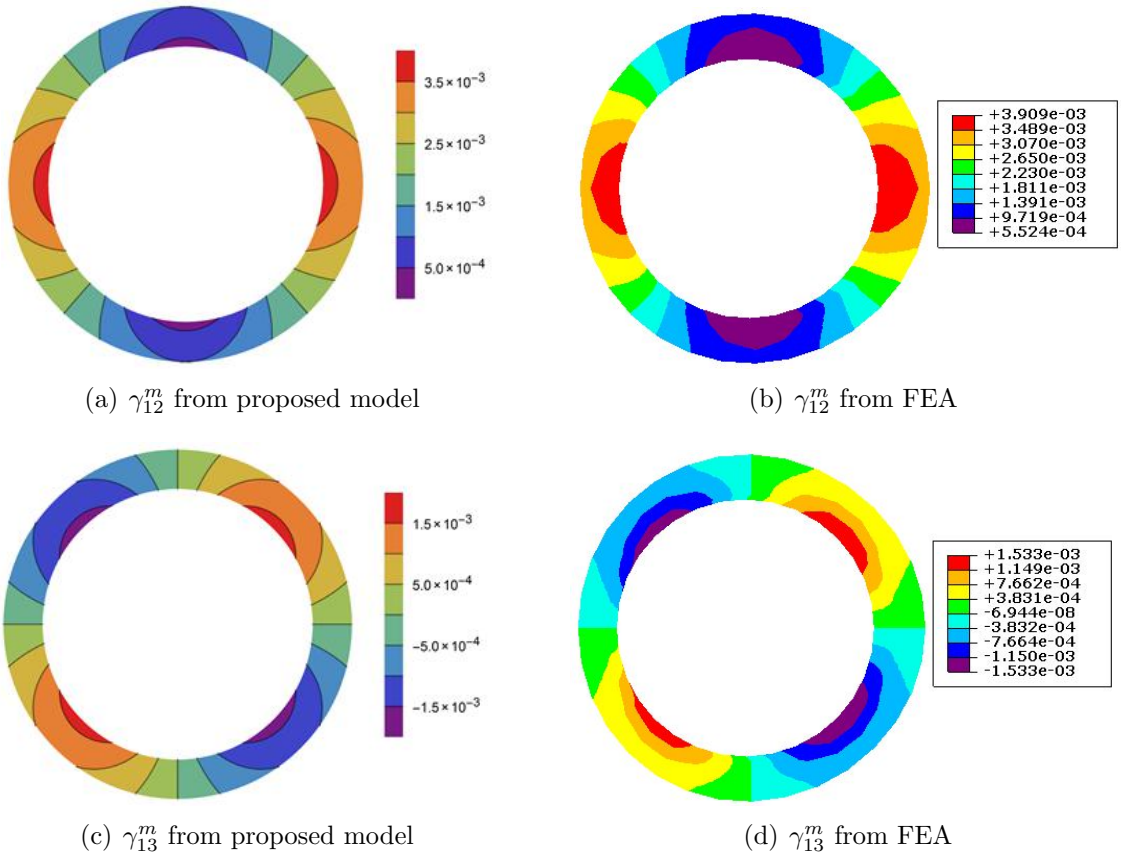

(a) γ_{12}^m from proposed model

(b) γ_{12}^m from FEA

(c) γ_{13}^m from proposed model

(d) γ_{13}^m from FEA

Figure 2.15: Matrix contours under $\gamma_{12}^c = 0.1\%$.

stress and strain fields are provided in closed form. A flowchart of the multiscale approach followed is shown in Figure 2.18. The commercially available finite element software, ABAQUS (version 6.14), is used for the macroscale FEA, and the micromechanics model at the subscale is implemented at each integration point of the macro scale, using a user defined material subroutine, UMAT. This subroutine is called at each integration point at each increment, and the material constitutive law is updated through user-defined options. At the start of each increment, the material state i.e. stress-strain and solution-dependent state variables from the previous equilibrium step and the strain increments in the current step are passed into the UMAT through the ABAQUS solver. In the n^{th} increment, the total strain, ϵ_{ij}^n, is calculated by adding the current strain increment, $d\epsilon_{ij}^n$, to the strain in the previous step, ϵ_{ij}^{n-1}, as $\epsilon_{ij}^n = \epsilon_{ij}^{n-1} + d\epsilon_{ij}^n$.

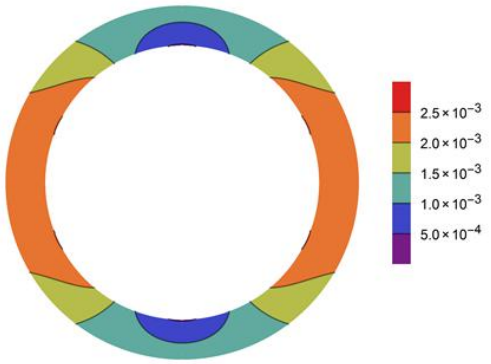

(a) ε_{22}^m from proposed model

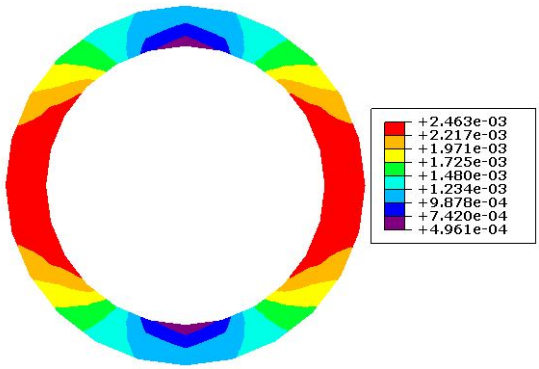

(b) ε_{22}^m from FEA

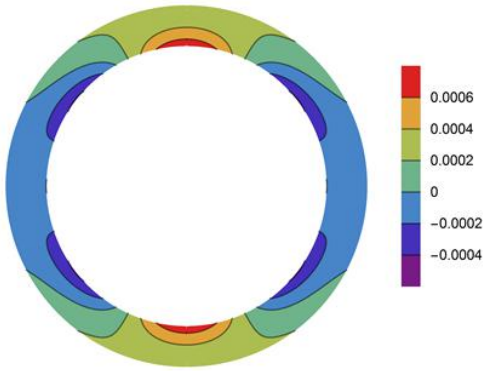

(c) ε_{33}^m from proposed model

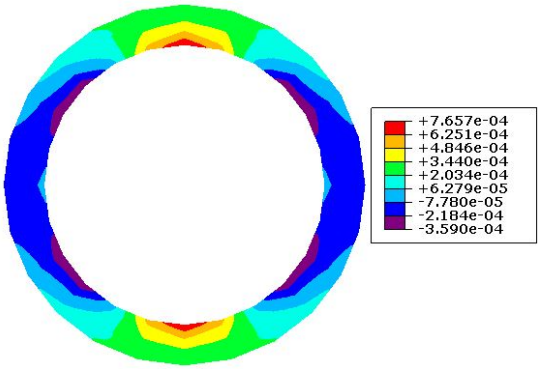

(d) ε_{33}^m from FEA

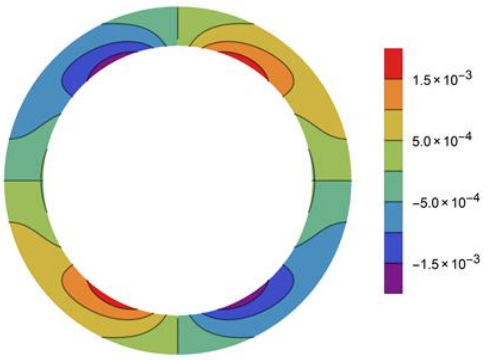

(e) ε_{23}^m from proposed model

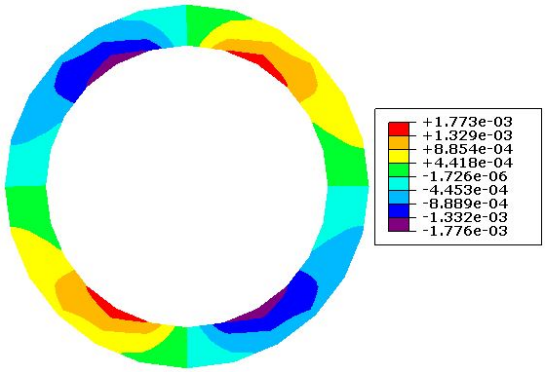

(f) ε_{23}^m from FEA

Figure 2.16: Matrix contours under $\varepsilon_{22}^c = 0.1\%$.

2.5.2 NCYL model and periodic boundary conditions (PBC)

In this multiscale computational framework, the strains at each integration point in the FEA of homogenized composite, are applied to the subscale micromechanics NCYL model. These integration point strains can be treated as the effective composite strains that are applied on a discrete fiber-matrix microstructure. The constituent

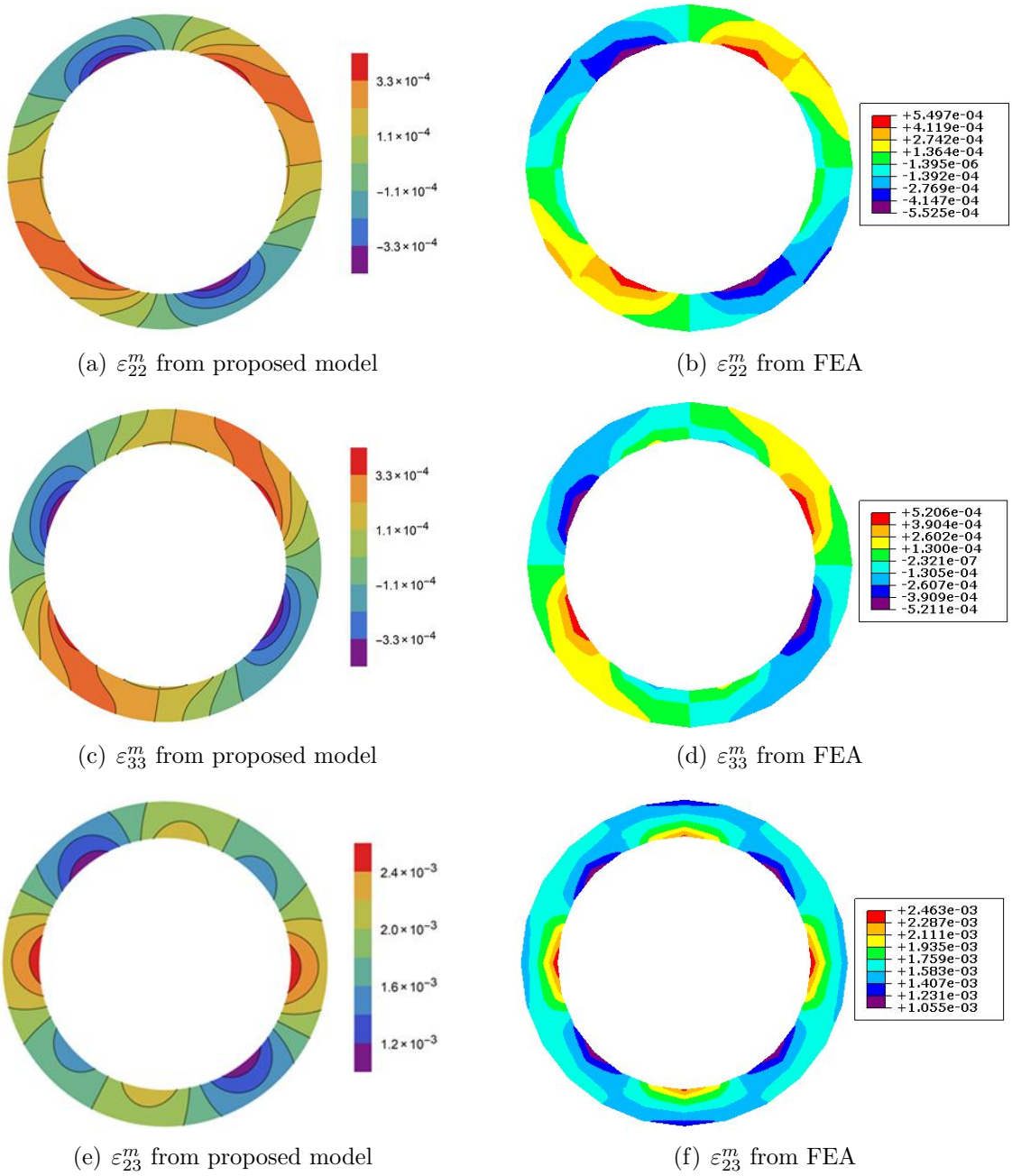

(a) ε_{22}^m from proposed model

(b) ε_{22}^m from FEA

(c) ε_{33}^m from proposed model

(d) ε_{33}^m from FEA

(e) ε_{23}^m from proposed model

(f) ε_{23}^m from FEA

Figure 2.17: Matrix contours under $\gamma_{23}^c = 0.1\%$.

strain fields therefore can be computed in closed form by knowing the globally applied strains through the micromechanical analysis.

However, it should be noted that the resulting matrix strain fields vary in space as shown in Figures 2.14-2.17, hence the matrix equivalent strain, computed using Equation 2.7, has spatial variation as well. In the current fully analytical computational scheme, it is hypothesized that the composite nonlinear behavior can be characterized

using two scalar variables that are related to the matrix equivalent strain. This idea is similar to the mean-field theories in which the average values of the strain fields are utilized to determine the matrix nonlinear progression. In the present study, the two scalar variables that govern the evolution of matrix microdamage are defined based upon the maximum and average value of the square of the matrix equivalent strain at the layers interface, respectively, as

$$V_{max} = \max\left\{\frac{1}{2}\left[(\bar{\epsilon}^m_{11} - \bar{\epsilon}^m_{22})^2 + (\bar{\epsilon}^m_{22} - \bar{\epsilon}^m_{33})^2 + (\bar{\epsilon}^m_{33} - \bar{\epsilon}^m_{11})^2\right] + \frac{3}{4}\left(\bar{\gamma}^{m^2}_{12} + \bar{\gamma}^{m^2}_{13} + \bar{\gamma}^{m^2}_{23}\right)\right\} \tag{2.43}$$

$$V_{avg} = \text{avg}\left\{\frac{1}{2}\left[(\bar{\epsilon}^m_{11} - \bar{\epsilon}^m_{22})^2 + (\bar{\epsilon}^m_{22} - \bar{\epsilon}^m_{33})^2 + (\bar{\epsilon}^m_{33} - \bar{\epsilon}^m_{11})^2\right] + \frac{3}{4}\left(\bar{\gamma}^{m^2}_{12} + \bar{\gamma}^{m^2}_{13} + \bar{\gamma}^{m^2}_{23}\right)\right\} \tag{2.44}$$

where $\bar{\epsilon}^m_{ij}$ is the matrix strain at the layers interface ($r = R_N$). Physically, the average term is dominant in the matrix strain field when the fiber volume fraction is low, while the maximum value dominates the result for high fiber volume fraction. Therefore, a weight function of V_{max} and V_{avg} can be written as,

$$V_{weight} = V_f^n V_{max} + (1 - V_f^n) V_{avg} \tag{2.45}$$

where n is dependent on the fiber-to-matrix stiffness ratio such that the effect of constituent properties can be accounted for. In this work, it is assumed that,

$$n = 2\sqrt{\left(\frac{E^m}{E^f_2} + \frac{G^m}{G^f_{23}}\right)} \tag{2.46}$$

Consequently, two matrix equivalent strains can be computed; one is based upon the weight function in Equation 2.45, while the other is based upon the average value in Equation 2.44, as,

$$\epsilon^{eq}_{m,1} = \frac{1}{1+\nu_s}\sqrt{V_{weight}} \qquad \text{and} \qquad \epsilon^{eq}_{m,2} = \frac{1}{1+\nu_s}\sqrt{V_{avg}} \tag{2.47}$$

Once the matrix equivalent strain is resolved, the matrix stiffness tensor is degraded as a secant solid according to the nonlinear damage model presented in Section 2.3. It is further hypothesized that the matrix secant moduli calculated using $\epsilon^{eq}_{m,1}$ are subsequently used to compute the composite effective secant moduli, E^c_1, ν^c_{12}, K^c_{23}, and G^c_{23}, while the matrix secant moduli determined from $\epsilon^{eq}_{m,2}$ is used to compute

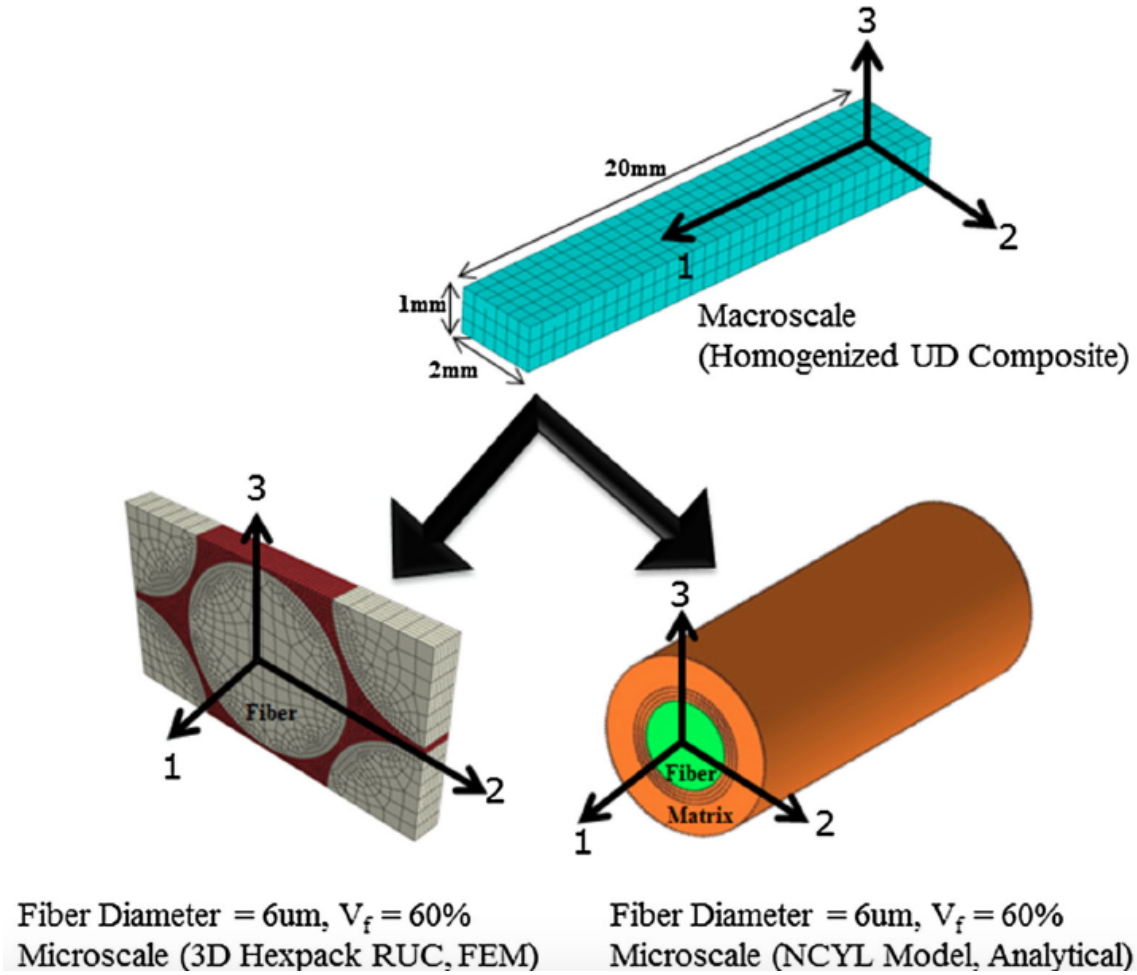

Figure 2.18: Multiscale approach length scales.

G_{12}^c. In the present NCYL model, where the number of cylinders keep increasing, the two scalar variables (V_{avg} and V_{max}) are computed for each layer individually. Hence, the equivalent strain and stress are also calculated individually for each layer and the matrix stiffness can be degraded independently depending on the damaged state of each layer. Consequently, if matrix microdamage occurs, the stiffness of the subscale microstructure is reduced based upon the proposed secant moduli approach. The subscale stiffness tensors are subsequently used to update the global stiffness and stresses in the macroscale FEA. Therefore, the influence of matrix microdamage at the subscale manifests as the degradation of the global stiffness of the composite at the macroscale.

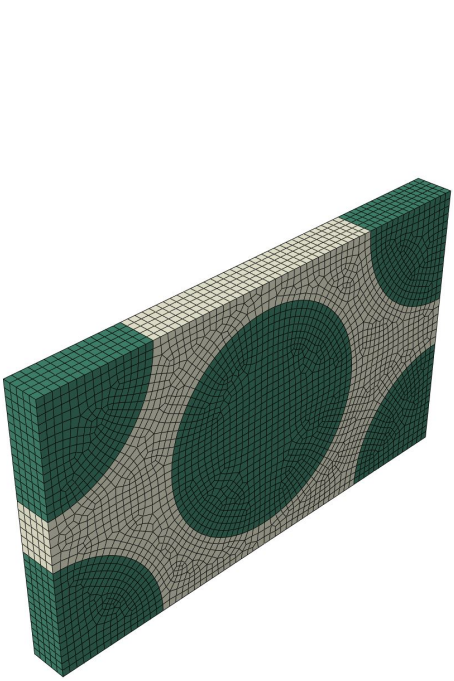

(a) Hexagonal array

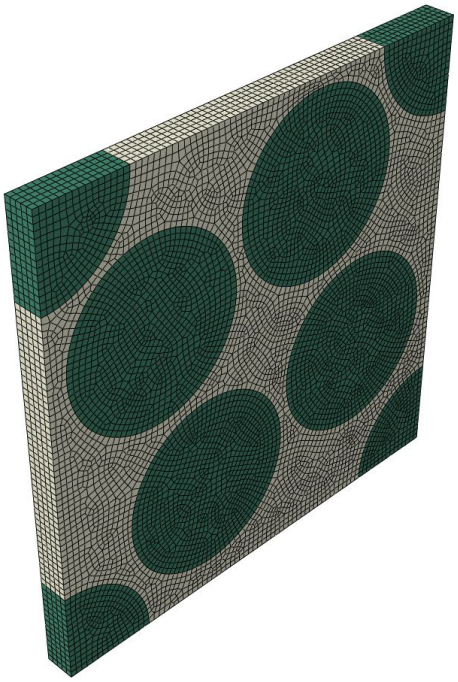

(b) 5 fibers random array

(c) 15 fibers random array

Figure 2.19: 3D RUC of UD composite (Fiber volume fraction=60%).

2.5.3 3D FE model and periodic boundary conditions (PBC)

In order to verify the proposed method to compute the composite nonlinear response, a finite element model is utilized to assess the accuracy of the prediction. IM-7/SC-15 fiber reinforced composite, which has a fiber volume fraction of 60% is utilized for analysis. The elastic properties of the fibers and matrix are provided in Table 2.3. The nonlinear properties of SC-15 matrix are given in Table 2.1. In this research, the results from the FEA model serves as a reference to verify the proposed NCYL-micromechanics based multi-scale model for computing the composite nonlinear response.

A unidirectional fiber reinforced composite can be modeled at the fiber-matrix level through a RUC with detailed fiber geometries and constituent properties. The microstructure of a unidirectional composite is represented by the RUC composed of three different arrangements of fiber packing; (a)hexagonally packed, (b) 5 fiber of random packed, and (c) 15 fiber random packed, as shown in Figure 2.19, resulting in a transversely isotropic solid with isotropic properties in the plane perpendicular to the fiber direction. The effect of fiber randomness and the size of RUC on the residual stress development in a cured composite have been addressed in [27]. The RUC deforms like a jigsaw puzzle such that periodic boundary conditions are required to ensure the continuity between the adjacent RUCs. The periodic boundary conditions are imposed on pairs of opposite boundary surfaces as explained in [1].

To obtain a full characterization of the composite nonlinear response, four loading scenarios are considered, including axial tension, transverse tension, axial shear and transverse shear for all the three different arrangements of fiber packing. The schematic loading directions for 15 fiber random packed array are shown in Figure 2.20 as an illustration. The carbon fiber is assumed linear elastic, while the matrix is modeled as an elastic-damaging solid using a secant modulus approach as presented in Section 2.3. The analysis was carried out using the commercially available code ABAQUS, in which the matrix constitutive law is implemented through a UMAT.

2.6 Results and discussion

The stress-strain responses of the homogenized unidirectional composite are evaluated for IM-7 carbon fiber with SC-15 epoxy for N=4, using the proposed NCYL micromechanics based multiscale method. Also, the global responses using the 3D FEA are calculated for IM-7 carbon fiber with SC-15 epoxy for hexagonal packed

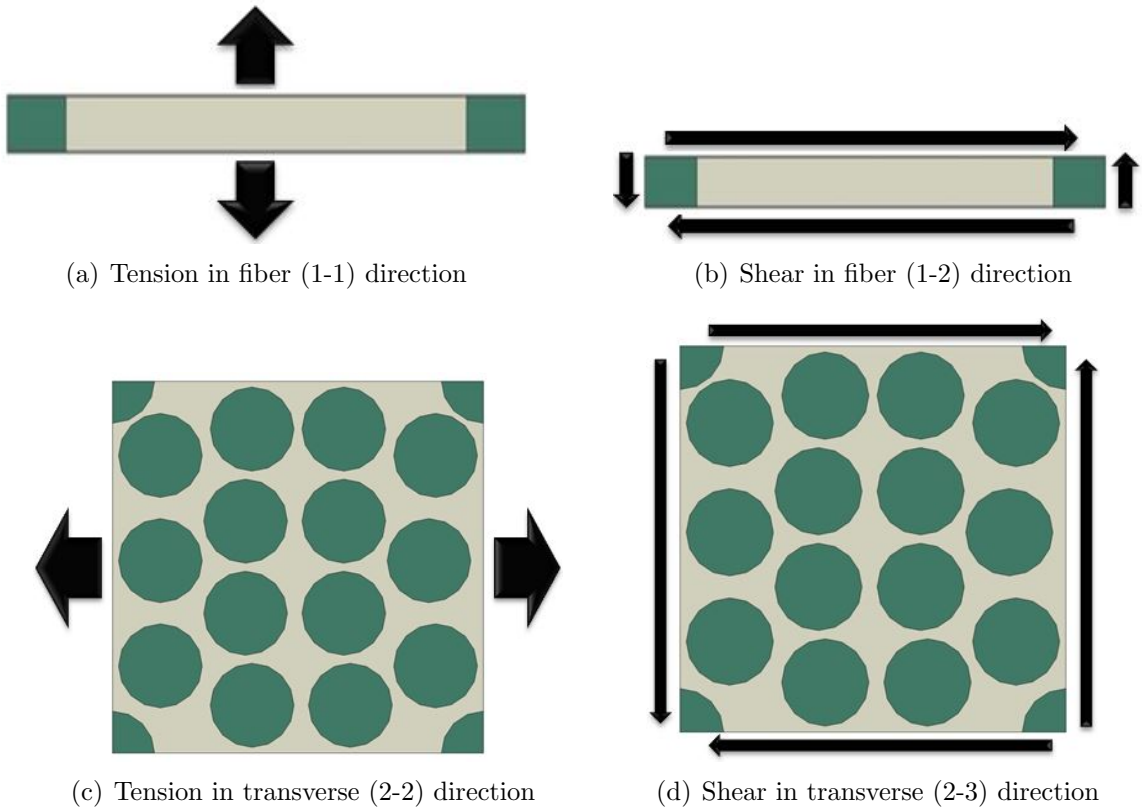

(a) Tension in fiber (1-1) direction

(b) Shear in fiber (1-2) direction

(c) Tension in transverse (2-2) direction

(d) Shear in transverse (2-3) direction

Figure 2.20: 3D RUC of UD composite for all loading cases.

microstructure. The comparison between the two methods on the prediction of the composite nonlinear stress versus strain response is shown in Figure 2.21 for fiber volume fraction varying from 50 to 70%. Here, the 3D FE results are taken as a reference to validate the proposed NCYL micromechanics model. The unidirectional composite axial behavior is mostly dominated by fiber failure strain and hence, the axial normal stress-strain response exhibits almost linear response during the deformation, as shown in Figure 2.21(a). In the transverse normal, axial shear and transverse shear loading directions, damage evolves in the matrix, which leads to significant nonlinearity in the stress versus strain response. The effective composite stiffness is degraded during the pre-peak nonlinear response and modeled using the secant stiffness approach. The transverse normal and transverse shear responses, as shown in Figures 2.21(b) and 2.21(d), respectively are determined from the weight function defined in Equation 2.45, suggesting that the fiber volume fraction affects the prediction and the accuracy increases when the fiber volume fraction increases from 50 to 70%. Even though the proposed method is an approximation based upon the choice of the scalar variables, it offers good predictions on IM-7 composite material system for fiber vol-

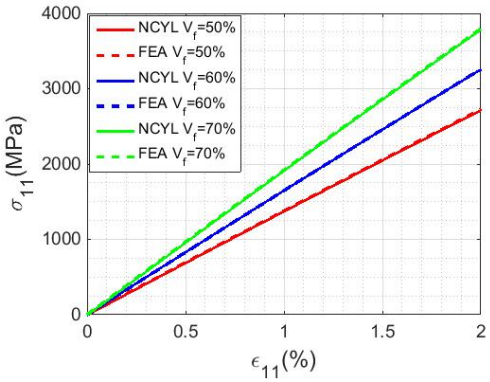

(a) Axial normal stress versus strain response

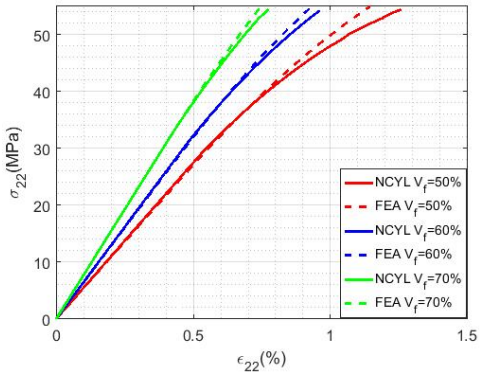

(b) Transverse normal stress versus strain response

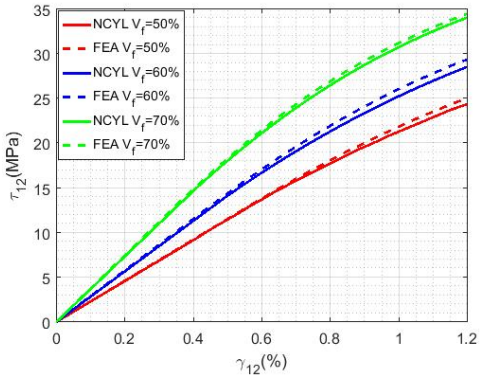

(c) Axial shear stress versus strain response

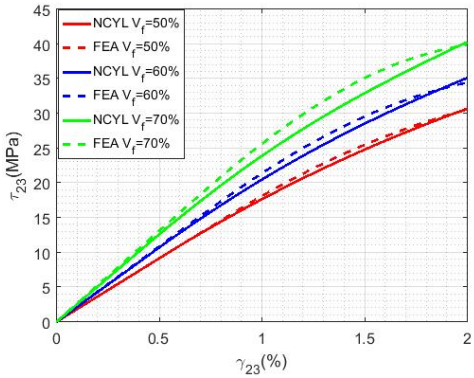

(d) Transverse shear stress versus strain response

Figure 2.21: Comparison between NCYL (N=4) and 3D FEA (IM-7 carbon - SC-15 epoxy).

ume fraction varying from 50 to 70%. The results for the axial shear response, as shown in Figure 2.21(c), is determined from the average matrix strain at the cylinder interfaces and the accuracy of the prediction increases when the fiber volume fraction decreases from 70 to 50%. Hence, it tends to overpredict the nonlinear response when the fiber volume fraction is high. However, the proposed method still offers a good prediction for fiber volume fraction range up to 70% and also compares well with the 3D FEA.

Microscale architectural effects on damage of composites is investigated in this research to study the effect of fiber randomness on the damage evolution and nonlinear progression of the stress-strain response of composite. Three different composite microstructures with fiber volume fraction 60% are considered as finite element repeating unit cells, with appropriate periodicity conditions applied at the boundaries,

as shown in Figure 2.19. Results representing predicted axial tensile, transverse tensile, axial shear and transverse shear stress-strain curves are presented in Figure 2.22, comparing with the global response of the homogenized unidirectional composite, using the NCYL model for N=2, 3 and 4 cylinders. For loading in axial direction, there is no difference among all the cases as the composite failure is caused by fiber failure strain as shown in Figure 2.22(a). As evident in Figure 2.22(c), the difference in hexpack, 5-fibers and 15-fibers nonlinear patterns are not so prominent and the curves converge to N=4 case in the sequence of hexpack-5 fibers-15 fibers. The fact that 15-fibers case response is becoming closer to analytical solution, N=4 indicates that, as a larger RUC with more fibers is considered, the model provides a better representation of the actual (transversely isotropic) material response. Similar behavior is observed in the case of transverse shear loading case in Figure 2.22(d), where 15-fibers stress-strain response approaches to NCYL response. While all cases predict nearly identical initial elastic stiffness in transverse loading case as shown in Figure 2.22(b), once damage initiates, there are significant differences in the global deformation (i.e., damage) response due to microstructural variation in the three RUC representations. In contrast to other loading cases, the transverse loading results in earlier onset of damage localization for hexpack RUC, compared to 5-fibers and 15-fibers. The local stress concentrations arising in the matrix between nearby fibers tend to cause early onset of localization due to damage. The effect of the RUC geometry on the predicted transverse shear stress-strain response of the composite is similar to its effect on the predicted axial shear stress-strain response. The influence of the repeating unit cell geometry and the effect of the directionality of the applied loading are studied here for a particular random fiber arrangement with fixed volume fraction 60%. Further detailed sensitivity study of damage progression with respect to different possible random arrangements of fiber and volume fraction is a scope of future research.

The stress-strain responses of the homogenized unidirectional composite for all loading cases, using the proposed NCYL micromechanics based multiscale method are evaluated for IM-7 carbon fiber and S-2 glass fiber with SC-15 epoxy for N=2, 3 and 4 cylinders. A comparison among increasing cylinders are discussed here to show the improvement of the results on the prediction of nonlinear stress versus strain response for all loading cases. The stress-strain responses are shown in Figure 2.23 for fiber volume fraction varying from 50 to 70% and for both the material systems. The axial normal stress-strain response is independent of the number of increasing matrix cylinders since unidirectional composite axial behavior is dominated by fiber stress-strain response and hence, exhibit almost a linear response for N=2, 3 and 4

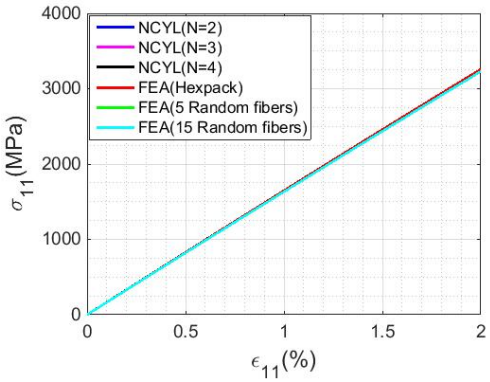

(a) Axial normal stress versus strain response

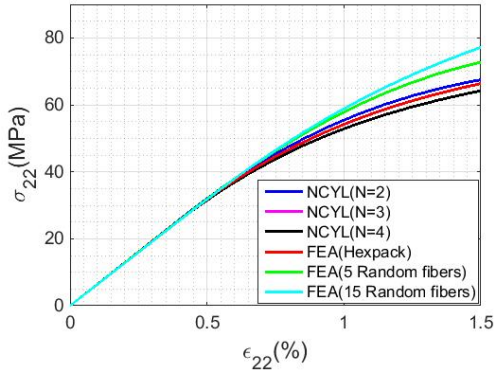

(b) Transverse normal stress versus strain response

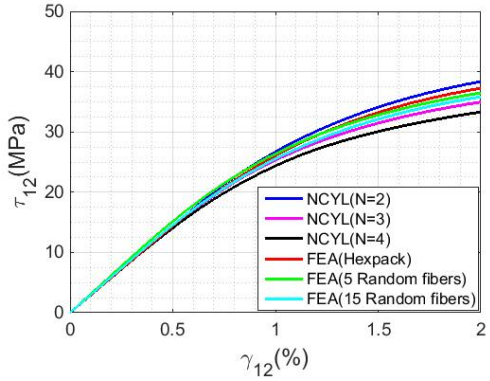

(c) Axial shear stress versus strain response

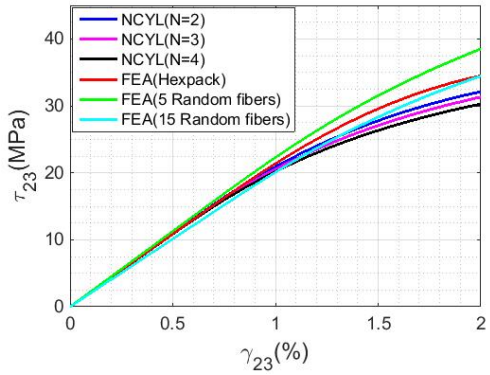

(d) Transverse shear stress versus strain response

Figure 2.22: Comparison of effective response as a function of fiber arrangement and direction of loading.

cases, as shown in Figures 2.23(a, b). As a result, the IM-7 carbon-epoxy composite presents higher stiffness than the S-2 glass-epoxy composite in the axial direction. In the transverse normal, axial shear and transverse shear loading directions, damage evolves in a non-uniform manner, (gradients) in all the discrete layers of matrix. For the case of two-phase fiber-matrix cylinders (N=2), the entire volume of matrix is assumed to be degraded by the same amount using the secant stiffness approach and hence, the global composite stiffness is underpredicted. When the number of cylinders goes up, the damage is more localized and the reduction in global stiffness is predicted in a more controlled and efficient way. As mentioned earlier, the transverse normal and transverse shear responses, as shown in Figures 2.23(c, d) and Figures 2.23(g, h), respectively are determined from the weight function defined in Equation 2.45, suggesting that the fiber volume fraction and the fiber-to-matrix stiffness ratio affect

the choice of the scalar variables that characterize the composite nonlinear responses. In particular, when the fiber volume fraction is low or the fiber-to-matrix stiffness ratio approaches one, the resulting composite nonlinear behavior tends to be dominated by the average value of the matrix strain at the concentric cylinder interfaces, while on the other hand, the maximum value is dominant for either high fiber volume fraction or large fiber-to-matrix stiffness ratio. It should be noted that IM-7 carbon fiber is transversely isotropic, and its transverse stiffness is significantly lower than that of S-2 glass, as shown in Table 2.3. The axial shear response, as shown in Figures 2.23(e, f), is determined from the average function defined in Equation 2.44 at all cylinder interfaces. But in all these loading cases, there is a significant change in pre-peak nonlinearity and the slope of the responses keep increasing as the number of matrix cylinders increases from N=2 to N=4. Also, this feature is observed for all the volume fraction range from 50 to 70%.

2.7 Conclusions

In this work, a subscale micromechanics model for N-layered concentric cylinders referred to as "NCYL" model is developed, which is able to capture the local stress and strain gradients of the constituent fiber and matrix layers in closed form, when the composite cylinder external boundary is subjected to strain loading. The local field gradients in each discrete layer of fiber and matrix are the key inputs to this progressive failure model, which is subsequently used to establish a multiscale computational framework to predict the effective nonlinear response of a homogenized unidirectional composite. The axial tension and axial shear problem are solved by a N-layers CCM method, while the transverse tension and transverse shear are solved using an extended (N+1) layers GSCM method. The matrix strains in each discrete layer are related to the applied composite strains through a transformation matrix, and the resolved spatial variations of the matrix strain fields are in good agreement with corresponding 3D finite element analysis results. The volume of matrix microdamage is controlled by the number of concentric cylinders and as the number of matrix layers increase, the effective stiffness goes up in a gradual manner as shown in Figure 2.23 and the accuracy of nonlinear behavior is seen to improve, displaying a converged response.

At the interface between all discrete layers, two scalar variables are defined as the maximum and mean value of the matrix equivalent strain, according to Equations 2.45 and 2.44, respectively. It is assumed that the evolution of the composite nonlinear

response is governed by these two scalar variables. The extent of local damage is calculated explicitly in all matrix layers and the matrix stiffness tensor of individual layer is degraded proportionately through a modified J_2 deformation theory. Once the matrix stiffness tensor is degraded, the matrix secant moduli are subsequently used to compute the composite secant moduli. In particular, E_1^c, ν_{12}^c, K_{23}^c, and G_{23}^c are computed based upon the matrix secant moduli determined from Equation (2.45), while G_{12}^c is calculated using the matrix secant moduli determined from Equation (2.44). The influence of matrix microdamage at the microscale manifests as the degradation of the effective composite stiffness at the macroscale through a secant moduli approach.

The nonlinear behavior is overpredicted by the two-phase (N=2) fiber-matrix cylinder model and the accuracy of the solution goes up by increasing the number of matrix cylinders. The proposed method provides better prediction of the composite nonlinear stress versus strain response and matches well against the results from 3D FEA. The predictive capability of the model is established here by two distinct composite material systems, IM-7 carbon and S-2 glass with SC-15 epoxy, for fiber volume fraction varying from 50 to 70% and the nonlinear responses converge from N=2 to N=4 for all loading cases. The optimal selection of N depends on various factors; (1) Material system, (2) Fiber to matrix stiffness ratio, (3) Volume fraction of composite and (4) Matrix degradation rate as observed in experiments. Detailed study of the NCYL model with respect to all these combined factors is the scope of future research. Since, fully analytical solutions are utilized for the subscale micromechanics analysis, the proposed method offers a significantly lower computational cost and is suitable for large-scale progressive damage and failure analysis of composite structures. The main focus in this work is achieved by establishing a multiscale method, which is capable of predicting the effective linear elastic properties and also the nonlinear response of the homogenized fiber reinforced unidirectional composites in a more efficient way.

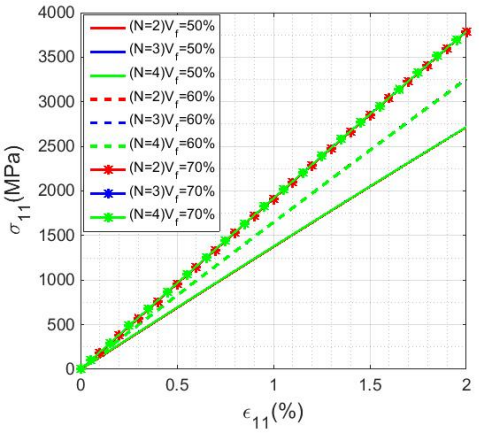

(a) IM-7-carbon - SC-15 epoxy for N=2,3,4

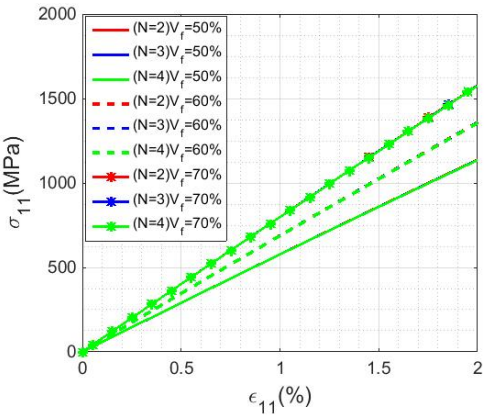

(b) S-2-glass - SC-15 epoxy for N=2,3,4

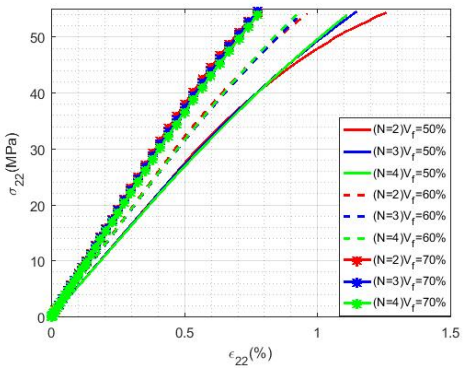

(c) IM-7-carbon - SC-15 epoxy for N=2,3,4

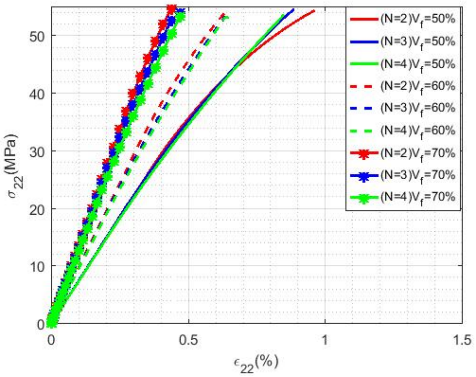

(d) S-2-glass - SC-15 epoxy for N=2,3,4

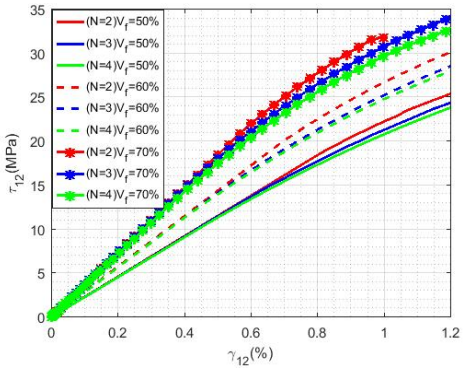

(e) IM-7-carbon - SC-15 epoxy for N=2,3,4

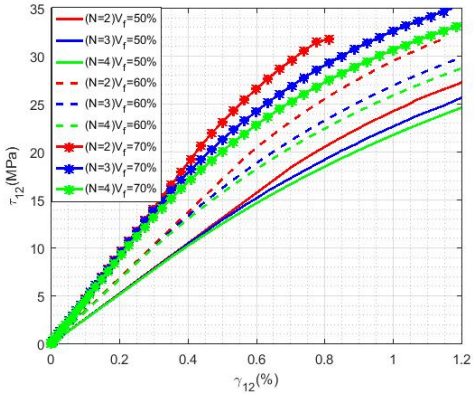

(f) S-2-glass - SC-15 epoxy for N=2,3,4

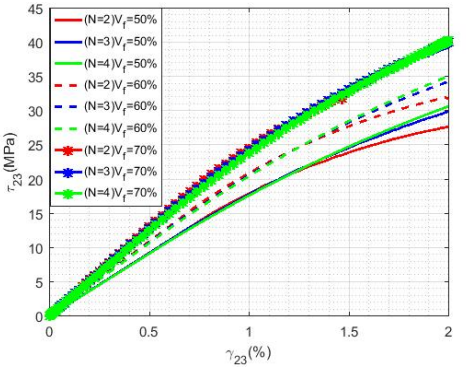

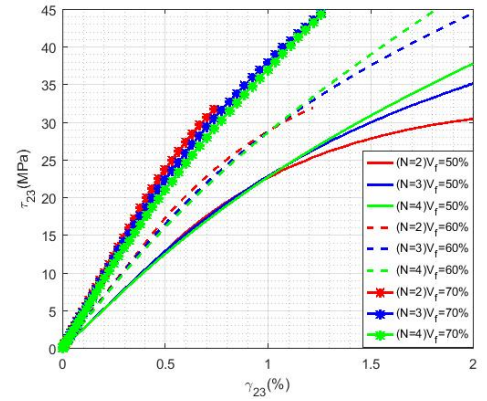

CHAPTER 3

Failure modeling of fiber tows and matrix using Smeared Crack Approach(SCA)

3.1 Introduction

The objective of my research work is to perform a multiscale analysis to study the progressive damage and failure of hybrid 3D woven textile composites at different length scales. In this computational model, the macroscale finite element analysis (FEA) is carried out at the representative volume element (RVE) or coupon level, while the micromechanics analysis is implemented simultaneously at the subscale level using material properties of the constituents (fiber and matrix) as input. The subscale micromechanics analysis uses the N-layers concentric cylinder model (NCYL) to compute the local fields in the fiber and matrix cylinders. The influence of matrix micro-damage at the subscale causes the progressive degradation of fiber tow stiffness at the macroscale by a secant moduli approach, resulting the pre-peak nonlinear response. The post-peak strain softening response resulting from different failure modes like fiber tow rupture, tow kinking, tow splitting and matrix cracking outside of fiber tow are modeled using a mesh-objective smeared crack approach (SCA) [28].

A three dimensional (3D) SCA model for isotropic materials and a 2D orthotropic model are presented in [29]. The 3D isotropic SCA model is useful to describe the crack progression in the matrix material in a composite and the 2D orthotropic SCA model is used to model crack and damage progression within the layers (lamina) of a laminate. The 2D orthotropic SCA model is extended to a 3D orthotropic SCA model [30, 31, 32] and the failure response of fiber tows (post-peak softening response) is modeled using a new formulation, where the fiber tow is assumed to fail either in compression due to kink band or in tension due to fiber breakage in the tows. It is further assumed that when the critical stress (either tension or compression) is reached, the crack plane aligns perpendicular to the fiber direction. Therefore, the

crack orientation transformation matrix is determined by the material orientation rather than the state of stress.

In hybrid textile composites, due to the heterogeneity of the microstructure and the complexity of the stress fields, fiber tows exhibit multiple failure modes, including tow kinking in compression, tow breakage in tension, shear banding and transverse cracking. In some instances, the fiber tow can be delaminated from the surrounding matrix at high strain rates, as shown by [33] through a split Hopkinson pressure bar test. Shear bands are observed when the textile composite is subjected to the through-the-thickness compression [33, 34]. Cracks that grow along the transverse normal, axial shear and transverse shear directions are considered as matrix failure modes, dominated by the strength and toughness of the polymer matrix material.

This chapter details the implementation of SCA approach in ABAQUS user-material (VUMAT) framework. All possible fiber and matrix failure modes in 1-2, 2-3 and 1-3 planes are introduced and implemented in the in-house developed 3D SCA code used for this research. The algorithms are documented in flow charts for a better explanation, as a part of this thesis. The crack orientation transformation matrix, as determined by the material orientation for all three mutually perpendicular crack planes are considered.

3.2 Tow failure mechanisms: Post-peak strain softening response

Since the fiber tow pre-peak nonlinear response is attributed to matrix micro-damage, no macroscopic damage criterion is required to drive the nonlinear damage progression. However, multiple catastrophic failure modes are observed in the experiment, including tensile failure due to fiber rupture and transverse and shear matrix failure in fiber tows which lead to tow splitting. These modes of failure result in a loss of load-carrying capability, followed by a post-peak strain softening response. Since the positive definiteness of the material tangent stiffness matrix is lost in the softening regime, the FE analysis will provide mesh dependent results if no characteristic length associated with the softening response is introduced. As a result, the pre-peak NCYL model has to be supplemented by a suitable mesh objective approach for modeling the post-peak softening response at the macro-scale. There are a variety of theories and numerical implementations with respect to modeling of progressive damage and failure in composites. In this study, the post-peak failure response at the macroscale

is modeled using the smeared crack approach (SCA). This method was initially proposed by [28] to model crack propagation and fracture in concrete. Extensions to modeling failure in composites are given in the papers [29, 30]. The implementation provides mesh objectivity with respect to numerical discretization and uses standard 3D finite elements available in most commercial packages. This latter aspect is of great concern to practicing engineers in industry who are concerned with validated computational methods.

In hybrid textile composites, fiber tows are surrounded by a polymer matrix, resulting in a complex state of stress. A unidirectional fiber tow is shown schematically in Figure 3.1, where fibers are aligned in 1-direction and the transverse 2-3 plane is assumed to be isotropic. The microstructure of each fiber tow consists of thousands of fibers distributed in the matrix medium with certain volume fraction, depending on the manufacturing process and the applications. The fibers arrangement inside the tow and the packing details have a great impact on the macroscopic global response, which can be studied in a more detailed manner. The fiber packing controls the distribution of matrix cracking inside the tow, but in our study the fiber tows are homogenized and we try to capture the matrix cracking and the tow splitting at the macroscale.

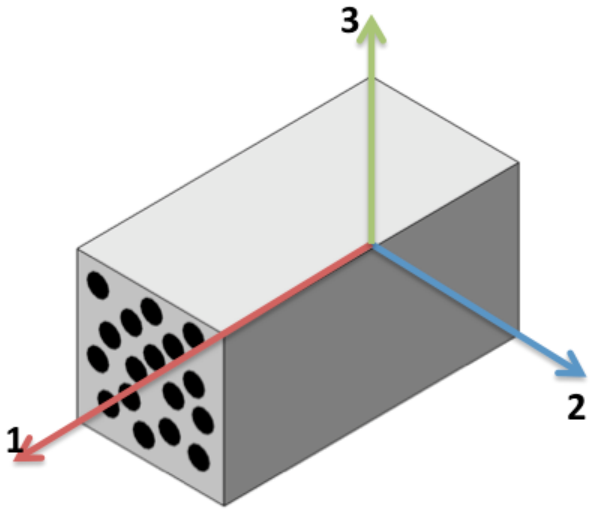

Figure 3.1: Unidirectional fiber tow (schematic).

Generally, the failure modes of a fiber tow can be grouped into two types, (1) fiber failure modes that include tow breakage in tension and tow kinking in compres-

sion as shown in Figures 3.2 and 3.3 respectively. For both tension and compression failure modes, the crack planes are aligned orthogonal to the fiber direction. Figure 3.2 indicates the mixed mode behavior for fiber tension in 1-1 direction and shear failure in 1-2 and 1-3 planes. The coupling between tension and shear failure modes in the failure initiation criteria can be due to the fiber misalignment and crookedness, as a consequence of manufacturing process. As the fibers are perfectly aligned and the quality of the manufacturing process improves, the shear failure modes get suppressed and fiber tensile breakage dominates. Figure 3.3 shows the fiber kinking behavior due to compressive load and no shear components are included in the failure initiation criteria for this study. (2) Matrix failure modes include transverse tension and compression along with corresponding shear components as shown in Figures 3.4, 3.5 and 3.6. In all these modes, crack plane is parallel to the fiber direction but are differentiated based on the crack normal aligned to 2-direction, as shown in Figure 3.4 compared to the crack normal aligned to 3-direction, as shown in Figure 3.5. The transverse and shear strengths in 3-direction are equivalent to 2-direction, due to assumed transverse isotropy but the crack orientation transformation matrix, as determined by the material orientation for all three mutually perpendicular crack planes are uniquely defined as explained in the following sections. For matrix failure modes due to shear, the failure plane can be orthogonal to the fiber direction for the S12 and S13 cases, whereas the failure plane remains parallel to the fiber direction for the S21, S31, S23 and S32 cases, as shown in Figures 3.4, 3.5 and 3.6. S12 is dominated by fiber shear failure, whereas S21 is failure within the matrix, but parallel to the fiber. In advanced composites, the interface shear strength is superior to the matrix shear strength, hence S12 is dictated by the matrix shear strength. The assumption of matrix failure due to combined transverse and shear loading in 3D is similar to that proposed by Hashin [35]. Thus the matrix failure modes account for cracks growing along the transverse normal, axial shear, and transverse shear directions, predicted based on the corresponding strength and toughness of the composite.

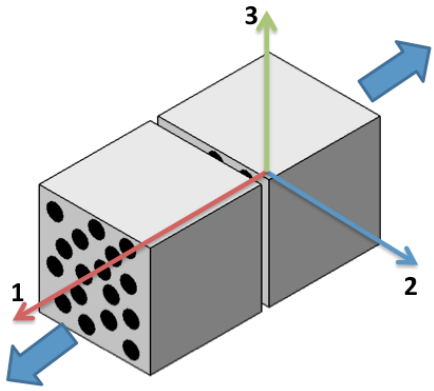

(a) Tensile failure (1-1)

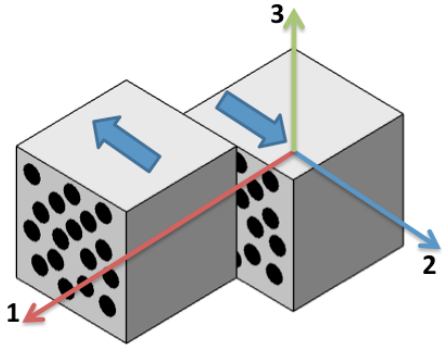

(b) Shear failure (1-2)

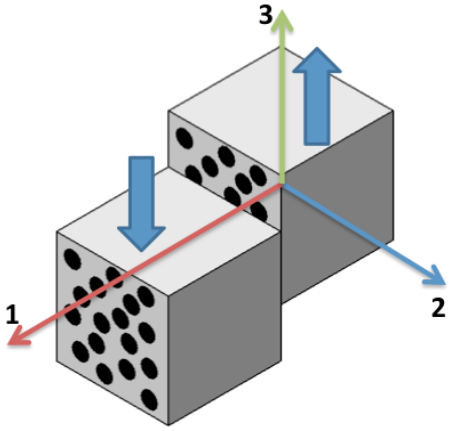

(c) Shear failure (1-3)

Figure 3.2: Fiber tension and shear failure modes for crack plane orthogonal to 1-direction.

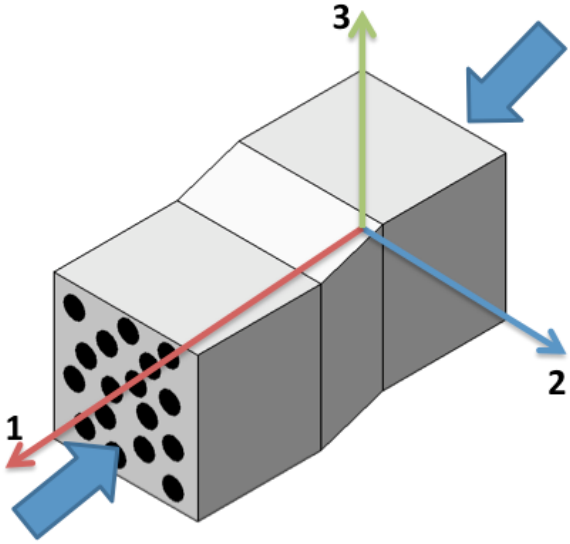

Figure 3.3: Fiber compression (kinking) for crack plane orthogonal to 1-direction.

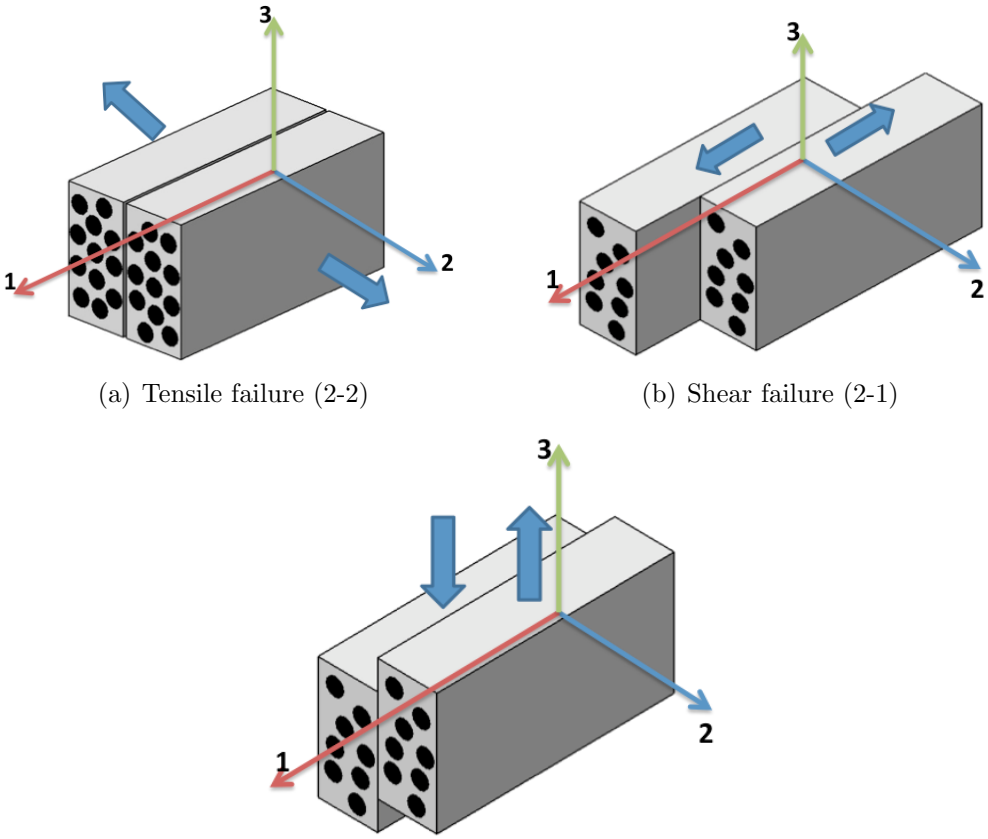

(a) Tensile failure (2-2)

(b) Shear failure (2-1)

(c) Shear failure (2-3)

Figure 3.4: Transverse tension and shear failure modes for crack plane orthogonal to 2-direction.

For a single fiber tow/lamina element, the following failure modes are included in this study: (a) Tension in 1 (fiber direction) and shear in 1-2 and 1-3 planes (b) Compression in 1 (fiber direction) (c) Tension in 2 and shear in 2-1 and 2-3 planes (d) Tension in 3 and shear in 3-1 and 3-2 planes (e) Compression in 2 and 3-directions.

The general methodology and formulation of the smeared crack code is explained in Section 3.3 below, which applies to all the failure modes mentioned above. The energy dissipation, fracture toughness and the characteristic length are calculated based on the mixed mode traction-separation laws as explained in Section 3.4. In Section 3.5, individual failure modes are explained in details depending on the corresponding local crack traction and strain components and the crack orientation transformation matrix. The flow chart of the main VUMAT and the smeared crack code are detailed in Section 3.5.

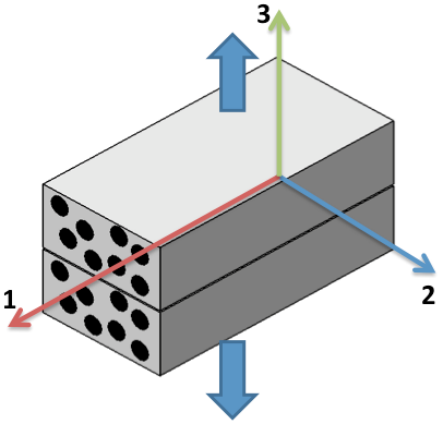

(a) Tensile failure (3-3)

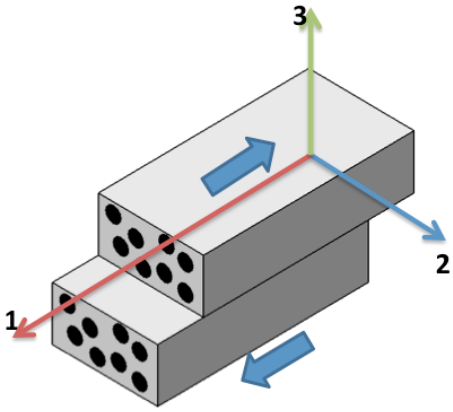

(b) Shear failure (3-1)

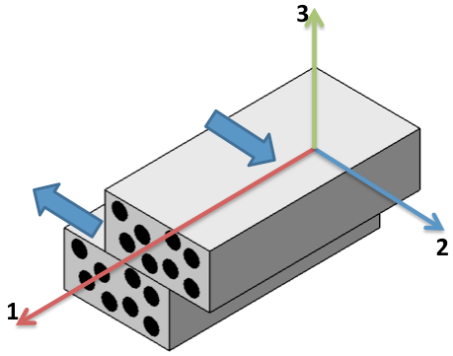

(c) Shear failure (3-2)

Figure 3.5: Transverse tension and shear failure modes for crack plane orthogonal to 3-direction.

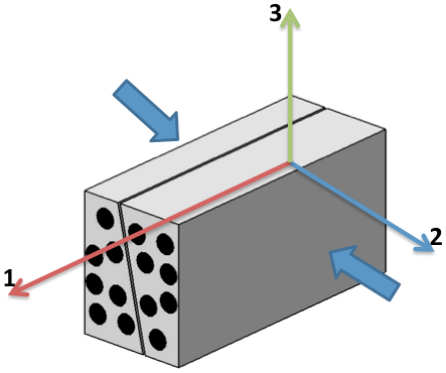

(a) Compressive failure (2-2)

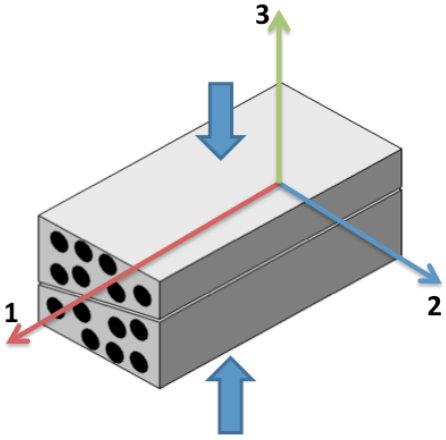

(b) Compressive failure (3-3)

Figure 3.6: Transverse compression failure modes for crack plane orthogonal to 2- and 3- directions.

3.3 3D Orthotropic smeared crack approach (SCA) for fiber tow

When failure initiates, the total strain $\boldsymbol{\epsilon}$ is decomposed into a continuum strain, $\boldsymbol{\epsilon}^{co}$ and cracked strain, $\boldsymbol{\epsilon}^{cr}$ as

$$\boldsymbol{\epsilon} = \boldsymbol{\epsilon}^{co} + \boldsymbol{\epsilon}^{cr} \tag{3.1}$$

This decomposition assumes small strain and the continuum strain, $\boldsymbol{\epsilon}^{co}$ can be further decomposed into elastic, plastic, thermal and any other type of strain if present. Here $\boldsymbol{\epsilon}$, $\boldsymbol{\epsilon}^{co}$ and $\boldsymbol{\epsilon}^{cr}$ are presented in the global coordinates. At the crack interface, there exist three relative displacements between the crack faces. One is the crack opening displacement, and the other two are the crack sliding displacements. The subscripts $\boldsymbol{n}$ and $\boldsymbol{t}$ are used to designate the directions normal to the crack and tangential to the crack, respectively. The key to the SCA is to embed cracks into a continuum, hence, the mode-I crack opening displacement is represented by a local smeared normal crack strain, $\boldsymbol{\epsilon}^{cr}_{nn}$, and the two mode-II crack sliding displacements are replaced by two local smeared shear crack strains, $\boldsymbol{\gamma}^{cr}_{t1}$ and $\boldsymbol{\gamma}^{cr}_{t2}$. These local crack strains are defined in the local coordinates that incorporate crack orientation, and can be related to the global coordinates through a transformation matrix, N, as,

$$\boldsymbol{\epsilon}^{cr} = \boldsymbol{N}\boldsymbol{e}^{cr} = \boldsymbol{N}\begin{Bmatrix} \epsilon^{cr}_{nn} \\ \gamma^{cr}_{t1} \\ \gamma^{cr}_{t2} \end{Bmatrix} \tag{3.2}$$

where $\boldsymbol{e}^{cr}$ is a vector that contains local crack strains, and N is a 6 by 3 transformation matrix depending on crack orientation. The derivation for N in terms of the direction cosines of the crack plane can be derived as,

$$\boldsymbol{N} = \begin{bmatrix} a_{11}^2 & a_{11}a_{21} & a_{11}a_{31} \\ a_{12}^2 & a_{12}a_{22} & a_{12}a_{32} \\ a_{13}^2 & a_{13}a_{23} & a_{13}a_{33} \\ 2a_{11}a_{12} & a_{11}a_{22} + a_{12}a_{21} & a_{11}a_{32} + a_{12}a_{31} \\ 2a_{11}a_{13} & a_{11}a_{23} + a_{13}a_{21} & a_{11}a_{33} + a_{13}a_{31} \\ 2a_{12}a_{13} & a_{12}a_{23} + a_{13}a_{22} & a_{12}a_{33} + a_{13}a_{32} \end{bmatrix} \tag{3.3}$$

and $a'_{ij}s$ are the direction cosines governing the space vector transformation as,

$$x'_i = a_{ip}x_p \tag{3.4}$$

When the SCA is implemented for a fiber tow failure due to tension or compression, the crack plane is assumed to be perpendicular to the fiber direction. Thus, the axis that defines the crack normal aligns with the 1-axis that denotes the fiber direction, and N is reduced to,

$$\boldsymbol{N} = \begin{bmatrix} 1 & 0 & 0 \\ 0 & 0 & 0 \\ 0 & 0 & 0 \\ 0 & 1 & 0 \\ 0 & 0 & 1 \\ 0 & 0 & 0 \end{bmatrix} \tag{3.5}$$

When the SCA is implemented for a fiber tow split in 2-direction due to transverse loading, the crack plane is assumed to be parallel to the fiber direction. Thus, the axis that defines the crack normal aligns with the 2-direction, and N is reduced to,

$$\boldsymbol{N} = \begin{bmatrix} 0 & 0 & 0 \\ 0 & 0 & 0 \\ 1 & 0 & 0 \\ 0 & 0 & 0 \\ 0 & 0 & 1 \\ 0 & 1 & 0 \end{bmatrix} \tag{3.6}$$

When the SCA is implemented for a fiber tow split in 3-direction due to transverse loading, the crack plane is assumed to be parallel to the fiber direction. Thus, the axis that defines the crack normal aligns with the 3-direction, and N is reduced to,

$$\boldsymbol{N} = \begin{bmatrix} 0 & 0 & 0 \\ 1 & 0 & 0 \\ 0 & 0 & 0 \\ 0 & 0 & 1 \\ 0 & 0 & 0 \\ 0 & 1 & 0 \end{bmatrix} \tag{3.7}$$

Similarly, the interface stresses at the crack interface, $\boldsymbol{s}^{cr}$, can be transferred to

the global stress state, $\boldsymbol{\sigma}$, through,

$$\boldsymbol{s}^{cr} = \begin{Bmatrix} \sigma_{nn}^{cr} \\ \tau_{t1}^{cr} \\ \tau_{t2}^{cr} \end{Bmatrix} = \boldsymbol{N}^T \boldsymbol{\sigma} \tag{3.8}$$

The crack interface stresses are related to the local crack strains through,

$$\boldsymbol{s}^{cr} = \boldsymbol{D}^{cr} \boldsymbol{e}^{cr} \tag{3.9}$$

where $\boldsymbol{D}^{cr}$ is the crack interface stiffness matrix that dictates the failure evolution in the post-peak strain softening regime. For a single crack in a 3D solid, $\boldsymbol{D}^{cr}$ can be expanded as,

$$\boldsymbol{D}^{cr} = \begin{bmatrix} E_{nn}^{cr} & 0 & 0 \\ 0 & G_{t1}^{cr} & 0 \\ 0 & 0 & G_{t2}^{cr} \end{bmatrix} \tag{3.10}$$

where E_{nn}^{cr} is the secant stiffness across the crack interface due to crack opening, and G_{t1}^{cr} and G_{t2}^{cr} are the two secant shear stiffness governed by crack sliding. These quantities identify the modes of failure and are related to the corresponding traction-separation laws with a characteristic length scale. The off-diagonal terms are assumed to be zero, indicating that there is no coupling between the normal and shear crack components. The determination of the components of the D^{cr} matrix is given in Section 3.4 for all failure modes. It should be pointed out that the sudden loss of the positive definiteness of the material tangent stiffness tensor may result in oscillations in the numerical solutions corresponding to the post-peak softening regime. Hence, a damping matrix, D^{da}, is introduced to modify the stress-strain relation at the crack interface, and Equation 3.9 becomes,

$$\boldsymbol{s}^{cr} = \boldsymbol{D}^{cr} \boldsymbol{e}^{cr} + \boldsymbol{D}^{da} \dot{\boldsymbol{e}}^{cr} \tag{3.11}$$

Consequently, the crack progression becomes a time dependent property by the use of a damping matrix. The crack strain rate is approximated at each time step using a backward finite difference scheme as,

$$\dot{\boldsymbol{e}}^{cr} = \frac{\boldsymbol{e}^{cr}(t+\delta t) - \boldsymbol{e}^{cr}(t)}{\delta t} = \frac{\boldsymbol{e}^{cr} - \boldsymbol{e}_{old}^{cr}}{\delta t} \tag{3.12}$$

Substituting Equation (3.12) into Equation (3.11) provides the expression for the local crack stresses as,

$$\boldsymbol{s}^{cr} = \boldsymbol{D}^{cr}\boldsymbol{e}^{cr} + \frac{\boldsymbol{D}^{da}\boldsymbol{e}^{cr}}{\delta t} - \frac{\boldsymbol{D}^{da}\boldsymbol{e}^{cr}_{old}}{\delta t} \tag{3.13}$$

The constitutive relation for a continuum is,

$$\boldsymbol{\sigma} = \boldsymbol{D}^{co}\boldsymbol{\epsilon}^{co} \tag{3.14}$$

where D^{co} is the continuum stiffness tensor. Combining Equations 3.1, 3.2, and 3.14 results in,

$$\boldsymbol{\sigma} = \boldsymbol{D}^{co}(\boldsymbol{\epsilon} - \boldsymbol{\epsilon}^{cr}) = \boldsymbol{D}^{co}(\boldsymbol{\epsilon} - \boldsymbol{N}\boldsymbol{e}^{cr}) \tag{3.15}$$

Noting Equations 3.8 and 3.13,

$$\boldsymbol{D}^{cr}\boldsymbol{e}^{cr} + \frac{\boldsymbol{D}^{da}\boldsymbol{e}^{cr}}{\delta t} - \frac{\boldsymbol{D}^{da}\boldsymbol{e}^{cr}_{old}}{\delta t} = \boldsymbol{N}^T\boldsymbol{\sigma} \tag{3.16}$$

Substituting Equation 3.15 into Equation 3.16 provides,

$$\boldsymbol{D}^{cr}\boldsymbol{e}^{cr} + \frac{\boldsymbol{D}^{da}\boldsymbol{e}^{cr}}{\delta t} - \frac{\boldsymbol{D}^{da}\boldsymbol{e}^{cr}_{old}}{\delta t} = \boldsymbol{N}^T\boldsymbol{D}^{co}(\boldsymbol{\epsilon} - \boldsymbol{N}\boldsymbol{e}^{cr}) \tag{3.17}$$

Consequently, the relation between the local crack strains and the total global strains can be obtained by rearranging Equation 3.17 as,

$$\boldsymbol{e}^{cr} = \left[\boldsymbol{D}^{cr} + \frac{\boldsymbol{D}^{da}}{\delta t} + \boldsymbol{N}^T\boldsymbol{D}^{co}\boldsymbol{N}\right]^{-1}\left[\boldsymbol{N}^T\boldsymbol{D}^{co}\boldsymbol{\epsilon} + \frac{\boldsymbol{D}^{da}\boldsymbol{e}^{cr}_{old}}{\delta t}\right] \tag{3.18}$$

Finally, the relation between the total stress and total strain in the post-peak regime is computed by substituting Equation 3.18 into Equation 3.15, which gives,

$$\boldsymbol{\sigma} = \begin{bmatrix} \boldsymbol{D}^{co}\boldsymbol{\epsilon} - \boldsymbol{D}^{co}\boldsymbol{N}\left(\boldsymbol{D}^{cr} + \frac{\boldsymbol{D}^{da}}{\delta t} + \boldsymbol{N}^T\boldsymbol{D}^{co}\boldsymbol{N}\right)^{-1}\boldsymbol{N}^T\boldsymbol{D}^{co}\boldsymbol{\epsilon} \\ -\boldsymbol{D}^{co}\boldsymbol{N}\left(\boldsymbol{D}^{cr} + \frac{\boldsymbol{D}^{da}}{\delta t} + \boldsymbol{N}^T\boldsymbol{D}^{co}\boldsymbol{N}\right)^{-1}\frac{\boldsymbol{D}^{da}\boldsymbol{e}^{cr}_{old}}{\delta t} \end{bmatrix} \tag{3.19}$$

Since the components in $\boldsymbol{D}^{cr}$ are related to the traction-separation law and are functions of local crack strains, Equation 3.18 represents a group of highly nonlinear equations involving local crack strains. Newton's method is employed to solve for $\boldsymbol{e}^{cr}$, that satisfies,

$$f(\boldsymbol{e}^{cr}) = \left[\boldsymbol{D}^{cr} + \frac{\boldsymbol{D}^{da}}{\delta t} + \boldsymbol{N}^T\boldsymbol{D}^{co}\boldsymbol{N}\right]\boldsymbol{e}^{cr} - \boldsymbol{N}^T\boldsymbol{D}^{co}\boldsymbol{\epsilon} - \frac{\boldsymbol{D}^{da}\boldsymbol{e}^{cr}_{old}}{\delta t} = 0 \tag{3.20}$$

Therefore, the local crack strains are computed using a successive iterative scheme. At the k^{th} iteration step,

$$[\boldsymbol{e}^{cr}]^k = [\boldsymbol{e}^{cr}]^{(k-1)} - [\frac{\delta f}{\delta \boldsymbol{e}^{cr}}]^{-1} f(\boldsymbol{e}^{cr}) \tag{3.21}$$

where $J = [\frac{\delta f}{\delta \boldsymbol{e}^{cr}}]$ defines the Jacobian matrix in a nonlinear system. Iteration continues until f($\boldsymbol{e}^{cr}$) approaches zero, or a suitable tolerance is met between two successive values of $\boldsymbol{e}^{cr}$. Once the local strains are solved, they are substituted into Equation 3.19 to compute the total stress at the end of an increment.

3.4 Characteristic length scale associated with the traction-separation law

To restore mesh objectivity, a characteristic length is introduced such that the total energy release rate during failure in a continuum element is equal to the fracture toughness. The fracture toughness, or the critical energy release rate, G_C, is defined by the area under the traction-separation law that dictates the cohesive behavior of crack propagation, as shown in Figure 3.7(b).

$$G_C = \int_0^{\delta_f} \sigma(\delta)\, \mathrm{d}\delta \tag{3.22}$$

where δ is the crack displacement within the fracture zone. In the SCA, δ represents the crack opening acting across a certain width within a finite element, denoted as the crack band width, h. Assuming that all the cracks are uniformly distributed over the crack band, and $\boldsymbol{\epsilon}^{cr}$ is the accumulation of all the crack strains over the fracture zone,

$$\delta = h\, \epsilon^{cr} \tag{3.23}$$

If g_c is defined as the area under the softening branch of the stress-crack strain response as shown in Figure 3.7(a), then substitute Equation 3.23 into Equation 3.22 results in,

$$G_C = \int_0^{\delta_f} \sigma(h\epsilon^{cr}) h\, \mathrm{d}\epsilon^{cr} = h \int_0^{\epsilon_f^{cr}} \sigma(\epsilon^{cr})\, \mathrm{d}\epsilon^{cr} = h\, g_c \tag{3.24}$$

Therefore, the strain-based description for a softening material is related to the displacement-based traction-separation laws through the characteristic length, h. In

a FE setting, h is chosen based upon the element type, element size, element shape, and the integration scheme. Typically the length of the element projected onto the crack normal is used as a characteristic element length. In the current study, secant crack stiffness is used so that the softening response follows the traction-separation law exactly, as shown in Figure 3.7(b). To prevent healing from happening, it is required that,

$$\dot{E}^{cr} < 0 \quad \text{and} \quad \dot{G}^{cr} < 0 \tag{3.25}$$

Hence, once the crack stiffness is degraded, it cannot be recovered. The loading and unloading behavior during the evolution of the failure process is explained in Section 3.5 below.

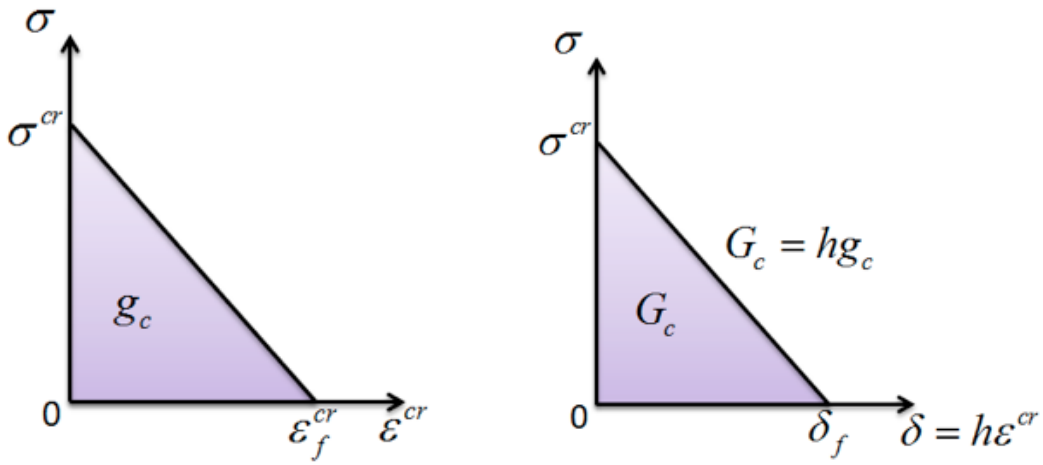

(a) Critical stress-strain response (b) Traction-separation law

Figure 3.7: Stress-strain softening response is related to the traction-separation law through a characteristic length, h.

3.5 Fiber tow failure modes and initiation criteria

The failure response of fiber tows (post-peak softening response) is modeled using the SCA formulated in Section 3.2. The fiber tow is assumed to fail in six different possible modes as listed above. Stress-based mixed mode failure criteria are used for crack initiation as proposed by Hashin [35]. It is further assumed that when the critical stresses are reached, the crack plane is decided based upon the first failure criterion met and therefore, the crack orientation transformation matrix, N, defined in Equation 3.3, is determined accordingly. Also, once the evolved in-situ stress state

at an integration point satisfies the first initiation criterion and enters into smeared crack, no other modes of failure are allowed for that point. Introduction of multiple cracks due to different failure modes at the same integration point is a scope of future research.

3.5.1 Fiber tensile failure

We name this failure mode as Mode-1 and the crack normal aligns to the fiber direction as shown in Figure 3.2. The failure initiation criterion is defined by

$$(\frac{\sigma_{11}}{X_T})^2 + (\frac{\sigma_{12}}{S_{12}})^2 + (\frac{\sigma_{13}}{S_{12}})^2 > 1, \sigma_{11} > 0 \tag{3.26}$$

The local crack strains are related to the global strains through a transformation matrix, N, defined in Equation 3.5 as,

$$\begin{Bmatrix} \epsilon_{11} \\ \epsilon_{22} \\ \epsilon_{33} \\ \gamma_{12} \\ \gamma_{13} \\ \gamma_{23} \end{Bmatrix} = \boldsymbol{N}\boldsymbol{e}^{cr} = \boldsymbol{N} \begin{Bmatrix} \epsilon_{11}^{cr} \\ \gamma_{12}^{cr} \\ \gamma_{13}^{cr} \end{Bmatrix} \tag{3.27}$$

The local stresses at the crack interface, s^{cr}, are transferred to the global stress state, σ, through,

$$\begin{Bmatrix} \sigma_{11}^{cr} \\ \tau_{12}^{cr} \\ \tau_{13}^{cr} \end{Bmatrix} = \boldsymbol{N}^T \begin{Bmatrix} \sigma_{11} \\ \sigma_{22} \\ \sigma_{33} \\ \tau_{12} \\ \tau_{13} \\ \tau_{23} \end{Bmatrix} \tag{3.28}$$

The crack interface stresses are related to the local crack strains through,

$$\begin{Bmatrix} \sigma_{11}^{cr} \\ \tau_{12}^{cr} \\ \tau_{13}^{cr} \end{Bmatrix} = \begin{bmatrix} E_{11}^{cr} & 0 & 0 \\ 0 & G_{12}^{cr} & 0 \\ 0 & 0 & G_{13}^{cr} \end{bmatrix} \begin{Bmatrix} \epsilon_{11}^{cr} \\ \gamma_{12}^{cr} \\ \gamma_{13}^{cr} \end{Bmatrix} \tag{3.29}$$

Let the onset stress states at the instant of failure initiation are denoted as σ_{11}^*, σ_{12}^* and σ_{13}^* which satisfy the Equation 3.26 as

$$(\frac{\sigma_{11}^*}{X_T})^2 + (\frac{\sigma_{12}^*}{S_{12}})^2 + (\frac{\sigma_{13}^*}{S_{12}})^2 > 1, \sigma_{11}^* > 0 \tag{3.30}$$

The traction-separation laws for each component of stress and the corresponding fracture toughness are shown in Figure 3.8 below.

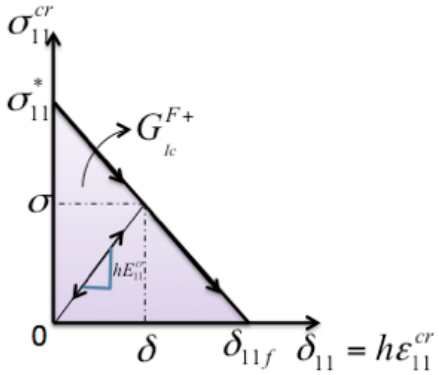

(a) Traction-separation law for σ_{11}^*

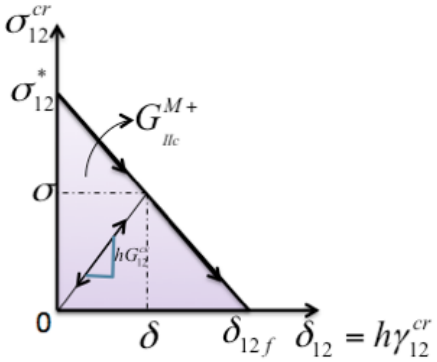

(b) Traction-separation law for σ_{12}^*

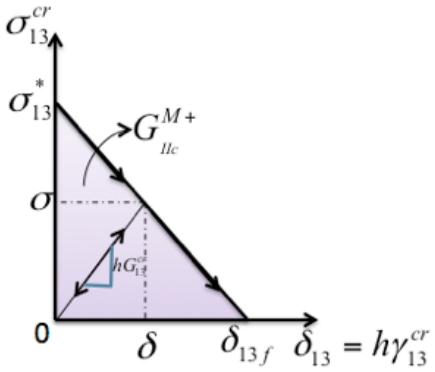

(c) Traction-separation law for σ_{13}^*

Figure 3.8: Traction-separation laws for fiber tensile failure.

3.5.2 Fiber compressive failure

We name this failure mode as Mode-2 and the crack normal aligns to the fiber direction as shown in Figure 3.3. The crack orientation transformation matrix, N is defined in Equation 3.5 and the failure initiation criterion is defined by

$$(\frac{\sigma_{11}}{X_C})^2 > 1, \sigma_{11} < 0 \tag{3.31}$$

The crack interface stresses are related to the local crack strains through,

$$\begin{Bmatrix} \sigma_{11}^{cr} \\ \tau_{12}^{cr} \\ \tau_{13}^{cr} \end{Bmatrix} = \begin{bmatrix} E_{11}^{cr} & 0 & 0 \\ 0 & G_{12}^{cr} & 0 \\ 0 & 0 & G_{13}^{cr} \end{bmatrix} \begin{Bmatrix} \epsilon_{11}^{cr} \\ \gamma_{12}^{cr} \\ \gamma_{13}^{cr} \end{Bmatrix} \tag{3.32}$$

Let the onset stress states at the instant of failure initiation are denoted as σ_{11}^{*}, which satisfies the Equation 6.2 as

$$(\frac{\sigma_{11}^{*}}{X_C})^2 > 1, \sigma_{11}^{*} < 0 \tag{3.33}$$

The traction-separation laws for each component of stress and the corresponding fracture toughness are shown in Figure 3.9 below.

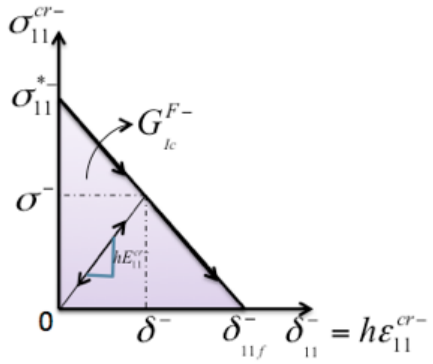

Figure 3.9: Traction-separation laws for fiber compressive failure.

3.5.3 Matrix tensile failure (Crack plane orthogonal to 2-direction)

We name this failure mode as Mode-3 and the crack normal aligns to 2-direction, as shown in Figure 3.4. The crack orientation transformation matrix, N is defined in Equation 3.6 and the failure initiation criteria is defined by

$$(\frac{\sigma_{22}}{Y_T})^2 + (\frac{\sigma_{12}}{S_{21}})^2 + (\frac{\sigma_{23}}{S_{21}})^2 > 1, \sigma_{22} > 0 \tag{3.34}$$

The crack interface stresses are related to the local crack strains through,

$$\begin{Bmatrix} \sigma_{22}^{cr} \\ \tau_{12}^{cr} \\ \tau_{23}^{cr} \end{Bmatrix} = \begin{bmatrix} E_{22}^{cr} & 0 & 0 \\ 0 & G_{12}^{cr} & 0 \\ 0 & 0 & G_{23}^{cr} \end{bmatrix} \begin{Bmatrix} \epsilon_{22}^{cr} \\ \gamma_{12}^{cr} \\ \gamma_{23}^{cr} \end{Bmatrix} \tag{3.35}$$

Let the onset stress states at the instant of failure initiation are denoted as σ_{22}^*, σ_{12}^* and σ_{23}^* which satisfies the Equation 3.34 as

$$(\frac{\sigma_{22}^*}{Y_T})^2 + (\frac{\sigma_{12}^*}{S_{21}})^2 + (\frac{\sigma_{23}^*}{S_{21}})^2 > 1, \sigma_{22}^* > 0 \tag{3.36}$$

The traction-separation laws for each component of stress and the corresponding fracture toughness are shown in Figure 3.10 below.

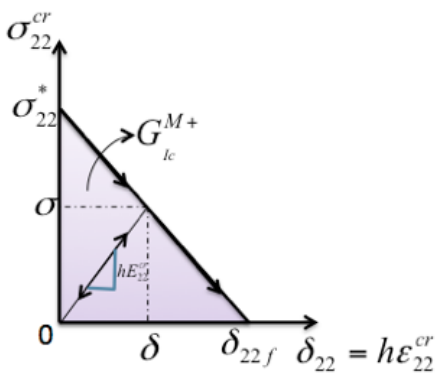

(a) Traction-separation law for σ_{22}^*

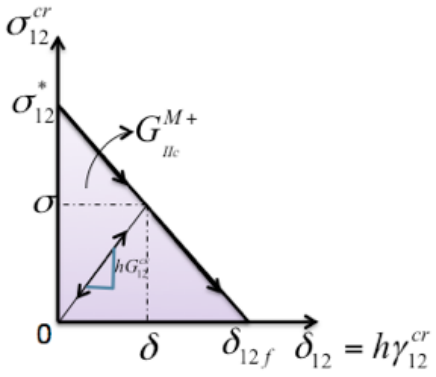

(b) Traction-separation law for σ_{12}^*

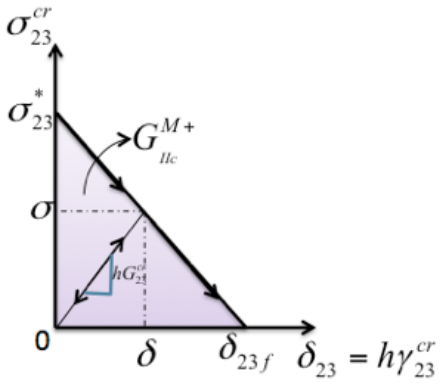

(c) Traction-separation law for σ_{23}^*

Figure 3.10: Traction-separation laws for matrix tensile failure in 2-plane.

3.5.4 Matrix tensile failure (Crack plane orthogonal to 3-direction)

We name this failure mode as Mode-4 and the crack normal aligns to 3-direction, as shown in Figure 3.5. The crack orientation transformation matrix, N is defined in Equation 3.7 and the failure initiation criterion is defined by

$$(\frac{\sigma_{33}}{Y_T})^2 + (\frac{\sigma_{13}}{S_{21}})^2 + (\frac{\sigma_{23}}{S_{21}})^2 > 1, \sigma_{33} > 0 \tag{3.37}$$

The crack interface stresses are related to the local crack strains through,

$$\begin{Bmatrix} \sigma_{33}^{cr} \\ \tau_{13}^{cr} \\ \tau_{23}^{cr} \end{Bmatrix} = \begin{bmatrix} E_{33}^{cr} & 0 & 0 \\ 0 & G_{13}^{cr} & 0 \\ 0 & 0 & G_{23}^{cr} \end{bmatrix} \begin{Bmatrix} \epsilon_{33}^{cr} \\ \gamma_{13}^{cr} \\ \gamma_{23}^{cr} \end{Bmatrix} \tag{3.38}$$

Let the onset stress states at the instant of failure initiation are denoted as σ_{33}^*, σ_{13}^* and σ_{23}^* which satisfies the Equation 3.37 as

$$(\frac{\sigma_{33}^*}{Y_T})^2 + (\frac{\sigma_{13}^*}{S_{21}})^2 + (\frac{\sigma_{23}^*}{S_{21}})^2 > 1, \sigma_{33}^* > 0 \tag{3.39}$$

The traction-separation laws for each component of stress and the corresponding fracture toughness are shown in Figure 3.11 below.

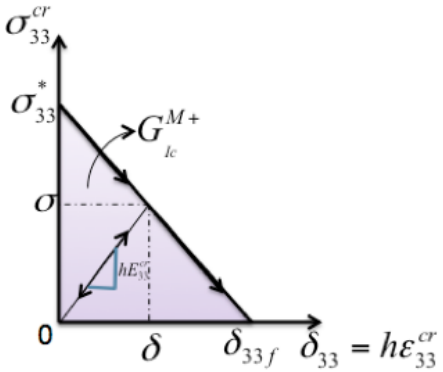

(a) Traction-separation law for σ_{33}^*

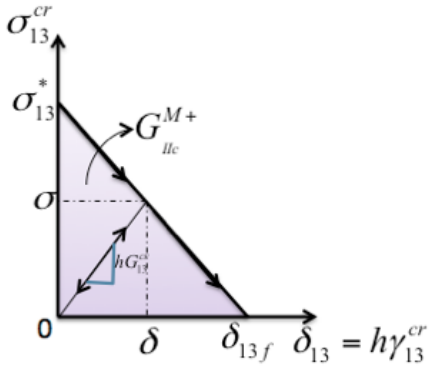

(b) Traction-separation law for σ_{13}^*

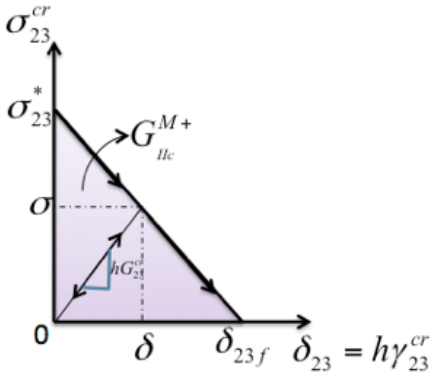

(c) Traction-separation law for σ_{23}^*

Figure 3.11: Traction-separation laws for matrix tensile failure in 3-plane.

3.5.5 Matrix compressive failure(Crack plane orthogonal to 2-direction)

We name this failure mode as Mode-5 and the crack normal aligns to 2-direction, as shown in Figure 3.6(a). The crack orientation transformation matrix, N is defined in Equation 3.6 and the failure initiation criteria is defined by

$$(\frac{\sigma_{22}}{Y_C})^2 + (\frac{\sigma_{12}}{S_{21}})^2 + (\frac{\sigma_{23}}{S_{21}})^2 > 1, \sigma_{22} < 0 \tag{3.40}$$

The crack interface stresses are related to the local crack strains through,

$$\begin{Bmatrix} \sigma_{22}^{cr} \\ \tau_{12}^{cr} \\ \tau_{23}^{cr} \end{Bmatrix} = \begin{bmatrix} E_{22}^{cr} & 0 & 0 \\ 0 & G_{12}^{cr} & 0 \\ 0 & 0 & G_{23}^{cr} \end{bmatrix} \begin{Bmatrix} \epsilon_{22}^{cr} \\ \gamma_{12}^{cr} \\ \gamma_{23}^{cr} \end{Bmatrix} \tag{3.41}$$

Let the onset stress states at the instant of failure initiation are denoted as σ_{22}^*, σ_{12}^* and σ_{23}^* which satisfies the Equation 3.40 as

$$(\frac{\sigma_{22}^*}{Y_C})^2 + (\frac{\sigma_{12}^*}{S_{21}})^2 + (\frac{\sigma_{23}^*}{S_{21}})^2 > 1, \sigma_{22}^* < 0 \tag{3.42}$$

The traction-separation laws for each component of stress and the corresponding fracture toughness are shown in Figure 3.12 below.

3.5.6 Matrix compressive failure(Crack plane orthogonal to 3-direction)

We name this failure mode as Mode-6 and the crack normal aligns to 3-direction, as shown in Figure 3.6(b). The crack orientation transformation matrix, N is defined in Equation 3.7 and the failure initiation criteria is defined by

$$(\frac{\sigma_{33}}{Y_C})^2 + (\frac{\sigma_{13}}{S_{21}})^2 + (\frac{\sigma_{23}}{S_{21}})^2 > 1, \sigma_{33} < 0 \tag{3.43}$$

The crack interface stresses are related to the local crack strains through,

$$\begin{Bmatrix} \sigma_{33}^{cr} \\ \tau_{13}^{cr} \\ \tau_{23}^{cr} \end{Bmatrix} = \begin{bmatrix} E_{33}^{cr} & 0 & 0 \\ 0 & G_{13}^{cr} & 0 \\ 0 & 0 & G_{23}^{cr} \end{bmatrix} \begin{Bmatrix} \epsilon_{33}^{cr} \\ \gamma_{13}^{cr} \\ \gamma_{23}^{cr} \end{Bmatrix} \tag{3.44}$$

Let the onset stress states at the instant of failure initiation are denoted as σ_{33}^*, σ_{13}^* and σ_{23}^* which satisfies the Equation 3.43 as

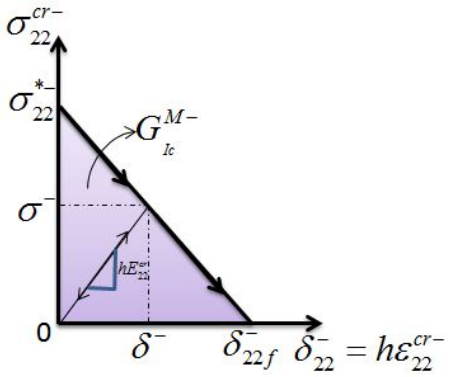

(a) Traction-separation law for σ_{22}^{*}

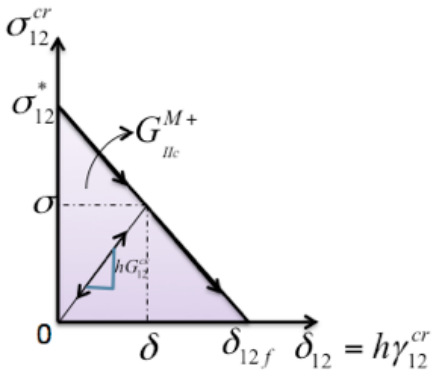

(b) Traction-separation law for σ_{12}^{*}

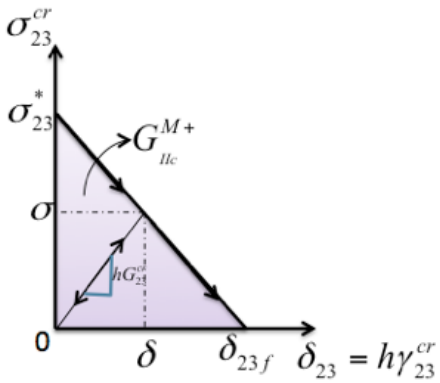

(c) Traction-separation law for σ_{23}^{*}

Figure 3.12: Traction-separation laws for matrix compressive failure in 2-plane.

$$(\frac{\sigma_{33}^{*}}{Y_C})^2 + (\frac{\sigma_{13}^{*}}{S_{21}})^2 + (\frac{\sigma_{23}^{*}}{S_{21}})^2 > 1, \sigma_{33}^{*} < 0 \tag{3.45}$$

The traction-separation laws for each component of stress and the corresponding fracture toughness are shown in Figure 3.13 below.

3.5.7 VUMAT Implementation

The commercially available finite element software, ABAQUS (version 6.14), is used for the macroscale FEA, and the NCYL micromechanics model at the subscale is implemented at each integration point of the macro scale, using a user defined material subroutine, VUMAT. This subroutine is called at each integration point at each increment, and the material constitutive law is updated through user-defined options. At the start of each increment, the material state i.e. stress-strain and solution-dependent state variables from the previous equilibrium step and the strain increments in the current step are passed into the VUMAT through the ABAQUS

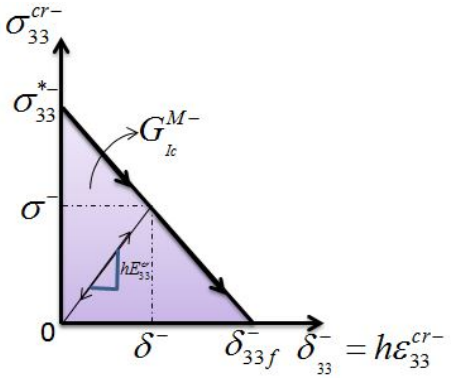

(a) Traction-separation law for σ_{33}^{*}

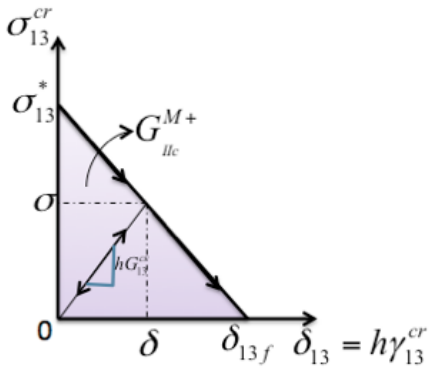

(b) Traction-separation law for σ_{13}^{*}

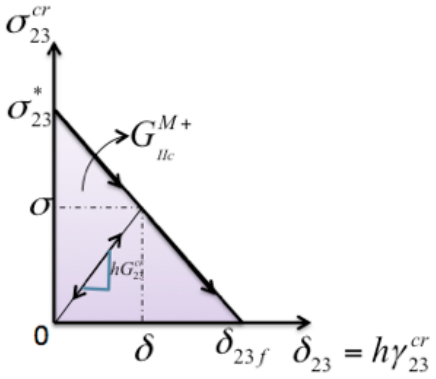

(c) Traction-separation law for σ_{23}^{*}

Figure 3.13: Traction-separation laws for matrix compressive failure in 3-plane.

solver. The algorithms of the main VUMAT subroutine and the smeared crack subroutine are shown in Appendices C and E respectively.

3.6 3D Isotropic smeared crack approach (SCA) for matrix

The thin layer of matrix pocket outside of the fiber tows and inside the volume of the textile is treated as isotropic material and subjected to tensile and compressive failure, when the textile material is subjected to loading. The matrix develops micro cracks due to the growth of voids or inclusions, when subjected to loading and consequently leads to degradation of stiffness of the structure, which also causes the pre-peak non-linear behavior in the global stress-strain curve. The accumulation of matrix microdamage leads to the initiation of matrix macroscopic cracking, followed by post-peak strain softening response. In this study, the evolution of matrix failure is modeled

using the 3D isotropic smeared crack approach (SCA), similar to the one formulated in the previous section for fiber tow as 3D orthotropic trasversely isotropic smeared crack approach. The basic formulation between two different material systems is the same except the fact that, the crack orientation transformation matrix is determined by the state of stress in isotropic material rather than the material orienation in orthotropic material. The formulation is described in the following section and the major changes are highlighted.

3.6.1 Determination of the crack constitutive relations

In the present study, a 1D uncoupled traction-separation law is employed and the crack interface stiffness matrix D^{cr} dictates the failure evolution in the post-peak starin softening regime. For a single crack in 3D solid, D^{cr} becomes,

$$\boldsymbol{D}^{cr} = \begin{bmatrix} E^{cr} & 0 & 0 \\ 0 & G_1^{cr} & 0 \\ 0 & 0 & G_2^{cr} \end{bmatrix} \tag{3.46}$$

where E^{cr} is the secant crack modulus resulting from normal crack strain (mode-I type of failure), while G_1^{cr} and G_2^{cr} are associated with shear crack strains (mode-II type of failure). In the current study, secant crack stiffness is used so that the softening response follows the traction-separation law exactly, as shown in Figure 3.14.

To prevent crack healing from happening, it is required that,

$$\dot{E}^{cr} < 0 \quad \text{and} \quad \dot{G}^{cr} < 0 \tag{3.47}$$

Hence, once the crack stiffness is degraded, it cannot be recovered. The loading and unloading responses during the evolution of the failure process are specified in Figure 3.14. In the SCA, it is assumed that distributed cracks are 'smeared' out over a certain width within the finite element such that the effect of progressive cracking is represented by macroscopic strain softening in a continuum scheme. To restore mesh objectivity, a characteristic length is introduced such that the total amount of energy dissipated during failure in a continuum element is equal to the fracture toughness defined for a cohesive element of the same size. The fracture toughness, or the critical energy release rate, G_C, is defined by the area under the traction-separation law that dictates the cohesive behavior of crack propagation (see Figure 3.15(b)) as,

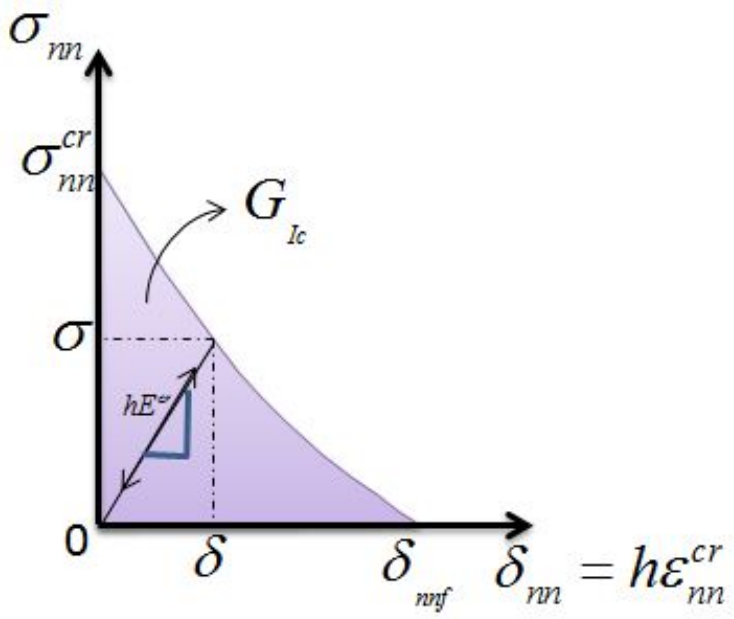

Figure 3.14: Crack evolution is dictated using degrading secant crack stiffness.

$$G_C = \int_0^{\delta_f} \sigma \, \mathrm{d}u \tag{3.48}$$

where u is the sum of crack displacements within the fracture zone. In the SCA, u represents the crack strain acting across a certain width within a finite element, denoted as the crack band width, h. Assuming that all the cracks are uniformly distributed over the crack band, and since u is the accumulation of all the crack strains over the fracture zone, it follows that,

$$u = h\,\epsilon^{cr} \tag{3.49}$$

If g_c represents the area under the softening branch of the stress-strain response (see Figure 3.15(a)), then substituting equation (3.49) into equation (3.48) results in,

$$G_C = \int_0^{\delta_f} \sigma(h\epsilon^{cr}) h \, \mathrm{d}\epsilon^{cr} = h \int_0^{\epsilon_f^{cr}} \sigma(\epsilon^{cr}) \, \mathrm{d}\epsilon^{cr} = h\, g_c \tag{3.50}$$

Therefore, the strain-based description for a softening material is related to the displacement-based traction-separation laws through the characteristic length, h. In a FE setting, h is chosen based upon the element type, element size, element shape, and the integration scheme [28]. Typically the length of the element projected onto the crack normal is used as a characteristic element length, as shown in Figure 3.16.

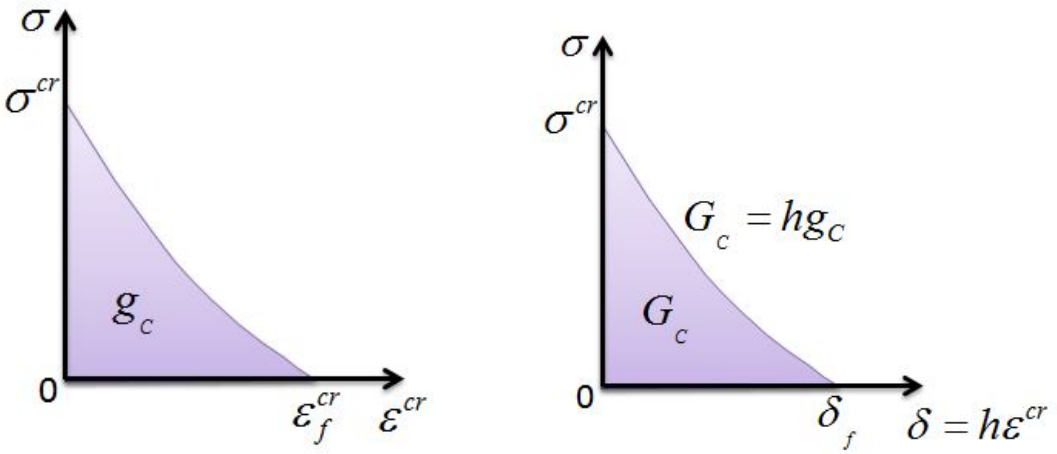

(a) Critical stress-strain curve. (b) Traction-separation law.

Figure 3.15: Stress-strain softening response is related to traction-separation law through a characteristic length, h.

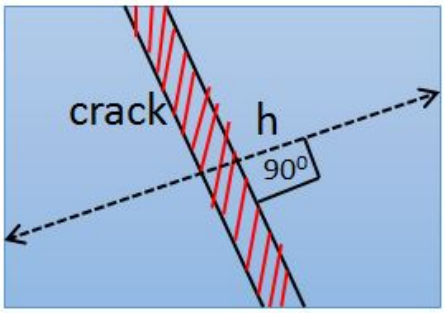

Figure 3.16: Characteristic element length. The length of the element projected on the crack model is used as characteristic element length

The 3D stress state inside the matrix material are updated through the user subroutine over the progressive loading and subjected to the smeared crack code when certain failure initiation criteria are met. Different stress based failure initiation criteria are implemented for tensile and compressive failure of matrix material, as described in the following sections. Single element test is carried out to check the validity of the code and various case studies are considered to demonstrate the mesh objectivity of both tensile and compressive failure using the smeared crack approach.

3.6.2 Matrix in tension (Principal stress criteria)

The matrix material surrounding the fiber tows are subjected to tensile failure, leading to debonding of the contact surfaces from the fiber tows. The Z-fiber tows undulate in top-bottom fashion and the thin matrix layer sandwiched in the gap between the

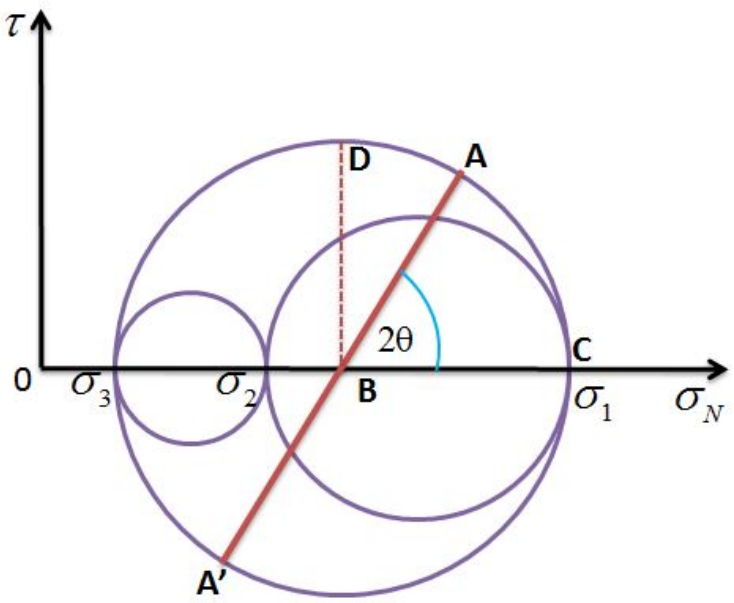

Figure 3.17: Mohr's circle and tensile failure criteria.

undulated and the in-plane fiber tows are seen through high level of 3D stress during the progressive loading. An equivalent stress, combining all six stress components in 3D framework, can be established and tensile failure initiation criteria can be expressed as a function of equivalent stress, which should also be able to describe the physics of the failure mode. In a monolithic material, cracks are likely to grow under pure mode-I conditions since this mode of failure is energetically favorable. However, in this study, it is assumed that the tensile cracks grow under pure mode-I conditions, oriented with the maximum principal stress plane. For a given stress state, the principal stresses, σ_1, σ_2, and σ_3, and the corresponding principal axes, $\boldsymbol{n_1}$, $\boldsymbol{n_2}$, and $\boldsymbol{n_3}$, are first computed and Mohr's circle can be drawn for the maximum and minimum principal stresses, as shown in Figure 3.17.

Every point on the Mohr's circle defines the unique state of stress at a material point. The normal and shear stresses on any plane whose normal $\boldsymbol{n}$ makes an angle $\boldsymbol{\theta}$ with the horizontal axis can easily be expressed as a set of equations in terms of principal stresses and related to the equations of a circle in $\boldsymbol{\sigma_N}$-$\boldsymbol{\tau}$ plane, with the angle $\boldsymbol{\theta}$ as a parameter. Consider, for example, the coordinates of any point $\boldsymbol{A}$ on the circle represent the values of $\boldsymbol{\sigma_N}$ and $\boldsymbol{\tau}$ for the plane whose aspect is defined by $\boldsymbol{\theta}$ in Figure 3.17. Thus all possible information about the stresses on various planes can be found from Mohr's circle. If either principal stress is compression, it must be taken with negative sign, so that in general the center $\boldsymbol{B}$ of Mohr's circle may lie to

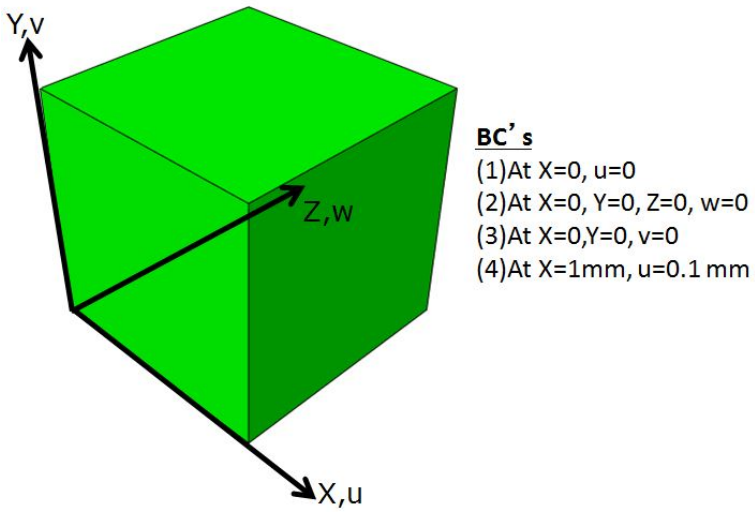

Figure 3.18: Boundary conditions for single element subjected to uniaxial tension.

either side of the origin in Figure 3.17, but always on the $\boldsymbol{\sigma_N}$ axis. Maximum tensile stress criterion is used for tensile crack initiation as,

$$\sigma_1 > \sigma_2 > \sigma_3 \quad \text{and} \quad \frac{\sigma_1}{\sigma_0} \geq 1 \tag{3.51}$$

where σ_0 is the tensile critical strength, in the mode-I traction separation law. In practical applications, it is further assumed that once the crack is initiated, the crack orientation, determined from the principal stress directions, is fixed during the failure evolution. It is further assumed that the crack interface is traction free in both normal and shear directions during and after fracture energy dissipation. The two crack shear moduli, G_1^{cr} and G_2^{cr}, are degraded as a function of ϵ_{nn}^{cr}, indicating that the cracks grow under mode-I dominated conditions. It is possible that the crack shear moduli are degraded with respect to γ_{t1}^{cr} or γ_{t2}^{cr}, and a mixed-mode traction-separation law could be introduced to ensure that the shear failure evolves under mode-II conditions [36]. However, such a complicated failure mechanism requires further study of cracks progressing at the microscale, and this aspect is not considered in the current study.

A single element test is carried out for uniaxial tension test with a suitable element length to satisfy Bazant's mesh size criteria and scaled fracture toughness. Figure 3.18 illustrates the boundary conditions for the single element subjected to uniaxial tension. All the material properties that are used in this study are summarized in Table 3.1. The resulting stress versus strain response is plotted in Figure 3.19. The area under the curve is calculated and it closely matches with the scaled fracture toughness used as input.

Table 3.1: Stiffness, strength and fracture toughness values for single element and mesh objectivity test.

Property	Value
E(GPa)	2.487
ν	0.35
σ_y(MPa)	30
$K_1(MPa)$	4500
K_2	58.31
σ_0(MPa)	60
G_{IC}(N/mm)	1.5

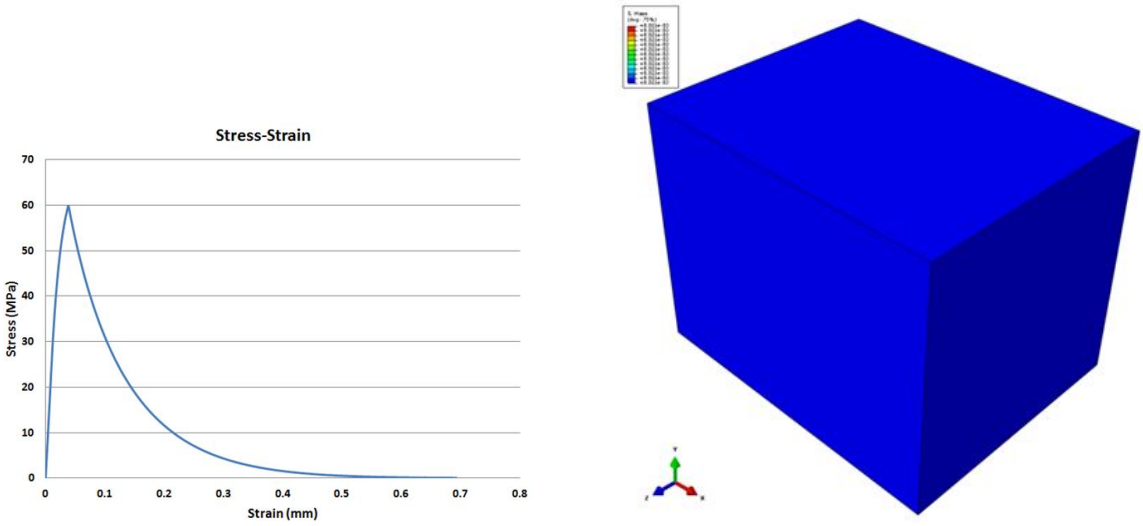

(a) Stress-strain response subjected to tension.

(b) ABAQUS simulation.

Figure 3.19: Single element test for matrix tensile failure.

In order to verify the mesh objectivity of the smeared crack code in FE framework, a uniaxial tension test was performed on a unit volume cube with four different mesh sizes, as shown in [31]. The in-situ matrix non-linear properties of SC-15 epoxy used and the elements that lie on the mid-plane perpendicular to the loading direction are assigned a 0.5% lower strength than the rest of the elements, so that the tensile failure is localized within the cube in these weak elements. The resulting load versus displacement responses for all the four mesh sizes clearly shows that the computed fracture toughness, peak load and the localized fracture zone, are independent of mesh

size, which clearly indiactes the mesh objectivity characteristics of the Smeared crack approach. Hence, mesh objectivity is verified for tensile failure of matrix material using 3D Isotropic smeared crack approach and the failure initiation criteria based on principal stress limit.

3.6.3 Matrix in compression (Mohr-Coulomb's criteria)

The matrix inside the textile involve complex stress state, when subjected to compressive loading and not much is known about the failure behavior of particular epoxy system under 3D stress conditions. Problems that involve polyaxial loading often makes it worst and a reliable computational physics-based failure model is ineveitable. The Mohr-Coulomb failure initiation criterion is widely applied to the matrix compression failure and to the description of shear frictional sliding. Matrix sliding friction is defined in terms of the effective stress normal to the sliding surface and to the shear stress resolved in the direction in which sliding occurs. It assumes that failure occurs at particular combinations of the greatest and least principal stresses, that the intermediate principal stress has no effect on failure and that failure criteria can be set out in terms only of the stress state. Matrix sliding friction is important to composite progressive failure modeling because it limits the differential stresses that can be obtained at the interface of fiber tows and the matrix pocket. Modeling matrix compression failure behavior demand knowledge of failure or frictional sliding under generalized stress conditions. More details about the implementation of Mohr-Coulomb's criteria combined with Smeared crack code, in the framework of ABAQUS VUMAT are explained in Chapter 6. Single element test along with mesh objectivity and imperfection sensitivity of the matrix compression modeling are studied in the framework of a micromechanics model.

3.7 Finite element implementation of NCYL and SCA

A multiscale framework is established in this research using a combined approach of NCYL and SCA models. NCYL is an analytical micromechanics model, which is able to captute the pre-peak non-linearity caused by matrix micro-damage. The detailed procedure to calculate the in-situ matrix non-linearity constants for N=2, 3 and 4 cylinders are explained in Chapter 2. It is an analytical discretization model, where N can be extended to any number of matrix layers in general and all the stress

and strain fields inside the cylinders can be expressed in closed form using the in-house developed Mathematica code, as a part of this research. All the closed form analytical expressions are formulated in explicit version of user-subroutine VUMAT to interface with ABAQUS and that enables the implementation of this micromechanics analytical model to run the finite element based numerical simulations. The main VUMAT for the combined approach is reported in Appendix C and the detailed flow chart for the implementation of NCYL (N=2, 3 and 4) in ABAQUS framework are explained in Appendix D. Stress based failure initiation criteria are used for different failure modes of both fiber tow and matrix material. The mixed-mode failure initiation criteria of homogenized fiber tow are followed by 3D Hashin criteria and implemented in 3D orthotropic transversely isotropic smeared crack code, as explained in above sections. The matrix pocket outside the fiber tow and inside the volume of textile is subjected to tensile and compressive failure modes. The tensile failure criterion is based on maximum principal stress theory and the compressive failure is initiated based on Mohr-Coulomb's theory. Both tensile and compressive failure are implemented using 3D isotropic smeared crack code, as explained above. A detailed procedure of numerical implementation of both 3D orthotropic and isotropic smeared crack codes in ABAQUS VUMAT framework are explained as flow charts in Appendix E. Various numerical tests are carried out in the following sections to strengthen and validate the implementation of NCYL and SCA models in ABAQUS framework.

3.7.1 Single element test

Single element test (SET) is a basic fundamental and building block approach to validate the in-house developed code for different failure modes. Matrix shear and transverse tension failure modes lead to tow splitting, as observed in experiments by many researchers. For laminated and hybrid textile composites, this mode of failure is important and a validated computational tool is indispensable to capture this failure phenomenon. As a scope of this research, the in-house developed code is tested for a single element case as explained below. To decide the element size and the model, following guidelines are followed: (1) Calculate the crack band characteristic length for all failure modes in the SCA code, (2) Pick the lowest characteristic length and divide by 10 (or as required, preferably >5) and this is the element size to be used for a single element test and (3) Construct an 8 noded cube with the dimension calculated. The unit cube element length of 0.001 mm is used for this exercise. For

a single fiber tow or lamina element, the following tests are listed: (a) Tension in 1 (fiber direction), (b) Compression in 1, (c) Tension in 2, (d) Compression in 2, (e) Pure shear and (f) Simple shear (parallel to fiber (1)).

Following guidelines are followed to decide boundary/loading conditions for each test case and verification of results: (1) Always perform the hand calculation prior to the element test to decide the appropriate boundary displacement for the case, i.e. essentially constructing the stress-strain plot of SCA and calculating the strain. Make sure that the final failure strain value is <50% (or even 20-30%). This is to avoid other issues with strain measure differences between the hand calculations and the ABAQUS results). Calculate the required BC displacement from final failure strain, (2) for each test case, extract all the relevant reaction force-displacement data. Area under these curves should always match with the energy released for crack formation (fracture toughness multiplied by crack area) and (3) study the mixed mode loading conditions in a similar way and decide if the mixed-mode law is satisfied at the final failure. The simulated results in ABAQUS are carried out using the user-subroutine VUMAT and shown in the figures below. For each case, all relevant stress-strain and the reaction force-displacement data are extracted and the areas under these curves are calculated. The whole exercise is based on mesh objective approach and to restore it, the energy release rate (area under the curve) is compared in each case with the hand calculated and scaled fracture toughness from real test data. The set of test data used for this exercise are summarized in the following Table 3.2 for IM-7/977-3 material system.

Table 3.2: Stiffness, strength and fracture toughness values for single element test.

Strength(MPa)		Fracture(N/mm)		Stiffness(GPa)	
Fiber tension(X_T)	2905	G_{IC}^{F+}	40	E_{1T}	164.3
Fiber compression(X_C)	1274	G_{IC}^{F-}	4	E_{1C}	137.4
Transverse tension(Y_T)	44.4	G_{IC}^{M+}	0.256	E_{2T}	8.977
Transverse compression(Y_C)	247.6	G_{IC}^{M-}	0.256	E_{2C}	8.694
In-plane shear(S_{12})	108	G_{IIC}^{M}	1.156	G_{12}	4.88

The detailed procedure to calculate the matrix in-situ non-linear properties for N=2, 3 and 4 cylinders are explained in Chapter 2. The computed values for IM-7/977-3 material system and volume fraction of 64% are summarized below in Tables

3.3, 3.4 and 3.5 respectively. These values are used for single element test to validate the Smeared crack code.

Table 3.3: In-situ nonlinear properties of 977-3 matrix for N=2.

	σ_y^m (MPa)	k_1 (MPa)	k_2
M1	48.3	5000	32

Table 3.4: In-situ nonlinear properties of 977-3 matrix for N=3.

	σ_y^m (MPa)	k_{11} (MPa)	k_{21}
M1	69.5	6000	24
	σ_y^m (MPa)	k_{12} (MPa)	k_{22}
M2	43.5	4000	19

Table 3.5: In-situ nonlinear properties of 977-3 matrix for N=4.

	σ_y^m (MPa)	k_{11} (MPa)	k_{21}
M1	83	8000	27
	σ_y^m (MPa)	k_{12} (MPa)	k_{22}
M2	55	5000	20
	σ_y^m (MPa)	k_{13} (MPa)	k_{23}
M3	42	5000	24

3.7.1.1 Single element test results

A linear traction law is assumed for SCA to hand calculate the failure strain. As a first case, high yield value of matrix is used as linear pre-peak matrix property to calculate the force-displacement curves in ABAQUS simulations for each loading case. The results for each test case are summarized in the following Table 3.6.

Table 3.6: Summary result for single element test (SET) and linear matrix property.

Loading case	Measured(N/mm)	Scaled(N/mm)	NCYL2	NCYL3	NCYL4
Fiber tension	40	0.25682	0.256	0.256	0.256
Fiber compression	4	0.0591	0.0606	0.0606	0.0606
Transverse tension	0.256	0.0011	0.0011	0.0011	0.0011
Transverse compression	0.256	0.0353	0.0386	0.0386	0.0386
Simple shear	1.156	0.0143	0.0143	0.0143	0.0143
Pure shear	1.156	0.0143	0.0143	0.0143	0.0143

As a second case, the nonlinear matrix in-situ properties are used from Tables 3.3, 3.4 and 3.5 for N=2, 3 and 4 respectively to calculate the force-displacement curves in ABAQUS simulations for each loading case. The results for each test case are summarized in the following Table 3.7.

Table 3.7: Summary result for single element test (SET) and non-linear matrix property.

Loading case	Measured(N/mm)	Scaled(N/mm)	NCYL2	NCYL3	NCYL4
Fiber tension	40	0.25682	0.256	0.256	0.256
Fiber compression	4	0.0591	0.0606	0.0606	0.0606
Transverse tension	0.256	0.0011	0.0011	0.0011	0.0011
Transverse compression	0.256	0.0353	0.041	0.0389	0.0388
Simple shear	1.156	0.0143	0.0164	0.0144	0.0144
Pure shear	1.156	0.0143	0.0164	0.0144	0.0144

As shown in Tables 3.6 and 3.7, the hand calculated scaled fracture toughness from test data closely match with ABAQUS simulation results for all failure modes. As a next step, the developed code is checked for demonstarting the tow split failure mode as explained in next section.

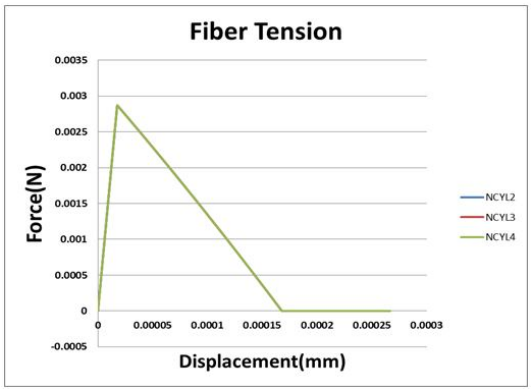

(a) Force-displacement

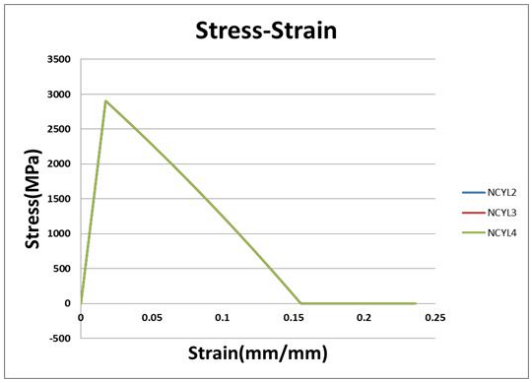

(b) Stress-strain

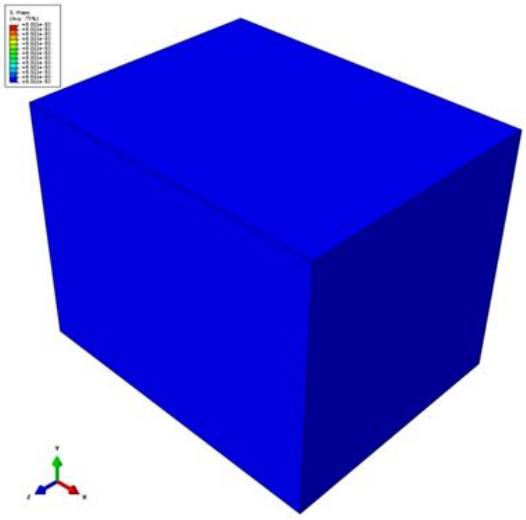

(c) ABAQUS simulation

Figure 3.20: Fiber tension (1).

3.7.2 Tow split test

Fiber tow split is a very common failure mode occuring mechanism, when the textile composites are subjected to transverse and shear loading. Figure 3.26 strengthens the eveidence of this failure mechanism, as shown by clear transverse cracks along the width of fiber tow cross-section. Each individual fiber tow consists of thousands of fibers embedded in a matrix medium in various packing arrangements. The matrix inside the tow and in-between the fibers develops micro-cracks due to the growth of voids and inclusions, when subjected to transverse and shear loading. These matrix micro-cracks cause the pre-peak non-linear behaviour of the fiber tow and eventually develop in to macroscopic cracks, which lead to two-piece failure of fiber tow due to a single macro transverse crack. The fibers and matrix can be modeled discretely

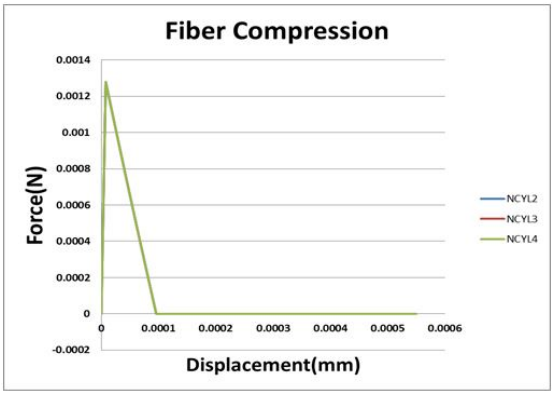

(a) Force-displacement

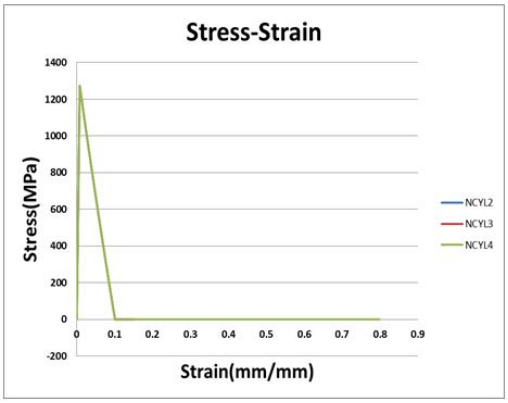

(b) Stress-strain

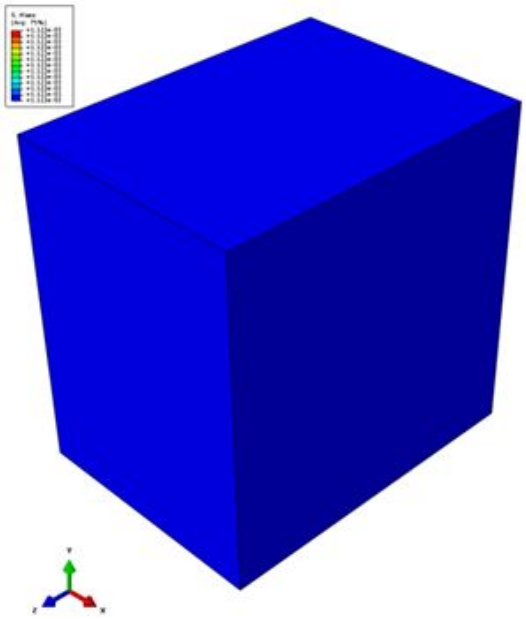

(c) ABAQUS simulation

Figure 3.21: Fiber compression (1).

in a microscopic RVE level and numerical simulations can be carried out to capture this failure phenomenon, but it computationally expensive to model individual fibers, when analyzing the global larger structure. The goal of this research is to capture these macroscopic transverse cracks at the homogenized fiber tow numerical model, which uses the constituent level properties as inputs in a multi-scale framework. A fiber tow is modeled inside a rectangular matrix box to represent the continuum medium and subjected to transverse loading, as shown in Figure 3.27. This finite element simulation demonstrates the capability of the multiscale method discussed in the previous sections, by using combined approach of NCYL and SCA. The stress-

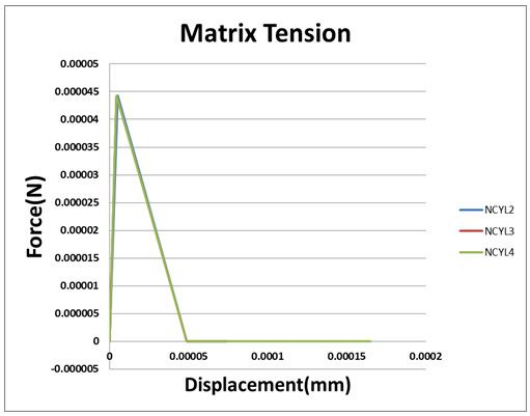

(a) Force-displacement

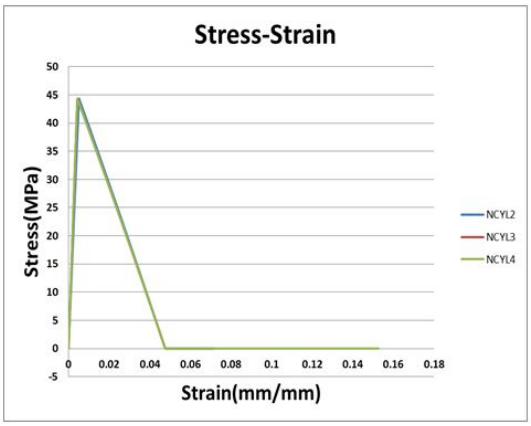

(b) Stress-strain

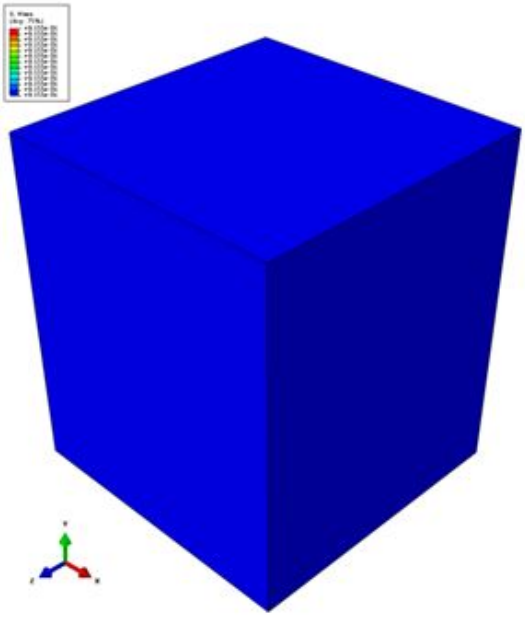

(c) ABAQUS simulation

Figure 3.22: Matrix tension (2).

strain behaviour and the progressive contour plot of matrix transverse cracks are shown in Figure 3.28.

3.7.3 Angle ply test

Open hole tension (OHT) coupon geometry and dimensions are referred from Tech Scout-1 to build up the 3D geometry model of a single ply in ABAQUS 6.14. A finite element mesh is generated from the 3D model, as shown below in Figure 3.29 to simulate the tensile test for both unidirectional and angle plies separately. The

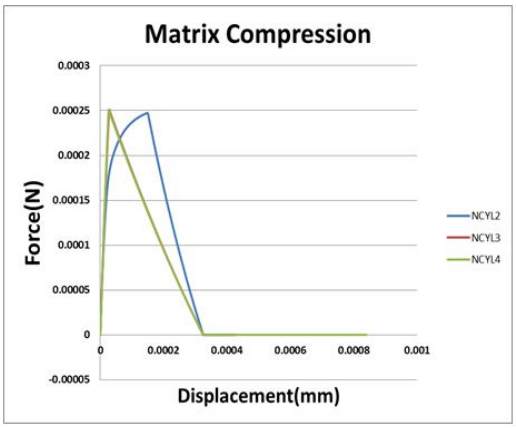

(a) Force-displacement

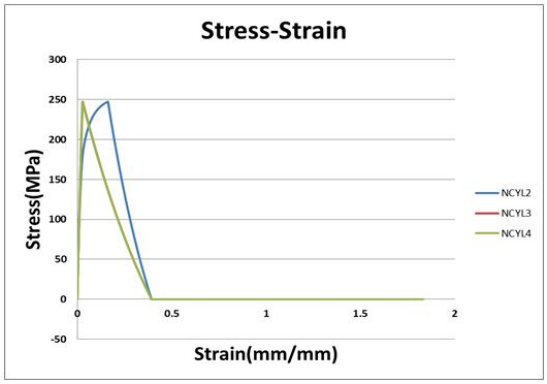

(b) Stress-strain

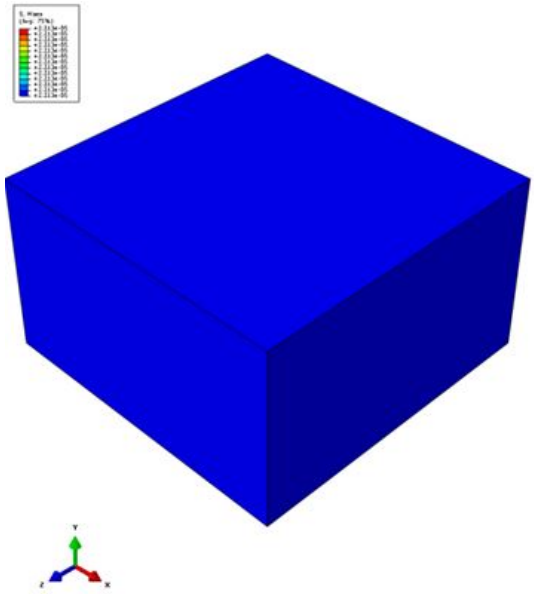

(c) ABAQUS simulation

Figure 3.23: Matrix compression (2).

purpose here is to validate the in-house developed smeared crack code by observing the failure mode in each ply and comparing with the experiments and literature. A non-radial, non-fiber-aligned mesh is used to elliminate the possibility of biasing the results with respect to the fiber aligned mesh. The failure prone gauge area near to the hole is discretized using a high mesh density, satisfying Bazant's mesh-ojectivity element length and a mesh gradient technique is used to gradually coarsen the mesh density towards the non-failure grip area of the coupon. As observed in the experiments, matrix micro-cracks initiate at the edge of hole at certain characteristic angle depending on the angle of individual ply. These micro-cracks develop into a prominent macroscopic crack between the fiber tows in the lamina and propagate

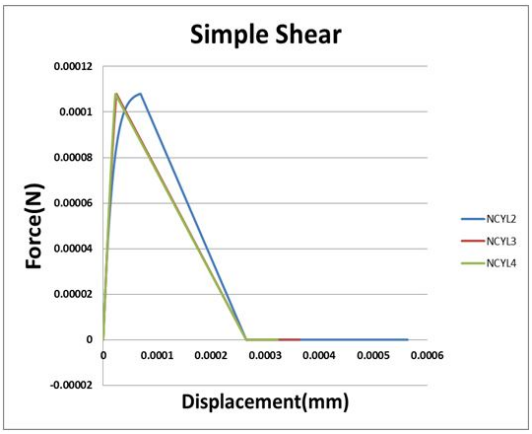

(a) Force-displacement

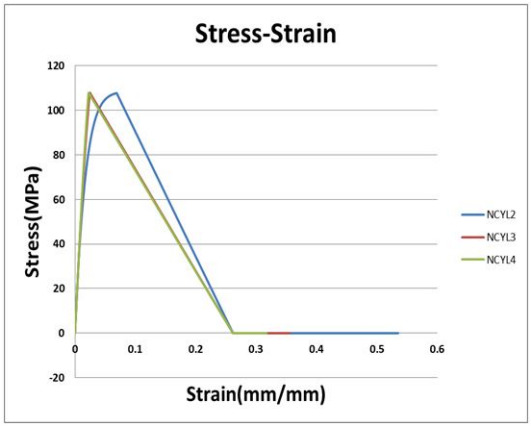

(b) Stress-strain

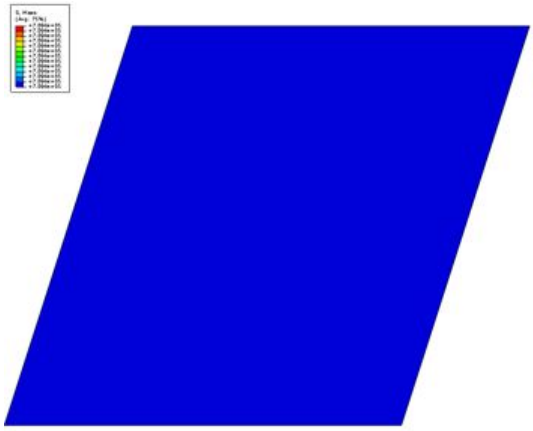

(c) ABAQUS simulation

Figure 3.24: Simple shear (BC parallel to fiber (1)).

along the length of the fibers. Open hole tension (OHT) numerical simulations are carried out for 0^0, 45^0 and 90^0 angle plies using the same code, tested for single element test and the contour plots of matrix cracking are shown below in Figures 3.30, 3.31 and 3.32 respectively. As shown in the figures, the developed smeared crack code can capture the tow split in unidirectional ply, mixed-mode matrix cracking in 45^0 ply and the transverse matrix cracking in 90^0 ply. Now, the developed tool will be implemented in the simulation of tensile test for three different notched laminates, as explained in the following section.

3.7.4 Laminate test

A study was conducted under the support of phase I of the Air Force Research Laboratory (AFRL) Tech Scout Project (TS-1) aimed at evaluation of existing progressive

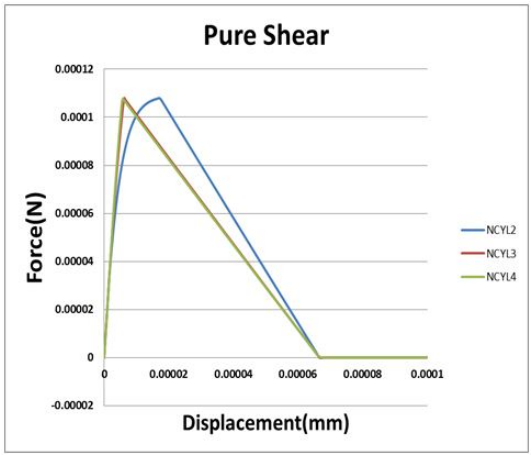

(a) Force-displacement

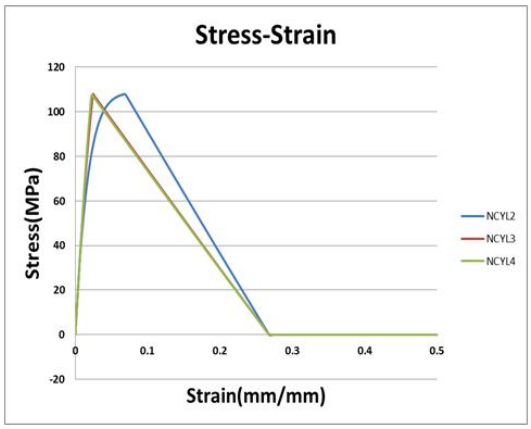

(b) Stress-strain

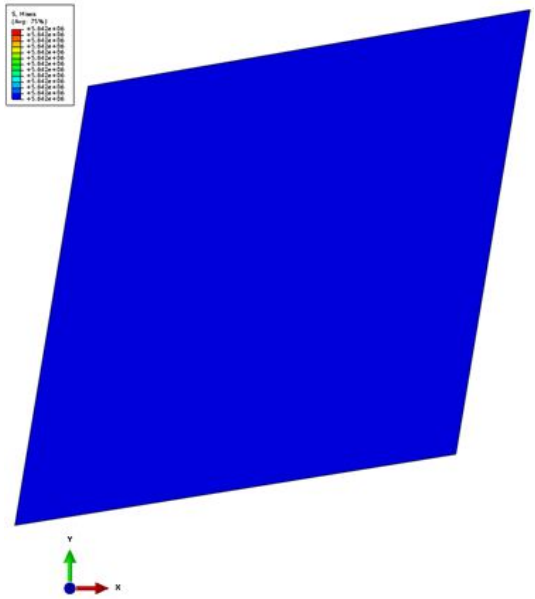

(c) ABAQUS simulation

Figure 3.25: Pure shear.

damage prediction methods and NCYL multiscale method was chosen to be one of potential tool to provide a more realistic representation of experiments. As a part of Tech Scout-1 project, three different lay-ups (i.e., Lay-up 1: $[0/45/90/-45]_{2s}$; Lay-up 2: $[30/60/90/-60/-30]_{2s}$; Lay-up 3: $[60/0/-60]_{3s}$) of notched tension specimens were modeled and blind static failure predictions were carried out. All experimental data used in this work were conducted by AFRL and provided a refernce to validate the predictive models. After submission of blind predictions, NCYL model was recalibrated in terms of constituent properties input to better correlate to the experimental results as part of the Tech Scout-1. A systematic mesh objective study

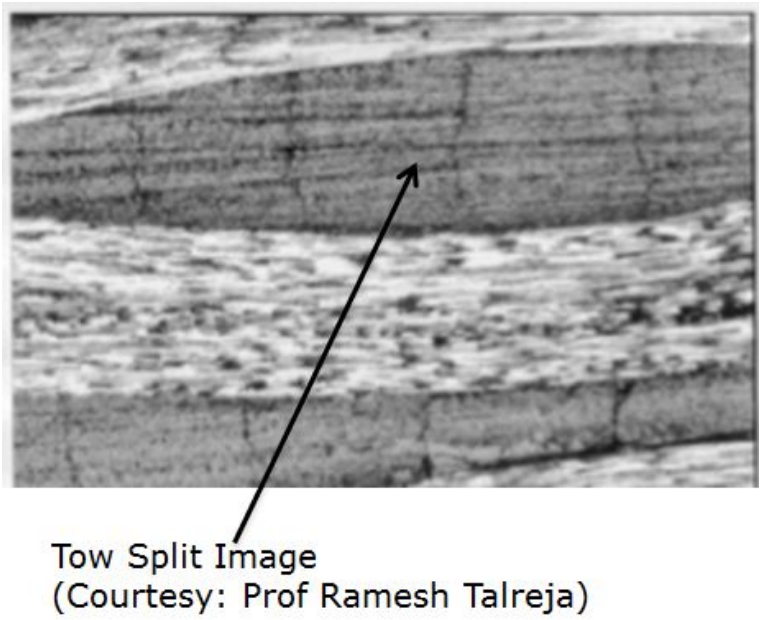

Figure 3.26: Experimental proof of tow split.

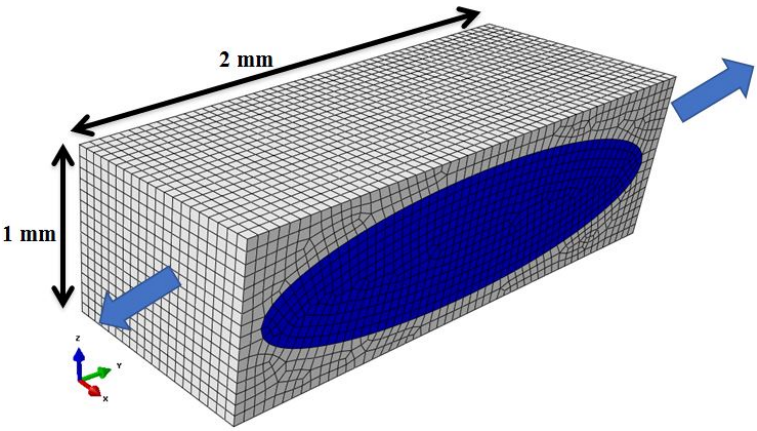

Figure 3.27: Tow mesh subjected to transverse loading.

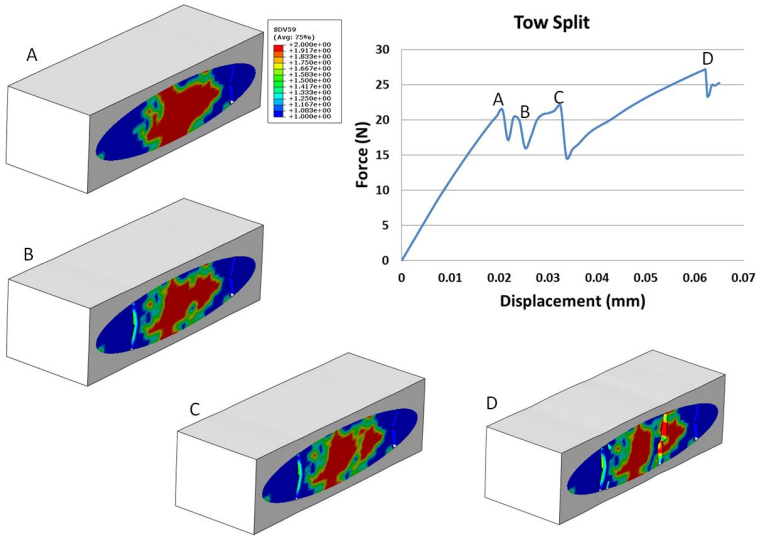

Figure 3.28: Progressive plot for tow split.

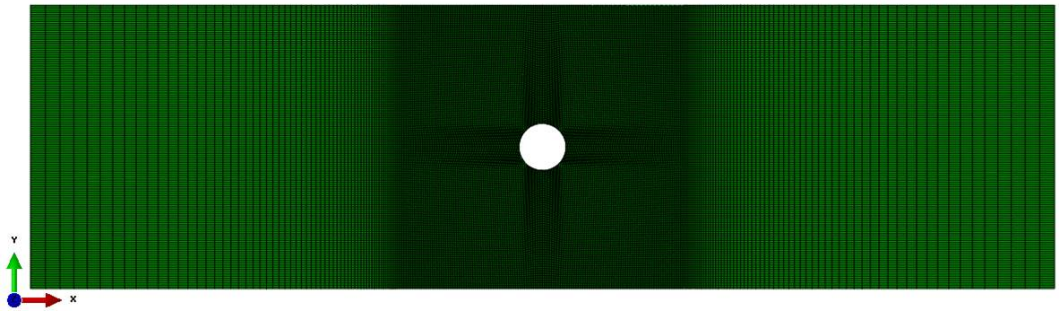

Figure 3.29: Mesh used to simulate OHT test for angle ply.

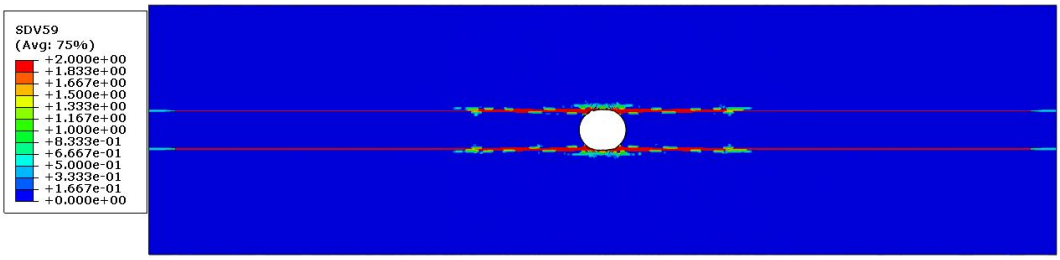

Figure 3.30: Tow split captured in 0^0 ply.

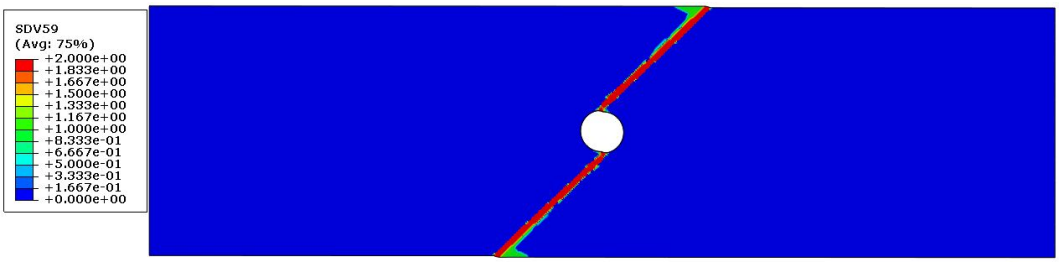

Figure 3.31: Matrix cracking captured in 45^0 ply.

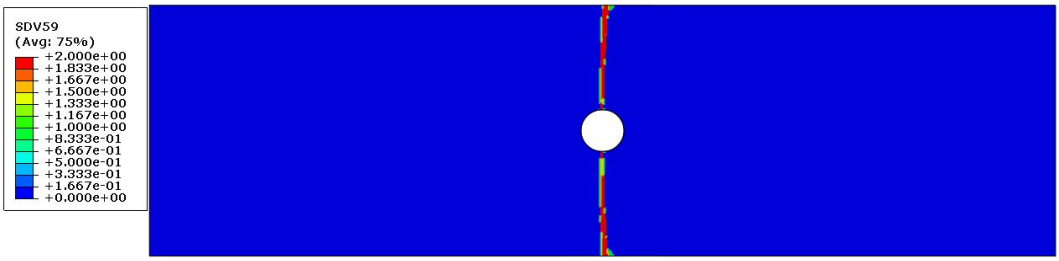

Figure 3.32: Matrix cracking captured in 90^0 ply.

could not be conducted due to the imposed project timeframe and a coarse mesh was used to help timely submission of the results. Since, the failure modes were not fully implemented in the Smeared crack code before the due date of TS-1 predictions, the failure modes in each lamina were not captured properly. Also, the strengths were under predicted due to insufficent mesh density, especially for notched shear dominated lay-ups. In this study, a more systematic approach is adopted in terms of choosing a finer mesh and including all possible failure modes for fiber and matrix in the revised 3D smeared crack code. The purpose of this research is to establish a reliable computational framework to be able to predict the progressive damage and complex failure mechanisms of laminated composites using the constituent properties in a multiscale framework obtained from a coupon level tests of a unidirectional lamina.

Three different lay-ups of IM-7/977-3 carbon fiber composite laminates are studied here. The constitutive fiber and matrix properties are obtained from the lamina properties using inverse CCM analysis and partially from the manufacturers data. The elastic properties for fiber and matrix materials are summarized in Table 3.2. The matrix nonlinear response is obtained from a tension test on a $[+45/-45]_{4s}$ symmetric laminate in conjunction with a computational micromechanics model, as proposed by Ng et al. [17]. The fiber volume fraction of each lamina is 64%. The strength characteristics are summarized in Table 3.2.

The dimensions of lay-ups and boundary conditions that are used for notched

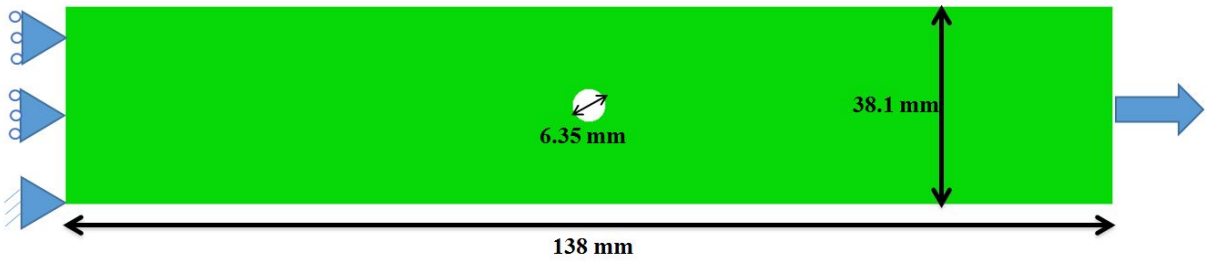

Figure 3.33: OHT loading and boundary conditions.

specimens are shown in Figure 3.33. Each lamina is modeled explicitly as a homogenized solid using 3D elements and are related to the micro-scale analysis of fiber/matrix constituents through an analytical micromechanics N-layer concentric cylinder (NCYL) model. A layer of discrete cohesive zone (DCZM) elements with a thickness of 5% of the lamina thickness is implemented in-between the lamina layers to account for possible delamination.

The finite element mesh is chosen based on two facts, (1) The characteristic element length around the notch area should satisfy the mesh-objectivity criteria, which is calculated based on fracture toughness, stiffness and strength for each individual failure mode. The minimum element length of all the failure modes is chosen to be 0.2 mm around the notch area and a coarser mesh of 0.6 mm length is used in the far field area for computational efficiency. (2) The chosen mesh is studied for stress gradients around the notch area in a linear elastic analysis and verified with Lekhnitskii's analytical solution for unidirectional and angle ply, which gives confidence to be used for current revised simulations. The finite element meshes used for the current simulations are shown in Figure 3.34 for demonstration.

The simulation results are compared with the experimental results along with the progressive damage contour plots in Appendix F for all the three laminate configurations.

3.8 Conclusions

A three dimensional (3D) orthotropic smeared crack model is developed including all possible failure modes for fiber and matrix inside the fiber tow. The crack planes are differentiated in all three orthogonal directions depending on the mode of failure and the crack orientation transformation matrix is decided based on the material orientation rather than the state of stress. Linear traction laws are used for both tension

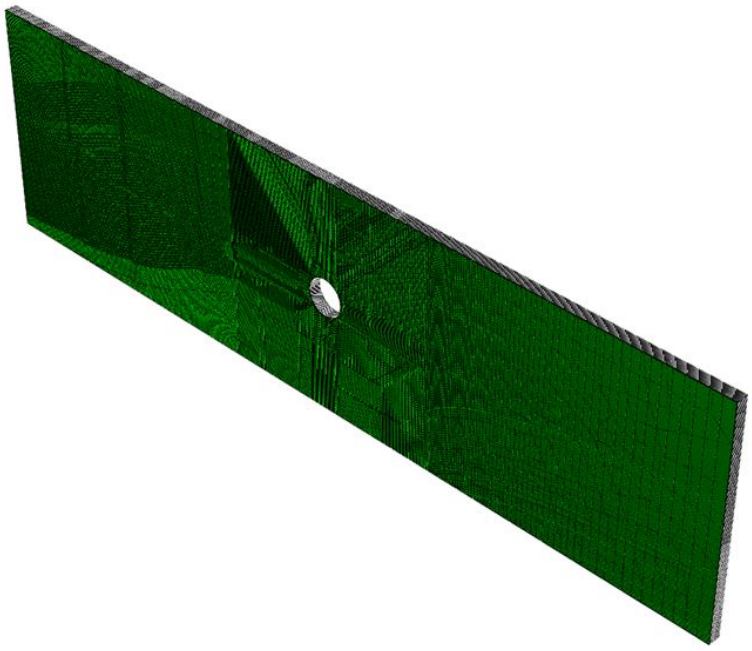

Figure 3.34: Finite element mesh used in OHT laminate simulation.

and compression failure modes of constituent materials (fiber and matrix) individually inside the tow and the mesh objectivity is maintained through a characteristic length parameter, as detailed in the formulation. Mixed mode failure initiation criteria are adopted from 3D Hashin criteria and the implementation of the smeared crack algorithms in ABAQUS VUMAT framework are explained in details, along with the flow charts. The matrix material outside the fiber tows is assumed to be isotropic and a 3D isotropic smeared crack model is developed for modeling matrix tensile and compressive failure. The tensile failure mode is based on pricipal stress based theory and the compressive failure is motivated by Mohr-Coulomb's theory. Detailed study on the implementation of Mohr-Coulomb's failure initiation criteria combined with Smeared crack approach are included in Chapter 6. An exponential traction law is used for both matrix tension and compression failure modeling and mesh objectivity is in-built by preserving the fracture energy through characteristic length, in a similar fashion for the linear traction laws for fiber tow failure modes. The differences between the two formulations are based on the fact that, the crack orientation transformation matrix is decided based on 3D state of stress in the case of isotropic smeared crack model rather than the material orientation, as in the case of orthotropic smeared crack model.

The smeared crack approach (SCA) is used to model the post-peak strain softening behavior of the material, whereas the pre-peak nonlinear behavior is modeled

using the NCYL micro-mechanics model, as described earlier in Chapter 2. The combined approach of NCYL and SCA completes the multi-scale framework to describe the stress-strain behavior of the material system under different loading scenarios. In this chapter, finite element implementation of the combined approach are demonstrated, using various case studies like single element test, tow split test, unidirectional ply split, angle plies matrix cracking and ultimately the whole open hole tension laminate modeling for three different lay-ups. All these exercises validate the successful implementation of NCYL and SCA in FE framework. The proposed computational multiscale analysis approach can be used as a predictive tool in the textile progressive failure analysis, which is demonstrated in the following chapters for tensile and compressive loading, along with the study on the effect of hybridization and architectural influence in the design of hybrid textile configurations.

CHAPTER 4

Material system: Hybrid 3D woven textile composites (H3DWTCs)

4.1 Introduction

Three-dimensional textile composites (3DTCs) are a relatively new class of 'out-of-autoclave' technology products that have the potential to replace conventional pre-impregnated (prepreg) tape laminates in terms of their excellent mechanical properties but at significantly reduced manufacturing cost and time. 3DTCs display high damage tolerance, high impact resistance and a distinct cost advantage and hence will likely see widespread use in the aerospace, automobile and defence industries due to their better structural properties tailoring capability. These composites can be created from a 3D weaving or braiding process by arranging the fiber tows into complex dry preform structures, following which a resin is applied to the 3D preform to create the composite material. A significant amount of work is done on the automated Robotic approach for processing of textile preforms [37]. Two distinct types of 3D woven textile composites (3DWTCs), a layer-to-layer angle interlock 3DWTC and a Z-fiber orthogonal interlock hybrid 3DWTC, are popular and both have a great advantage over laminated materials. Angle-interlock 3D woven structures are common in order to create much thicker woven preforms. In the interlock structures, yarns can be woven from one layer to another and then back to the original layer to lock adjacent layers to each other. In complex interlock structures, yarns may be woven at specified points into several layers in order to join multiple layers. In this research, Z-fiber orthogonal interlock hybrid 3DWTCs are studied in detail and analysed for progressive failure analysis.

Three dimensional, orthogonal woven composites are a class of 3DWTC composite structures containing a set of fiber tows spreading in all three mutually perpendicular directions (x, y and z-axes). These structures display high resistance to layer

delamination, as the latter is a common problem in conventional laminated composites. 3DWTCs are manufactured by laying up the warp and weft fiber layers and consequently running a Z-fiber in the thickness direction to bind the in-plane layers together. A matrix material is impregnated into these complex woven lay-ups and cured under specifed conditions to obtain a woven solid structure. The weaving process followed ensures high consistency of the preform architecture and minimal waviness of the in-plane fibers in both warp and weft directions. Several experimental studies [38, 39, 40, 41, 42, 43, 44] show that there is very low waviness of the warp and weft directional tows, which allows to achieve enhanced mechanical properties. This category of composites is characterized with practically straight and well aligned in-plane fibers. As a consequence, this type of textile composite show significant improvement in in-plane elastic moduli and strengths than composites reinforced with more conventional 3D angle interlock weaves usually produced by traditional 2D weaving machines.

The hybridization of the composite material can be tailored for the specific need of the structure by varying the fiber type and configuration of the weaving layers. The material system (fiber and matrix materials) used in manufacturing these hybrid complex architectures are detailed in Section 4.2. Although, there are many forms of 3D orthogonal woven composites with the variations of Z-fiber depth in thickness direction, we will focus here mainly on three different configurations, which are described in the Section 4.3. These hybrid architectures are manufactured by Textile Engineering and Manufacturing (T.E.A.M.), Inc., Woonsocket, RI, USA. Every manufacturing process comes with their unique signature of induced imperfections in the outcome structure and the identification of these imperfections are significant to improve the design and the manufacturing process, as described in Section 4.4. The purpose of this research is to establish a multiscale computational framework to predict the progressive damage and failure response of these complex 3D woven textile composites using constitutive properties measured from coupon level tests. The microstructure characterization studies and the micro-computed tomography (Micro-CT) analysis of geometric imperfections are provided in Section 4.5. Details of the 3D computer aided design (CAD) modeling strategy, including the construction of the finite element (FE) model directly from the Micro-CT real data are presented in Section 4.6, followed by conclusions in Section 4.7.

Table 4.1: The elastic properties for IM-7 carbon fiber, S-2 glass fiber, kevlar fiber and SC-15 matrix.

	E_1 (GPa)	E_2 (GPa)	ν_{12} -	ν_{23} -	G_{12} (GPa)	G_{23} (GPa)
IM7 carbon fiber	276.0	15.0	0.279	0.49	12.0	5.02
S-2 glass fiber	93.8	93.8	0.23	0.23	38.1	38.1
Kevlar fiber	112	112	0.36	0.36	41.2	41.2
SC-15 matrix	2.487	2.487	0.35	0.35	0.921	0.921

4.2 Material system

This research focuses on 'hybrid' Z-fiber orthogonal interlock textile architecture 3D woven composite (H3DWC), where 'hybrid' refers to different constituent fibers, including IM-7 carbon, S2 glass and Kevlar that are integrally woven into a single preform. The carbon fibers are used because of their high specific strength and stiffness, the glass for its relatively low cost (high strength per unit cost) and kevlar for its high resistance (characterized by its toughness) to failure. Material properties for each fiber type and the matrix are provided in Table 4.1.

4.3 Textile architecture

A series of warp and weft fibers run in-plane throughout the panel with little or no undulation. A set of Z-fibers run in the direction of warp fibers and are drawn from bottom to top to bind all the layers together. Z-fibers are usually inserted in-between the spaces of the warp fibers. In this research, three different hybrid architectures, as schematically shown in Figure 4.1 are investigated to understand the effect of hybridization on the resulting tensile and compressive response. The schematic figures of these configurations provide some details of the Z-fiber path. The first two architectures contain four layers of carbon (two layers in the warp and weft directions, respectively) at one side, and the remainder are the glass layers. These hybrid configurations are unsymmetric architecture that consist of orthogonally oriented in-plane carbon and the glass tows, for a total of 9 layers, named as Thin Asymmetric and of total 17 layers, named as Thick Asymmetric respectively. The difference in the overall thickness allows for studying the size-scaling effects by normalizing the result with respect to the panel thickness. These two architectures are considered to be unsymmetric in the sense that the types of the layered constituent fibers are unsymmetric with respect to the mid-plane of the composite panel. The third architecture contains

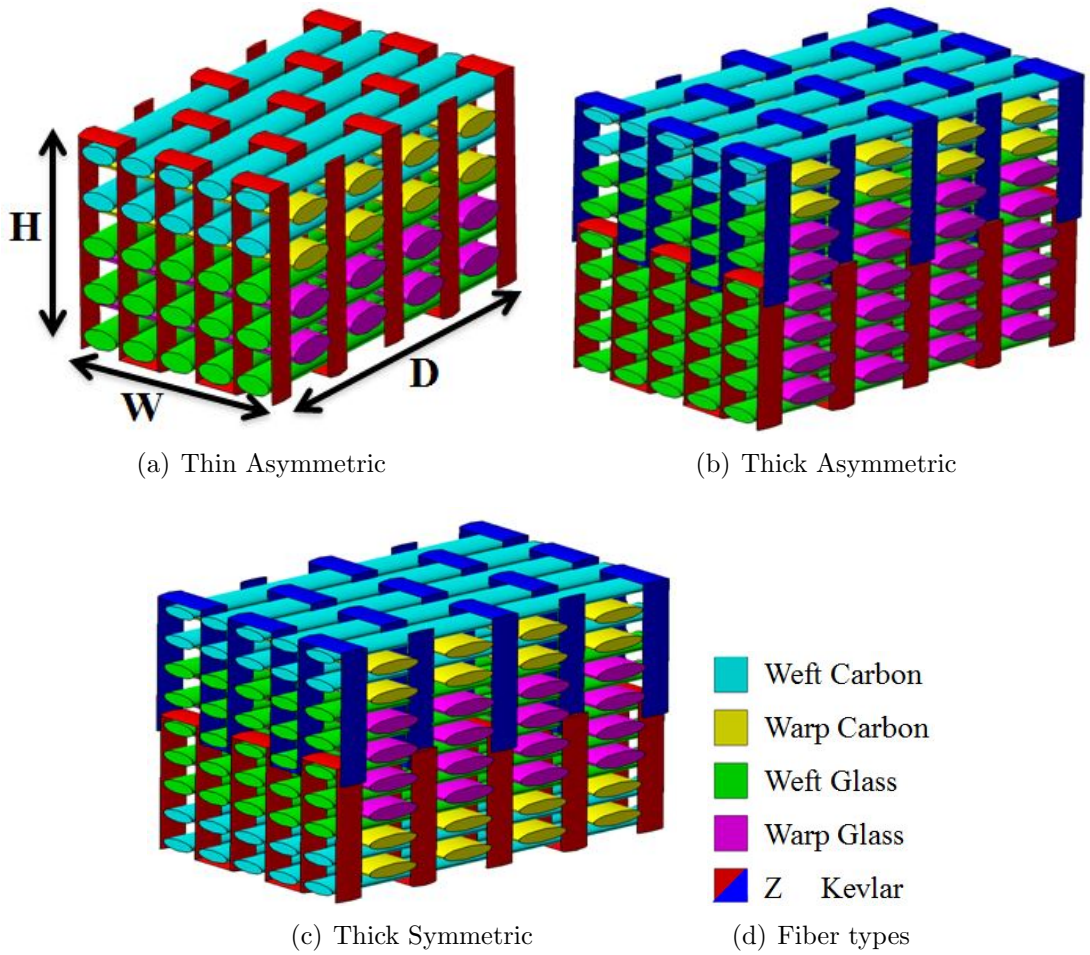

(a) Thin Asymmetric (b) Thick Asymmetric

(c) Thick Symmetric (d) Fiber types

Figure 4.1: Hybrid 3D woven textile configurations (Schematic).

the carbon layers for both outer surfaces (four layers of carbon on each side) and nine layers of glass in the middle. This hybrid configuration is a symmetric architecture that consists of orthogonally oriented in-plane carbon and glass tows of total 17 layers and named as Thick Symmetric. The Z-fibers run half the thickness in two layers in all Thick configurations to bind the layers together. This is a distinct feature of these thick architectures (compared to the through thickness binding in the 3D Thin Asymmetric configuration). These types of woven composites are categorized as 2.5D Thick Symmetric and Thick Asymmetric configurations for Z-fibers running half the thickness.

Among all the architectures, the planes that contain Z-fibers alternate along the weft direction with a period of two to achieve a repeating textile pattern. These configurations are infused with SC-15 polymer matrix material using a VARTM process. The three hybrid architectures are further examined under microscopy to identify

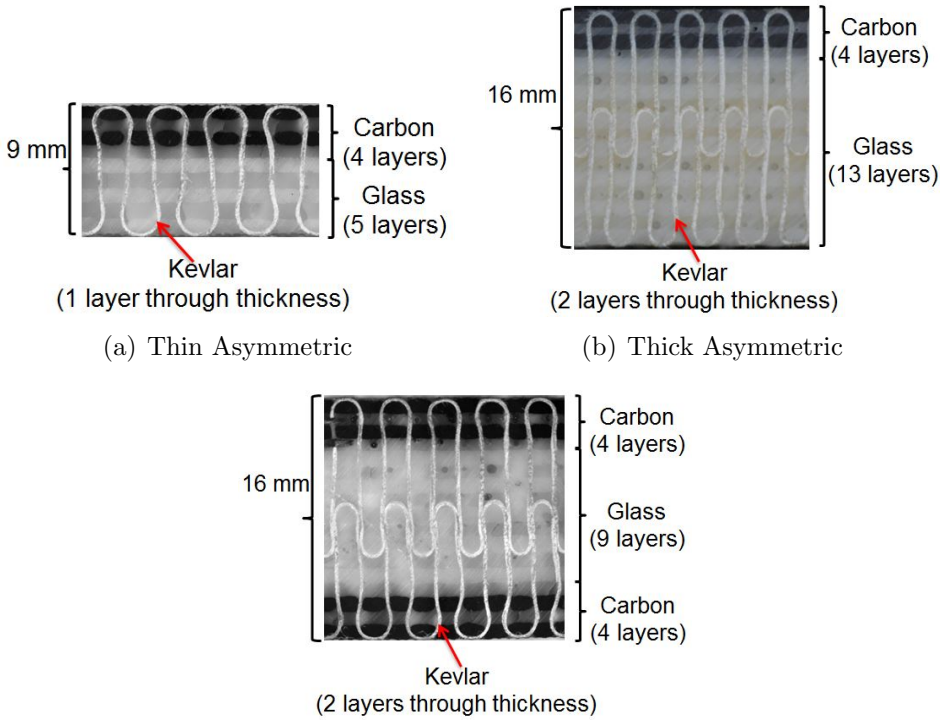

(a) Thin Asymmetric

(b) Thick Asymmetric

(c) Thick Symmetric

Figure 4.2: Cross sections parallel to the warp direction (Ref: Dr M. Pankow et al. [26], Dr D. Zhang [31]).

unit cells and characterize the in-situ imperfections.

The percentage of the carbon and glass content in each architecture is calculated by dividing the number of carbon and glass layers by the total layers of the composite. The images of the polished surface as shown in Figure 4.2 demonstrate high straightness of the in-plane tows and high uniformity of the geometry for all configurations. For weft tows, the waviness is highest in certain layers, as caused by the Z-fibers, where the kevlar fibers change directions from top to bottom or vice-versa and clearly visible in the figures. The fiber tow waviness and the crookedness are further examined with optical microscopy to characterize the textile architecture and geometric imperfections.

4.4 Fabrications and manufacturing induced imperfections

The hybrid orthogonal Z-fiber textile preforms are infused with SC-15 epoxy resin using a VARTM process to form a solid panel. VARTM is adapted from traditional

Resin Transfer Molding (RTM) by replacing the upper half mold with a vacuum bag to enhance the impregnation of the fiber reinforcements. Details of the VARTM technique and fabrication process are provided in [45, 34, 46, 47]. VARTM offers distinct advantages over RTM including lower tooling cost, shorter mould time, and ability to manufacture large structural components.

4.4.1 Geometry imperfections in the hybrid woven textile composites

The Z-fiber orthogonal interlock hybrid woven composites do experience geometric distortion of the textile architecture during the fabrication process due to their weaving practice along the thickness direction. In these architectures, the kevlar Z-fiber tows are used as weaves, that are woven through multiple layers, showing small undulations along the weaving path. Compared with the rigid warp and weft tows running straight, the Z-fiber shows much more compliance, and therefore it is easily affected by the fabrication process, for example, the tension exerted on the fiber tows during the weaving process and the mold pressure applied during the curing process. In the VARTM process with a single-sided mold, atmospheric pressure is exerted on the textile preform through the vacuum bag covering, forcing the fiber tows to be settled in a new position that is different from the predesigned one. This manufacturing induced geometric imperfection of the textile architecture in the as-fabricated composite panel is evident from the Micro-CT analysis of the sample, as described in detail in section 4.5.

It has been pointed out by Song et al.[48] that each manufacturing process is associated with a unique set of characteristics that result in a produced part deviating from the expected ideal geometry. The set of such deviations, which is unique to each manufacturing process, is termed the 'manufacturing imperfection signature'. Obtaining the manufacturing imperfection signature of the textile composite is important to determine the damage characteristics, such as strength, strain to failure and fatigue life, which has been studied by many researchers [49, 50, 51, 52, 53, 54, 55, 56, 30]. The importance of incorporating the unintended geometric deviations of the woven fabric into a textile architecture based finite element model has been recently addressed by Zhang et al. [57]. A voxel based numerical model is studied by [58] to predict the deformed shape of 3D woven fabric during weaving and to investigate the effect of geometrical imperfections.

4.5 Micro-computed tomography (Micro-CT) analysis of textile configurations

In order to obtain a thorough understanding of the microstructure of the cured composite, cross sectional microscopic images are used to characterize the textile geometry. The 2D images at various cross sections along the length of the specimen are rendered and reconstructed into 3D volume for the purpose of characterization, and the measured dimensions are used as inputs to textile architecture based finite element models presented in Section 4.6.

4.5.1 Micro-CT scanning parameters settings

The high energy Micro-CT scanner Skyscan 1173 system, with 40-130kV X-ray source and pixel size of 6-140μm was chosen, as it has a large sample chamber for scanning objects of 140 mm in diameter and 140 mm in height. Specimens were cut along the warp and weft directions into 25 x 50 mm blocks and polished using a multi-speed rotating grinder/polisher. For this sample, we could potentially run between 70 and 80kV with 17μm resolution. A schematic diagram of different steps carried out during the scanning process and reconstructing the 3D images is shown in Figure 4.3. The Micro-CT image data are analysed in detail, as described in the following sections.

4.5.2 Determining meso-scale RVE

A representative volume element (RVE) scanned image data were cropped down from the larger specimen volume data of 25 x 50 mm sample size, as shown schematically in Figure 4.4. Cross sections along the mid-plane of fiber tows were chosen selectively to capture the periodicity of the RVE in both in-plane directions. The RVEs in the black box are indicated in both warp and weft directions for all Thick Asymmetric, Thick Symmetric and Thin Asymmetric configurations, as shown in Figure 4.5. The geometric dimensions of RVEs and layers breakdown for these architectures are summarized in Table 4.2.

4.5.3 Determining fiber tow cross-sectional details

Fiber tow cross section dimensions are measured from the RVE image data using a measuring tool in both warp and weft directions, as indicated in Figure 4.6. Both the warp and weft tows are assumed to be straight with rectangular cross sections and

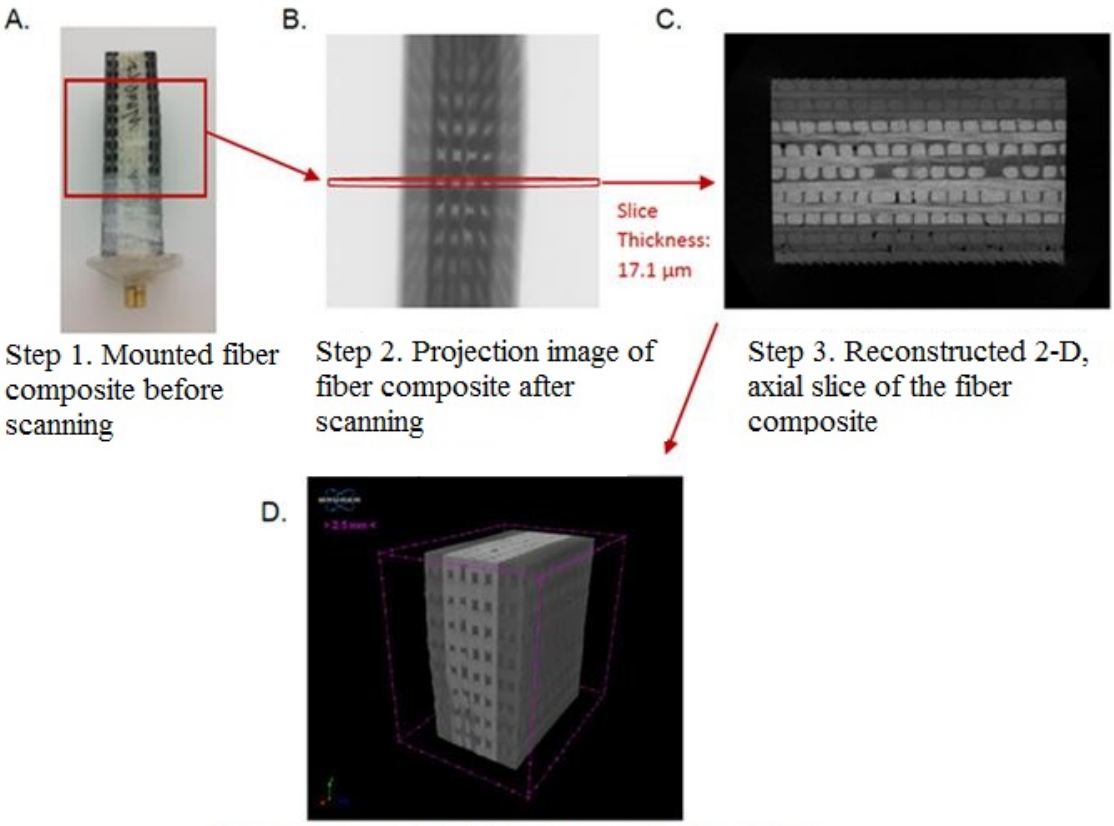

Figure 4.3: Steps in Micro-CT scanning process.

Table 4.2: RVE dimensions and layer breakdown

$Configuration$	$Dimension(mm)$ $(WxHxD)$	$Total$ $Layers$	$Carbon$ $Layers$	$Carbon$ $(\%)$	$Glass$ $Layers$	$Glass$ $(\%)$
Thin Asymmetric	9.6x8.75x17.2	9	4	44.4	5	55.6
Thick Asymmetric	6.8x16.8x16	17	4	23.5	13	76.5
Thick Symmetric	6.8x15.96x16	17	8	47.1	9	52.9

Table 4.3: Fiber tow cross-section dimensions

$FiberType$	$a(mm)$	$b(mm)$
Weft Carbon	2.2	0.85
Warp Carbon	2.6	0.75
Weft Glass	2.1	1.00
Warp Glass	2.5	0.85
Kevlar	1.4	0.25

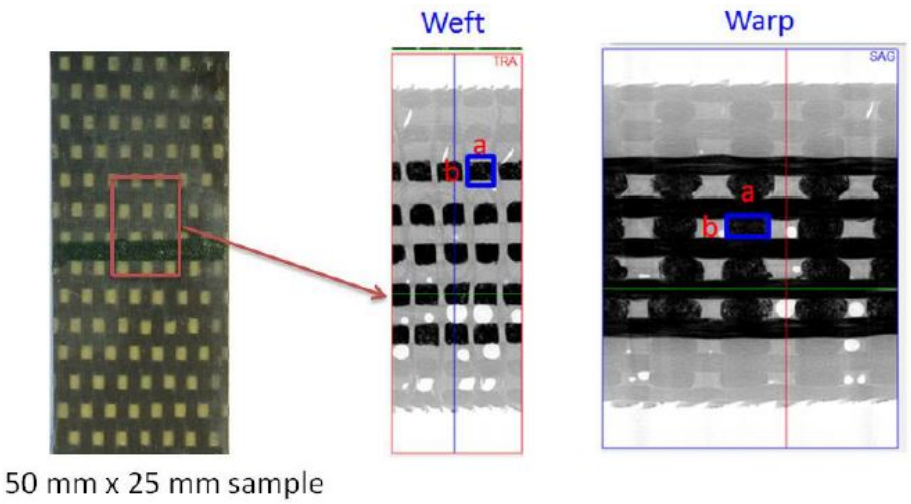

Figure 4.4: Identification of meso-scale RVE.

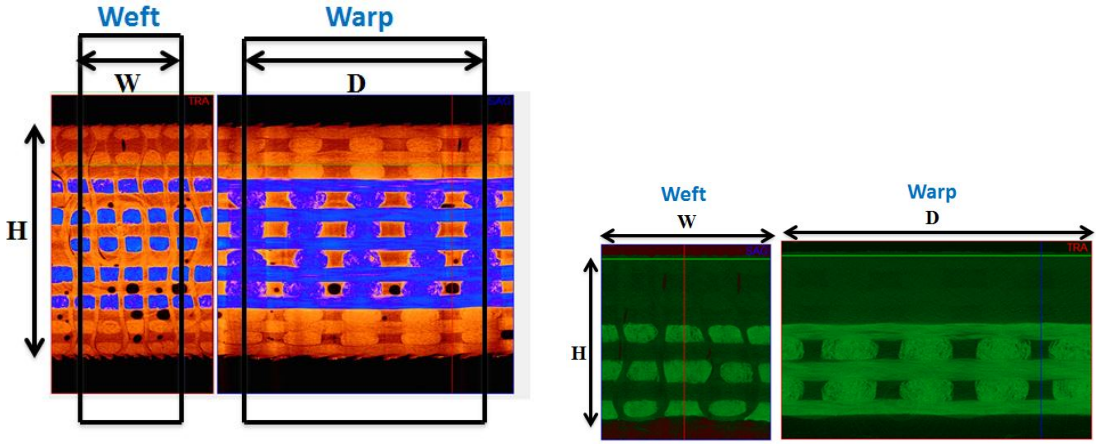

(a) Thick Asymmetric/Symmetric

(b) Thin Asymmetric

Figure 4.5: Micro-CT analysis to determine RVE.

the measured fiber tow dimensions are summarized in Table 4.3. Scanning electron microscopy (SEM) images are taken on the cross section of each type of constituent fiber tow to investigate how the fibers are distributed inside the tow and to determine the average fiber volume fraction. The fiber volume fraction of each constituent tow is summarized in Table 4.4.

It is assumed that the fiber volume fraction in both weft and warp tows are same for each constituent tow. In the present study, the volume fraction of Kevlar tow is 76%, however, the modeling framework can be used to study the effects of Kevalr volume fraction on the composite performance (stiffness degradation and failure).

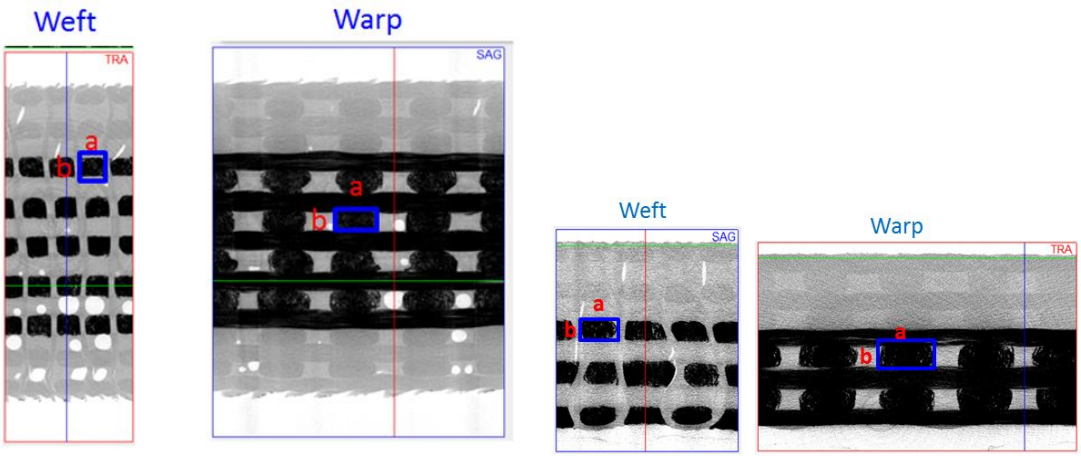

(a) Thick Asymmetric/Symmetric (b) Thin Asymmetric

Figure 4.6: Measurement of fiber tow details.

Table 4.4: Volume fraction data for different fiber types

$FiberType$	$VolumeFraction$
Carbon	$60.9 \pm 3.6\%$ (60%)
Glass	$55.4 \pm 4.5\%$ (56%)
Kevlar	76%

4.5.4 Porosity analysis

A study is carried out by calculating the volume percentage of the pores in the RVE by adjusting the grey scale difference in the scanned 3D image data. The volume fraction of pores in the RVE is calculated as 0.91851%, which is negligible. Hence, the RVE is assumed to be filled with materials without any pores and the effect of the pores is not included in the damage modelling and failure analysis of the textile composites.

4.5.5 Summary of microstructure output details from Micro-CT analysis

Here, all the outputs from Micro-CT analysis are summarized as follows: (i) measurement of RVE dimensions (ii) measurement of fiber tow cross-section details in both the weft and warp directions and (iii) porosity analysis. An idealized 3D computer-aided design (CAD) RVE of the Thin Asymmetric, Thick Asymmetric and Thick Symmetric woven textile composites are modeled in the commercial finite element (FE) software ABAQUS 6.14, as shown in Figure 4.7, taking into account all the above input values from Micro-CT study without any geometrical imperfections. We

will refer to these perfect models as 'Model-I' in the remainder of this thesis.

4.6 Modeling in-situ geometry imperfections

Finite element (FE) modeling of 3D woven textile composites is still a challenging task for the research community because of the complexity of the textile architecture of fiber tows and very thin layers of matrix between winding fiber bundles. The manufacturing induced geometrical imperfections have a strong impact on the performance and mechanical behavior of the structure in the physical loading scenario and hence, must be included in FE modeling to accurately capture its effect on the prediction of progressive damage and failure of the composite. In this work, an innovative approach of numerical modeling of imperfections is demonstarted where a mesh is generated directly from Micro-CT data using a commercially available software package, 'Simpleware'. The point to be noted here is that, the generated mesh is the real replication of the in-situ microstructure imperfections.

'Simpleware' deals with real scanned image data from Micro-CT analysis. It can generate finite element (FE) meshes from the scanned image data, which help in measuring and modeling the real imperfections in the structure. Each fiber tow is segmented separately and assigned material properties with a well-defined fiber orientation in both warp and weft directions. The thin layers of matrix between the undulated fiber tows are meshed explicitly and assigned the material properties of SC-15 epoxy. A schematic modeling of imperfections at meso-scale RVE for Thick Symmetric configuration is shown below in Figure 4.8. In this novel and unique approach, modeling and meshing the in-situ geometrical imperfections are possible in a detailed and efficient manner. These real measured imperfections can be taken as a reference to introduce imperfections to an idealized perfect geometry. The identified RVEs of all three configurations are segmented and modeled explicitly using the features of 'Simpleware', as shown in Figure 4.9. We will refer to these imperfect models as 'Model-II' in the remainder of this thesis. It should be noted here that, the generated mesh is a replication of the in-situ geometric imperfections in the 3DWTC architectures, induced due to the manufacturing process.

4.7 Conclusions

A representative volume element (RVE) not only defines the repetitive nature of the geometry of the structure, but also represents the continuum in a small scale to carry

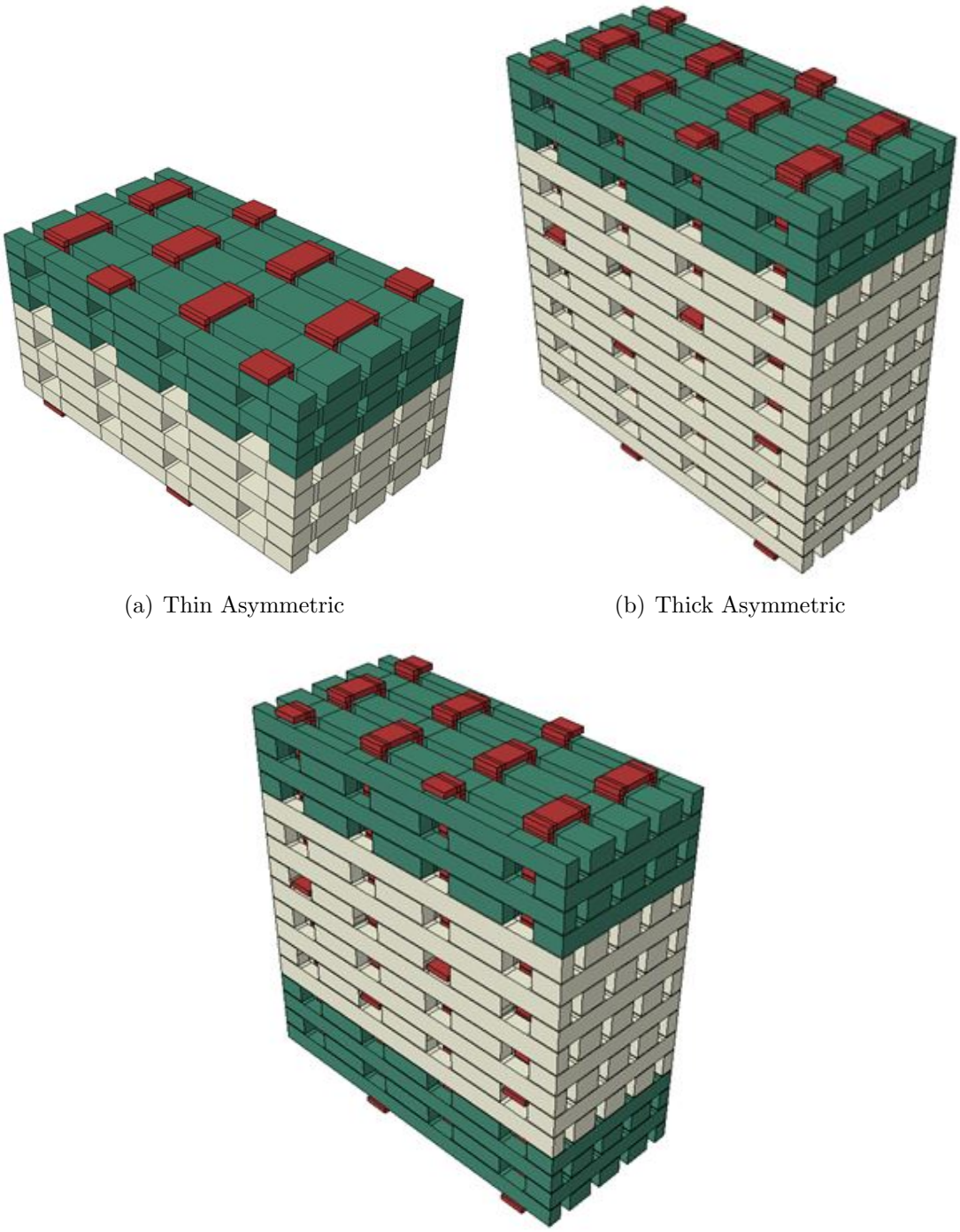

(a) Thin Asymmetric

(b) Thick Asymmetric

(c) Thick Symmetric

Figure 4.7: 3D geometric model of perfect RVEs (Model-I).

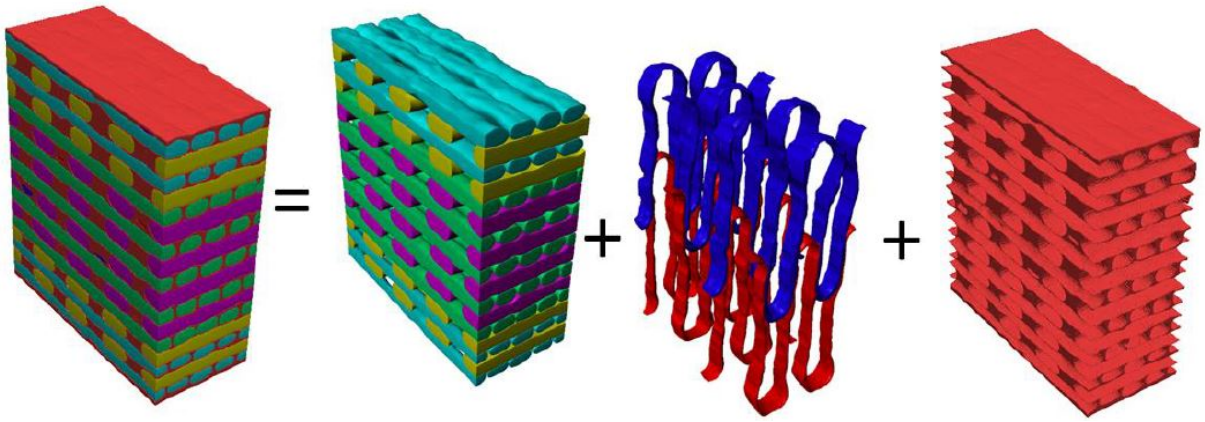

Figure 4.8: Segmentation of fiber tows using 'Simpleware'.

out all the progressive damage and failure study of the material system. On the other hand, a repeat unit cell (RUC) represents the smallest unit of the structure in terms of geometry only, which is repetitive. The selection of RVE should be sufficient enough to predict the global stiffness and also capture the failure mechanisms observed in the structural scale. Progressive failure analysis based on RVE is computationally effcient to model all geometry details inside RVE explicitly. In this study, RVEs of all three textile architectures are identified based on detailed Micro-CT study and subsequently used for progressive analysis in Chapters 5 and 6 for tensile and compressive loading respectively. Various inputs required to model the geometry of the textile architectures are extracted from the scanned image data of bigger sample in a statistical way. These 3D geometry models are essential to carry out the progressive failure analysis using the multiscale framework described earlier in the previous chapters and hence, the accuracy of the model is crucial to capture the physics of different failure mechanisms at different length scales. The fiber tows are homogenized in this work and each fiber tow is segmented separately using the tool 'Simpleware'. In that way, the fiber crookedness and the geometric imperfections are modeled in a detailed matter and subsequently included in the numerical simulations. This aproach is novel in the way that, the in-situ imprefection sensitivity of the structure with respect to different failure mechanisms and the global response can be studied in a more detailed manner. The same approach is being used in the modeling of laboratory scaled coupon analysis for tensile and compressive loadings in the following chapters. It is important to study the size effect on the global response of the structure, when we move from RVE to coupon level analysis, but at the same time the effect of manufacturing imprefections at different length scales of the structure cannot be ignored

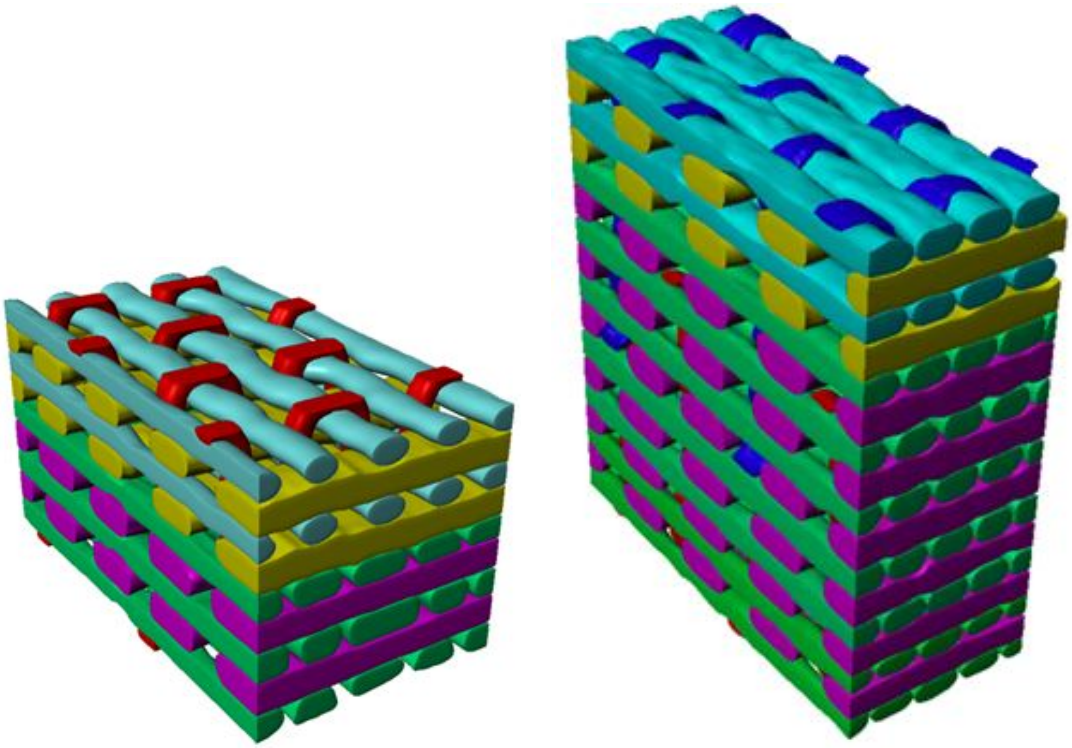

(a) Thin Asymmetric

(b) Thick Asymmetric

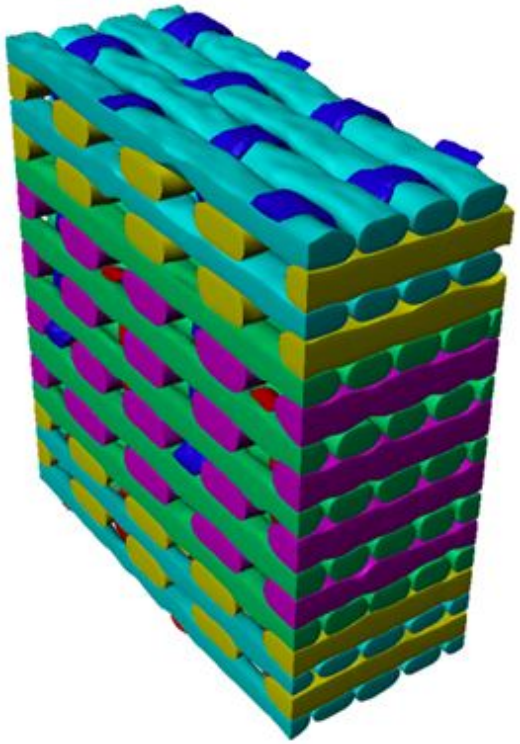

(c) Thick Symmetric

Figure 4.9: 3D geometric model of imperfect RVEs (Model-II).

and must be included in the geometry models of both RVE and coupon. The detailed measurement of tow imperfections and characterization are provided in Appendix G.

CHAPTER 5

Damage and failure modeling of H3DWTCs : a study of hybridization and architectural effects on tensile response

5.1 Introduction

This chapter presents results of numerical simulations on predicting the progressive damage and failure response of hybrid 3D woven textile composites (H3DWTCs) subjected to tensile loading, using the novel two-scale computational mechanics framework explained in previous chapters. Here the term 'hybrid' refers to different constituent fibers, including carbon, glass and kevlar that are infused with SC-15 polymer matrix and integrally woven into a single preform. The hybrid 3DWTCs are made through a 3D textile weaving process. Three different versions of hybridized architectures are examined at the representative volume element (RVE) level to determine the progression of damage and failure under tensile loading. Progressive damage and failure of 3DWTCs at different length scales are captured in the present model by using a macroscale finite element analysis (FEA) at the RVE level, while a closed-form micromechanics analysis is implemented simultaneously at the subscale level using material properties of the constituents (fiber and matrix) as input. Manufacturing induced geometric imperfections are considered in the simulation, where the FE mesh is generated directly from Micro-computed tomography (MCT) real data using a code, 'Simpleware'. These FE models are the real replication of in-situ geometric imperfections in the structure and subsequently included for progressive damage and failure analysis. Micro-CT analysis of all three architectures are conducted in details. The fiber tows and the thin layers of matrix in-between the tows are modeled explicitely inside the RVE for each configuration.

The N-layer concentric cylinder (NCYL) micromechanics model is then introduced

inside the fiber tow to compute local stress, srain and displacement fields in the fiber and matrix used at the subscale. The 2-CYL fiber-matrix concentric cylinder model is extended to fiber and (N-1) matrix layers, keeping the volume fraction constant, hence called NCYL model and the matrix damage can be captured locally in the discrete layers of matrix volume, as explained in details in Chapter 2. The influence of matrix microdamage at the subscale causes progressive degradation of fiber tow stiffness and matrix stiffness at the macroscale. The global stiffness matrix remains positive definite, until strain softening response resulting from different failure modes (such as fiber tow breakage, tow splitting in the transverse direction due to matrix cracking inside tow and surrounding matrix failure outside of fiber tows) are initiated. The failure initiation criteria are introduced at the tow level to facilitate analysis of the post-peak softening failure response and are modeled using the mesh-objective 3D orthotropic smeared crack approach (SCA) in a two-scale framework. The matrix pocket surrounding the fiber tows inside the RVE is subjected to tensile failure and the post-peak softening failure response is modeled using the mesh-objective 3D isotropic smeared crack approach (SCA). The implementation of both 3D orthotropic and 3D isotropic smeared crack approach (SCA) are explained in details in Chapter 3. Results from multiscale analysis for both an idealized perfect geometry and one that includes geometric imperfections are compared with experimental results [26]. The three different types of hybrid 3DWTCs are compared against one another at RVE scale to understand the benefits of hybridization and the resulting performance enhancements. The effect of microstructure geometric imperfections on the prediction of progressive damage and failure response of these complex architecture mterials are studied.

A three-scale modeling strategy is adopted to simulate the entire laboratory tested coupon and investigate the progressive damage and failure behavior at the structural level. The meso-scale RVEs are modeled explicitly in the failure prone gauge-area to consider the tow architecture scale and the homogenized orthotropic elastic properties are considered in the non-failure area of the coupon for computational efficiency. The proposed three-scale strategy predicts the global stress-strain response and the detailed local complex failure mechanisms of the 3D woven composites. The coupon level simulation results are compared with RVE scale results and the experimental results [26] to further validate the proposed model. This novel modeling approach includes the in-situ geometric imperfections for progressive damage and failure analysis, at both RVE and coupon level.

5.2 Matrix nonlinear constitutive model

Polymer matrix materials exhibit a nonlinear stress versus strain response prior to failure and when within a composite. Such nonlinear behavior is attributed to matrix microdamage due to microcracking [59, 60, 61, 17]. The nonlinear matrix response is modeled using a modified J_2 deformation theory of plasticity, as formulated in Chapter 2. The evolution of nonlinearitry accounts for progressive deterioration of the material stiffness, however, the tangent stiffness tensor still remains positive-definite. The coalescence of matrix micro damage finally results in matrix macroscopic cracking, followed by a post-peak strain softening regime. In this instance, the positive definiteness of the matrix stiffness tensor is lost, which is categorized as a failure. The post-peak strain softening behavior is modeled through the smeared crack approach (SCA) to capture matrix macroscopic cracking, as described in Chapter 3.

5.2.1 Modeling microdamage in a polymer matrix

As discussed in [17], the matrix in-situ response can be characterized through a tensile test on a $\pm 45^{\circ}$ symmetric laminate. Furthermore, it is assumed that the matrix nonlinear response can be characterized using an exponential relation,

$$\sigma_{eq} = \sigma_y - \frac{K_1}{K_2}\left(\mathrm{e}^{-K_2\epsilon_{eq}} - \mathrm{e}^{-K_2\frac{\sigma_y}{E}}\right) \tag{5.1}$$

where σ_y is the yield stress of the matrix in a uniaxial tension test, E is the elastic modulus, K_1 and K_2 are two material constants that govern the evolution of matrix microdamage. Different nonlinear responses have been reported for the matrix within a carbon tow than that in a glass tow [32]. Table 5.1 summarizes the matrix nonlinear properties used in the two-scale micromechanics model for computing the response of each constituent tow. In addition, the pre-peak nonlinear properties of the surrounding matrix in the macro model is assumed to be the same as the one used for the glass tow.

Table 5.1: Matrix nonlinear properties used in this research.

	σ_y (MPa)	K_1 (MPa)	K_2
Matrix (macroscale)	25	1700	40
In-situ carbon	25	3500	60
In-situ glass	25	1700	40

5.2.2 Modeling failure progression in a polymer matrix using the 3D isotropic SCA

In the experiment, matrix cracking is observed in regions of predominant tensile stress, as presented in [26]. In a monolithic material, cracks are likely to grow under pure mode-I conditions since this mode of failure is energetically favorable. The detailed formulation of matrix tensile failure using 3D isotropic smeared crack approach is explained in Section 3.6.2. In H3DWTCs, the cracks in the surrounding matrix may be subjected to mixed-mode loading due to the presence of fiber tows. However, in this study, it is assumed that the tensile cracks grow under pure mode-I conditions, oriented with the maximum principal stress plane. It is further assumed that, once the crack is initiated, the crack orientation, determined from the principal stress directions, is fixed during the failure evolution.

The off-diagonal terms in the crack interface stiffness matrix $\boldsymbol{D}^{cr}$ are assumed to be zero, indicating that there is no coupling between the normal and shear crack components. The coupling between the crack shear and opening displacements, known as crack dilatancy, has been extensively studied by Bažant and Gambarova [62], Walraven [63], Walraven and Reinhardt [64], and Gambarova and Karakoç [65].

5.3 Fiber tow constitutive model

The experimental results of the $\pm 45^{\circ}$ symmetric laminate tensile tests indicate that the matrix exhibits a nonlinear stress versus strain response due to the evolution of microdamage. In the proposed computational scheme, each fiber tow is homogenized as a 3D solid, therefore, micromechanical analysis must be implemented at the subscale to capture such nonlinear behavior. Since the fiber tow pre-peak nonlinear response is attributed to matrix microdamage, no macroscopic damage criterion is required to drive the nonlinear damage progression. However, multiple catastrophic failure modes are observed in the experiment, including tensile failure due to fiber breakage and fiber tow splitting. These modes of failure result in a loss of load-carrying capability of composite structure, followed by a post-peak strain softening response. Since the positive definiteness of the material tangent stiffness matrix is lost in softening regime, the FEA will provide mesh dependent results if no characteristic length is introduced. As a result, the aforementioned two-scale NCYL model has to be supplemented by a suitable mesh objective approach for modeling the post-peak softening response.

In the present study, fiber tow breaking and splitting are considered as the two major failure modes for H3DWTCs subjected to tensile loading, which is evident from the experimental investigation discussed in [26]. In addition, when the tow breakage is initiated in axial tows due to tensile stress, the crack plane is assumed to be aligned perpendicular to the fiber direction. On the other hand, the crack plane is assumed to be parallel to the fiber direction when the tow splitting criterion is reached due to transverse tensile loading. Details of the implementation of the 3D orthotropic SCA within a FE framework are demonstrated in Chapter 3.

5.3.1 Tow pre-peak nonlinear response: NCYL model

Recently, Zhang and Waas [1] developed a two-scale, micromechanics-based model for computing the nonlinear response of a unidirectional composite. In their model, a fiber-matrix concentric cylinder is used as the repeat unit cell (RUC), to represent a composite fiber tow. The two layers fiber-matrix analytical model has been extended to N-layer fiber-matrix cylinders to analyze the stress and strain fields for all constituent matrix layers. A representative N-layer concentric cylinder unit with fiber radius 'a' and matrix outer radius 'b' is shown in Figure 5.1 and the resulting fiber volume fraction is $V_f = a^2/b^2$.

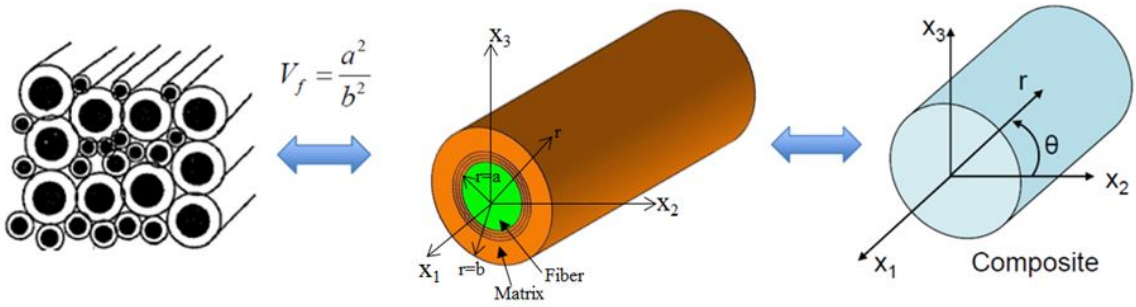

Figure 5.1: N-Layers Concentric Cylinder Model (NCYL).

Micromechanics is used to relate the globally applied composite strains to the fiber and matrix strains at the microscale through a six by six transformation matrix. A detailed description of the NCYL micromechanics model and its implementation in a multiscale analysis for progressive damage of textile composites is provided in Chapter 2.

5.3.2 Tow failure mechanisms: post-peak strain softening response

The smeared crack approach (SCA) formulated in Section 3.3 for 3D orthotropic material is utilized to model the failure progression of a single fiber tow, which include tensile breakage in axial direction and tow splitting in the transverse direction. It is further assumed that when the critical stress is reached, the crack plane is aligned perpendicular to the fiber direction for tow breaking and the crack orientation transformation matrix, $\boldsymbol{N}$, is determined as given in Section 3.3. Tow splitting occurs due to matrix cracking inside the fiber tow subjected to transverse and shear loading. In this work, it is assumed that when the transverse critical stress is reached, the crack plane is aligned parallel to the fiber direction for tow splitting. Therefore, the crack orientation transformation matrix, $\boldsymbol{N}$, is determined as given in Section 3.3. When two-piece failure occurs in tensile loading, the recorded load drops significantly during the experiment, indicating a considerable amount of fracture energy dissipation.

In the present study, it is assumed that when the tensile failure mode occurs, the fracture energy is dissipated completely. The failure properties, including the critical stress and fracture toughness for each mode of failure, are summarized in Table 5.2 for fiber tows and in Table 5.3 for SC-15 matrix respectively. The tensile strength values for carbon and glass tows are taken from [66] and [67], respectively. It is worth mentioning that characterizing the failure progression of fiber tows within H3DWTCs is critical to understand the progressive failure response of this class of materials.

Table 5.2: Fiber tow failure properties used in the SCA model.

Failure mode	Carbon	Glass	Kevlar
0° tension (MPa)	3000	3700	3600
0° compression (MPa)	977	720	720
90° tension (MPa)	55	65	65
90° compression (MPa)	247.3	247.3	247.3
Shear (MPa)	37	35	35
G^{+}_{ICF} (N/mm)	40	60	40
G^{-}_{ICF} (N/mm)	4	4	4
G^{+}_{ICM} (N/mm)	0.296	0.296	0.296
G^{+}_{IICM} (N/mm)	0.647	0.647	0.647

Table 5.3: SC-15 matrix failure properties used in the SCA model.

Failure mode	σ_{cr} (MPa)	G^{+}_{ICM} (N/mm)	G^{+}_{IICM} (N/mm)
Matrix tension	30	0.296	0.647

5.4 Results and discussion for individual textile configuration

Stress-starin responses, linear elastic moduli, Poisson's ratios, peak strength and failure strains have been experimentally determined in [26]. The tensile test simulations are carried out for Model-I (idealized perfect model with no imperfections) and Model-II (imperfect model with in-situ geometric imperfections generated by 'Simpleware') simultaneously in both weft and warp directions for all the three configurations described earlier in Chapter 4. The RVE scale simulation results are compared with the experimental results as summarized in the following sections.

5.4.1 Results for Thick Symmetric(2.5D) configuration

Three dimensional (3D) geometry models of meso-scale RVE (Model-I and Model-II) are shown below in Figure 5.2 for Thick Symmetric hybrid configuration and the finite elements are generated using ABAQUS 6.14. The Model-I had nearly 50,000 elements and took 20 hours to run on a high performance computing system using 32 CPUs, whereas, Model-II had nearly 590,000 elements and took 2 days to run on the same computing system using 32 CPUs.

5.4.1.1 Elastic and strength properties

Considerable gradual linear growth of the elastic moduli under loading in the weft and warp directions are observed for strains from 0.1% to 0.5% (Figure 5.3). The linear growth is followed by a slow gradual reduction of the moduli with further increase of strains. The 'non-linear' behaviour is attributed to a combination of matrix microdamage and fiber splitting. The latter appears to be a minor cause contributing less to the modulus versus strain variations. The stress-strain response, as shown in Figure 5.3(a), exhibits a higher degree of linearity in the weft direction due to the fact that loading occurs directly on the fiber tows situated in the outer most surface. The warp direction shows more of a progression in failure of the material as shown in Figure 5.3(b) and deviations from linearity occur relatively early in the loading regime. However, due to the fact that different fiber tows will have different stresses at the same externally applied displacement indicates that the carbon may fail earlier than the glass and the failure envelope is progressive due to the hybrid materials before two-piece failure. Numerical predictions using the two-scale multiscale method showed excellent agreement with experimental data for in-plane elastic moduli in both

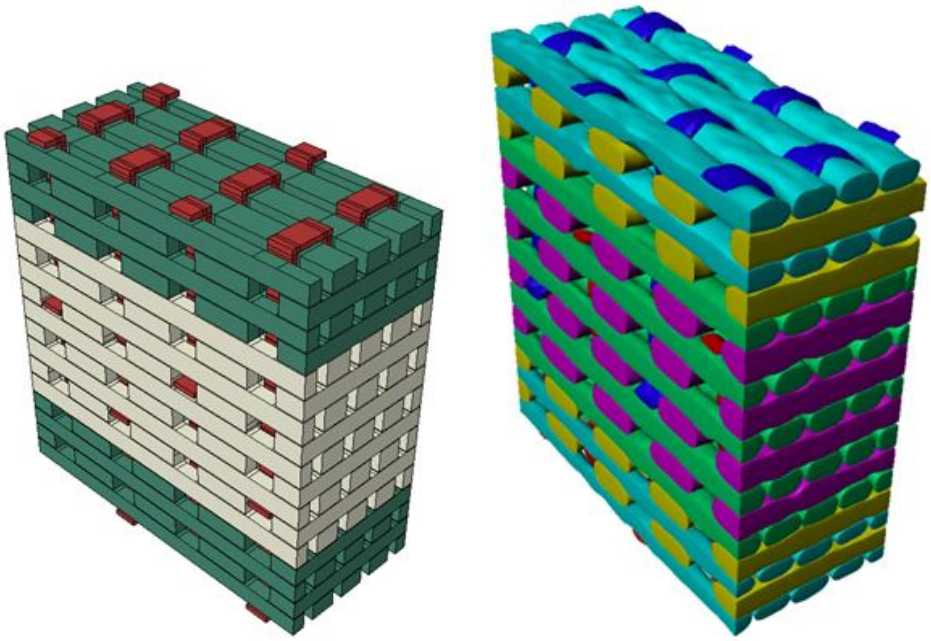

(a) Perfect RVE (b) Imperfect RVE

Figure 5.2: Meso-scale RVE of Thick Symmetric configuration (a) Model-I & (b) Model-II.

weft and warp directions for the idealized perfect geometry without any imperfections (Model-I). After including the in-situ geometrical imperfections and the fiber crookedness in the FE model (Model-II), the predicted elastic moduli reduced the respective Model-I values (e.g. warp-directional modulus 34.12 GPa and weft-directional modulus 39.95 GPa) by only 2.2% in warp and 2.3% in weft-directions. As we can see, there is a reduction in stiffness after including the geometric imperfections. For this hybrid configuration, the weft direction is stiffer than the warp direction due to the fact that there is one additional glass fiber tow layer in the weft direction as summarized in Table 5.4.

The weft-direction tensile strength was found to be 467.61 MPa and warp-direction strength 446.81 MPa as reported in Table 5.5 for Model-I; the former is 4.7% larger due to a 5.8% higher fiber weight fraction in the weft direction. In Model-II, because of the imperfections of fiber alignment in both in-plane and thickness directions, there is significant fiber tow splitting observed in transverse and Z-fiber tows. The predicted tensile strength reduced the respective Model-I values (e.g. warp-directional strength 403 MPa and weft-directional strength 449.7 MPa) by only 9.8% in warp and 3.8% in weft-directions. As observed, there is a degradation of tensile strength after including the geometric imperfections and predictions are closer to the experimental

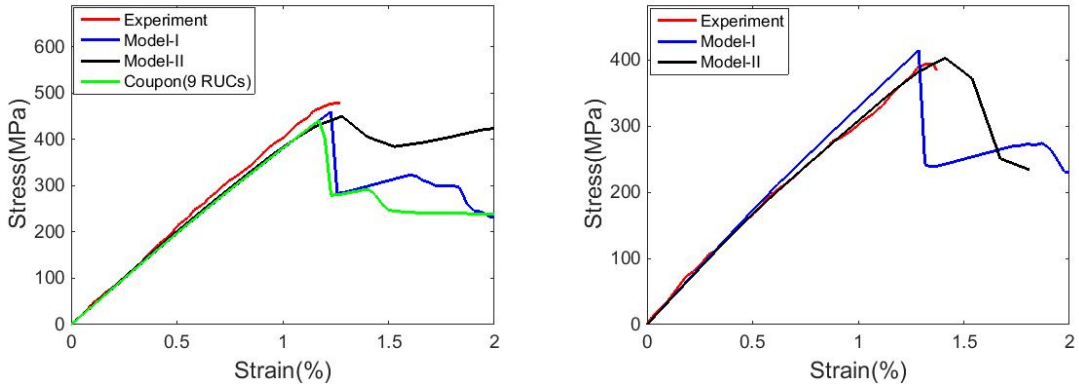

(a) Weft direction (b) Warp direction

Figure 5.3: Effective stress versus strain response for tensile loading in (a) Weft direction & (b) Warp direction.

Table 5.4: Stiffness comparison between Experiment and Simulation results

$EffectiveModulus$	$Experiment$ (GPa)	$Simulation(Model-I)$ (GPa)	$Simulation(Model-II)$ (GPa)
Warp	$37.023 \pm 11.34\%$	34.87	34.12
Weft	$41.775 \pm 3.58\%$	40.85	39.95

values. The global response tends to be highly nonlinear and matches well with experimental results for Model-II as shown in Figure 5.3(b), which demonstrates the effect of including manufacturing induced imperfections in the progressive damage and failure analysis of these textile composites.

5.4.1.2 Progressive damage during quasi-static tensile loading

The multiscale methodology described in Sections 5.2 and 5.3, which combine modeling pre-peak nonlinearity using the NCYL secant stiffness method and the post-peak strain softening response using Smeared crack approach (SCA), are used together to conduct a thorough investigation of the damage and failure mechanisms in the hybrid textile composite under consideration. The progressive damage and failure response

Table 5.5: Strength comparison between Experiment and Simulation results

$Ultimatestrength$	$Experiment$ (MPa)	$Simulation(Model-I)$ (MPa)	$Simulation(Model-II)$ (MPa)
Warp	393.32	446.81	403
Weft	469.33	467.61	449.7

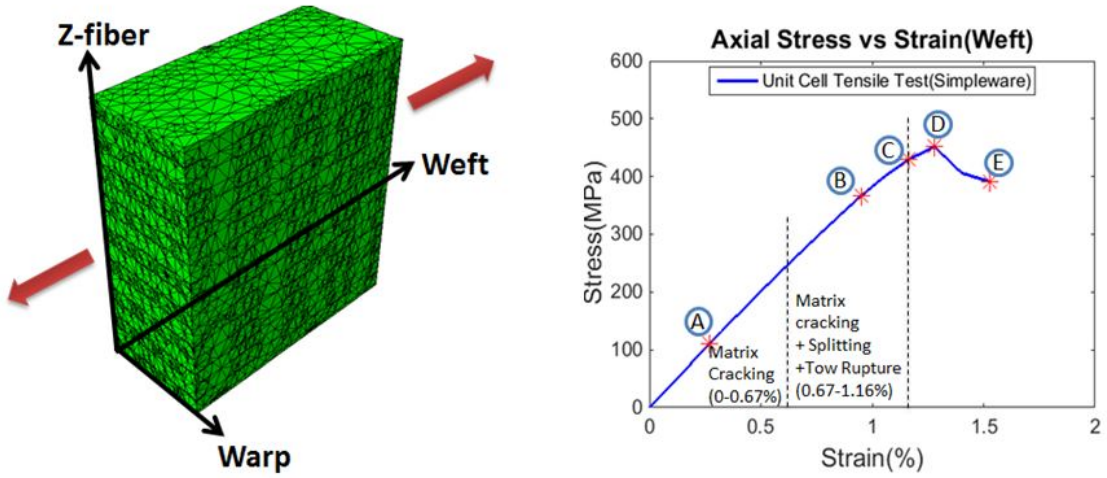

Figure 5.4: Stress-strain response for tensile loading in the weft direction.

of textile RVE in both weft and warp directions subjected to uniaxial quasi-static tensile tests are shown in Figure 5.4 to Figure 5.7 for imperfect RVEs with geometrical imperfections (Model-II). In these figures, the progressive failure status at different percentages of the failure strength are shown as contour plots of progressive failure flags of the elements.

Firstly, a delayed damage initiation has been observed in weft direction loading. First matrix cracking in warp direction loading is observed at 0.45% strain, which is much ealier than weft loading (observed at 0.67% strain). The damage initiation for the loading in weft or warp directions occurs in the range of applied strain 0.4-0.7% (Figures 5.4-5.7, showing the data for weft and warp directions loading). This range of damage initiation strains is significantly higher than the respective ranges observed for other carbon/epoxy textile composites, and is at the lower end of the typical damage initiation strain range (0.6-0.7%) for conventional cross-ply prepreg tape laminated composites.

The damage in these composites starts near the location of Z-fiber tows and at the edges of the in-plane fiber tows oriented transversely to the loading direction. Due to this reason, there is significant amount of local disbonds and matrix cracking occuring in the case of warp direction loading, as shown in Figure 5.7. This failure event leads to development of transverse cracks inside the in-plane and vertical tows (referred to as 'tow splitting') during the progressive loading process; these are followed by fiber tow breakage in the axial direction at a very late stage of loading and finally causes the 'two-piece' failure. A comparison study is being conducted from the simulation results for progressive damage and failure, for both weft and warp direction loading.

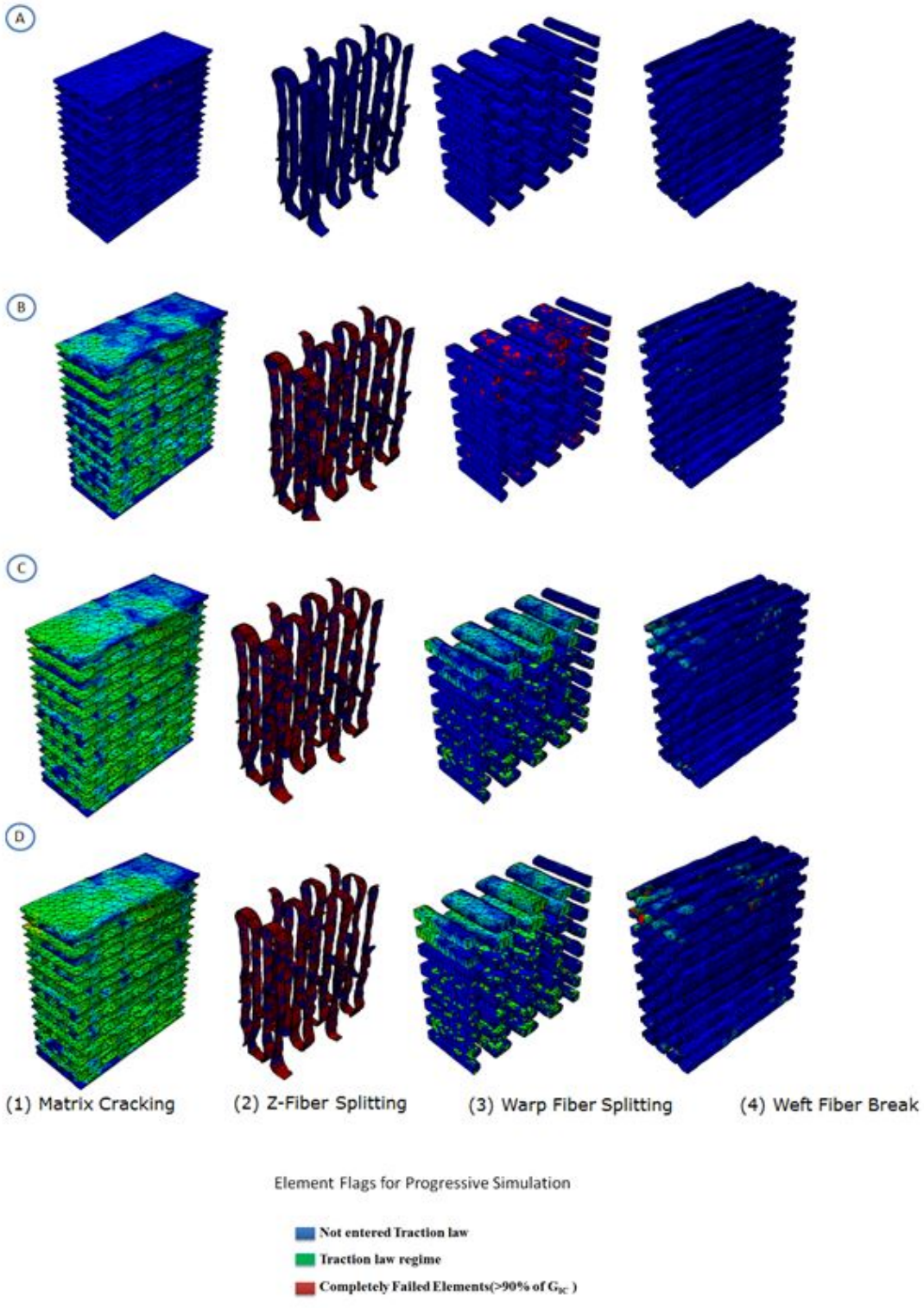

Figure 5.5: Progressive failure for tensile loading in weft direction.

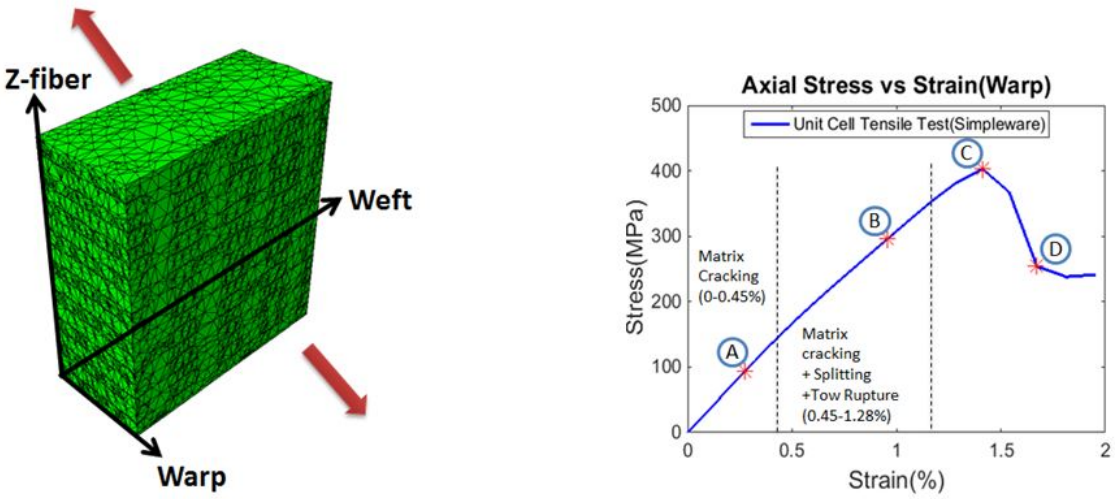

Figure 5.6: Stress-strain response for tensile loading in the warp direction.

The study is based on the figures shown above (Figures 5.4-5.7) and summarized in Figure 5.8.

Damage initiation and evolution in both weft and warp directions are investigated numerically using the NCYL multiscale framework and the matrix microdamage model based on J2-deformation theory of plasticity. Previous experimental studies [68, 69, 70] discuss the damage progression in 3D woven composites in a detailed manner, which correlates well with the sequence of damage events captured with our propsed model. Transverse cracks kinetics inside homogenized fiber tow is explained in the literature [71] by bridging micro-meso scale. We have implemented the physics of this failure mode in our Smeared carck code and captured the transverse cracks. A micro-mechanics based damage approach is applied to the macro scale unit cell model by Saleh et al. [70], which approximates the 3D woven composites as a cross-ply laminate without considering the effects of the binder yarns in thickness direction and also neglects the void contents and the geometrical imperfections induced due to manufacturing process. Our modeling and analysis of unit cell includes in-situ geometric imperfections and the predicted simulation results match closely with the sequence of damage events described by them. The scope of this work is to establish a computationally efficient progressive damage and failure analysis tool and the goal is achieved by using the NCYL micromechanics multiscale model, which is based purely on analytical solutions. The recommended matrix damage model improvements will be the focus of a future work for off-axis tension and shear loading simulations.

Overall, the FE model results, that include imperfections (Model-II) show a good

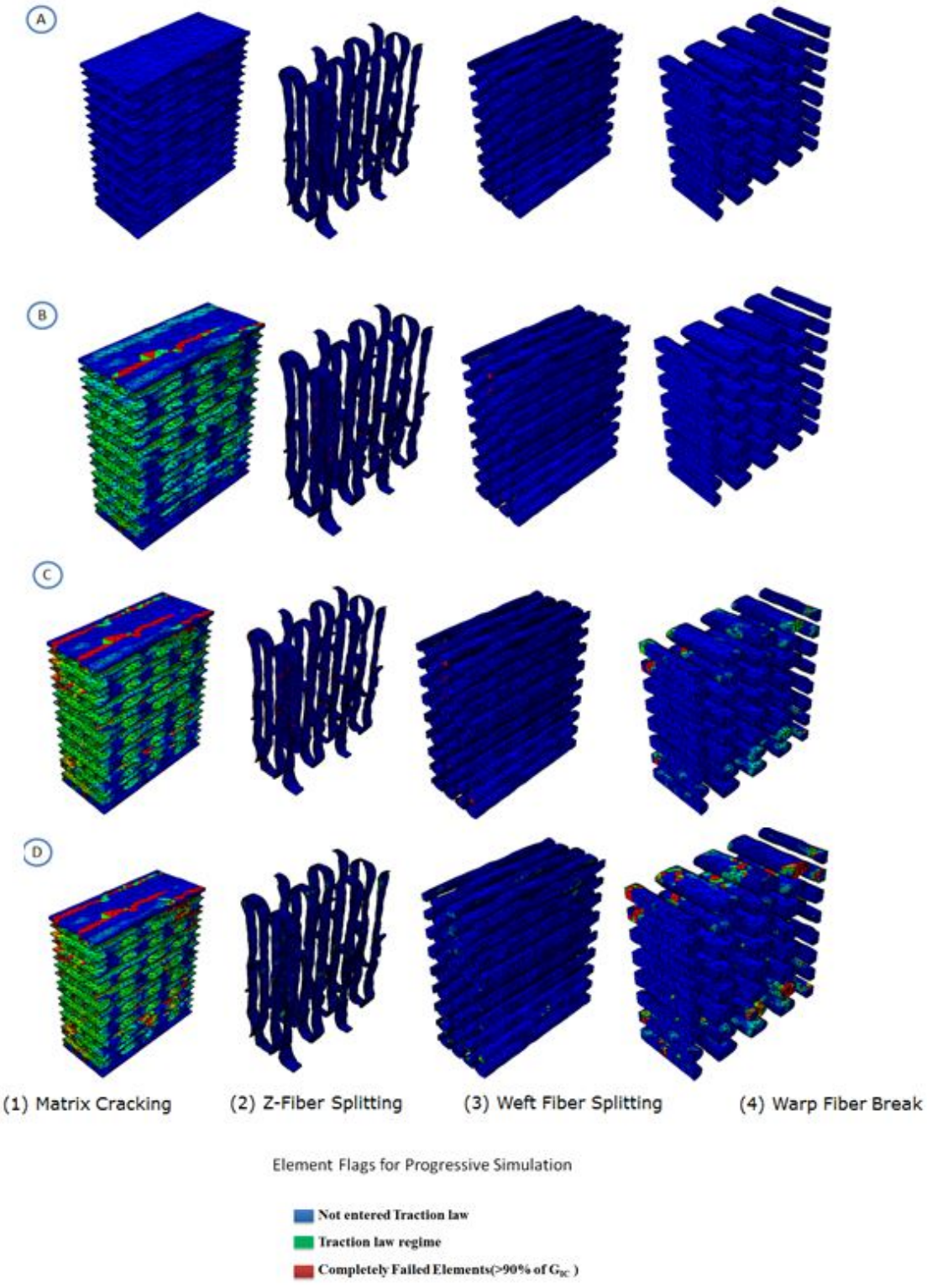

Figure 5.7: Progressive failure for tensile loading in warp direction.

weft direction	warp direction
(1) elastic stiffness = 39.95 GPa	(1) elastic stiffness = 34.12 GPa
(2) failure strain = 1.28%	(2) failure strain = 1.41%
(3) failure strength = 449.7 MPa	(3) failure strength = 403 MPa
(4) first matrix cracking observed at 0.67% strain	(4) first matrix cracking observed at 0.45% strain, much earlier than the weft direction
(5) matrix cracking, tow split and tow breakage occur mostly in the range of 0.67–1.16%	(5) matrix cracking, tow split and tow breakage occur mostly in the range of 0.45–1.28%
(6) stress–strain response is more stiff and mostly linear	(6) stress–strain response is less stiff and highly nonlinear
(7) significant splitting observed in the Z-fibre and warp direction tows	(7) less splitting observed in the Z-fibre and weft direction tows

Figure 5.8: Comparison between weft and warp directions results.

prediction for the elastic stiffness in each case. Also, the model is able to capture the non-linear stress-strain response to a close extent. It is noted that this model includes real in-situ microstructure imperfections inside the RVE and the multiscale analysis is carried out to capture the progressive failure. The difference in global stress-strain responses, between the idealized perfect RVE (indicated as a blue line) and the one with real in-situ microstructure imperfections (indicated as a black line) are visible in Figure 5.3.

5.4.1.3 Uniaxial coupon level tensile test for multiple RVEs

Test specimens of suitable dimensions are to be decided based on the number of RVEs, which should be sufficient to run the simulations and capture the main features of the progressive damage and failure characteristics. Nine RVEs (3x3) are assembled and studied for uniaxial coupon level test simulations using the multiscale analysis. A breakdown of 3x3 RVEs for Thick Symmetric (2.5D) woven textile composite is shown in Figure 5.9 for illustration.

The coupon level global stress-strain response is shown in Figure 5.3(a) for weft direction, which matches fairly well with the single RVE results. Also, the progressive damage and failure response of the coupon in the weft direction subjected to uniaxial tensile loading is shown in Figure 5.10. In these figures, the progressive failure status at the failure strength are shown as the contour plots of progressive failure flags of the elements.

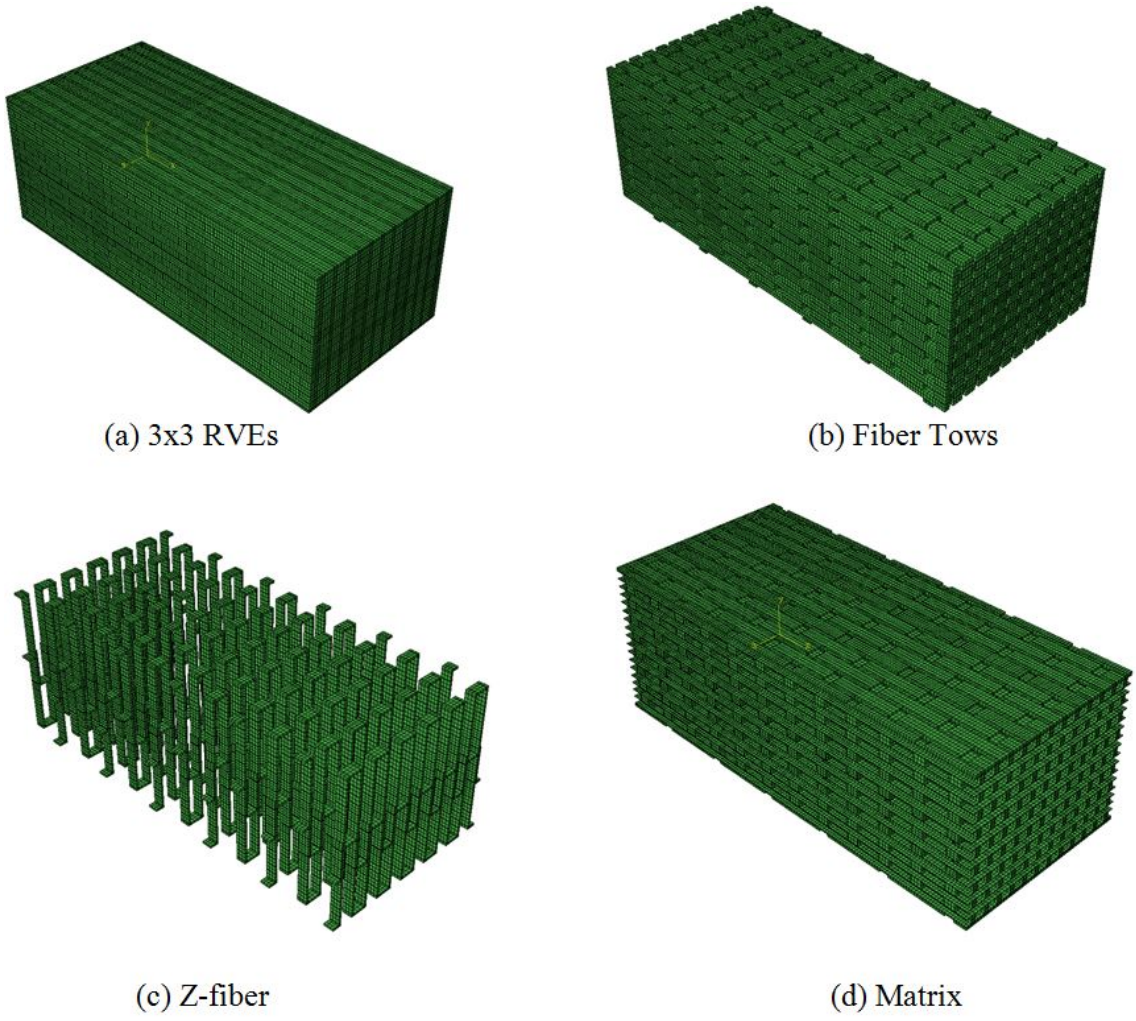

Figure 5.9: Breakdown of components for 3x3 RVEs.

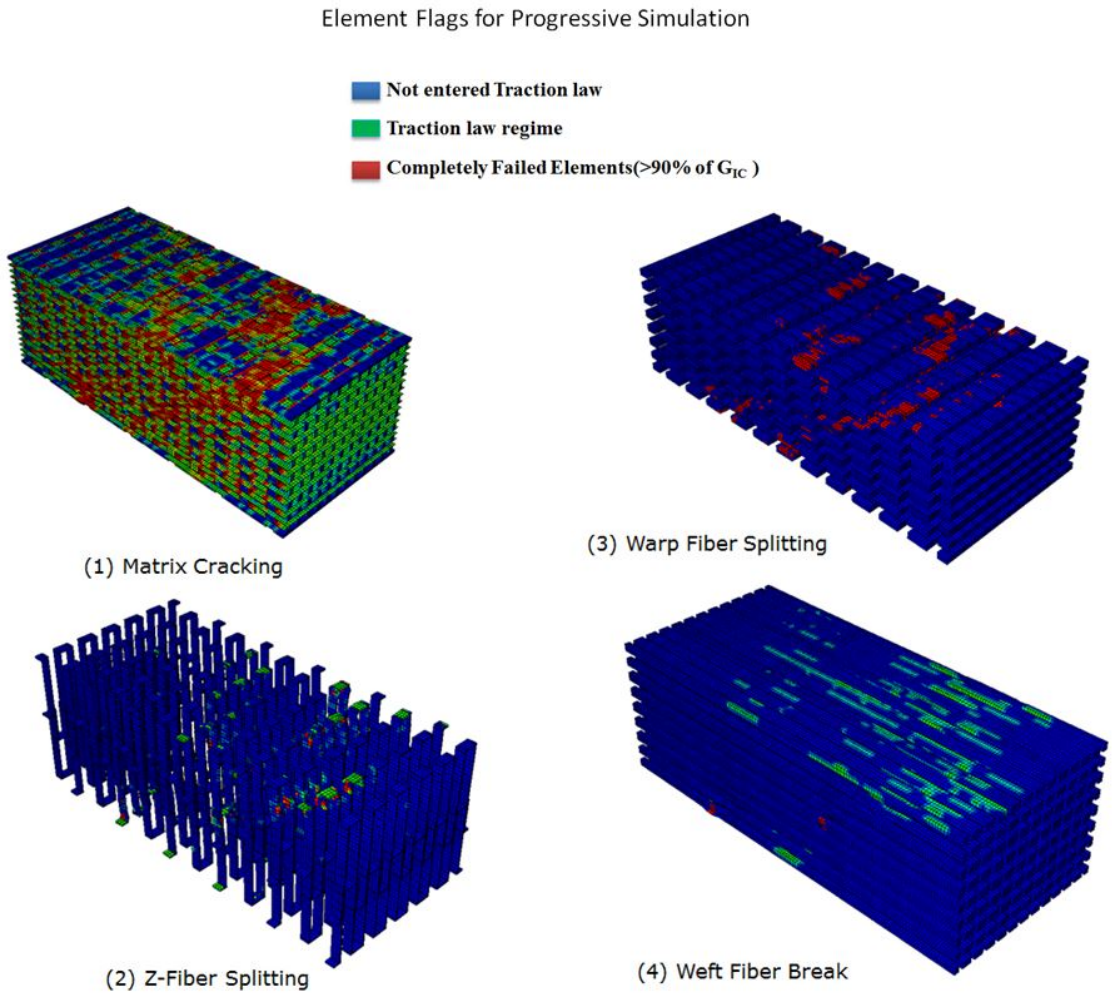

Figure 5.10: Progressive failure status for 3x3 RVEs at failure strength.

5.4.1.4 Summary and conclusions

In this study, Hybrid 2.5D Thick Symmetric woven textile composites having symmetric fiber architecture at the top and bottom, with two layers of Z-fibers running through thickness direction is simulated for uniaxial tensile response to determine the effect of hybridization and compute the effective stiffness and tensile strength for both warp and weft directions, including progressive damage and failure. A Micro-CT analysis is carried out to determine and measure real in-situ microstructural imperfections. This Micro-CT analysis helps to extract essential inputs (cross-sectional details of fiber tows in both warp and weft directions and volume fraction of pores) for constructing representative unit cells. Based on these inputs, an idealized 3D CAD model of a unit cell is constructed and multiscale analysis is carried out for progressive failure analysis. A subscale micromechanics 2CYL model is used to establish a multiscale computational framework to predict the effective nonlinear response of a homogenized fiber tow. The influence of matrix microdamage at the microscale manifests as the degradation of the effective fiber tow stiffness at the macroscale through a secant moduli approach. Since, fully analytical solutions are utilized for the subscale micromechanics analysis, the proposed method offers a lower computational cost and is suitable for large scale progressive damage and failure analysis of composite structures. The multiscale homogenization of the fiber tows are used as building blocks for an explicit FE model of 3D woven textile composite RVE. The linear elastic stiffness of this textile architecture matches well to the experimental results in both warp and weft directions. Also, the predicted failure strength and the global nonlinear stress-strain responses are in good agreement with the experiments.

It is a challenging task to accurately model geometric imperfections, such as crookedness and misalignment of fiber tows to study the effect of microstructure imperfections on the global response of a textile composite structure. An effective software tool, *'Simpleware'* is used to generate a FE mesh from real MCT in-situ data, which is able to capture the microstructure details and provide a platform to carry out multiscale analysis on a real RVE model. The progressive failure response from both models, namely, (1) Idealized RVE with no imperfections (Model-I) and (2) *'Simpleware'* generated model with in-situ imperfections (Model-II), are compared to demonstrate the effect of including geometric imperfections on the overall behaviour of the composite. The coupon level simulation is carried out to understand the size effect by a combination of multiple RVEs. Overall, the main objective of this research is achieved by establishing a multiscale method, which is capable of predicting the effective linear elastic stiffness, global nonlinear stress-strain response and two-piece

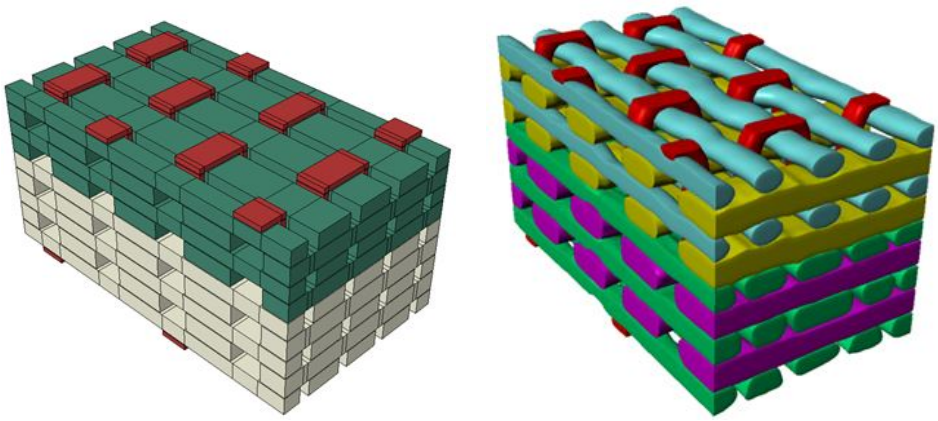

(a) Perfect RVE (b) Imperfect RVE

Figure 5.11: Meso-scale RVE of Thin Asymmetric configuration (a) Model-I & (b) Model-II.

failure strength of Hybrid 2.5D Thick Symmetric textile composites. The progressive analysis methodology can be extended to other configurations of woven and braided textile composites including the effect of hybridization and architectural variations. In this study, the multiscale analysis combines the 2CYL micromechanics model for pre-peak nonlinear response and the smeared crack approach (SCA) to model the post-peak failure analysis. This combined computational approach is used in model I and model II. The approach in model II, which uses a mesh generated directly using MCT data is novel, and provides a means to capture unintended microstructural imperfections due to manufacturing process related effects.

5.4.2 Results for Thin Asymmetric(3D) configuration

Three dimensional (3D) geometry models of meso-scale RVE (Model-I and Model-II) are shown in Figure 5.11 for Thin Asymmetric hybrid configuration and the finite element models are generated using ABAQUS 6.14.

5.4.2.1 Elastic and strength properties

The global responses of both perfect and imperfect RVEs for Thin Asymmetric configuration are shown in Figure 5.12. The differences in stress-strain response are observed for both weft and warp directions, which show the effect of including manufacturing induced imperfections in the progressive damage and failure analysis of these textile composites.

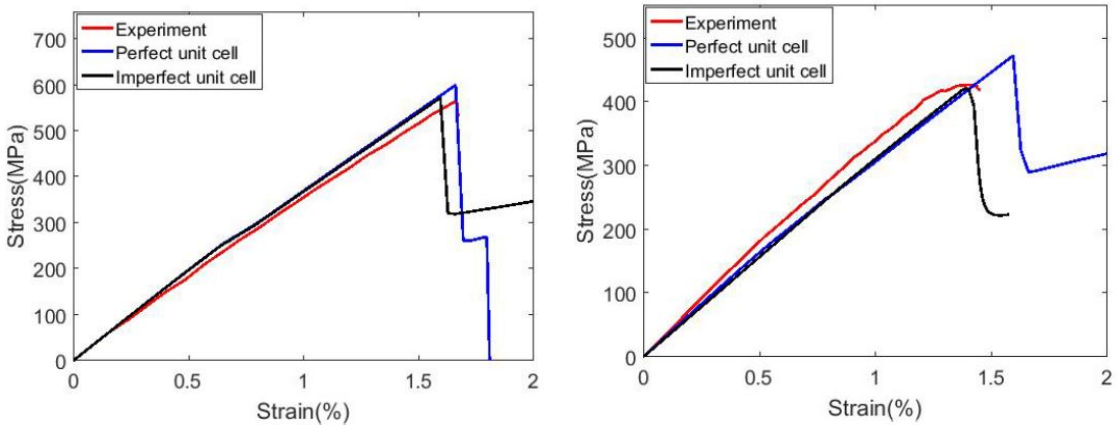

(a) Weft direction (b) Warp direction

Figure 5.12: Effective stress versus strain response for tensile loading in (a) Weft direction & (b) Warp direction.

5.4.2.2 Progressive damage during quasi-static tensile loading

The multiscale methodology described earlier combines pre-peak nonlinearity using the NCYL secant stiffness method and the post-peak strain softening response using the smeared crack approach (SCA). The combined models are used together to conduct a thorough investigation of the damage and failure mechanisms in the 3D hybrid textile configuration discussed above. The progressive damage and failure response of Thin Asymmetric configuration, in both weft and warp directions subjected to uniaxial quasi-static tensile tests are shown in Figure 5.13 to Figure 5.16 for perfect RVEs without geometrical imperfections. In these figures, the progressive failure status at different percentages of the failure strength are shown as contour plots of progressive failure flags of the elements.

The damage in these composites starts near the location of Z-fiber tows and at the edges of the in-plane fiber tows oriented transversely to the loading direction. Due to this reason, there is significant amount of local matrix cracking occurring in the case of warp direction loading compared to weft direction, as shown in Figures 5.13-5.16. This failure event leads to development of transverse cracks within the in-plane and vertical tows (referred to as 'tow splitting') during the progressive loading process; these are followed by fiber tow breakage in the axial direction at a very late stage of loading and finally causes the 'two-piece' failure.

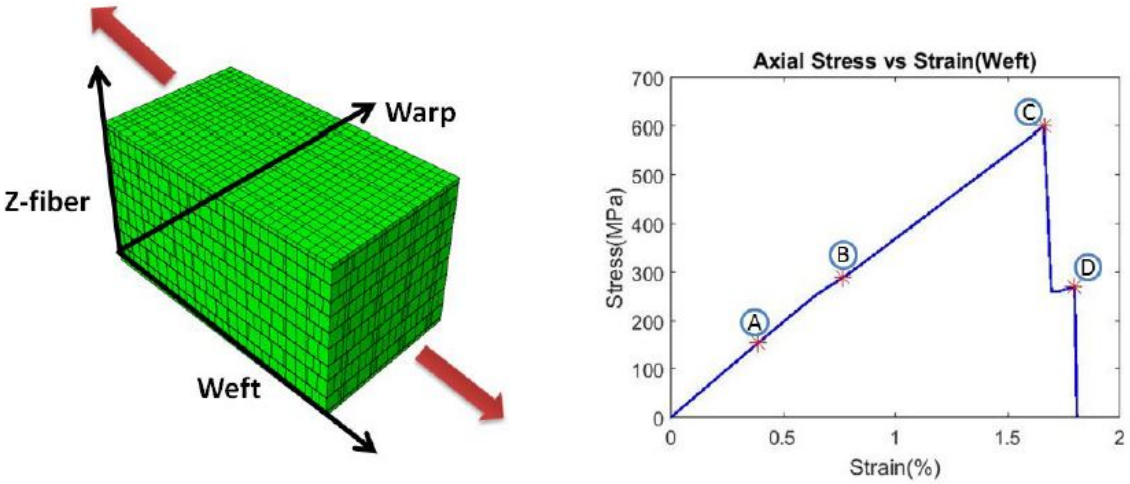

Figure 5.13: Stress-strain response for tensile loading in the weft direction.

5.5 Effect of hybridization and conclusions

To obtain a full characterization of the composites nonlinear response and to extract the effective linear stiffness properties along with strength, two loading scenarios are considered, including tension in weft and warp directions for all the three hybrid configurations.

5.5.1 Stiffness and strength comparison

Effective stress-strain relations, based on applied load and cross sectional area of RVEs and global strains are determined from the simulations of all three configurations. The effective elastic moduli, strength and failure strains are extracted from these results for both perfect and imperfect RVEs. The elastic axial response show linearity in both weft and warp loading directions, followed by a slow gradual reduction of the tangent moduli and 'non-linear' behavior. The stress-strain response in the weft direction exhibits a higher degree of linearity, whereas the warp direction shows more of a progression and early deviation from linearity due to large amount of matrix cracking, occurring in the thin matrix layers between the fiber tows. This phenomenon is attributed to the architectural influence and the orientation of Z-fibers with respect to weft and warp loading directions. The effective moduli for all three architectures are summarized in Table 5.6. Numerical predictions using the two-scale multiscale method showed excellent agreement with experimental data for in-plane elastic moduli in both weft and warp directions for the idealized perfect geometry without any imperfections. After including the in-situ geometrical imperfections and

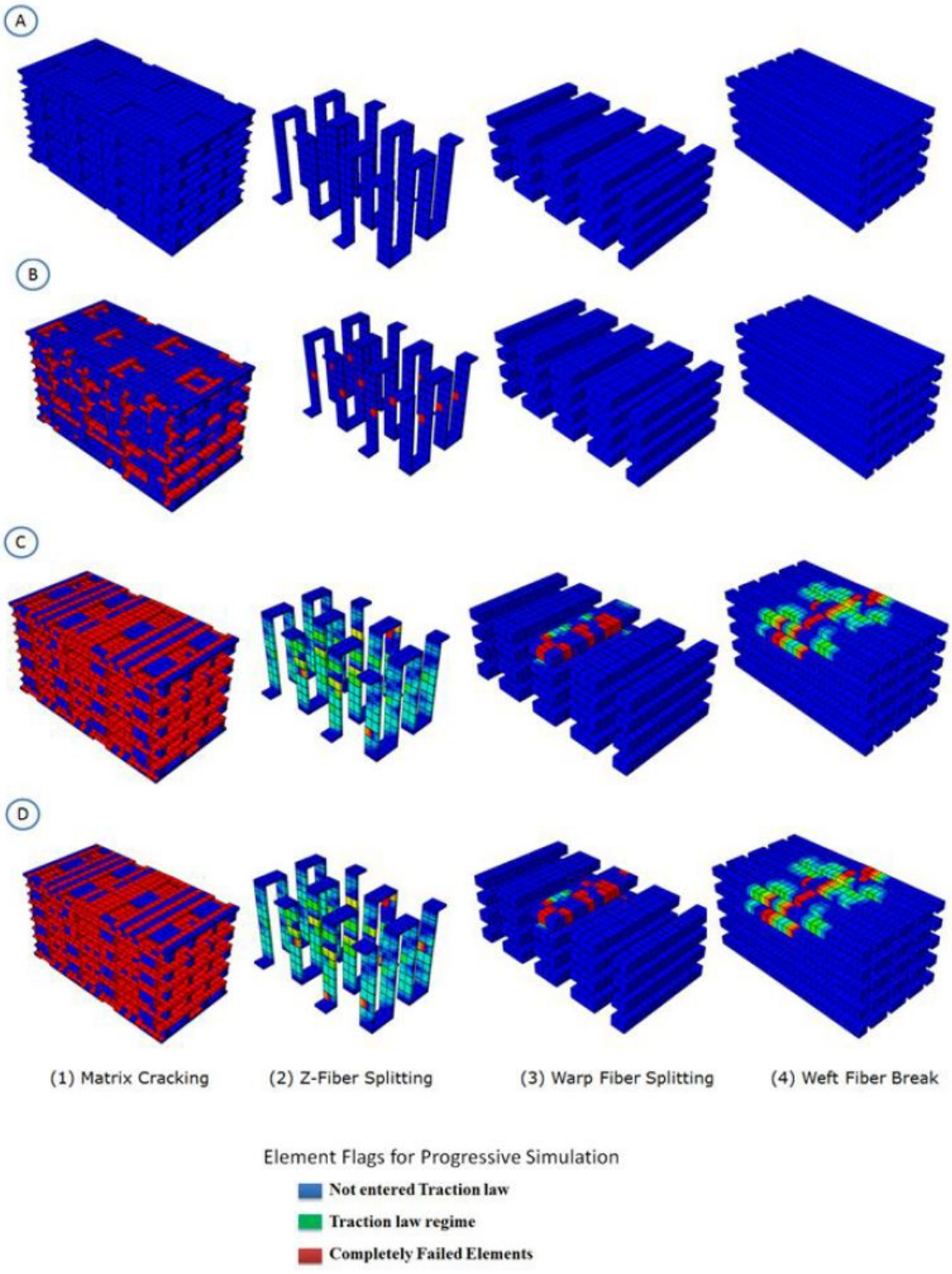

Figure 5.14: Progressive failure for tensile loading in weft direction.

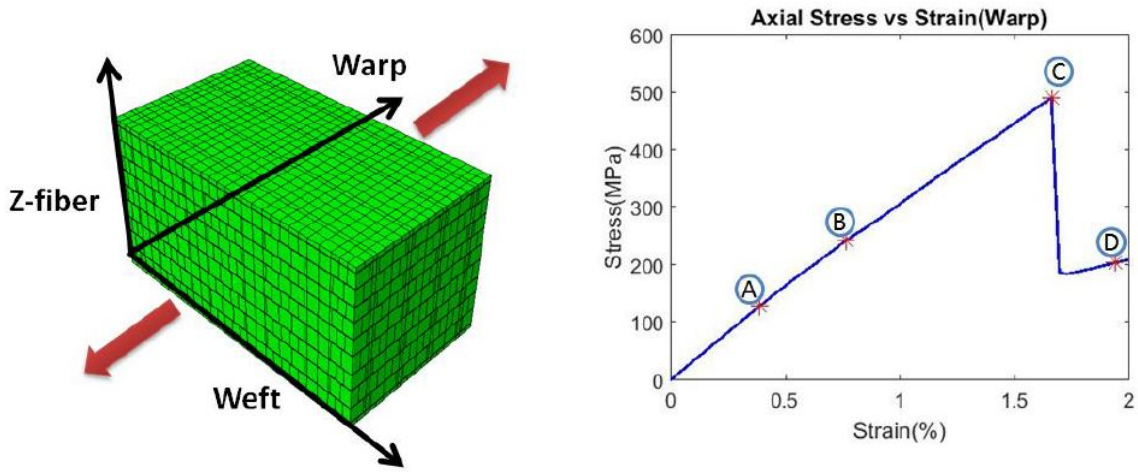

Figure 5.15: Stress-strain response for tensile loading in the warp direction.

Table 5.6: Stiffness comparison between Experiment and Simulation results.

Architecture	*Modulus*	*Experiment* (GPa)	$Model - I$ (GPa)	$Model - II$ (GPa)
Thin Asymmetric	Warp	$36.5 \pm 11.34\%$	34.6	34.4
	Weft	$39.6 \pm 3.58\%$	39.7	39.6
Thick Asymmetric	Warp	$29.1 \pm 13.78\%$	28.4	28.2
	Weft	$57.2 \pm 5.47\%$	55.8	55
Thick Symmetric	Warp	$37 \pm 11.34\%$	34.8	34.1
	Weft	$41.8 \pm 3.58\%$	40.8	39.9

the fiber crookedness in the FE model, the predicted elastic moduli reduced with respect to the corresponding perfect models to some extent, depending on the amount of imperfections existing in different configurations. As shown, there is a reduction in stiffness after including the geometric imperfections. For these hybrid configurations, the weft direction is stiffer than the warp direction due to the fact that there is one additional glass fiber tow layer in the weft direction.

The weft and warp-direction tensile strength for all three architectures are summarized in Table 5.7. The weft direction strengths are larger due to a higher fiber weight fraction compared to the warp direction. In imperfect RVEs, because of the imperfections in fiber alignment in both in-plane and thickness directions, there is significant fiber tow splitting observed in transverse and Z-fiber tows. The predicted tensile strength for imperfect models reduced the respective perfect model values in all the configurations and predictions are closer to experimental values.

The tensile test simulations are carried out for both weft and warp directions and the stress versus strain responses are obtained as shown in Figure 5.17. These sim-

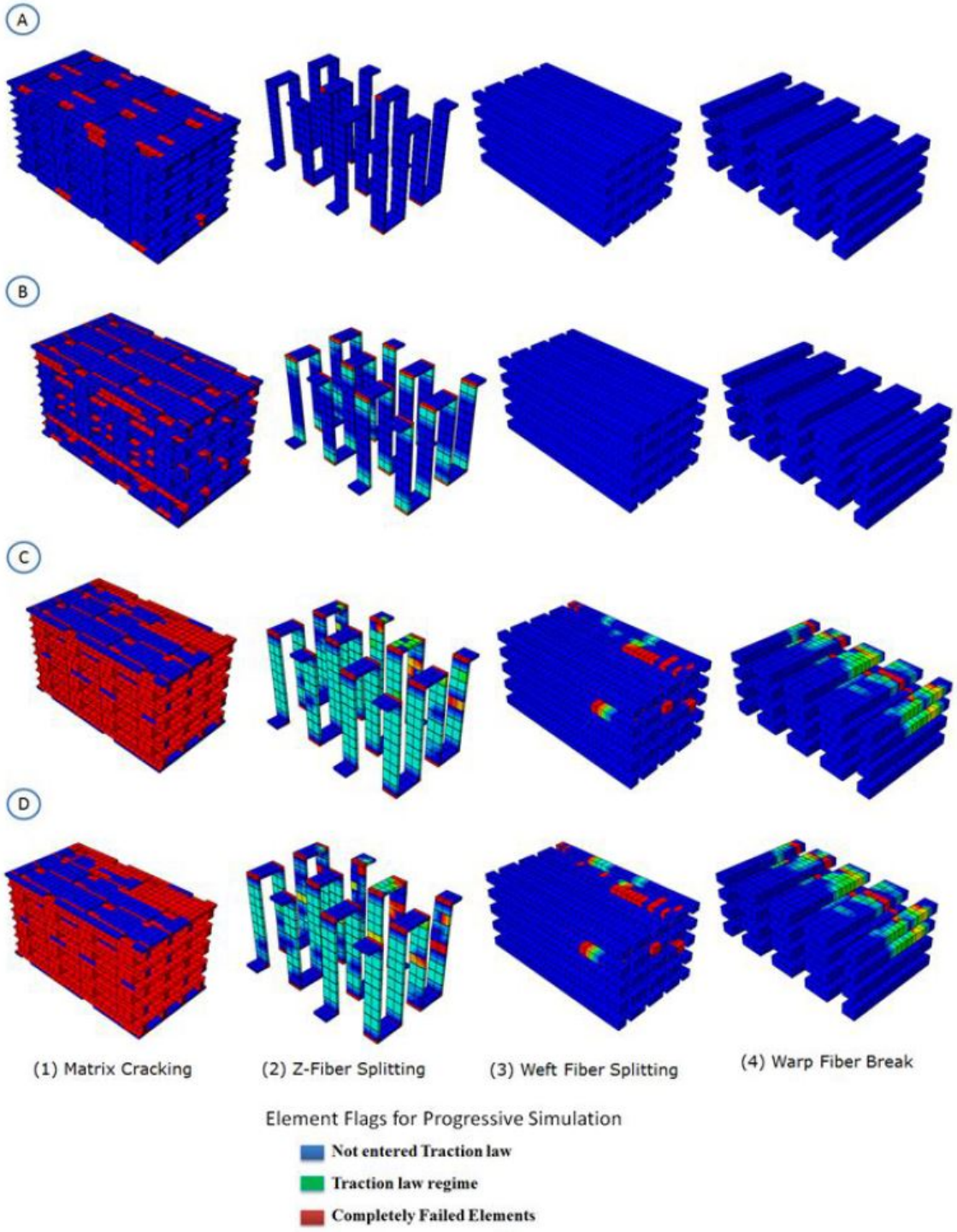

Figure 5.16: Progressive failure for tensile loading in warp direction.

Table 5.7: Strength comparison between Experiment and Simulation results.

Architecture	*Strength*	*Experiment* (MPa)	$Model - I$ (MPa)	$Model - II$ (MPa)
Thin Asymmetric	Warp	427.4	491.3	410.4
	Weft	566.8	600.5	572.6
Thick Asymmetric	Warp	346.6	380.7	322.8
	Weft	510.6	467.6	461.3
Thick Symmetric	Warp	393.3	446.8	403
	Weft	469.3	467.6	449.7

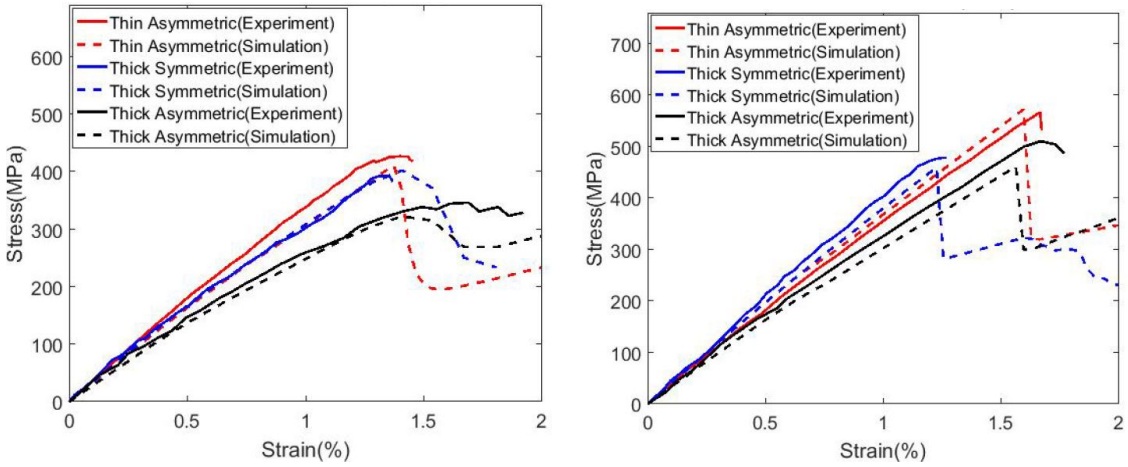

(a) Tension in warp direction

(b) Tension in weft direction

Figure 5.17: Comparison of Stress vs. Strain responses for the different H3DWTCs.

ulation results are compared with the experimental results reported in, [26]. Hybrid 3DWTC of three different architectures are examined and the effect of hybridization is investigated to understand the effective stiffness and strength in tension. Thin Asymmetric configuration shows the highest strength in both warp and weft directions. Due to higher stiffness of the carbon fiber tows compared to glass, it will reach its failure strength earlier than glass, even though both are subjected to same displacement loading. The failure of carbon tows lead to progressive failure of glass tows and the whole dynamics of failure pattern change due to addition of carbon layers, that leads to decrease in overall strength. The architectures and orientations of fiber tows have a strong impact on the localization of strains in the thin matrix layers between fiber tows, which cause matrix micro-cracking and initiates the failure event. Hybridization, by adding carbon to an existing glass fiber system, appears to provide change in tensile stiffness but at the expense of a lower ultimate tensile strength.

5.5.2 Conclusions

In this work, three different configurations of hybridized 3DWTCs are simulated for uniaxial tensile response to determine the effect of hybridization and compute the effective stiffness and strength in tension for both warp and weft directions. A micro-CT analysis is carried out to characterize in-situ microstructural geometric imperfections. This micro-CT analysis helps to extract essential inputs like dimensions of unit cell, RVE, cross-sectional details of fiber tows in both warp and weft directions and volume fraction of pores. Based on these inputs, an idealized 3D geometry model of RVE is constructed. Furthermore, the micro-CT data is used in conjunction with a software tool, 'Simpleware', to generate a FE mesh that captures in-situ geometry, and providing a platform to carry out a 2-scale analysis on realistic imperfect RVEs. A subscale micromechanics 2CYL model, with an analytical solution at the sub-scale is used to establish a computational framework to predict the effective nonlinear response of 3DWTCs. The influence of matrix microdamage at the microscale manifests as the degradation of the effective fiber tow stiffness at the macroscale through a secant moduli approach. Since, fully analytical solutions are utilized for the subscale micromechanics analysis, the proposed method offers a lower computational cost and is suitable for large scale progressive damage and failure analysis of textile composite structures. The linear stiffness and strength of all the textile architectures studied are predicted well when compared to experimental results. The approach presented here can be used to understand and quantify the effects of hybridization and textile architecture on the tensile response of textile composites, in terms of constituent properties. Furthermore, the modeling framework can be used to quantify the effects of uncertain constituent properties on the overall response of textile composites, an essential task in an ICME (integrated computational materials engineering) of composites.

5.6 Multi-scale modeling of test coupon (Macro-meso-micro scale)

The complex multi-phase material systems of 3D woven textile composites are modeled in three scales, (1) the homogenized macro scale, (2) the tow/matrix meso scale and (3) the fiber/matrix micro scale. Figure 5.18 presents the framework of the multi-scale method of 3D textile composites adopted here for the finite element (FE) modeling and progressive failure analysis. The far field non-failure region (indicated

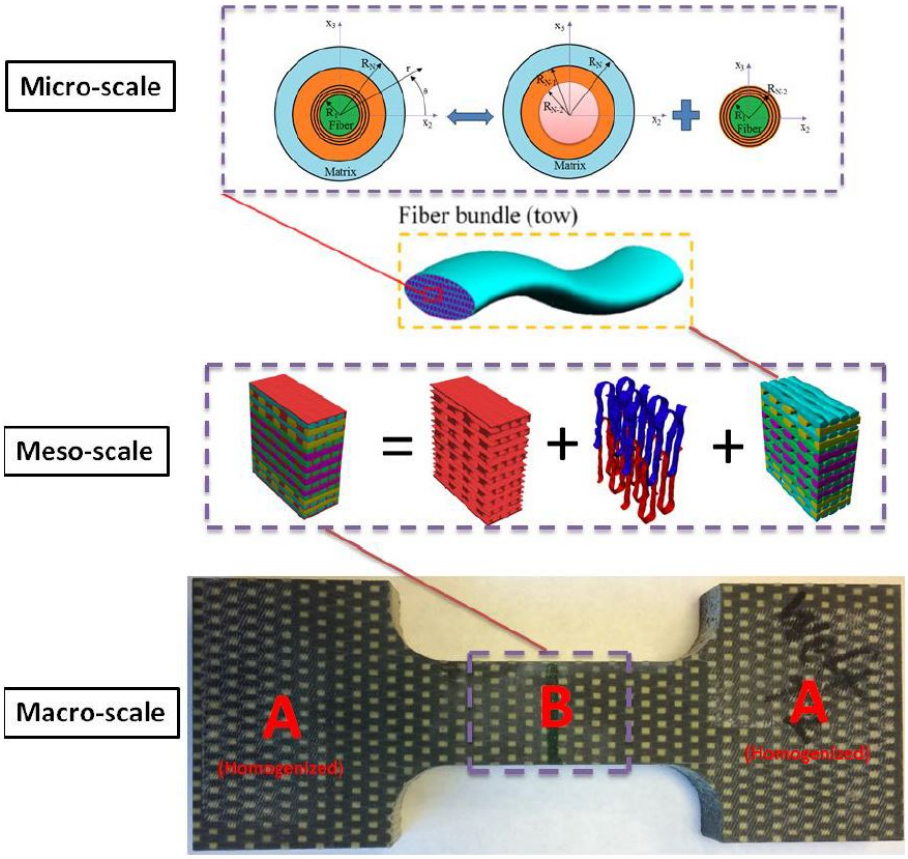

Figure 5.18: Frame work of the multi-scale model of 3D textile woven composites.

A) is defined with homogenized elastic orthotropic properties extracted from meso-scale RVE using periodic boundary conditions for computational efficiency. These hybrid textile configurations are non-periodic in the thickness direction and hence, periodic boundary conditions are excluded in that direction for analysis. The detailed procedure of the meso-scale modeling is discussed in the previous sections. The failure prone gage region (indicated B) is defined as a collection of periodic multiple RVEs in both length and width directions of the coupon. The meso RVEs define the internal structures of the weave and consist of fiber tows running in all three directions inside the matrix pocket. The fiber tows are modeled explicitly and are related to the micro-scale analysis of fiber/matrix constituents through an analytical micromechanics N-layer concentric cylinder (NCYL) model. The homogenized mechanical properties of the fiber tows are calculated through the NCYL model and the tow composite strain at each integration point of the finite element model is related to the analytical strain field of the fiber/matrix cylinders in the micro-scale through a 6x6 transformation matrix, as described in Chapter 2.

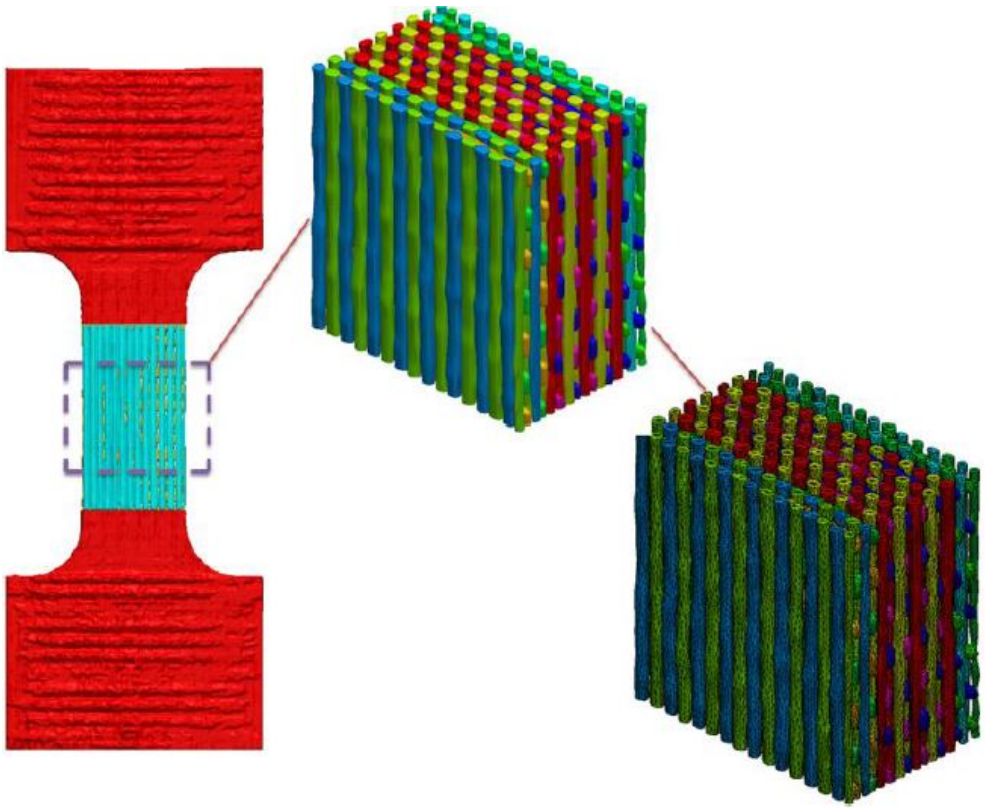

Figure 5.19: FE meshing of coupon including geometry imperfection.

5.6.1 Geometry and finite element modeling of coupon

As damage and failure initiation mechanisms are highly sensitive to the internal structures of the weave and the distribution of local imperfections, the waviness and crookedness of the fiber tows are modeled explicitely using the in-situ micro-CT scanned data. A micro-CT study is conducted for the entire coupon and the finite element mesh is generated directly from the scanned image data using a tool called SIMPLEWARE. Figure 5.19 explains the workflow of the coupon modeling and the mesh generation method for the Thin Asymmetric configuration and similar procedure is followed for other two configurations.

The fiber tows run in all three orthogonal directions inside the matrix pocket and the undulation of the fiber tows leave behind thin-layered of matrix in between tows, which makes it extremely difficult to model in 3D CAD and generate a finite element mesh for failure analysis. The novelty of this approach is to include the real in-situ imperfections for progressive failure analysis at the entire coupon level, as demonstrated in Figure 5.20 for all the three hybrid architectures. The gage region is designed and modeled in such a way that, at least 3 RVEs are covered across width

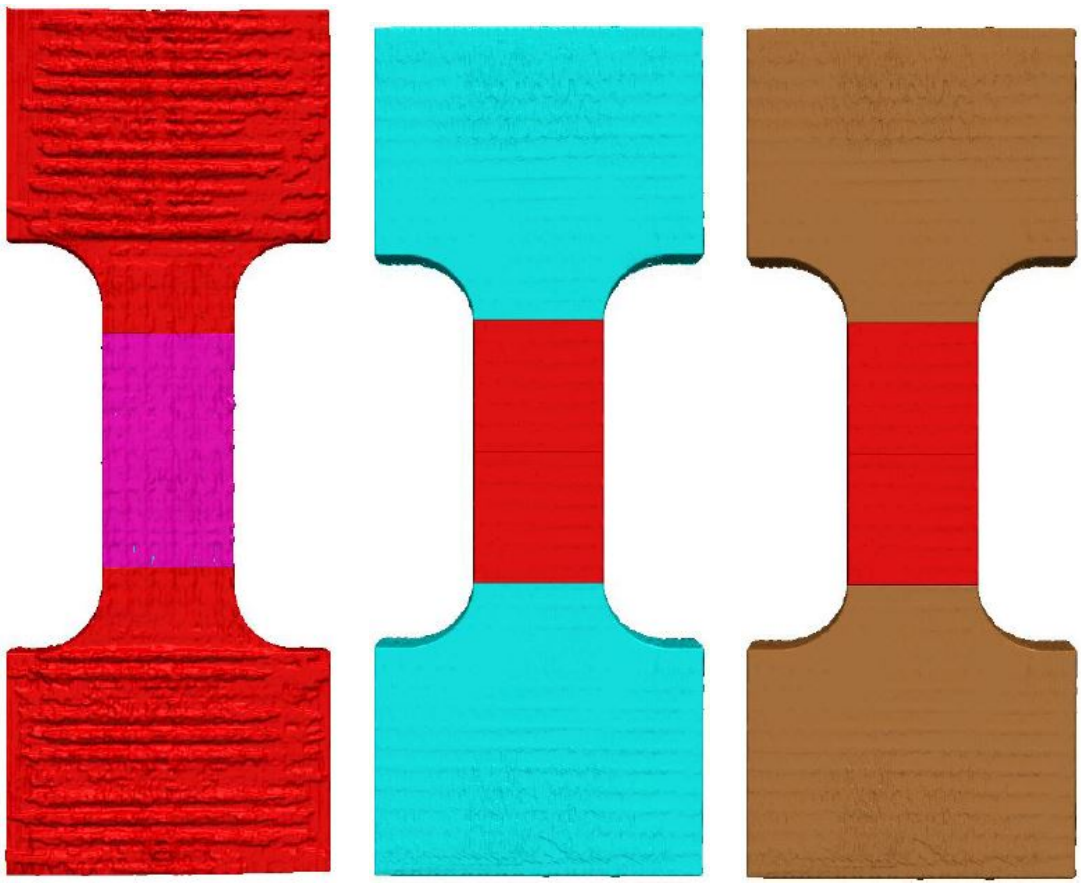

(a) Thin Asymmetric (b) Thick Asymmetric (c) Thick Symmetric

Figure 5.20: 3D geometry modeling of coupons including imperfection.

and length directions of the coupon.

5.6.2 Coupon analysis results and Conclusions

Figure 5.21 shows the comparison of the global stress versus strain response obtained from the coupon with the meso-scale RVE for the Thick Symmetric weft configuration. Also, these simulation results are compared with the experimental results, as available in Reference [26]. Generally, the computational results are in good agreement with the experiment. The failure evolution in the fiber tow is illustrated by the absolute index values of the failure flag. Figure 5.22 shows the failure pattern of the coupon at the peak load, which is caused ultimately by the weft fiber tow breakage in the gage area extremity. It is noted that, the transition from the micromechanics mesh to the homogenized region may influence this failure mode. Therefore, in a future study, this effect is evaluated by extending the gage area mesh further into the homogenized area.

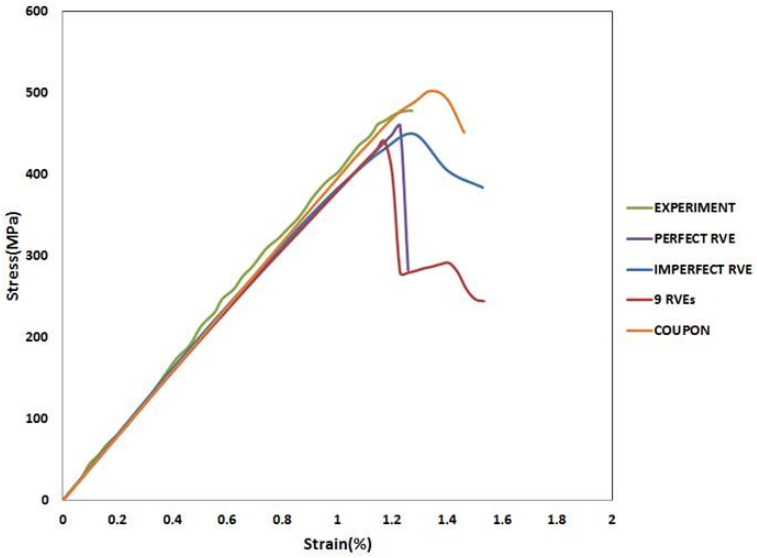

Figure 5.21: Comparison of stress vs. strain response for Thick Symmetric architecture.

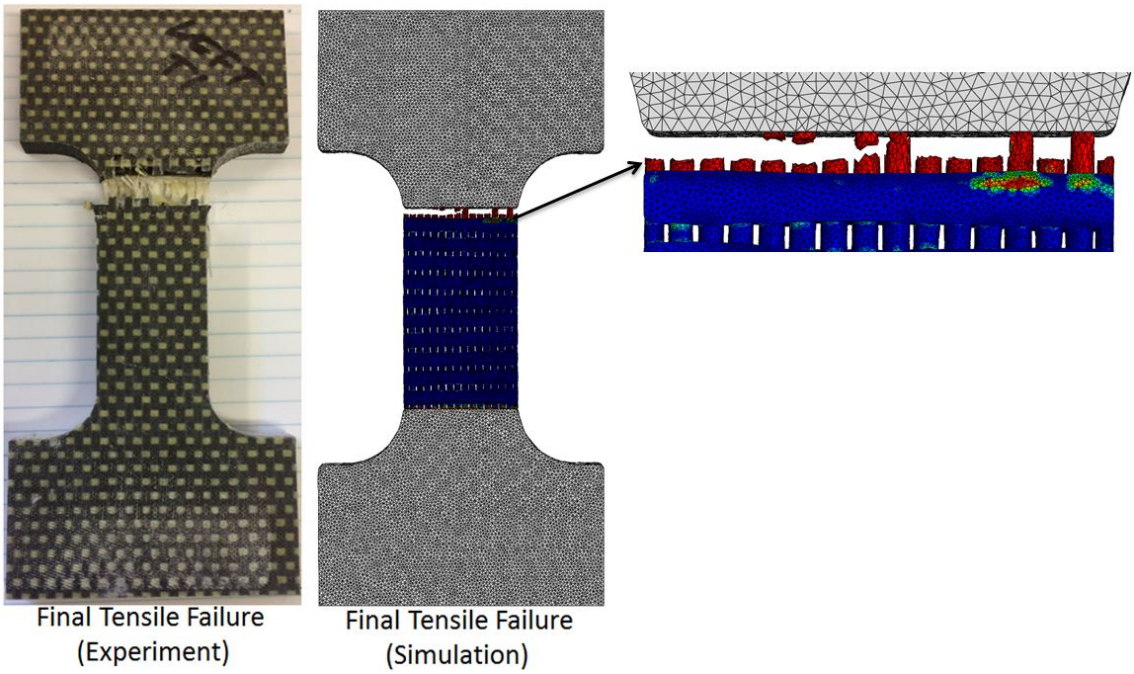

Figure 5.22: Final tensile failure of coupon (Matrix not shown for clarity).

Three different textile configurations are modeled at coupon level to determine the effect of hybridization and compute the effective stiffness and strength in tension for weft direction. A global-local modeling strategy is implemented using the three different length scales and the real in-situ microstructure imperfections are included in this study, obtained from micro-CT analysis. A subscale micromechanics NCYL model is used to predict the effective nonlinear response of a homogenized fiber tow. The influence of matrix microdamage at the micro-scale manifests as the degradation of the effective fiber tow stiffness at the meso-scale through a secant moduli approach. Since, fully analytical solutions are utilized for the micromechanics analysis, the proposed method offers a lower computational cost and is suitable for large scale progressive damage and failure analysis of composite structures. The linear stiffness and strength of the textile architectures at coupon level are closely predicted compared to the RVEs and experimental results. The novelty of the approach lies in modeling the in-situ imperfections at the laboratory tested coupon level and carrying out the progressive damage and failure analysis in a multiscale framework, which enables of predicting the global response and the local complex failure mechanisms of 3D textile woven composites including the effects of hybridization.

CHAPTER 6

An experimental investigation of hybridization on compressive response of hybrid 3D woven textile composites (H3DWTCs) and numerical prediction

6.1 Introduction

Results for the compression response of hybrid 3D woven textile composites (H3DWTCs) that consist of carbon, glass and kevlar fiber tows and a polymer matrix material are presented in this report, using a combination of experiments and a multi-scale analysis. An experimental investigation of three different architectures of hybrid textile composites are studied under quasi-static loading and those experimental results are used to develop a mechanics model for the compressive deformation response of H3DWTCs using the finite element method. The modeling strategy incorporates both representative volume element (RVE) and coupon level modeling to study the compressive failure response. The RVE model considers micro scale based modeling, where tows are considered homogenized entities of fibers and matrix, and the matrix as an isotropic material. The coupon level model uses an actual representation of the fiber tows and matrix, obtained using microCT images and subsequently discretized using a commercial software tool, SIMPLEWARE. The effect of using multiple unit cells in the RVE and the gage section of the test coupon, on the predicted compression strength, is studied. The fiber and matrix compression failure modes that are observed in the experiments are seen to be captured by the models developed here.

Past literature on failure theories of composite materials have studied failure at the meso scale and to a limited extent at the micro scale. However, it is now accepted that the mechanisms that lead to compressive failure, both for the matrix

and fiber-dominated failure modes are highly complex and require careful modeling (see for example, [55], [72], [73] and [74]). Strength and strain-based failure criteria are commonly used with the finite element method to predict failure in composites. In the past, homogenized, continuum based criteria have been presented to relate internal (averaged) stresses to experimental results of material strength to the onset of failure. These approaches, unfortunately, use averaged values and thus, failure which initiates at the constituent level, are not properly captured. In this research, mechanism-based failure models are discussed and proposed for each compressive failure mode in 3D woven textile composites, for the orthotropic homogenized fiber tow and for the isotropic matrix. If textile composites are to be used in structural applications, then the understanding of how each failure mode takes place i.e. having a mechanism based model for different failure modes is imporant. The mechanism based models clearly show the contributions of the constituents to the failure mode of concern. For instance, it is shown by Pavana and Waas [73] how matrix shear nonlinearity and fracture toughness of the matrix contribute to kinking and splitting failure observed in compressive failure of fiber tows. The dominant damage and failure modes of H3DWTCs subjected to compressive loading are: (1) fiber tow compressive failure, (2) matrix compressive failure outside of fiber tows and inside the volume of the textile and (3) matrix shear cracking, occuring close to the tow-matrix interface. It is well established that the fiber compressive failure mode is governed by the nonlinear resin shear behavior and imperfections such as the initial fiber misalignment angle and voids, [75]. However, when a kink band sets in, splitting of the matrix due to the large transverse strain can also occur as described in [73]. Matrix compressive failure is associated with an instability in shear, typically governed by a Mohr-Coulomb type criterion and this mode of failure may also precipitate the onset of kink band formation.

Three different configurations of 3D woven textile composites are considered here to compare their compressive strength and study the effect of hybridization and architectural effects on the compressive response and failure behavior. In these configurations, fiber tows run orthogonally in all directions, held by the matrix. The thin layer of matrix volume between fiber tows start to develop micro cracks due to shear stress, even though the structure is subjected to compressive loading in a global scale. These micro cracks in the matrix can precipitate a large macroscopic crack that can separate the tow from the matrix. In this study, the matrix and fiber tows are the entities that are modeled and each entity is assumed to have a variety of failure modes as discussed later. It is noted that, at the micro-mechanics scale,

individual fibers and matrix inside the fiber tow can be modeled numerically, using a representative volume element (RVE), to study the compressive failure and kinking behavior in detail, which has been done previously, [76] and [73]. However, it is impractical to model a fiber tow using a fiber-matrix RVE (micromechanics) at the level of the textile architecture (meso scale). Therefore, fiber kinking is modeled at the (homogenized) fiber tow scale and macroscopic failure initiation criteria (informed from the micromechanics modeling) are implemented to predict this failure behavior for computational efficiency. A discussion of the modeling of fiber tow compressive failure is included later in this report.

An important mode of matrix failure is compressive failure which is captured using the Mohr-Coulomb model. Puck et al. ([77], [78], [79], [80]) were the first researchers to propose a matrix failure model based on the Mohr-Coulomb criterion. The analysis includes matrix failure for a three dimensional (3D) stress state. In this study, the significance of this failure mode for tow compressive failure is discussed using a simple fiber-matrix tow model. It is seen that, for the material system studied here, the Mohr-Coulomb mode of matrix compressive failure does not influence the tow compressive strength, even though the matrix material is seen to initiate combined compressive-shear failure. The peak load is still governed by resin shear nonlinearity and fiber misalignment.

6.2 Material system

The material system considered is a 'hybrid' Z-fiber orthogonal interlock textile 3D woven composite (H3DWC), where 'hybrid' refers to different constituent fiber tows. The terms fibers and fiber tows are are used interchangeably and their meaning is clear from the context. In-plane carbon and glass fiber tows are stacked together in multiple layers in a cross-ply manner and kevlar fiber tows run orthogonally in the thickness direction to bind the in-plane layers and prevent delamination. Kevlar fibers are flexible and more ductile compared to carbon and glass fibers and that enables it to run in the up-down-up fashion through the thickness of the laminate. The dry preform is woven through 3D textile weaving process, with carbon and glass fibers subjected to pretension, which enhances in-plane mechanical properties. The architecture of the H3DWC helps to improve the damage tolerance behavior, and failure is progressive in comparison to catastrophic failure of isolated brittle materials. The constituent materials are IM-7 carbon fiber, S-2 glass fiber, kevlar fiber and SC-15 matrix, which is a two-phase toughened thermoset polymer, used for high temperature applications.

Table 6.1: The elastic properties for IM-7 carbon fiber, S-2 glass fiber, kevlar fiber and SC-15 matrix.

	E_1 (GPa)	E_2 (GPa)	ν_{12} -	ν_{23} -	G_{12} (GPa)	G_{23} (GPa)
IM7 carbon fiber	276.0	15.0	0.279	0.49	12.0	5.02
S-2 glass fiber	93.8	93.8	0.23	0.23	38.1	38.1
Kevlar fiber	112	112	0.36	0.36	41.2	41.2
SC-15 matrix	2.487	2.487	0.35	0.35	0.921	0.921

Material properties for each fiber type and the matrix are provided in Table 6.1.

6.3 Textile architecture

In this research, three different hybrid architectures, as schematically shown in Figure 4.1 are investigated to understand the effect of hybridization on the resulting compressive response, [34]. Detailed description of these hybrid textile confogurations are covered in Section 4.3.

6.4 Matrix nonlinear constitutive model

In this material system, the matrix non-linearity caused due to microdamage is modeled in two different length scale, i.e.(1) Matrix cracking inside the fiber tow is modeled using the degraded secant stiffness properties of the matrix, in combination with elastic fiber properties to homogenize the fiber tow stiffness at macro scale. Matrix material behaves differently in the presense of fibers, in comparison to the pure matrix only. Hence, it is important to extract the in-situ non-linear properties of matrix to use in the predictive computational model. (2) The surrounding matrix cracking outside of fiber tow and inside the volume of textile material is modeled using the secant degraded stiffness and a modified J_2 deformation theory of plasticity. The evolution of non-linearitry accounts for progressive deterioration of the material stiffness, however, the tangent stiffness tensor still remains positive-definite. The coalescence of matrix micro damage finally results in matrix macroscopic cracking, followed by a post-peak strain softening regime. In this instance, the positive definiteness of the matrix stiffness tensor is lost, which is categorized as a failure. The post-peak strain softening behavior of matrix failure inside the fiber tow is not considered here and only the pre-peak non-linearity is taken into account to capture the macroscopic pre-peak non-linear response. The post-peak strain softening behavior for fiber tow is

modeled at the macroscopic level using the 3D orthotropic smeared crack approach (SCA). The post-peak strain softening behavior for the surrounding matrix outside the fiber tow is modeled through the 3D isotropic smeared crack approach (SCA) to capture matrix macroscopic cracking, as described in the following sections.

6.4.1 Modeling microdamage in a polymer matrix

As discussed in [17], the matrix in-situ response can be characterized through a tensile test on a ±45° symmetric laminate. Furthermore, it is assumed that the matrix nonlinear response can be characterized using an exponential relation,

$$\sigma_{eq} = \sigma_y - \frac{K_1}{K_2}\left(\mathrm{e}^{-K_2\epsilon_{eq}} - \mathrm{e}^{-K_2\frac{\sigma_y}{E}}\right) \tag{6.1}$$

where σ_y is the yield stress of the matrix in a uniaxial tension test, E is the elastic modulus, K_1 and K_2 are two material constants that govern the evolution of matrix microdamage. Different nonlinear responses have been reported for the matrix within a carbon tow than that in a glass tow [32]. Table 6.2 summarizes the matrix nonlinear properties used in the two-scale micromechanics model for computing the response of each constituent tow. In addition, the pre-peak nonlinear properties of the surrounding matrix in the macro model is assumed to be the same as the one used for the glass tow.

Table 6.2: Matrix nonlinear properties used in this research.

	σ_y (MPa)	K_1 (MPa)	K_2
Matrix (macroscale)	25	1700	40
In-situ carbon	25	3500	60
In-situ glass	25	1700	40

6.5 Fiber tow constitutive model

The experimental results of the ±45° symmetric laminate tensile tests indicate that the matrix exhibits a nonlinear stress versus strain response due to the evolution of microdamage. In the proposed computational scheme, each fiber tow is homogenized as a 3D solid, therefore, micromechanical analysis must be implemented at the subscale to capture such nonlinear behavior. Since the fiber tow pre-peak nonlinear response is attributed to matrix microdamage, no macroscopic damage criterion is required to drive the nonlinear damage progression. However, multiple catastrophic

failure modes are observed in the experiment, including fiber kinking. These modes of failure result in a loss of load-carrying capability of composite structure, followed by a post-peak strain softening response. Since the positive definiteness of the material tangent stiffness matrix is lost in softening regime, the FEA will provide mesh dependent results if no characteristic length is introduced. As a result, the aforementioned two-scale NCYL model has to be supplemented by a suitable mesh objective approach for modeling the post-peak softening response.

In the present study, fiber kinking is considered as the major failure mode for H3DWTCs subjected to compressive loading, which is evident from the experimental investigation discussed in [72]. In addition, when the fiber kinking is initiated in axial tows due to compressive stress, the crack plane is assumed to be aligned perpendicular to the fiber direction. Details of the implementation of the 3D orthotropic SCA within a FE framework are demonstrated in Section 6.5.2.

6.5.1 Tow pre-peak nonlinear response: NCYL model

Recently, Zhang and Waas [1] developed a two-scale, micromechanics-based model for computing the nonlinear response of a unidirectional composite. In their model, a fiber-matrix concentric cylinder is used as the repeat unit cell (RUC), to represent a composite fiber tow. The two layers fiber-matrix analytical model has been extended to N-layer fiber-matrix cylinders to analyze the stress and strain fields for all constituent matrix layers, as described earlier in Chapter 2. Micromechanics is used to relate the globally applied composite strains to the fiber and matrix strains at the microscale through a six by six transformation matrix. A detailed description of the NCYL micromechanics model and its implementation in a multiscale analysis for progressive damage of textile composites is provided in [81].

6.5.2 Fiber tow kinking failure: 3D orthotropic SCA

Fiber compression failure is a field where significant research is still being performed. However, the mechanics of the failure mode involving fiber compression is more complex. Depending on the material, different fiber compressive failure modes are possible [82]: (1) Microbuckling is a failure mode that consists of the microbuckling of the fibers in the elastic matrix. The first mechanical model for this failure mode can be tracked back to Rosens work [83] where the fibers are represented by infinite beams in an elastic matrix and failure is attained when the compressive load equals the buckling load. This model provides an upper bound for the failure stress, as it generally

predicts a failure stress typically two to three times larger than the experimental one (for carbon reinforced composites [82]). Models based on microbuckling have been widely studied over the last decades. For these models, the matrix shear properties as well as material imperfections play an important role. (2) Kinking can be defined as the localized shear deformation of the matrix, along a band. Typically, the fibers break at the edges of the band, and sometimes also in the interior. It should be noted that some authors consider kinking as a consequence of microbuckling, while others consider it as a separate failure mode [82]. Argon [84] was the first researcher to develop a mechanical model for fiber kinking as a separate failure mode. For Argon, failure is the result of matrix shear failure, prompted by an initial fiber misalignment. For this model, and those that follow it, matrix elastic behavior and initial material imperfections play an important role. (3) Fiber failure can be expected to occur for fibers with low compressive strength, such as Aramid, but is not expected to happen for carbon or glass fibers [82].

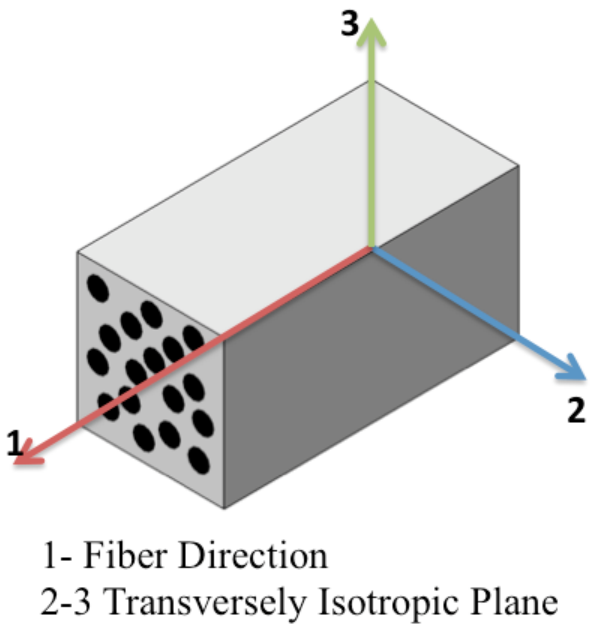

Figure 6.1: Unidirectional fibre tow (schematic).

In hybrid textile composites, fiber tows are surrounded by a polymer matrix, resulting in a complex state of stress. A unidirectional fiber tow is shown schematically in Figure 6.1, where fibers are aligned in 1-direction and the transverse 2-3 plane is assumed to be isotropic. The microstructure of each fiber tow consists of thousands of fibers distributed in the matrix medium with certain volume fraction, depending on the manufacturing process and the applications. The fibers arrangement inside the

tow and the packing details have a great impact on the macroscopic global response, which can be studied in a more detailed manner. The fiber packing controls the distribution of matrix cracking inside the tow, but in our study the fiber tows are homogenized and we try to capture the fiber kinking at the tow level.

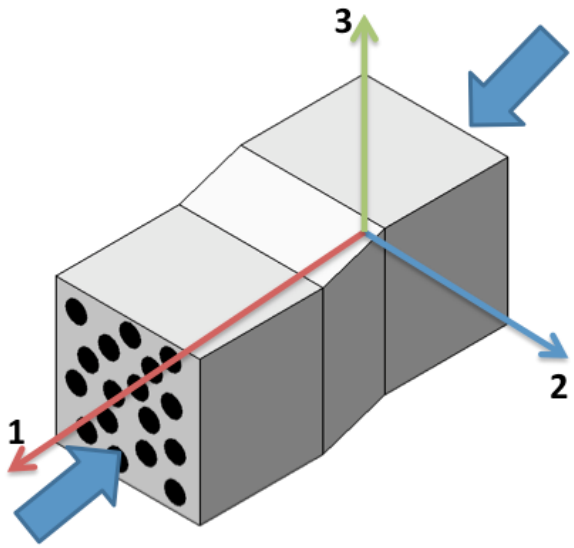

Figure 6.2: Fiber compression (kinking) for crack plane orthogonal to 1-direction.

The smeared crack approach (SCA) formulated in [31] for 3D orthotropic material is utilized to model the failure progression of a single fiber tow, which include fiber kinking in axial direction. Fiber failure mode that include tow kinking in compression is shown in Figures 6.2. It is further assumed that when the critical stress is reached, the crack plane is aligned perpendicular to the fiber direction for tow kinking and the crack orientation transformation matrix, $\boldsymbol{N}$, is determined as given in [31]. The failure initiation criterion is defined by

$$(\frac{\sigma_{11}}{X_C})^2 > 1, \sigma_{11} < 0 \tag{6.2}$$

The crack interface stresses are related to the local crack strains through,

$$\begin{Bmatrix} \sigma_{11}^{cr} \\ \tau_{12}^{cr} \\ \tau_{13}^{cr} \end{Bmatrix} = \begin{bmatrix} E_{11}^{cr} & 0 & 0 \\ 0 & G_{12}^{cr} & 0 \\ 0 & 0 & G_{13}^{cr} \end{bmatrix} \begin{Bmatrix} \epsilon_{11}^{cr} \\ \gamma_{12}^{cr} \\ \gamma_{13}^{cr} \end{Bmatrix} \tag{6.3}$$

Let the onset stress states at the instant of failure initiation are denoted as σ_{11}^{*}, which satisfies the Equation 6.2 as

$$(\frac{\sigma_{11}^*}{X_C})^2 > 1, \sigma_{11}^* < 0 \tag{6.4}$$

When kinking failure occurs in compressive loading, the recorded load drops significantly during the experiment, indicating a considerable amount of fracture energy dissipation. It is worth noting that the tow compressive failure evolution is different from the tensile failure behavior. In the experiment, when the fiber tow fails under compression, the formation of kink band limits the peak load, while additional kink bands are developed with continued deformation, resulting in a load plateau. It indicates that even though the fibers are broken within the kink band, load is still transferred through the band, allowing for stress redistribution. On the other hand, when the tensile failure occurs, the material loses the load-carrying capability completely, resulting in a significant load drop. Therefore, a specific traction-separation law is designed to account for the different failure characteristics for compression, as illustrated in Figure 6.3. It is assumed that when failure progresses under compression, the crack interface can carry 50% of the compressive strength in the post-peak regime, while fracture energy is completely dissipated for tensile failure. The failure properties, including the critical stress and fracture toughness for each mode of failure, are summarized in Table 6.3 for fiber tows and in Table 6.4 for SC-15 matrix respectively. The compressive strength values for carbon and glass tows are taken from [31]. It is worth mentioning that characterizing the failure progression of fiber tows within H3DWTCs is critical to understand the progressive failure response of this class of materials.

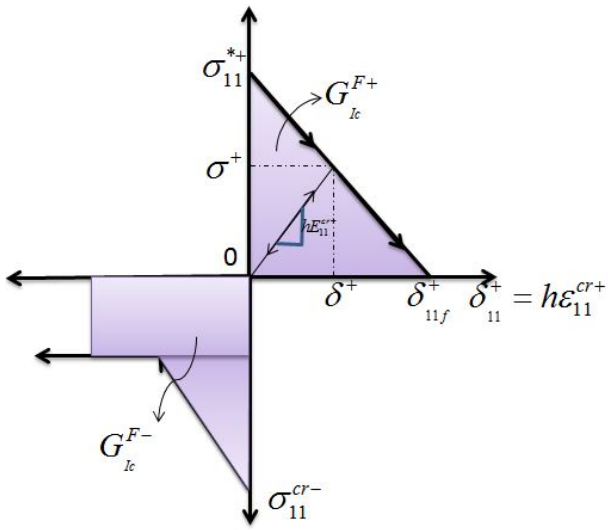

Figure 6.3: Traction-separation laws for fiber tensile and compressive failure.

Table 6.3: Fiber tow failure properties used in the SCA model.

Failure mode	Carbon	Glass	Kevlar
0° tension (MPa)	3000	3700	3600
0° compression (MPa)	977	720	720
90° tension (MPa)	55	65	65
90° compression (MPa)	247.3	247.3	247.3
Shear (MPa)	37	35	35
G^{+}_{ICF} (N/mm)	40	60	40
G^{-}_{ICF} (N/mm)	4	2	2
G^{+}_{ICM} (N/mm)	0.296	0.296	0.296
G^{+}_{IICM} (N/mm)	0.647	0.647	0.647

Table 6.4: SC-15 matrix failure properties used in the SCA model.

Failure mode	Cohesion strength (MPa)	μ	G^{+}_{IICM} (N/mm)
Matrix compression	30	0.75	1.5

6.6 Matrix compression failure: Mohr-Coulomb criterion and 3D isotropic SCA

Shear fracture is the dominant mode of failure for matrix under all but the lowest confining stress. The compressive strength of matrix is a function of the confining stresses between the fibers and the strength increases with increase in confining stress. The simplest and the best known failure criterion of failure is the Mohr-Coulomb (M-C) criterion, where the variation of failure strength is linear approximation of the shear and normal stresses on the failure plane. It has been established that the matrix in composite materials fails in compression by shearing along a 'failure' plane oriented at an angle θ with respect to the axial loading, that is specific for a particular epoxy system. The M-C linear strength criterion implies that θ stays the same regardless of the stresses applied.

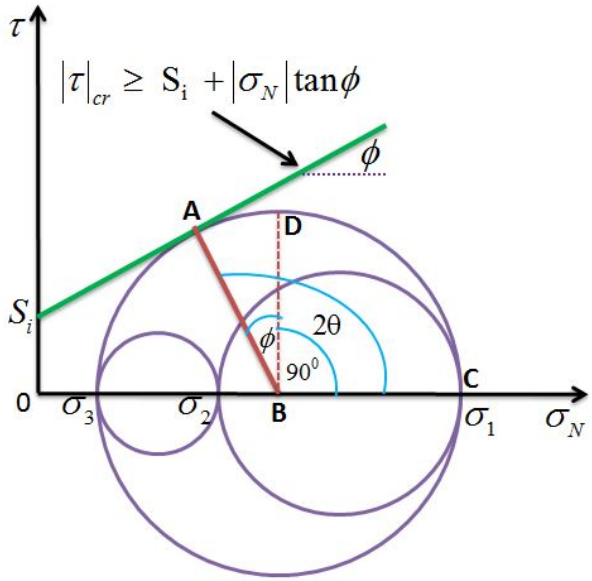

Figure 6.4: Mohr-Coulomb's criterion.

M-C criterion is in terms of shear and normal stress on the plane of failure, defined by

$$|\tau|_{cr} = S_i + \sigma_N \tan\phi, \sigma_N < 0 \tag{6.5}$$

where $|\tau|_{cr}$ is the shear stress, σ_N is the normal stress, S_i is the cohesion strength of the epoxy and the intercept with the τ axis of the linear envelope, and ϕ ('angle of friction') is the slope angle of the linear envelope of failure, as shown in Figure 6.4. The relationship between the angle θ (the angle between the normal to the plane of failure, point 'A' and the direction of the maximum principal stress) and ϕ is given by,

$$2\theta = \phi + \frac{\pi}{2} \tag{6.6}$$

The M-C criterion can also be given in terms of the maximum and minimum principal stresses

$$|\sigma_1| > |\sigma_2| > |\sigma_3|, \sigma_1 < 0 \tag{6.7}$$

The shear and the normal stress on the failure plane can be expressed in terms of maximum and minimum principal stresses from Mohr's cicle and can be replaced in Equation 6.5. By separating all the terms containing σ_1 from the rest of the expression, and recalling the above relation between θ and ϕ from Equation 6.6 and

also performing some trigonometric manipulations, we finally obtain M-C criterion in terms of the principal stresses only, as followed:

$$\sigma_1 = 2S_i \tan(45^0 + \frac{\phi}{2}) + \sigma_3 \tan^2(45^0 + \frac{\phi}{2}) \tag{6.8}$$

which can be reduced to

$$\sigma_1 = C_0 + \sigma_3 \tan^2(45^0 + \frac{\phi}{2}) \tag{6.9}$$

where $C_0 = 2S_i \tan(45^0 + \frac{\phi}{2})$. The two principal stresses can be plotted from Equation 6.9, as shown in Figure 6.5 below.

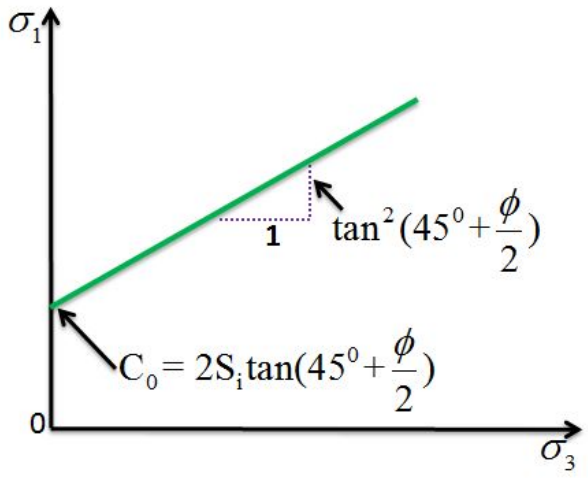

Figure 6.5: Mohr-Coulomb's criterion in terms of principal stresses only.

For uniaxial compression case, failure occurs when σ_1 attains its peak value C_0. Failure plane (point 'A') normal is at $\theta = (45^0 + \frac{\phi}{2})$ to σ_1 direction, as shown in Figure 6.6.

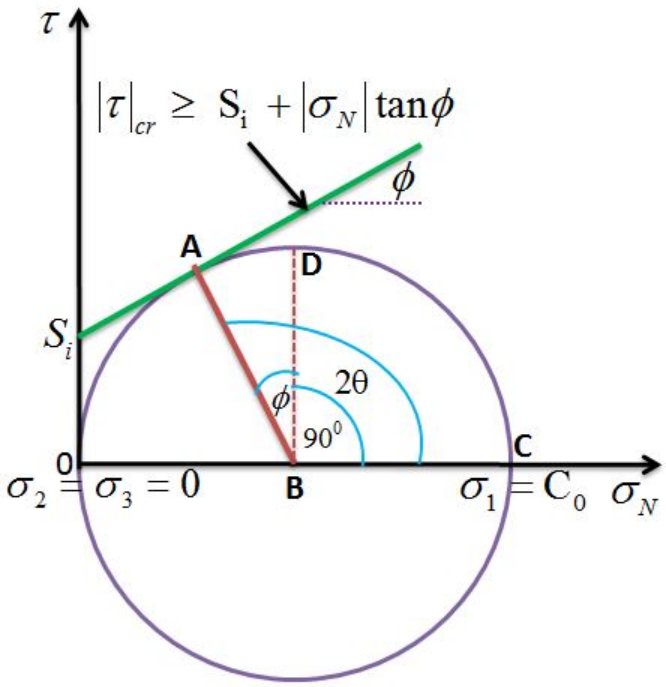

Figure 6.6: Mohr-Coulomb's criterion for uniaxial compression case.

Matrix material is actually subjected to shear failure, when the textile composites are subjected to compressive loading, but the failure mechanisn is commonly referred as matrix compression failure. Indeed, failure occurs at an angle with the loading direction, which is evidence of the shear nature of the failure process. A physical model for matrix compression failure should predict that failure occurs when some stress state is achieved, as well as what orientation the fracture plane should have and how much energy the crack formation should dissipate.

The orientation of the fracture surface of specimens failing by matrix compression suggests that the Mohr Coulomb criterion is applicable to matrix compression failure ([77], [78], [79], [80]). Matrix compression specimens fail by shear. For a pure compression loading, this fact suggests that the angle of the fracture surface with the through-the-thickness direction should be $\theta = 45°$, i.e. fracture should occur in the plane of the maximum shear stresses. However, it is experimentally seen that the angle is generally $\theta = 53 \pm 2°$ for most technical composite materials ([79], [80]). This can be explained through the existence of a compressive stress acting on the potential fracture surfaces, and an associated friction stress. The 3D stress state inside the matrix material are updated through the user subroutine over the progressive loading and subjected to the smeared crack code when M-C failure initiation crieria is met. An exponential traction law is accounted for both tensile and compressive failure of

matrix material, as shown in Figure 6.7. Single element test is carried out to check the validity of the in-house developed code and various case studies are considered to demonstrate the mesh objectivity of matrix compressive failure using the smeared crack approach.

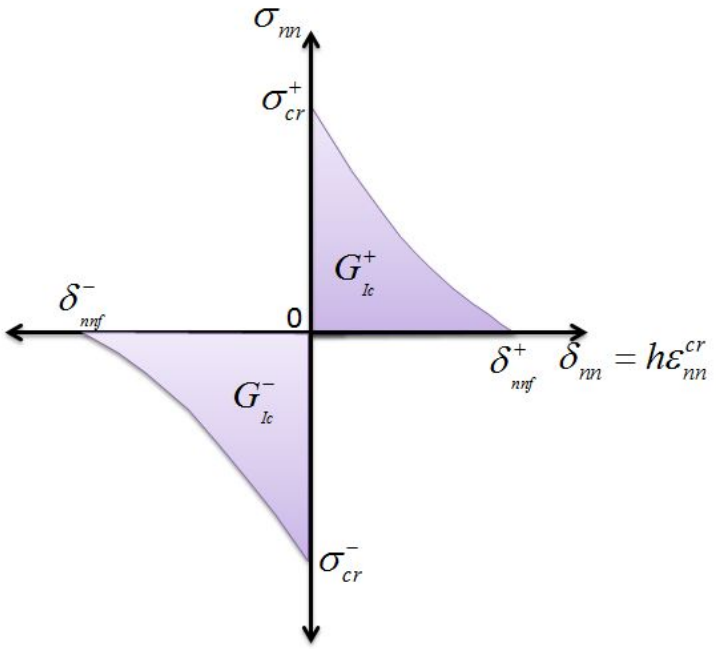

Figure 6.7: Traction-separation laws for matrix tensile and compressive failure.

In this study, a 3D finite element micro-mechanics model of IM-7 carbon fiber and SC-15 matrix system is presented to understand the compressive response and failure of unidirectional fiber reinforced polymer matrix composites. A 3D rectangular representative volume element (RVE) of volume fraction, $V_f = 50\%$ is modeled as a sandwiched matrix between the fibers, as shown in Figure 6.8 below. Previous studies indicate the presence of complex three dimensional stress state in the matrix medium, which influence the development of kink bands due to localization of shear stresses. Few aspects of particular interest in this study are: (1) Implementation of Mohr-Coulomb's failure criteria for matrix compression in combination with 3D isotropic smeared crack approach for modeling post-peak strain-softening response, (2) Capability of the method to capture the deformation localization and formation of kink bands in the sandwiched matrix medium at a given angle of fiber misalignment, (3) The imperfection sensitivity of the compressive strength with respect to the angle of fiber misalignment, and (4) Mesh objectivity of the model. This research would establish the predictive capability of the proposed numerical model for fiber kinking

failure mechanism in a micro-scale and its exiension to multiscale framework at macro-scale.

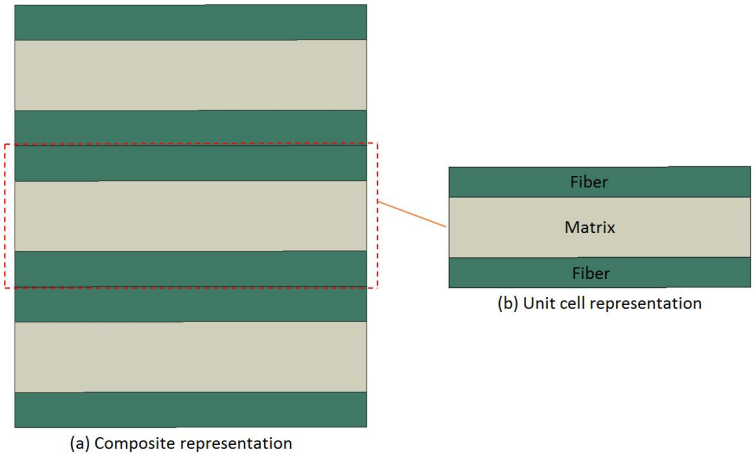

Figure 6.8: Micro-scale RVE for uniaxial compression test.

Table 6.5: Stiffness, strength and fracture toughness values for single element and mesh objectivity test.

Property	Value
E(GPa)	2.487
ν	0.35
σ_y(MPa)	30
$K_1(MPa)$	4500
K_2	58.31
Cohesion strength(MPa)	30
μ	0.75
G_{IIC}(N/mm)	1.5

A uniaxial compression test is carried out for the chosen RVE of fiber and matrix volume, with a suitable element length to satisfy Bazant's mesh size criteria and an initial fiber misalignment angle of 0.1^0. The geometry of fiber-matrix assembly is tilted by the imperfection angle but the end surfaces remain flat. Figure 6.9 illustrates the boundary conditions for the RVE subjected to uniaxial compression. The fibers are assumed to be linearly elastic orthotropic and the matrix non-linearity is modeled as a secant damaging solid using J2-deformation theory of plasticity. All the

material properties that are used in this study are summarized in Table 6.5. The compressive response studies are carried out in a setting of both geometric and material non-linearity and the resulting stress versus strain response along with the progressive contour plots are shown in Figure 6.10. The maximum shear stress localizes at a certain characteristic angle in the sandwiched matrix medium between the fibers and the microcracks develop in those elements. Consequently, all the microcracks accumulate into a single visible macro crack at a slip angle, which depends on the co-efficient of friction of the matrix material. The cohesion strength and the angle of friction are the inputs to the Mohr-Coulomb's model, which are the material properties for a particular matrix material and can be measured experimntally in geotechnical tests. The progressive contour plots of shear stress are shown in the Figure 6.10. The cracked elements which satisfy the Mohr-Coulomb's failure initiation crierion are subjected to enter into the Smeared crack code and shown in red in the progressive plots of Figure 6.11.

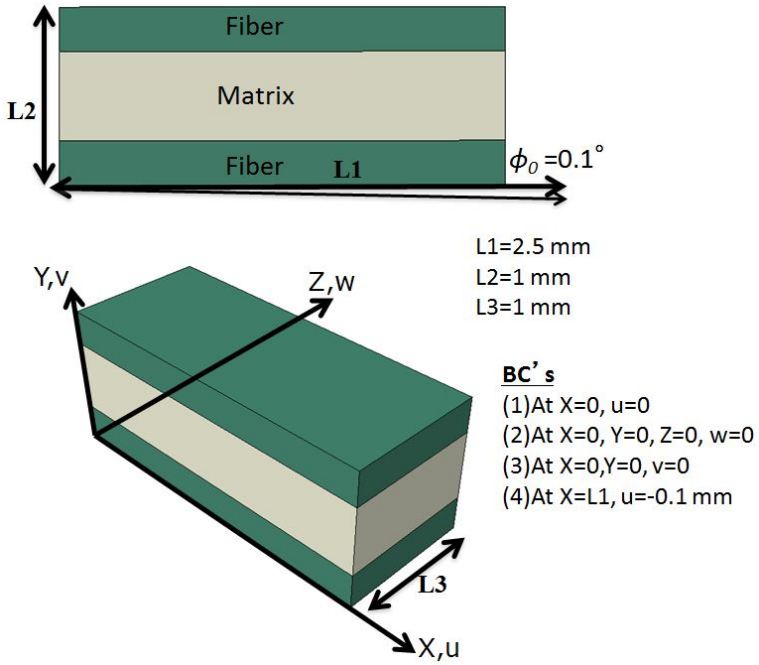

Figure 6.9: Boundary conditions for RVE uniaxial compression test.

An important study to be considered here is the sensitivity of the initial geometric imperfection angle on the compressive strength and load-displacement curve. Geometric models of the RVE are constructed with various fiber misalignment angles ranging from 0.1^0 to 2.5^0 and the corresponding axial stress-strain plots are shown in Figure 6.12. For all the imperfection angles, the model behaves linearly at first

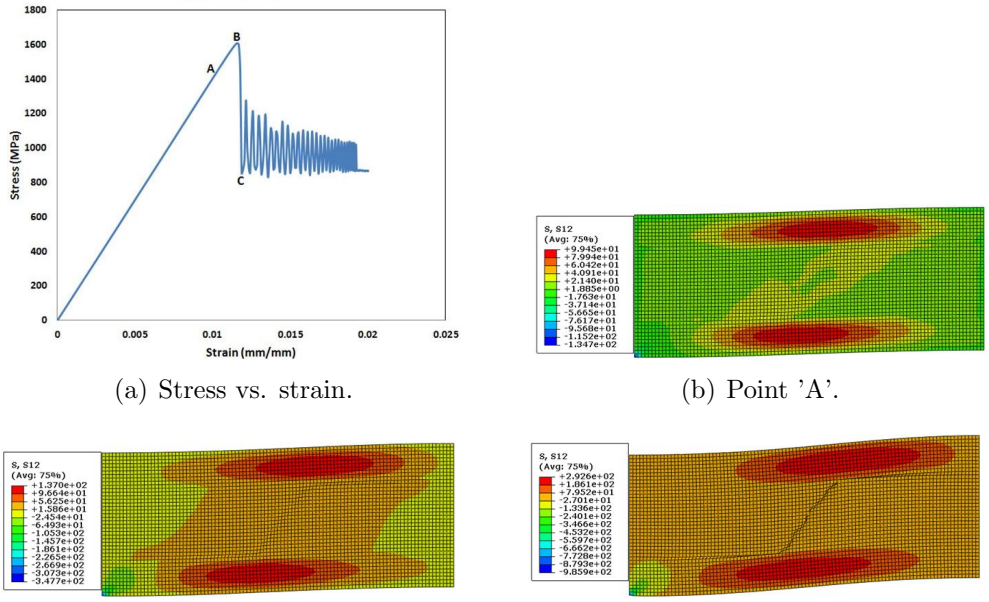

(a) Stress vs. strain. (b) Point 'A'.

(c) Point 'B'. (d) Point 'C'.

Figure 6.10: Progressive contour plots of shear stress.

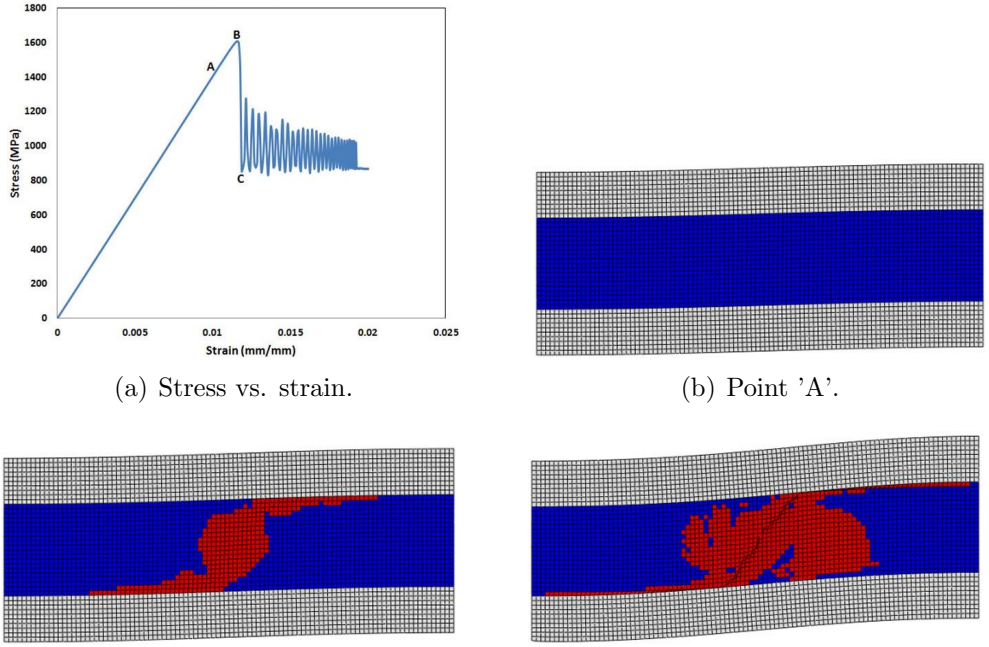

(a) Stress vs. strain. (b) Point 'A'.

(c) Point 'B'. (d) Point 'C'.

Figure 6.11: The cracked elements are shown in red.

in the pre-peak regime and the initial stiffness closely match, indicating that the range of imperfections considered here are smaller in magnitude. The matrix stiffness is degraded using the secant stiffness approach and modeled using J2-deformation

theory of pasticity, as described in Section 6.4. With increasing strain, the matrix shear stiffness decreases and follows the non-linear curve as evident in experiments. The degraded matrix stiffness allows to rotate the fiber progressively and the continued fiber rotation induces more shear strain in the matrix and hence establishes a closed loop feed back network. The loop breaks when the matrix stiffness is degraded sufficiently to provide any further resistance and slips into some characteristic angle causing a shear band. After peak load, a sudden vertical drop in load is observed in the displacement controlled experiments with increasing strain. As observed in Figure 6.12, the compressive strength is sensitive to the initial imperfection angle and there is a gradual drop in strength with increase in imperfection angle. The post-peak compressive behavior is also affected by the misalignment angle. Consider the case of imperfection angle 0.1^0 in Figure 6.12, where the decrease in stress in the post-peak regime is very rapid and the drop is almost vertical. As the imperfection angle increases, the compressive strength decreases and the decrease in stress is gradual in the post-peak regime, approaching a near constant value in the plateau region. The difference between the compressive strength and the plateau regime is also diminishing slowly with increase in imperfection angle, as observed in these plots.

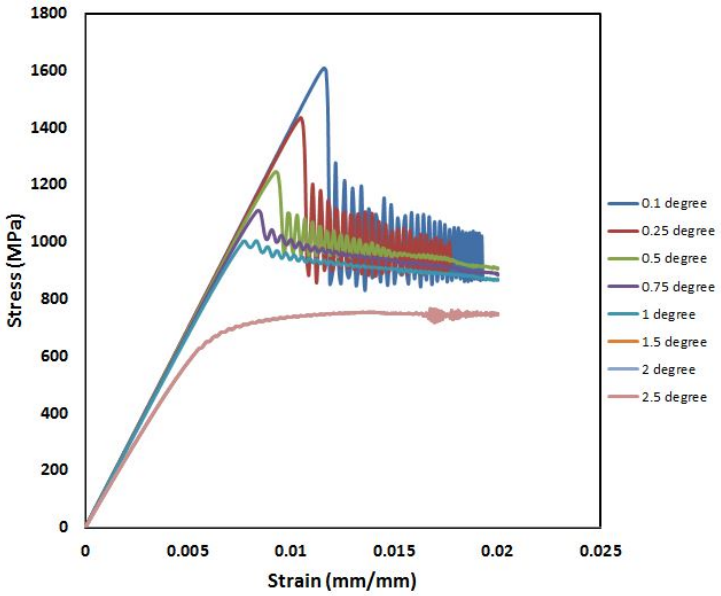

Figure 6.12: Imperfection sensitivity of compressive strength.

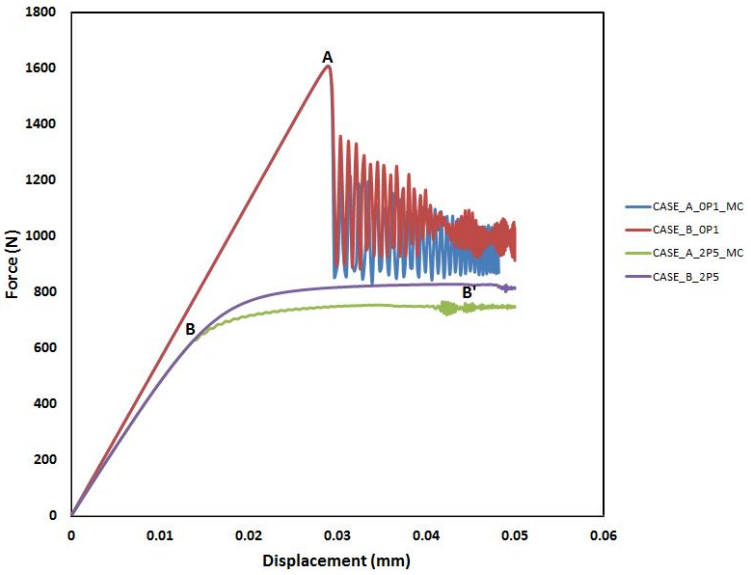

Figure 6.13: Mohr-Coulomb's sensitivity of compressive strength.

The tow compressive strength is governed by both material and geometric nonlinearity and the kinking failure mechanism is the culmination of a structural instability. As shown in Figure 6.12, the tow strength is also sensitive to the degree of imperfection in the structure. It is of interest to know how the Mohr-Coulomb failure initiation in the matrix influences the tow compressive strength. The load drop in the stress-strain plot is an indication of loss in load carrying capability of the structure governed either by the instability or induced by matrix elements that are pushed into the compressive failure via the Mohr-Coulomb (MC) criterion. Two cases of imperfection angles, 0.1^0 and 2.5^0 from the micromechanics study are revisited without using the MC criterion for matrix compressive failure. The same boundary conidtions, material properties and loading are used as before. The matrix remains as a secant solid with an indefinite value of strain, without a limit. As shown in Figure 6.13, for the case of angle of 0.1^0 (Case-A), the peak load is about the same (indicated by A). This clearly indicates that, Mohr-Coulomb mode of matrix compressive failure does not influence the tow compressive strength for low angles of imperfection for the material system of interest here. Furthermore, fiber kinking is driven by an instability due to fiber misalignment and resin nonlinearity. For the case of angle 2.5^0 (Case-B), the first element going through the MC criterion corresponds to point B, which is much earlier in the load-deflection response than the case with the absense of the MC criterion, (indicated by B'). It is also seen that the plateau load is now reduced in comparison with the case where the MC criterion is absent. Therefore, for tow com-

pressive failure, when the fiber misalignment angle is small, the compressive strength is governed by a limit load instability, whereas for larger angles, the maximum load is slightly reduced when the MC criterion is in effect.

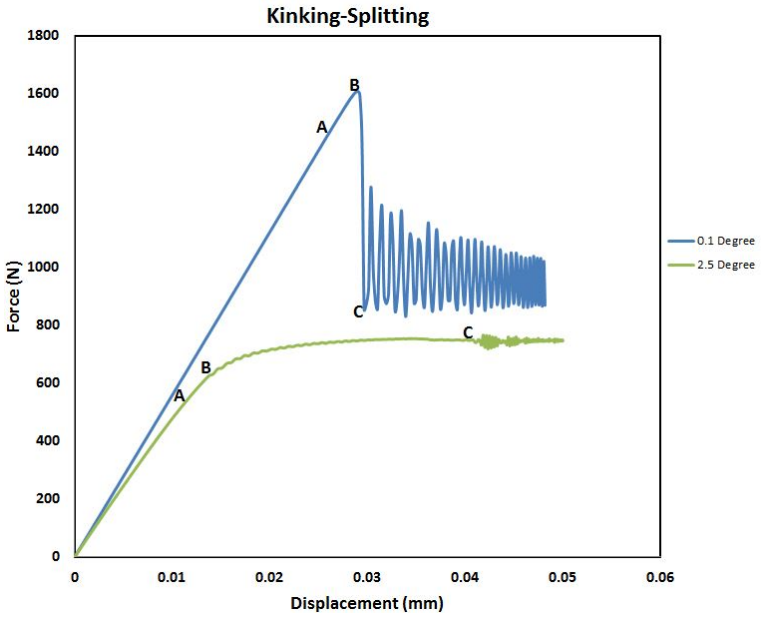

Figure 6.14: Study on interaction between kinking and splitting.

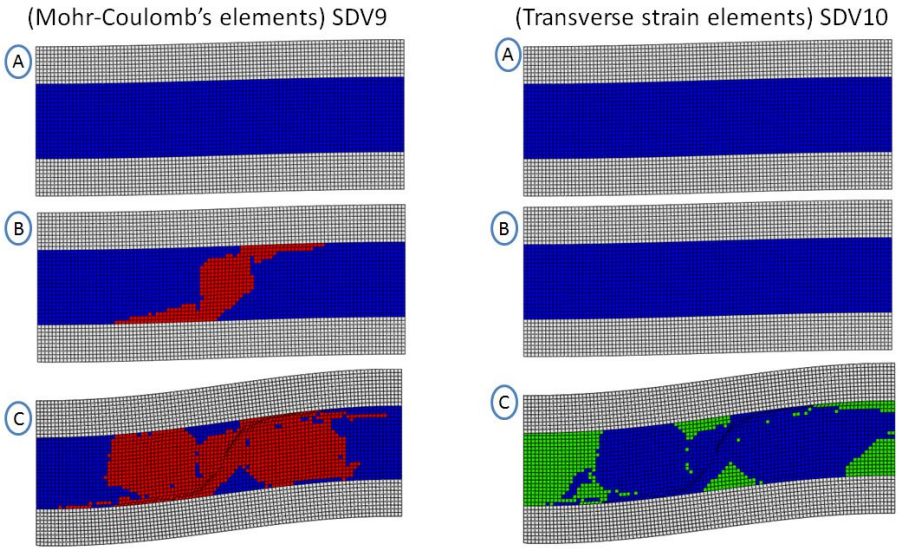

Figure 6.15: Progressive kinking-splitting plots for 0.1^0 (Case-A).

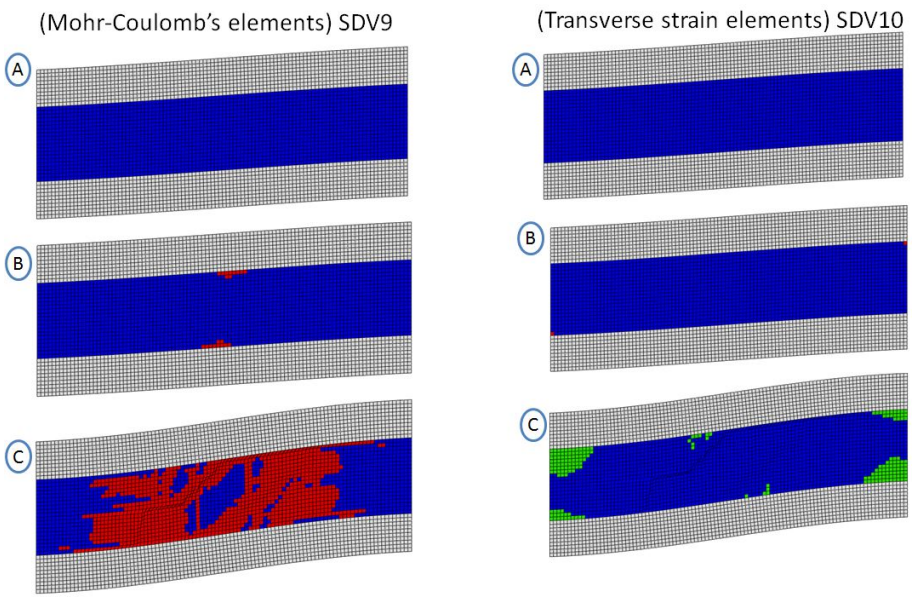

Figure 6.16: Progressive kinking-splitting plots for 2.5^0 (Case-B).

The fiber tow kinking is the most dominant failure mode observed in compressive failure of fiber tows. However, when certain matrix elements within the kink band sets into Mohr-Coulomb's criterion, the diagonal matrix elements perpendicular to it will be subjected to large transverse strain. The kink band occurs at a certain friction angle, which is the characteristic of the particular material system, but nonetheless, the interest here is to study the interaction between splitting and kinking failure mode, which may interact with one another. For the micromechanics model studied here, two cases of misalignment of fiber tows, 0.1^0 and 2.5^0 are considered here to study the interaction behavior between these two failure modes. A transverse strain based failure criterion is being added to Mohr-Coulomb's criterion, keeping the same boundary conidtions, material properties and loading as used before. The load-deflection plots for both the cases are shown in Figure 6.14. There is no difference between the peak load, even after adding the strain failure criterion, which implies, matrix elements are going through Mohr-Coulomb's crieterion first, leading to formation of kink band. For the case of 0.1^0 angle, the first matrix element sets into kinking mode at peak load (indicated by 'red elements' at B in Figure 6.15) and no transverse strain failure is observed till that point. In the post-peak regime, the fiber tow is kinking and can still hold the load of the structure till the fibers break completely. During this period, the diagonal elements fail because they exceed the maximum transverse strain failure criterion, leading to splitting (indicated by 'green elements' at C). Kinking leads to splitting, as observed in this simulation for the case of 0.1^0 imperfection angle. For

the second case of 2.5^0 imperfection angle, there is no vertical load drop and the load regime turns into a plateau zone. The matrix elements sets into Mohr-Coulomb's criterion pre-maturely (indicated by 'red elements' at B in Figure 6.16), but even in that case, splitting occures as a post-failure mechanism to kinking as seen in Figure 6.16(c), indicated by 'green elements'. In both the cases, the splitting happens as post-kinking failure mechanism, irrespective of angle of imperfection. It is noted here that, without any failure criteria (Mohr-Coulomb and transverse strain), the maximum load computed is almost the same for small angle of imperfection (0.1^0), suggesting that for this material system, the maximum compressive strength is a case of structural instability, driven by fiber misalignment and matrix non-linearity. But for larger angle of imperfection (2.5^0), it is clear that Mohr-Coulomb's criterion leads to reduced plateau load.

In order to verify the mesh objectivity of the smeared crack matrix compression code in the finite element framework, a uniaxial compression test was performed on the same RVE with four different mesh sizes, as shown in Figure 6.17. The in-situ matrix non-linear properties of SC-15 epoxy are calculated as shown in Section 6.4. The compressive failure is localized within the matrix in the failure prone area. The resulting load versus displacement responses for all the four mesh sizes are plotted in Figure 6.18. This simulation is executed using the Explicit solver of ABAQUS in VUMAT framework with the MC criterion active. It clearly shows that the computed fracture toughness, peak load and the localized fracture zone, are independent of mesh size, which clearly indicates the mesh objectivity characteristics of the Smeared crack approach. Hence, mesh objectivity is verified for compressive failure of matrix material using 3D Isotropic smeared crack approach. The cracked elements which satisfy the Mohr-Coulomb's failure initiation crierion are subjected to enter into the smeared crack code and shown in red in the progressive plots of Figure 6.19 at peak load for all the four different meshes.

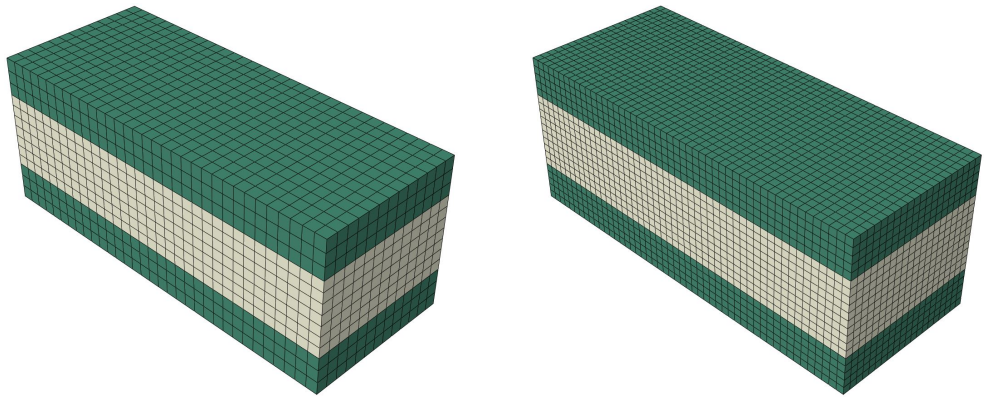

(a) Mesh-1 (5577 elements).

(b) Mesh-2 (20000 elements).

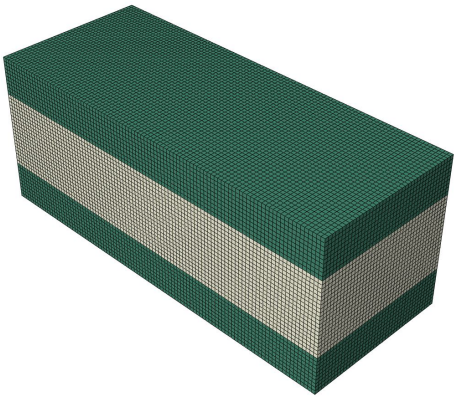

(c) Mesh-3 (160000 elements).

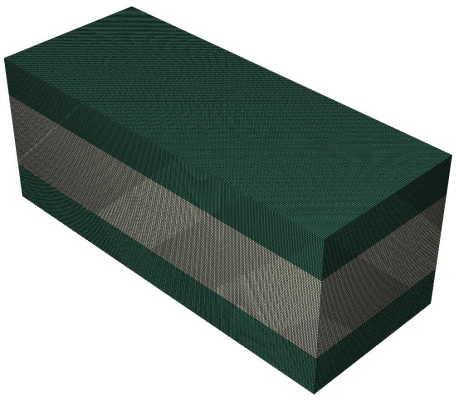

(d) Mesh-4 (2500000 elements).

Figure 6.17: Four different mesh sizes used in mesh objectivity study.

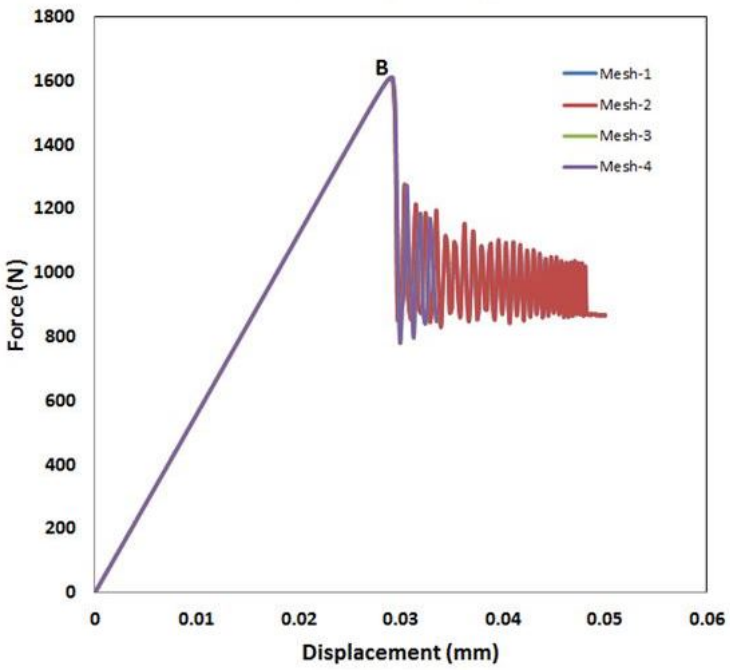

Figure 6.18: Load-displacement responses for RVE subjected to compression with four different mesh sizes. The peak load and the fracture energy are unaffected by the element size.

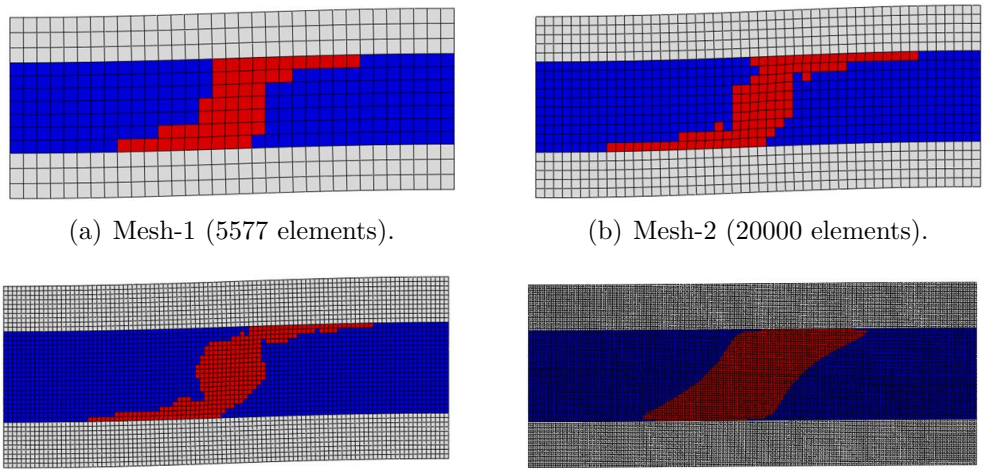

(a) Mesh-1 (5577 elements). (b) Mesh-2 (20000 elements).

(c) Mesh-3 (160000 elements). (d) Mesh-4 (2500000 elements).

Figure 6.19: Four different mesh sizes used in mesh objectivity study. The cracked elements are shown in red.

6.7 Quasi-static experimental results

Uniaxial compression tests were carried out to investigate the compressive response of the 3D hybrid textile composites. Specimens were cut along the weft direction, with a length of 7 inch and a width of 1.4 inch using a water jet and the thickness is 0.63 inch, as shown in the Figure 6.20. A notch of radius 0.0625 inch is drilled at the center of the specimen.

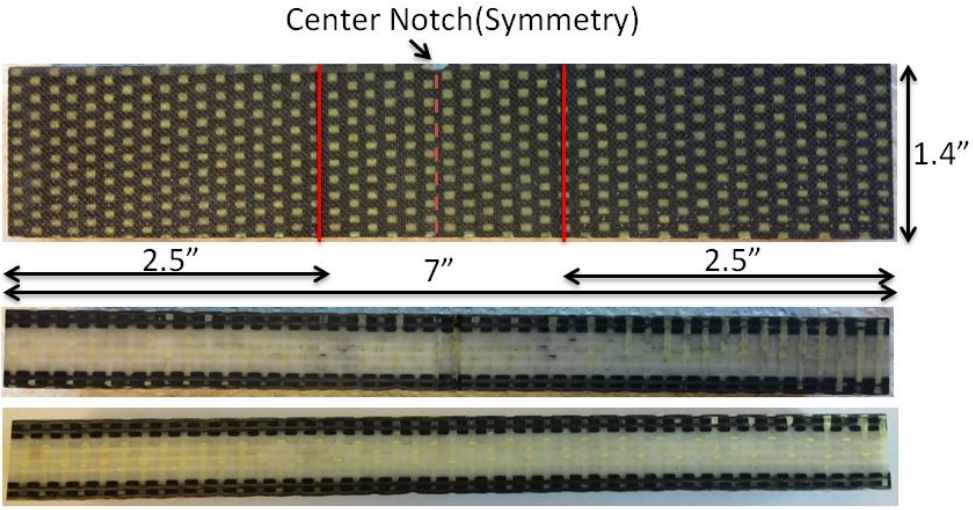

Figure 6.20: Geometry and dimensions of test specimen.

The thickness of different hybrid architectures vary according to the manufacturing specifications, as described in Section 6.3. Tests were performed on a hydraulically activated MTS machine at a loading rate of 0.0004 inch/sec to achieve a quasi-static loading condition, and the load-displacement were recorded, as shown in the Figure 6.21. A manually hydraulic operated HCCF compression fixture was used to secure the specimens on the MTS machine test bed. Different sets of jaws were machined to clamp the specimens of different thickness on the compression fixture using the hydaulic pumps, as shown in the Figure 6.22.

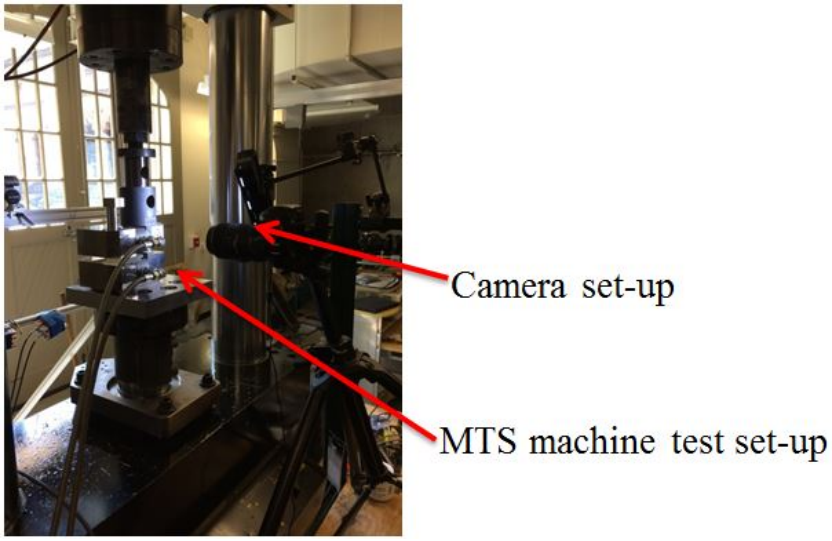

Figure 6.21: MTS machine test set-up.

In order to investigate the failure modes associated with the deformation history, the notched and the back surfaces of the samples were speckled using air-brush, which can be subsequently used to obtain surface strain fields via a digital image correlation (DIC) technique. Images of the notched surface were taken during deformation using a 12 Megapixel camera at 1-second time intervals. The full field surface strain histories were obtained via the DIC software ARAMIS. In order to obtain a thorough understanding on the compressive response of hybrid textile composites, tests were performed on various configurations to investigate the architecture-dependent effect.

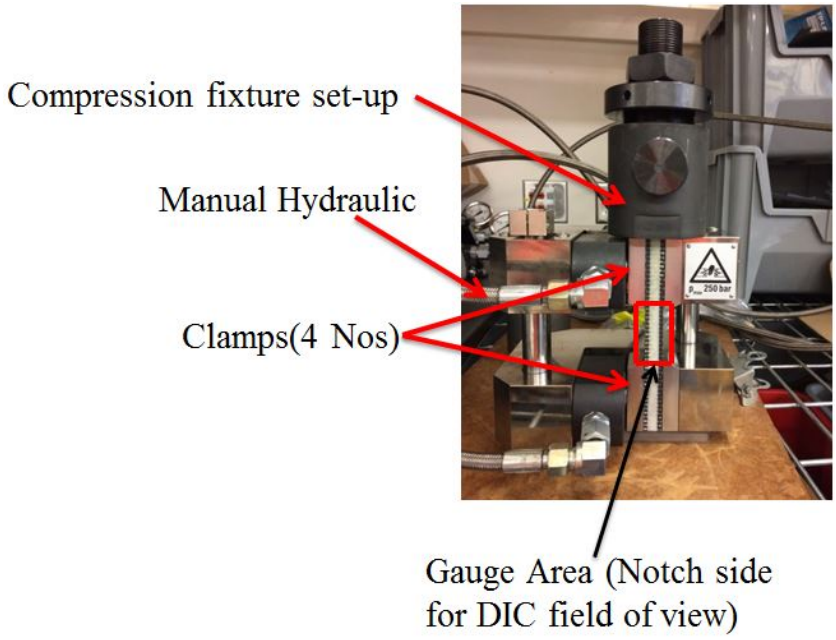

Figure 6.22: HCCF compression fixture set-up.

6.7.1 Progressive damage mechanisms

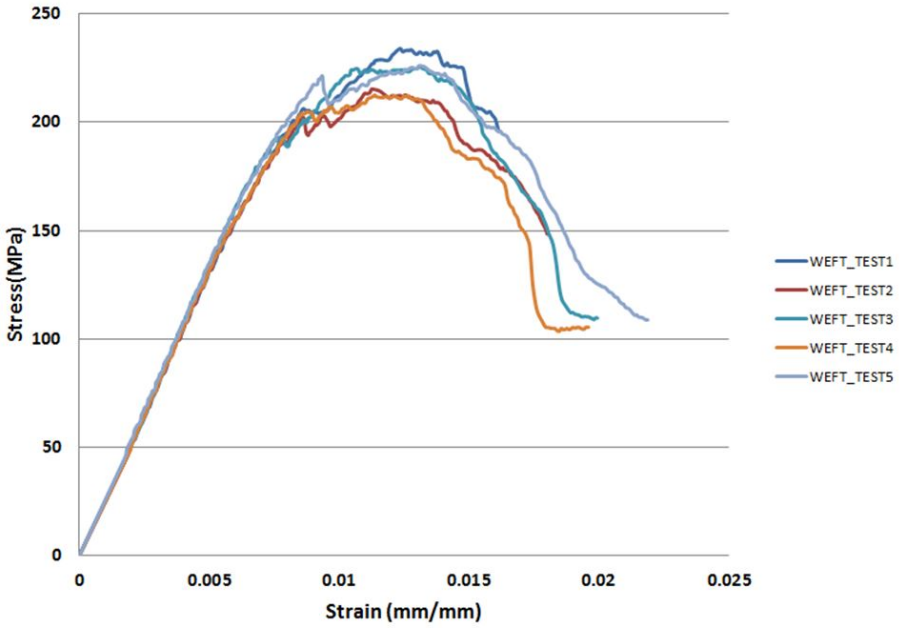

Figure 6.23: Experimental stress-strain curves for Thick Symmetric architecture.

The experimental load-deflection curves for the Thick Symmetric configuration are recorded from the tests and the macroscopic stress-strain curves are extracted from

these data. Macroscopic stress is calculated by dividing the load with the cross-sectional area of the test specimen and macroscopic strain is calculated by dividing the DIC measurement of displacement with the specimen length. The experimental stress-strain curves for 5 different tests are shown in Figure 6.23.

These curves exhibit similar trends, in that the initial propertional loading is followed by an approximate load plateau, indicating considerable damage tolerance for this class of materials. Figures 6.24 and 6.25 show the deformation response for Thick Symmetric specimen loaded along the weft direction, in which a series of images show the observed damage events, which are related to the loading history. These images clearly show that the first damage that occurred which corresponds to deviation from propertional loading is carbon fiber tow kinking on one side of the notch. When the specimen is loaded further, additional kink bands are formed in glass tows at the middle, accompanied by matrix cracking in between the fiber tows. There is a small load drop due to first kink formation and the load raise subsequently due to additional kink bands. At some instant, all the fiber tows are under the kink zone but still has a residual load carrying capability, which leads to a plateau region in the load-deflection plot. The failure is progressive, until a macroscopic wide kink band forms through thickness leading to a significant load drop, when the fibers inside the kink band break accompanied by lots of matrix cracking around it and loose their load carrying capacity completely.

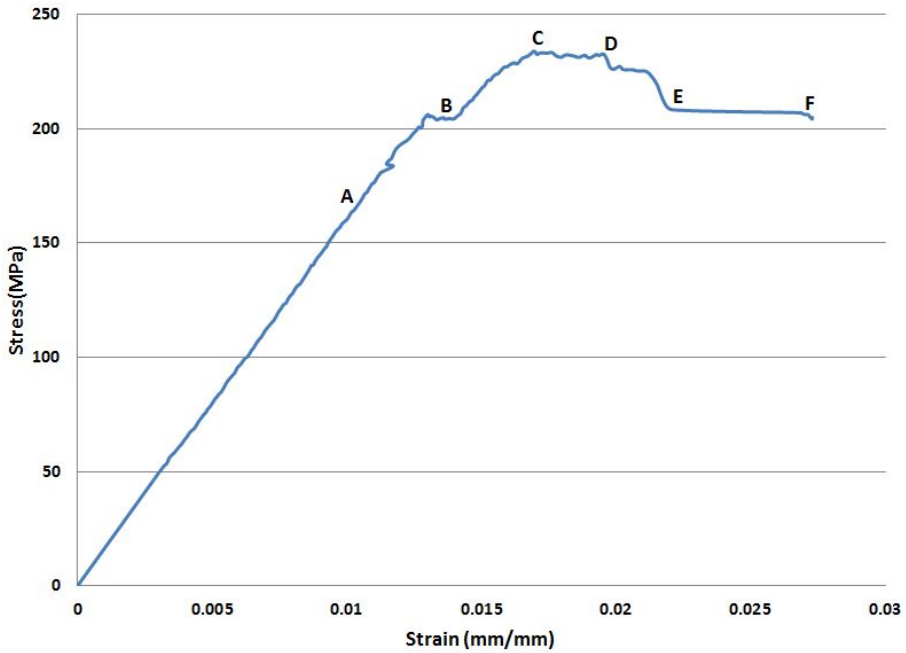

Figure 6.24: Progressive plot.

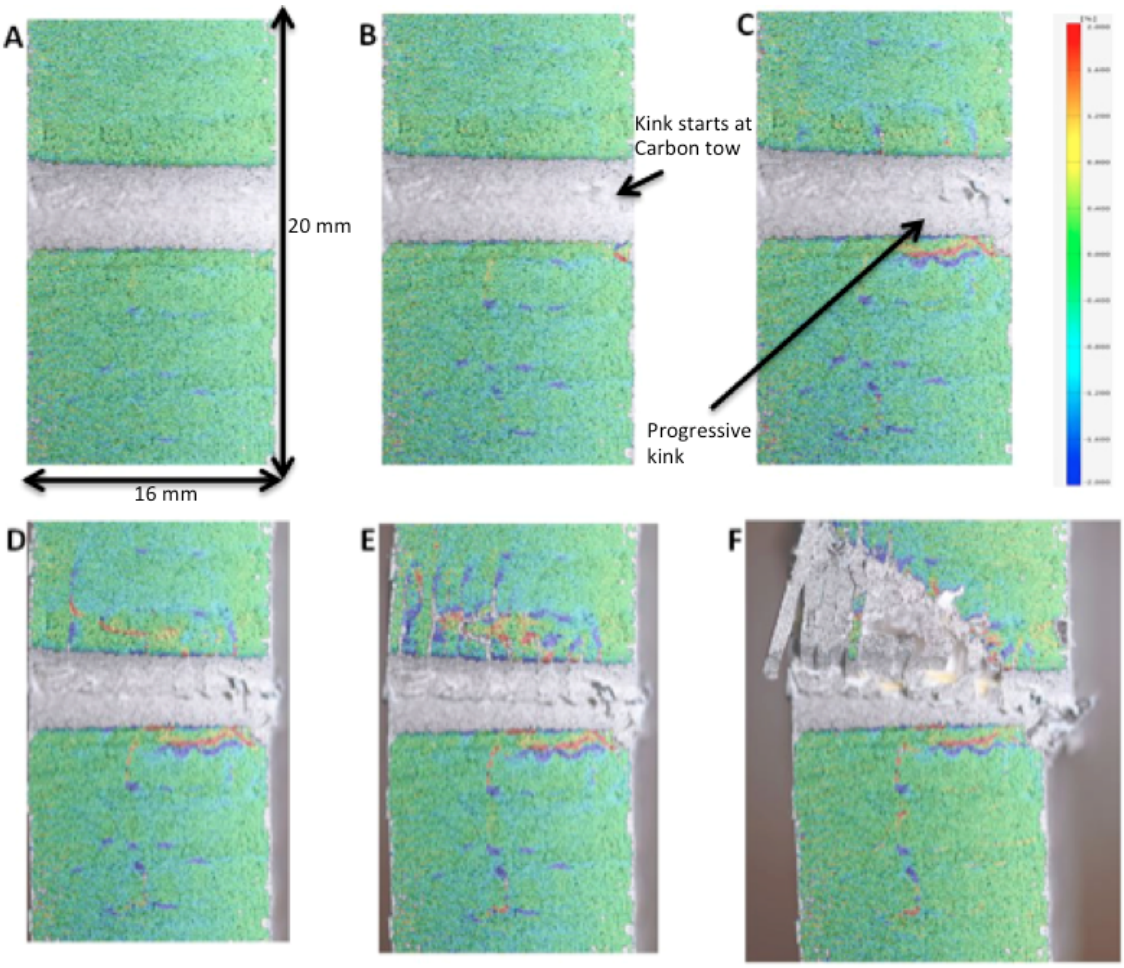

Figure 6.25: Progressive damage events during test - view of notch side. Note the markings in the figures indicating where kinking starts.

6.7.2 Micro-CT study of failed specimen

The matrix cracking is clearly observed in the DIC results, as shown in Figure 6.25. The surface strain contours show the area of strain localization due to the textile architecture, indicating the location that the matrix materials start to crack. The post-peak failure response from the experimental results indicate that, there is a single wide kink band formation through thickness and the specimen slips at certain characteristic angle during the final failure, which is evident from the visual inspection of the failed specimen shown in Figure 6.26.

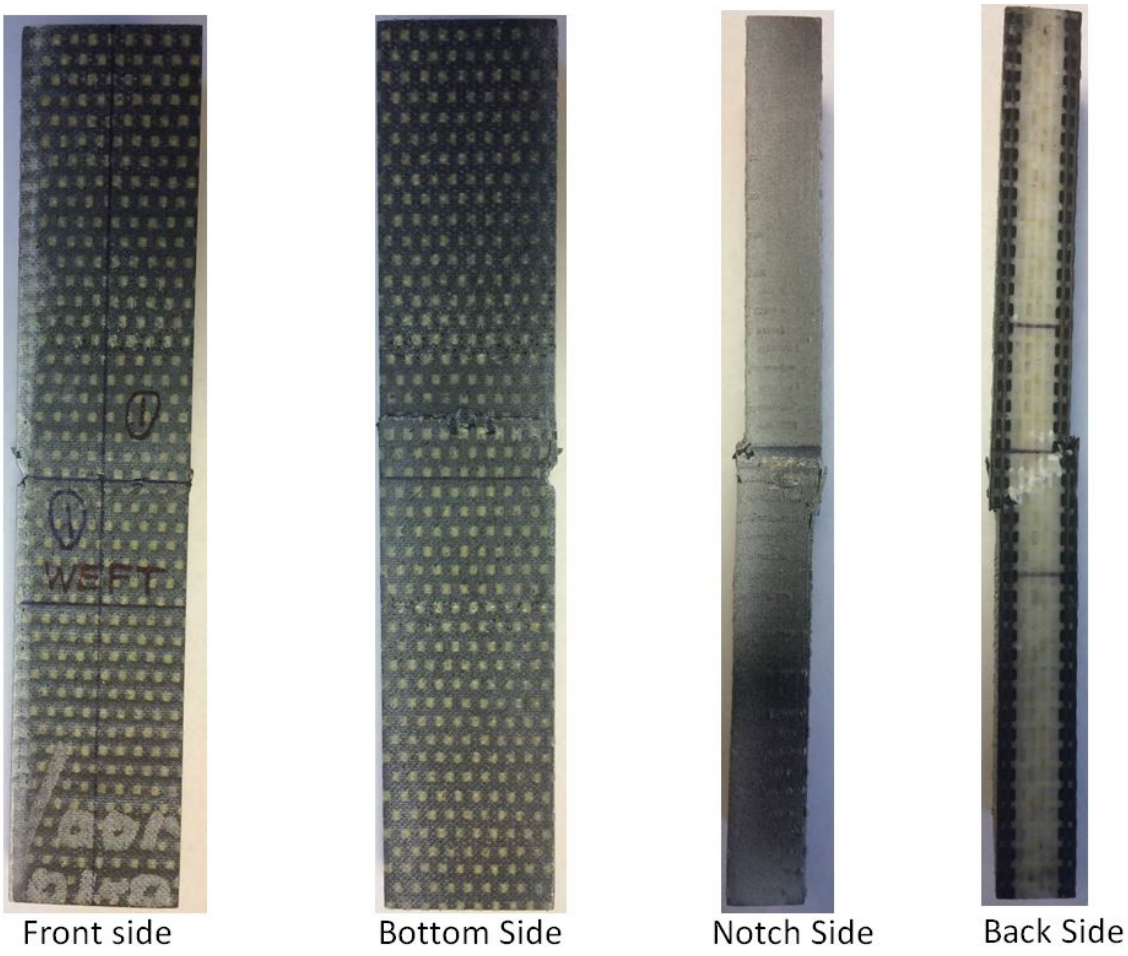

Figure 6.26: Test-3 failed specimen.

The damage events exhibited in the experiments are consistent for all the 5 tests. The kink band is formed at a slip angle of approximately 40^0-45^0 from front to back surface, across the thickness of specimen. Test-3 failed specimen is studied under Micro-CT to measure the kink band angle and the 2D image of the mid plane is shown in Figure 6.27. Also, cross-sectional images are taken from the side surface of the specimen, as shown in Figure 6.28, which clearly indicates the presence of a distinct transverse crack across the width and the mid plane fiber tows are misplaced due to slip.

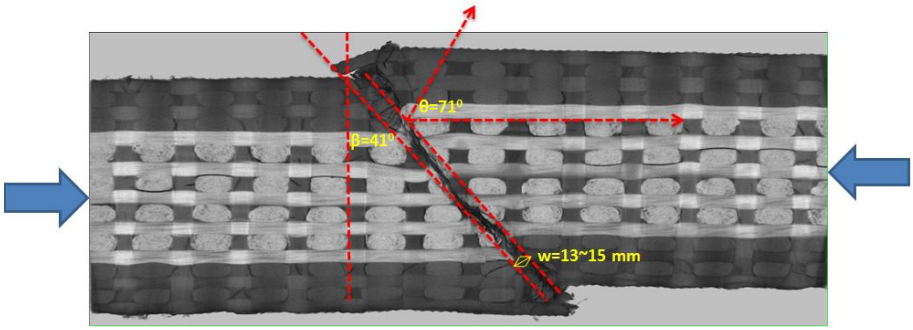

Figure 6.27: Measurement of kink band angle from Micro-CT study.

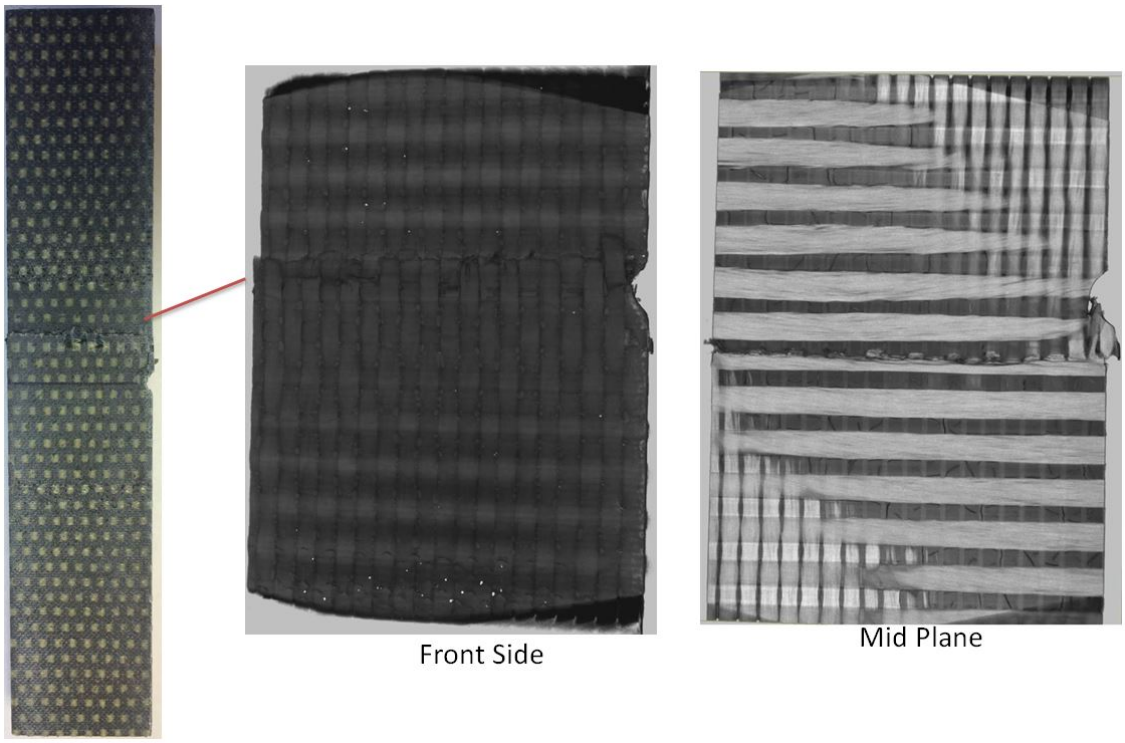

Figure 6.28: Micro-CT study of failed specimen.

6.8 Computational results

Stress-starin response, linear elastic moduli, compressive strength and failure strains have been experimentally determined in previous Section 6.7. The compressive test simulations are carried out for Model-I (Idealized perfect model with no imperfections) and Model-II (Imperfect model with in-situ geometric imperfections) simultaneously in weft direction for 'Thick Symmetric' configuration described earlier. The RVE

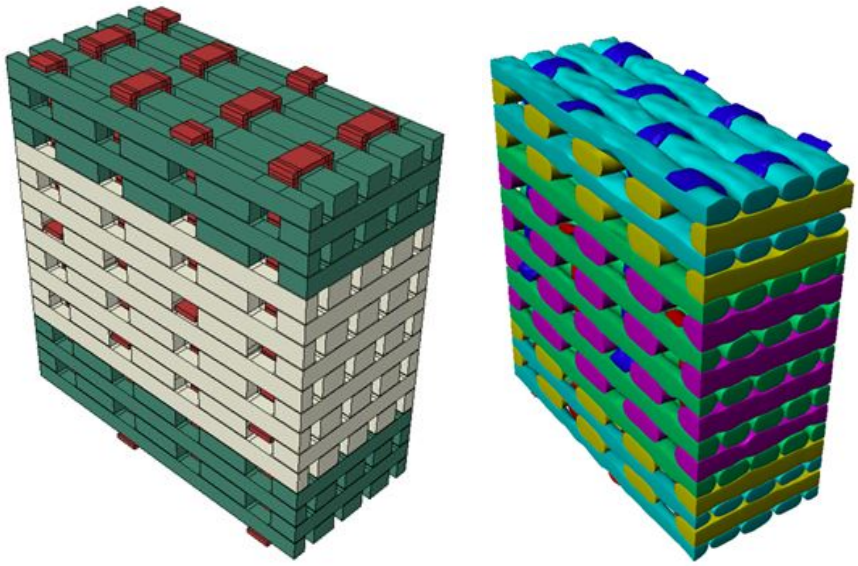

(a) Perfect RVE (b) Imperfect RVE

Figure 6.29: Meso-scale RVE of Thick Symmetric configuration (a) Model-I & (b) Model-II.

scale simulation results are compared with the experimental results and summarized in the following sections.

6.8.1 Single RVE compression test

Three dimensional (3D) geometry models of meso-scale RVE (Model-I and Model-II) are shown in Figure 6.29 for Thick Symmetric hybrid configuration and the finite elements are generated using ABAQUS 6.12. The Model-I had nearly 79,000 elements and took 5 hours to run on a high performance computing system using 64 CPUs, whereas, Model-II had nearly 590,000 elements and took 7 hours to run on the same computing system using 64 CPUs.

6.8.1.1 Elastic and strength properties

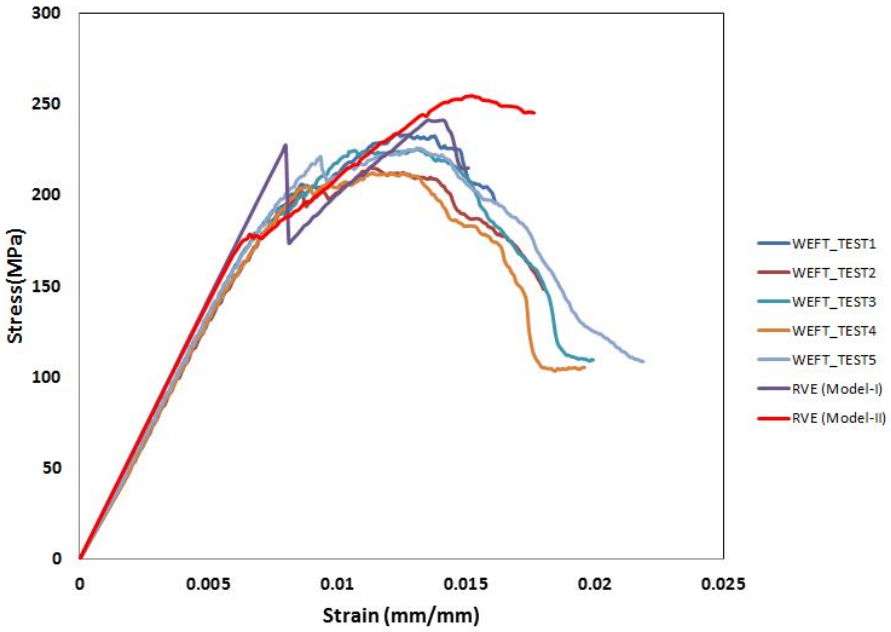

Figure 6.30: Macroscopic stress vs. strain response comparing the different models.

Considerable gradual linear growth of the elastic moduli under loading in the weft direction is observed for strains from 0.1% to 0.7% for both the models (Model-I and Model-II) (Figure 6.30). For Model-I, the linear growth continues upto 0.9% and there is a sudden drop in load, whereas, the linear growth is followed by a slow gradual reduction of the moduli with further increase of strains in the case of Model-II. The 'non-linear' behaviour is attributed to a combination of matrix microdamage and fiber kinking. The fiber kinking appears to be a major cause contributing more to the modulus versus strain variations. The stress-strain response, as shown in Figure 6.31(a), exhibits a higher degree of linearity due to the assumption of straight fiber tows and no imperfections. The Model-II shows more of a progression in failure of the material as shown in Figure 6.31(b) and deviations from linearity occur relatively early in the loading regime. However, due to the fact that different fiber tows will have different stresses at the same externally applied displacement indicates that the carbon may kink earlier than the glass and the failure envelope is progressive due to the hybrid materials before global kinking behavior. Numerical predictions using the two-scale multiscale method showed excellent agreement with experimental data for compressive elastic modulli in the case of idealized perfect geometry with no imperfections (Model-I). The matrix in-situ non-linear shear properties have little

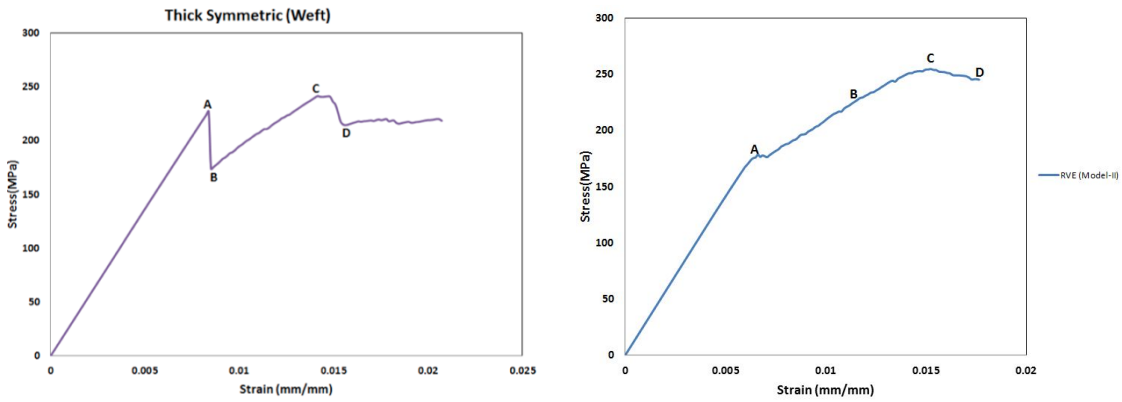

(a) Model-I (b) Model-II

Figure 6.31: Progressive plots for different models.

Table 6.6: Stiffness comparison between Experiment and Simulation results.

$EffectiveModulus$	$Experiment$ (GPa)	$Simulation(Model-I)$ (GPa)	$Simulation(Model-II)$ (GPa)
Weft	$28.7 \pm 3.58\%$	28.6	28.2

influence on the macroscopic non-linear response of Model-I. After including the in-situ geometrical imperfections and the fiber crookedness in the FE model (Model-II), the predicted elastic moduli reduced the respective Model-I values by only 1.2%. As we can see, there is a reduction in stiffness after including the geometric imperfections. For this hybrid configuration, the stiffness comparison is summarized in Table 6.6.

The weft-direction compressive strength was found to be 241.6 MPa as reported in Table 6.7 for Model-I; In Model-II, because of the imperfections of fiber alignment in both in-plane and thickness directions, there is significant fiber tow kinking observed in axial tows. The predicted compressive strength increased the respective Model-I values (254.7 MPa) by only 5.4%. As observed, there is a rise of compressive strength after including the geometric imperfections and predictions are closer to the experimental values. The global response tends to be highly nonlinear and correlates well with experimental results for Model-II as shown in Figure 6.30, which demonstrates the effect of including manufacturing induced imperfections in the progressive damage and failure analysis of these textile composites.

6.8.1.2 Progressive damage during quasi-static compressive loading

The multiscale methodology described in Sections 6.4 and 6.5, which combine modeling pre-peak nonlinearity using the NCYL secant stiffness method and the post-peak

Table 6.7: Strength comparison between Experiment and Simulation results.

$Ultimatestrength$	$Experiment$ (MPa)	$Simulation(Model-I)$ (MPa)	$Simulation(Model-II)$ (MPa)
Weft	238.8	241.6	254.7

strain softening response using Smeared crack approach (SCA), are used together to conduct a thorough investigation of the damage and failure mechanisms in the hybrid textile composite under consideration. The progressive damage and failure responses of textile RVE in weft direction subjected to uniaxial quasi-static compressive test are shown in Figures 6.32 and 6.33 for Model-I and Model-II respectively. In these figures, the progressive failure status at different percentages of the compressive strength ('A', 'B', 'C' and 'D') are shown as the contour plots of progressive failure flags for both fiber tows elements going through kinking failure and the matrix elements satisfying Mohr-Coulomb's compression failure criteria.

The damage in these composites starts near the location of Z-fiber tows and at the edges of the in-plane fiber tows oriented transversely to the loading direction. Due to this reason, there is significant amount of local disbonds and matrix cracking occuring in the matrix pocket, as shown in Figure 6.32. This failure event leads to development of matrix cracks inside the axial fiber tows during the progressive loading process and followed by fiber tow kink in the axial direction at a very late stage of loading. Carbon fiber tows kink first at both top and bottom layers that cause the first load drop. There is progressive kinking happening afterwards in the middle glass fiber tows and the global kink angle slowly becomes prominent. The fibers in the kink zone can still carry load and there is a rise in load deflection plot again after the first load drop. When there is significant amount of fiber kink and the matrix failure around it, the structure looses its load carrying capability and there is a major load drop, named as 'compressive' failure. In the post-peak regime, a single macroscopic visible kink band is formed along the thickness direction, as seen in Figure 6.32(d), which also resembles the failed specimens from the experiments.

Damage initiation and evolution are investigated numerically using the NCYL multiscale framework and the matrix microdamage model based on J2-deformation theory of plasticity. Previous experimental studies [72] discuss the damage progression in 3D woven composites due to compressive loading, in a detailed manner, which correlates well with the sequence of damage events captured with our propsed model. We have implemented the physics of fiber kinking failure mode in smeared carck code and captured the kinking behavior. Our modeling and analysis of RVE includes in-situ

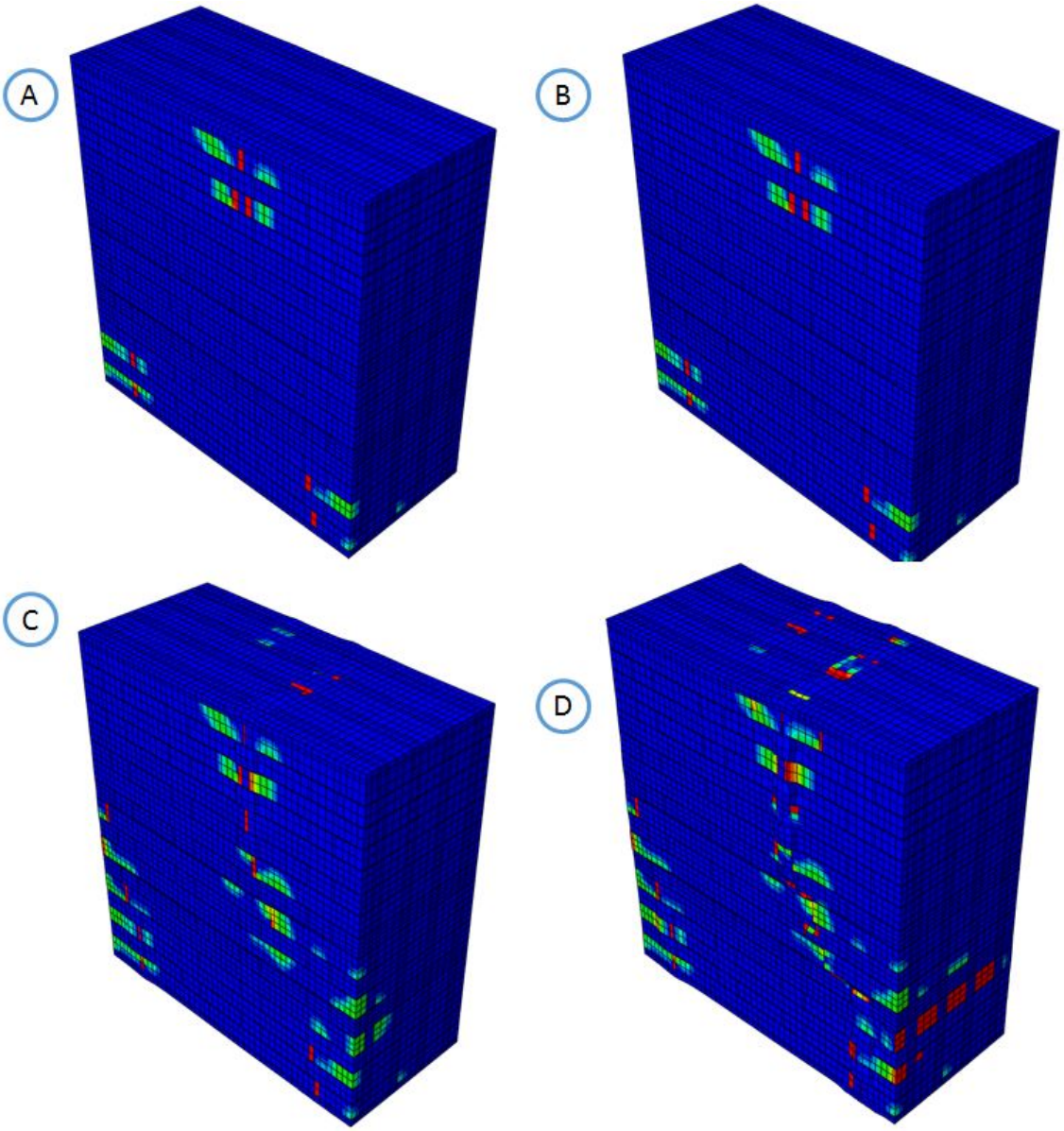

Figure 6.32: Fiber kinking progressive plots for single RVE (Model-I).

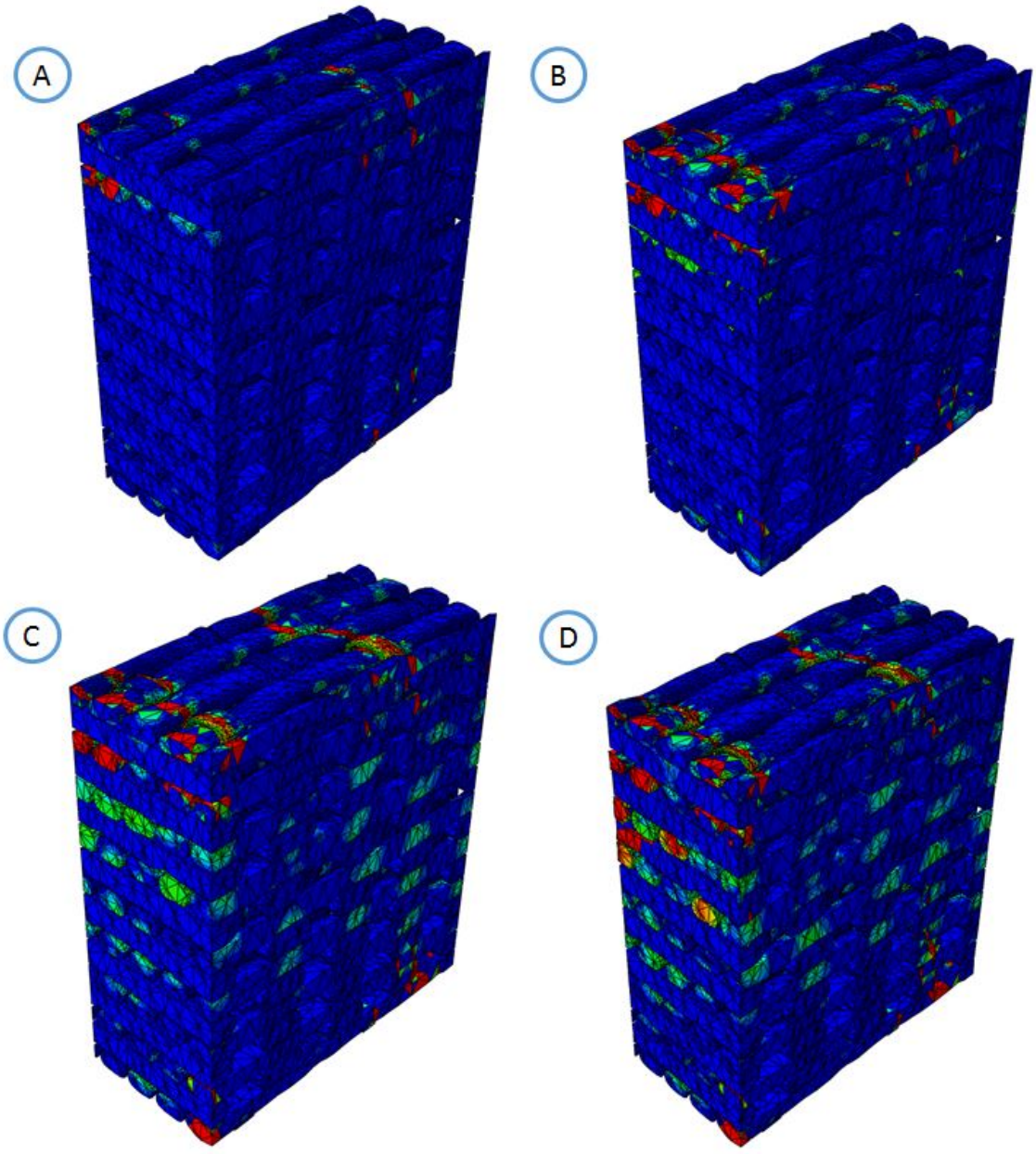

Figure 6.33: Fiber kinking progressive plots for single RVE (Model-II).

geometric imperfections and the predicted simulation results match closely with the sequence of damage events observed in experiments. The matrix compression failure mode is implemented using the Mohr-Coulomb's failure initiation criterion combined with 3D isotropic smeared crack code. Cohesion strength and the angle of friction are the inputs used for this research, where the initial Cohesion strength is assumed constant with variation of plastic strain of matrix. The present matrix compression model can be improved by establishing the experimental data for compression test of matrix, where the Cohesion strength variation with respect to the plastic strain of matrix can be studied and used as input to the computational model, which will be the focus of future work.

Overall, both the FE model results show a good prediction for the elastic stiffness. Also, the model, that include imperfections (Model-II) is able to capture the non-linear stress-strain response to a close extent. It is noted that this model includes real in-situ microstructure imperfections inside the RVE and the multiscale analysis is carried out to capture the progressive failure. The difference in global stress-strain responses, between the idealized perfect unit cell (indicated as a blue line) and the one with real in-situ microstructure imperfections (indicated as a red line) are visible in Figure 6.30. The real imperfections are measured at tow level from the Model-II and embedded in Model-I using the linear superposition of eigen buckling modes. The detailed procedure of modeling the imperfections in the perfect RVE and the sensitivity analysis with respect to carbon and glass fiber tow compressive strength are described in Appendix H.

6.8.2 Multiple RVEs compression test

Compression test specimens of suitable dimensions are to be decided based on the number of RVEs, which should be computationally efficient to run the simulations and capture the main features of the progressive damage and failure characteristics. Nine RVEs (3x3) are assembled in both warp and weft directions and studied for uniaxial compression test simulations using the multiscale analysis approach described earlier. A breakdown of 3x3 RVEs for Thick Symmetric (2.5D) woven textile composite is shown in Figure 6.34 for illustration.

The 9RVEs model has 716650 elements and provides a similar mesh density to the initial model used for single RVE. All of the constituent level material properties described earlier are used in this model again and the same boundary conditions are implemented that were imposed on the single RVE. The global stress-strain response

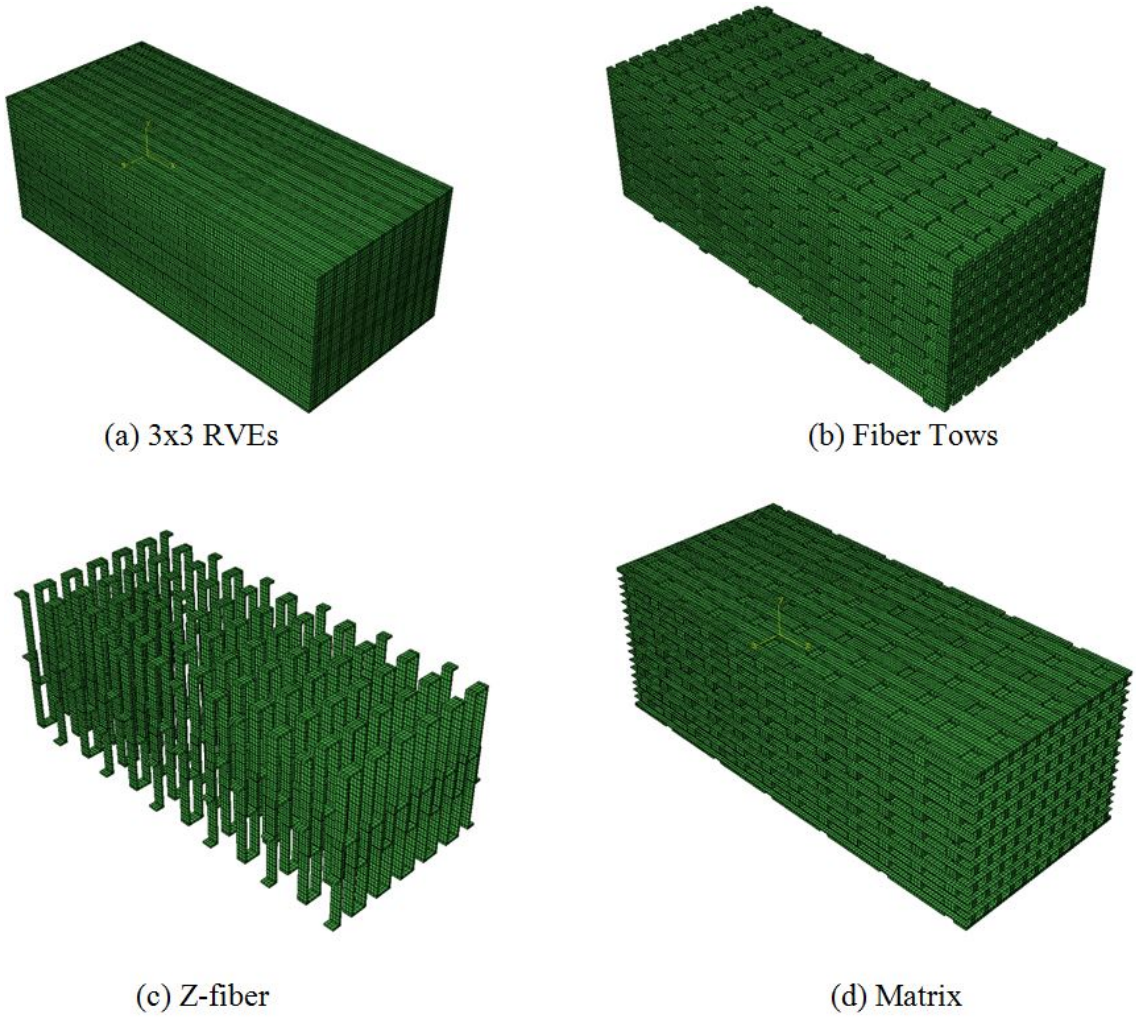

Figure 6.34: Breakdown of components for 9RVEs.

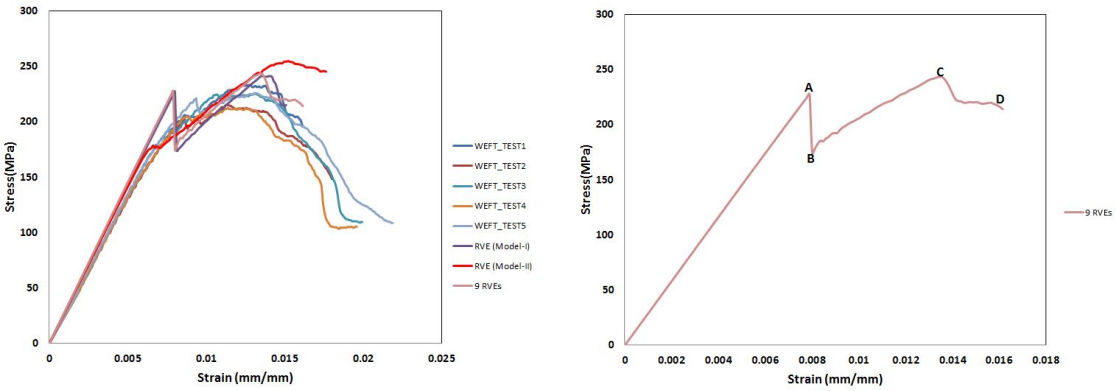

(a) Stress vs. strain plot

(b) Progressive plot

Figure 6.35: Macroscopic stress vs. strain response comparing the different models.

is shown in Figure 6.35(a) for weft direction, which correlates well with the single RVE results. Also, the progressive damage and failure response of the 9RVEs subjected to uniaxial compression loading is shown in Figure 6.36. In these figures, the progressive failure status at various points ('A', 'B', 'C' and 'D') of the stress-strain history are shown as the contour plots of progressive failure flags for both fiber tows elements going through kinking failure and the matrix elements satisfying Mohr-Coulomb's compression failure criteria.

The 9RVEs simulation is carried out to understand the size effect by a combination of multiple RVEs in comparison to single RVE results. The progressive failure response from both models, namely, (1) Perfect RVE with no imperfections (Model-I) were compared to (2) Imperfect RVE with in-situ geometric imperfections in Section 6.8.1 to demonstrate the effect of including geometric imperfections on the compressive behavior of the textile composite.

6.8.2.1 Elastic and strength properties

The linear elastic stiffness of 9RVEs textile architecture matches well to the single RVE and experimental results in weft direction. The in-situ non-linear matrix shear properties have very little influence on the macroscopic non-linear stress-strain behavior for 9RVEs, as was shown previously in the single RVE Model-I results. The predicted compressive strength for this simulation is in good agreement with the experiments and single RVE simulations.

The progression of matrix cracking and the fiber kinking are somewhat similar to the failure mechanisms observed in the case of single RVE. Carbon fiber tows kink first at both top and bottom layers that cause the first load drop and there is

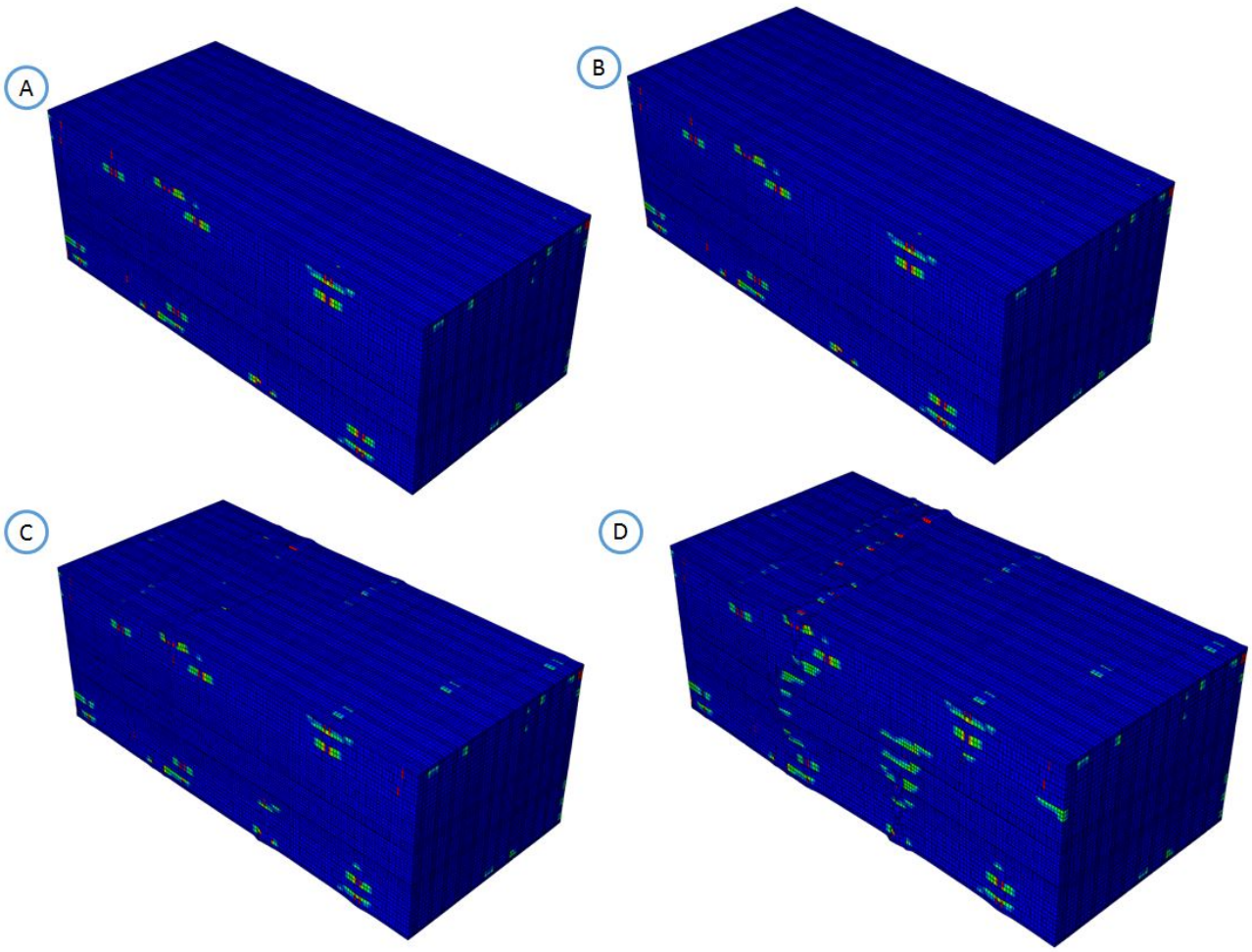

Figure 6.36: Fiber kinking progressive plots for 9RVEs.

progressive kinking happening afterwards in the middle glass fiber tows. After the first load drop, the fibers in the kink zone still have residual load carrying capacity, that causes the rise in load-deflection plot before there is a major load drop causing structural failure. The kink angle is similar, except the fact that mutiple visible kink bands are developed, as seen in Figure 6.36(d), in stead of single major kink band observed in single RVE. The predicted global strength and stiffness are unaffected by the formation of multiple kink bands, and hence provide a scope for investgation of multiple kink band formations in the unnotched coupon and bring out the size effect on fiber kinking failure mechanisms.

Overall, the main objective of this research is achieved by establishing a multiscale method, which is capable of predicting the certain aspects of experimental results like, effective linear elastic stiffness and compressive failure strength of Hybrid 3D woven textile composites. These results clearly indicate that the geometric imprefections of the fiber tows have a great impact on the non-linear behavior of the composites and must be included in the coupon level simulation. Even though the predicted compressive strength for single RVE and 9RVEs are within good agreement of experimental results, the global nonlinear stress-strain response and the kinking behavior can be studied by including the geometric imprefections in the simulation of the notched coupon, which is explained in the following section.

6.9 Multi-scale modeling of notched coupon (Macro-meso-micro scale)

The complex multi-phase material systems of 3D woven textile composites are modeled in three scales, (1) the homogenized macro scale, (2) the tow/matrix meso scale and (3) the fiber/matrix micro scale. Figure 6.37 presents the framework of the multi-scale method of 3D textile composites adopted here for the finite element (FE) modeling and progressive failure analysis. The far field non-failure region (indicated 'A') is defined with homogenized elastic orthotropic properties extracted from meso-scale RVE using periodic boundary conditions for computational efficiency. These hybrid textile configurations are non-periodic in the thickness direction and hence, periodic boundary conditions are excluded in that direction for analysis. The detailed procedure of the meso-scale modeling is discussed in the previous sections. The failure prone notched gauge region (indicated 'B') is defined as a collection of periodic multiple RVEs in both length and width directions of the coupon. The schematic diagram

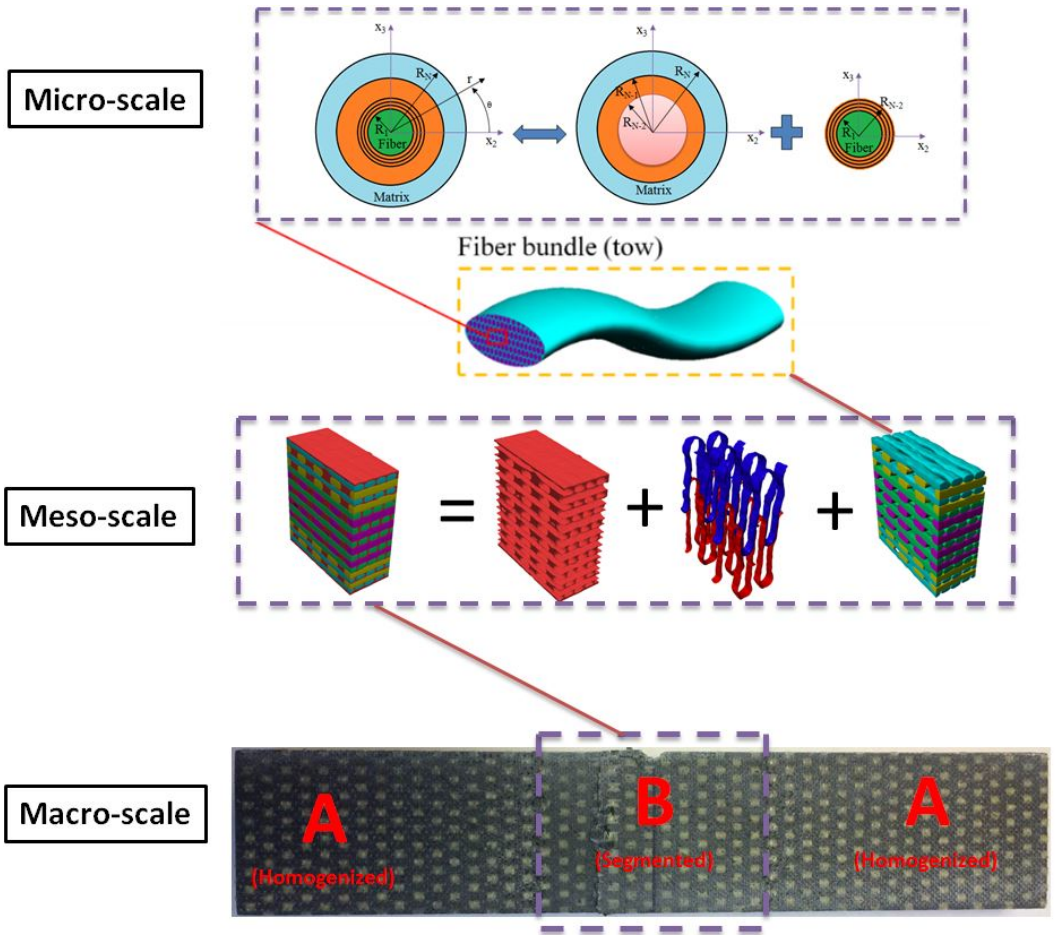

Figure 6.37: Frame work of the multi-scale model of 3D woven textile composites.

of the compression notched coupon with indicated regions 'A' and 'B' and physical dimensions are shown in Figure 6.38. The meso RVEs define the internal structures of the weave and consist of fiber tows running in all three directions inside the matrix pocket. The fiber tows are modeled explicitly and are related to the micro-scale analysis of fiber/matrix constituents through an analytical micromechanics N-layer concentric cylinder (NCYL) model. The homogenized mechanical properties of the fiber tows are calculated through the NCYL model and the tow composite strain at each integration point of the finite element model is related to the analytical strain field of the fiber/matrix cylinders in the micro-scale through a 6x6 transformation matrix.

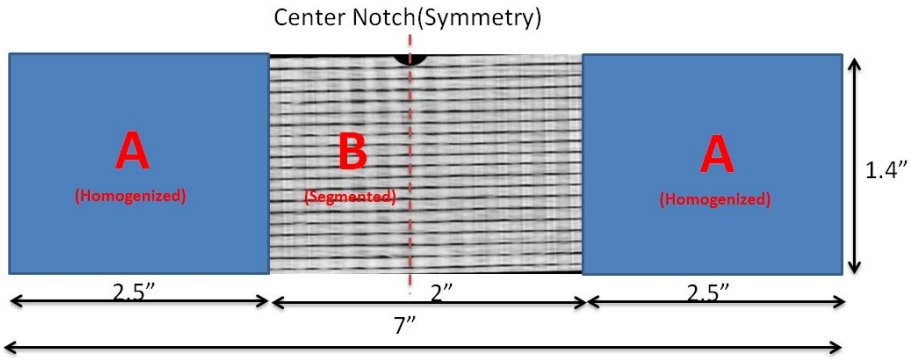

Figure 6.38: Geometric dimensions of the notched compression coupon.

6.9.1 Geometry and finite element modeling of coupon

As damage and failure initiation mechanisms are highly sensitive to the internal structures of the weave and the distribution of local imperfections, the waviness and crookedness of the fiber tows are modeled explicitely using the in-situ micro-CT scanned data. A micro-CT study is conducted for the entire coupon and the 3D geometry model is generated directly from the scanned image data using a tool called 'Simpleware'. Figures 6.39 and 6.40 explain the workflow of the coupon geometry modeling and the mesh generation method for the Thick Symmetric configuration and similar procedure is followed for other two configurations.

The fiber tows run in all three orthogonal directions inside the matrix pocket and the undulation of the fiber tows leave behind thin-layered of matrix in between tows, which makes it extremely difficult to model in 3D CAD and generate a finite element mesh for failure analysis. The novelty of this approach is to include the real in-situ imperfections for progressive failure analysis at the entire coupon level, as demonstrated in Figure 6.41 for Thick Symmetric hybrid architecture. The gauge region is designed and modeled in such a way that, at least 3 RVEs are included across width and length directions of the coupon.

6.9.2 Coupon analysis results

Uniaxial compression test boundary conditions are applied to the numerical coupon model, as shown in Figure 6.42. One end is constrained from all degrees of freedom and displacement loading is applied on the opposite end in axial direction. The clamped faces are constrained to move in transverse directions and only allowed in axial direction. The notch-side and the back surface are allowed to move freely, as observed in the experiments. Figure 6.43 shows the comparison of the global stress

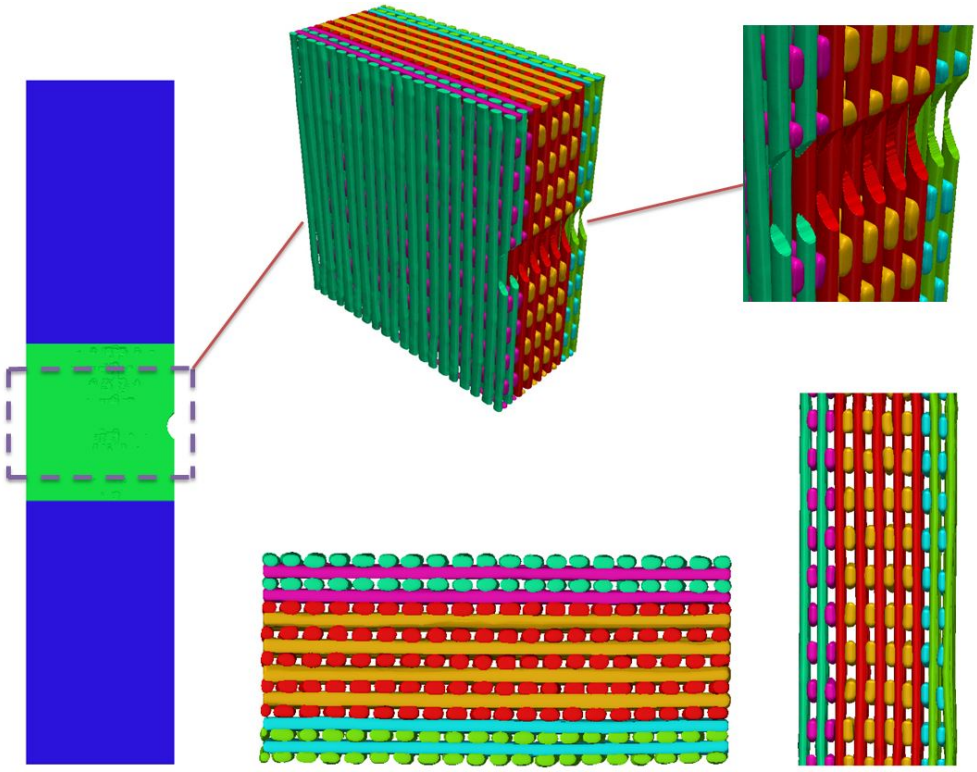

Figure 6.39: Work flow of 3D geometry modeling of coupon.

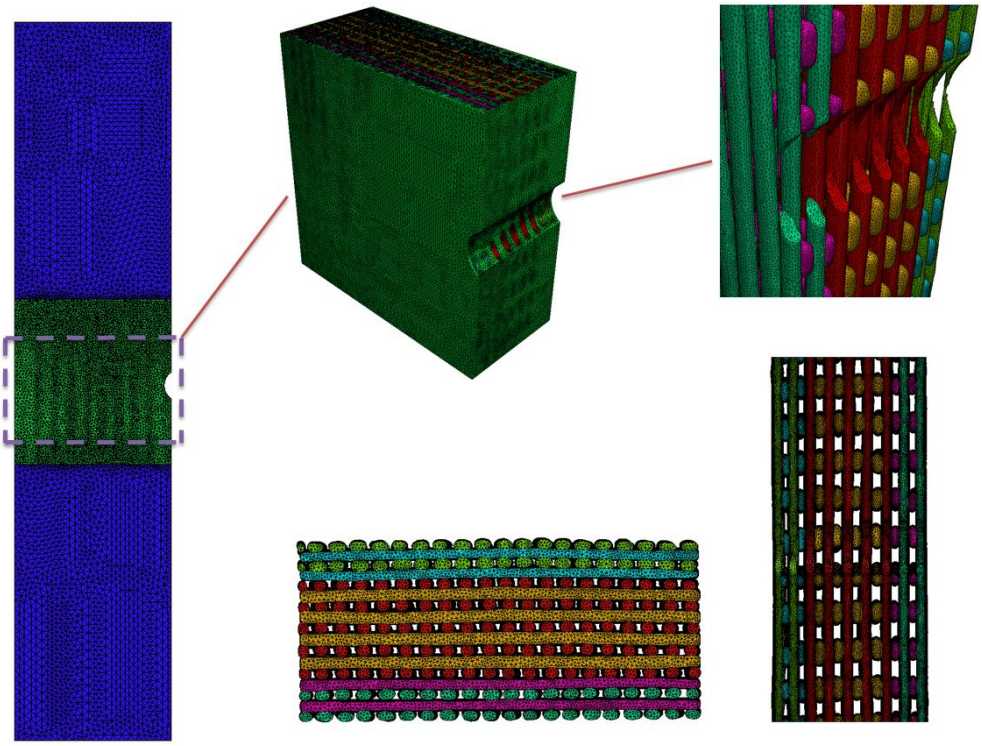

Figure 6.40: FE meshing of coupon including geometry imperfection.

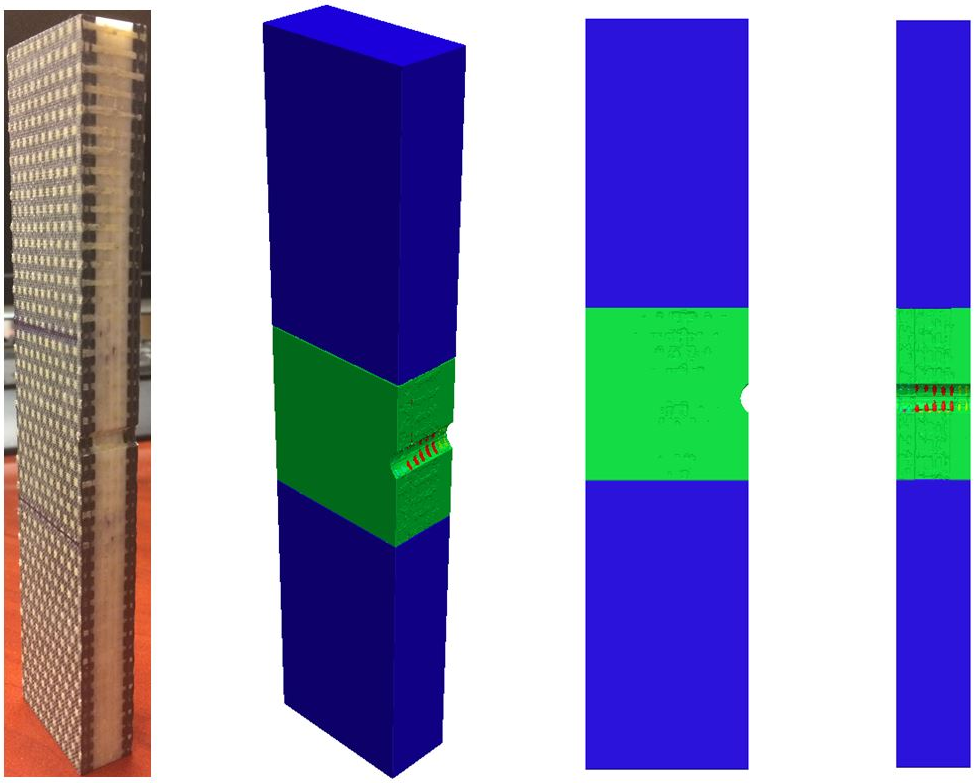

Figure 6.41: 3D geometry modeling of coupons including geometry imperfection.

versus strain response obtained from the coupon simulation with the experimental results, discussed in Section 6.7. Generally, the computational results are in good agreement with the experiment. The failure evolution in the fiber tow is illustrated by the absolute index values of the failure flag. The progressive damage and failure responses of textile coupon in weft direction subjected to uniaxial quasi-static compressive test are shown in Figure 6.44. In these figures, the progressive failure status at different percentages of the compressive strength ('A', 'B', 'C' and 'D') are shown as the contour plots of progressive failure flags for both fiber tows elements going through kinking failure and the matrix elements satisfying Mohr-Coulomb's compression failure criteria. Figures 6.45 and 6.46 show the final failure pattern of the coupon at the end of simulation in comparison with the failed specimen from the experiment.

The Thick Symmetric textile configuration is modeled at coupon level to determine the effect of hybridization and compute the effective stiffness and strength in compression for weft direction. A global-local modeling strategy is implemented using the three different length scales and the real in-situ microstructure imperfections are included in this study, obtained from micro-CT analysis. A subscale micromechanics

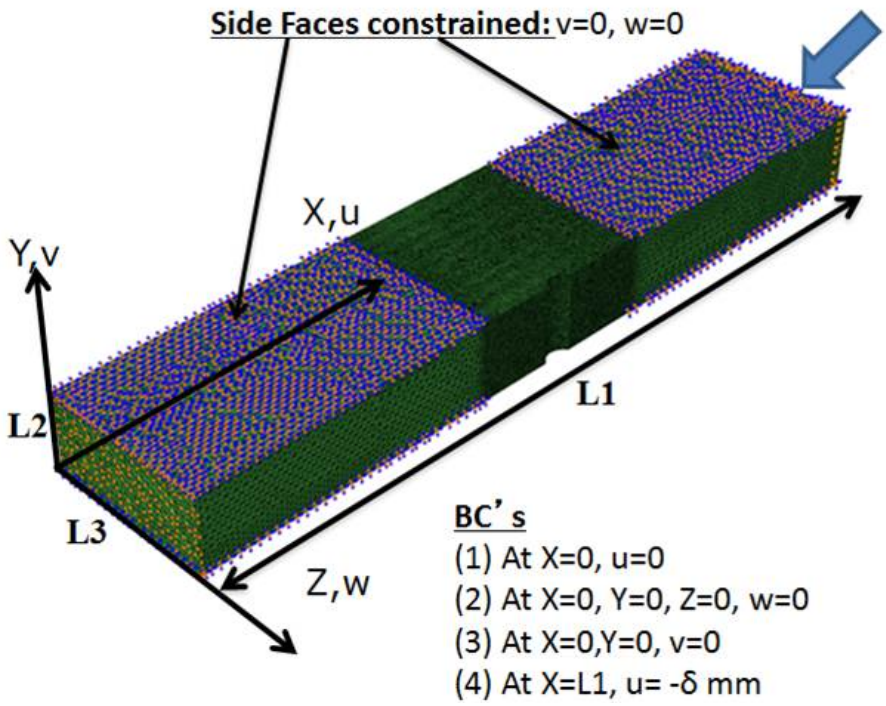

Figure 6.42: Boundary conditions applied to coupon simulation.

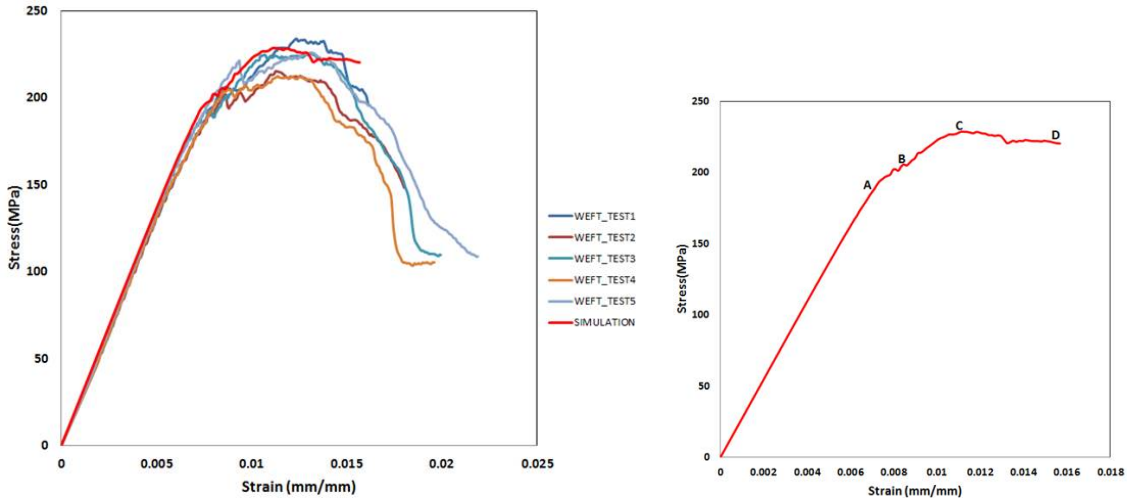

(a) Stress vs. strain plot

(b) Progressive plot

Figure 6.43: Simulation results comparing with experiments.

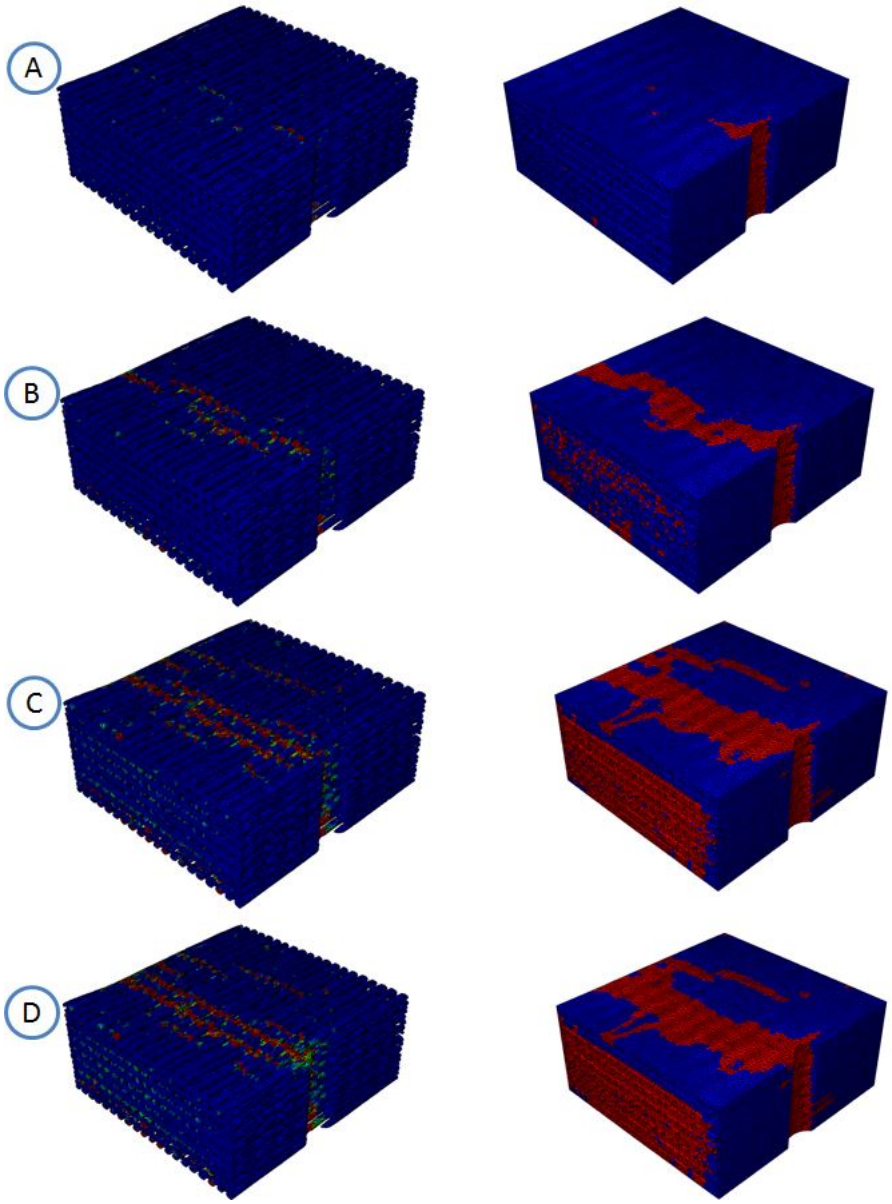

Figure 6.44: Progressive plots for the compression coupon simulation.

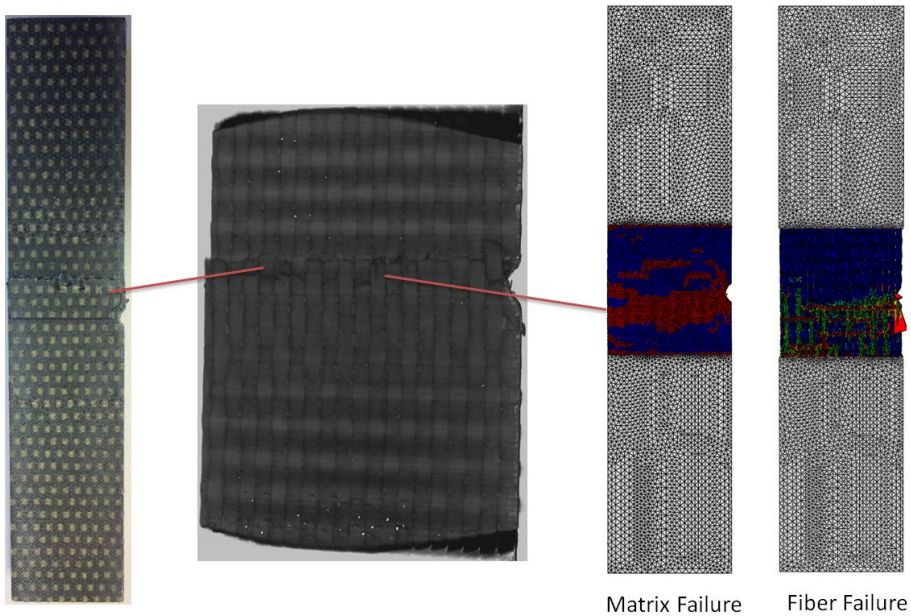

Figure 6.45: Final compressive failure of coupon at the side faces.

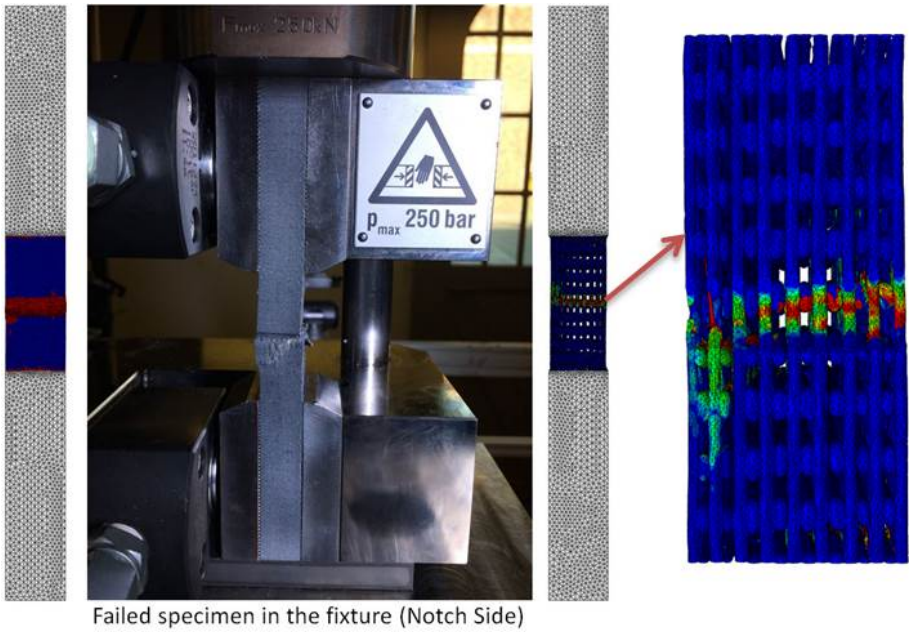

Figure 6.46: Final compressive failure of coupon at the notch side.

NCYL model is used to predict the effective nonlinear response of a homogenized fiber tow. The influence of matrix microdamage at the micro-scale manifests as the degradation of the effective fiber tow stiffness at the meso-scale through a secant moduli approach. Since, fully analytical solutions are utilized for the micromechanics analysis, the proposed method offers a lower computational cost and is suitable for large scale progressive damage and failure analysis of composite structures. The linear stiffness and strength of the textile architectures at coupon level are closely predicted compared to the RVEs and experimental results. The novelty of the approach lies in modeling the in-situ imperfections at the laboratory tested coupon level and carrying out the progressive damage and failure analysis in a multiscale framework, which enables of predicting the global response and the local complex failure mechanisms of 3D textile woven composites including the effects of hybridization.

6.10 Conclusions

In this work, Thick symmetric configuration of hybridized 3DWTCs are simulated for uniaxial compressive response to determine the effect of hybridization and compute the effective stiffness and strength in compression for weft direction. A micro-CT analysis is carried out to characterize in-situ microstructural geometric imperfections. This micro-CT analysis helps to extract essential inputs like dimensions of RVE, cross-sectional details of fiber tows in both warp and weft directions and volume fraction of pores. Based on these inputs, an idealized 3D geometry model of RVE is constructed. Furthermore, the micro-CT data is used in conjunction with a software tool, 'Simpleware', to generate a FE mesh that captures in-situ geometry, and providing a platform to carry out a 2-scale analysis on realistic imperfect RVEs. A subscale micromechanics 2CYL model, with an analytical solution at the sub-scale is used to establish a computational framework to predict the effective nonlinear response of 3DWTCs. The influence of matrix microdamage at the microscale manifests as the degradation of the effective fiber tow stiffness at the macroscale through a secant moduli approach. Since, fully analytical solutions are utilized for the subscale micromechanics analysis, the proposed method offers a lower computational cost and is suitable for large scale progressive damage and failure analysis of textile composite structures. The linear stiffness and strength of the textile architectures studied are predicted well when compared to experimental results. Quasi-static experimental results for compressive test of 3D woven composite materials are reported. The 3-scale modeling strategy adopted for the computational modeling of laboratory

scale coupon, which also includes the in-situ geometric imperfections from Micro-CT study, seems to capture most of the features of experimental results. The modeling strategy is unique and novel in the way that captures compressive response and the complex failure mechanisms, involved at fiber and matrix level. Also, the size effect study indicates the inadequacy of single RVE represenation to capture the multiple kink bands, although it can predict the compressive strength closely. Fiber tows crookedness and geometric imperfections play an important role for the compressive response of textile composites and must be included in the compuational modeling. The coupon level modeling was found to predict the compressive strength and kink band angle closely to the experimental results. The approach presented here can be used to understand and quantify the effects of hybridization and textile architecture on the compressive response of textile composites, in terms of constituent properties. Furthermore, the modeling framework can be used to quantify the effects of uncertain constituent properties on the overall response of textile composites, an essential task in an ICME (integrated computational materials engineering) of composites.

CHAPTER 7

Concluding Remarks

In this work, compressive response of 3DWTCs are studied experimentally and the entire laboratory scale coupon is modeled using the macro-meso-micro scale modeling strategy, which includes in-situ geometric imperfections from Micro-CT measurements. The modeling approach also includes single RVE and multiple RVE simulations to study the size effect on the compressive response of textile composites. The novelty of the modeling approach is to include the in-situ geometric imperfection at the coupon level simulation, as the compressive strength is seen to be sensitive to the fiber misalignment and other geometric imperfections in the structure. A detailed Micro-CT study of the failed specimens reveals the kink band angle and other damage mechanisms and fiber kinking in compressive failure. The Mohr-Coulomb criterion is implemented to model matrix compressive failure in combination with the smeared crack approach and a detailed micromechanics study is carried out to demonstrate mesh objectivity of the method. Tow compressive strength is sensitive to fiber misalignment angle, which has been shown using numerical simulations, alongside the study on the interaction between splitting and kinking failure mechanisms. Fiber kinking is driven by both geometric and material non-linearity in the matrix and splitting failure is seen to be a post-kinking failure mechanism irrespective of the misalignment angle of imperfection. The coupon level modeling was found to predict the compressive strength and kink band angle closely to the experimental results. Both single RVE and multiple RVE simulations predict the experimental compressive strength closely, even though the analysis indicates that a larger RVE develops multiple kink bands and the single RVE representation is inadequate to capture those effects. The laboratory specimen is scanned before the test and a geometric model is developed from the scanned image data using the tool 'Simpleware'. Hence, the coupon geometric model is the real replication of the test specimen with all the microstructure details.

The compression experimental results for Thick Symmetric configuration show

fiber tow kinking starts on the carbon side and propagates to glass tows in the middle with a rise in load. A significant amount of progressive kinking is observed. Finally, there is a large load drop when most fibers break within the kink band. The experimental results are used to develop and validate a multiscale computational model. The far field non-failure area at the ends of the coupon are homogenized and the center notch area is segmented with homogenized fiber tows within a matrix material. This center gage area is a collection of mesoscale RVEs, where each fiber tow is homogenized and modeled explicitly along with matrix. A similar modeling approach also used in the modeling of an unnotched dog-bone tensile coupon, as shown in Chapter 5. The experimental results from [26] are used to validate the tensile simulation results. Both RVE and coupon level modeling approach is followed for uniaxial tensile test simulations. Modeling in-situ geometric imperfections has an impact on the behavior of the structure and must be included in the progressive failure analysis, which is demonstrated in the tensile response. Also, the hybridization and the architecture has a great influence on the tensile response of 3DWTC, as provided with details, by comparing the three different textile configurations in previous chapters.

An image based modeling approach for textile composites is well established at both RVE and the entire coupon level. Imperfections in textile composites have been characterized and a Micro-CT study has been helpful to get inputs for geometric modeling. The fiber tow is modeled as macroscopically homogeneous and a 2-scale multiscale method is developed by introducing the NCYL micromechanics model at each integration point of the homogenized fiber tow. The 2-layer fiber-matrix concentric cylinder is extended to any number of discretized matrix layers for a fixed volume fraction and all the stress and strain information are obtained in a closed form. The matrix microdamage and the tow pre-peak non-linearity are modeled using a secant stiffness approach in conjunction with J2-deformation theory of plasticity for the matrix material. The matrix in-situ non-linear properties are extracted from coupon level tests and can be calculated for any 'N' in general. The post-peak strain softening behavior is modeled using the smeared crack approach (SCA) and various fiber and matrix failure modes are included in this research. It is concluded that a nine RVE representation and a single RVE representation are adequate to establish the compressive strength of 3DWTCs, within 5% of the peak values that are obtained for the whole coupon modeling of an imperfect (real) microstructure specimen and the experimental results. Furthermore, the same model is also seen to predict the tensile strength accurately. The results in Appendix H on the RVE compressive strength

suggests that carbon fiber compressive strength dictates the initiation of kink banding failure while the glass fiber tow compressive strength dictates the maximum load sustainable. Thus, this important finding suggests how progressive failure occurs and how different aspects of the compressive response is related to constituent structural properties. It is noted that each tow strength is related to fiber misalignment within a tow and the matrix nonlinear shear response. These conclusions as shown in Appendix H have been obtained by studying an RVE that has tow undulations which are bounded by the measured values, where the measurements are summarized in Appendix G.

A validated computational multiscale framework as established in this thesis is very useful in design iterative studies of various textile architectures for structural applications where damage tolerance and strength allowables dictate the boundaries of the design envelope.

APPENDIX A

Transformations between Cartesian and Cylindrical Coordinates

It is convenient to formulate the concentric cylinder model in cylindrical coordinates $(x - r - \theta)$, and the resulting strains are transformed to Cartesian coordinates $(x_1 - x_2 - x_3)$ through,

$$\begin{aligned}
\epsilon_{11} &= \epsilon_{xx} \\
\epsilon_{22} &= \epsilon_{rr}\cos^2\theta + \epsilon_{\theta\theta}\sin^2\theta - \gamma_{r\theta} sin\theta\cos\theta \\
\epsilon_{33} &= \epsilon_{rr}\sin^2\theta + \epsilon_{\theta\theta}\cos^2\theta + \gamma_{r\theta} sin\theta\cos\theta \\
\gamma_{12} &= \gamma_{xr}\cos\theta - \gamma_{x\theta}\sin\theta \\
\gamma_{13} &= \gamma_{x\theta}\cos\theta + \gamma_{xr}\sin\theta \\
\gamma_{23} &= 2(\epsilon_{rr} - \epsilon_{\theta\theta})\sin\theta\cos\theta + \gamma_{r\theta}(\cos^2\theta - \sin^2\theta)
\end{aligned} \tag{A.1}$$

APPENDIX B

Formulations for the Extended Generalized Self-Consistent Method

The stresses can be derived from the Airy's stress function as shown in Timoshenko and Goodier [26] as,

$$\begin{aligned} \sigma_{rr} &= \frac{1}{r}\frac{\partial \phi}{\partial r} + \frac{1}{r^2}\frac{\partial^2 \phi}{\partial \theta^2} \\ \sigma_{\theta\theta} &= \frac{\partial^2 \phi}{\partial r^2} \\ \sigma_{r\theta} &= -\frac{\partial}{\partial r}\left(\frac{1}{r}\frac{\partial \phi}{\partial \theta}\right) \end{aligned} \tag{B.1}$$

and the strains are related to the displacements as,

$$\begin{aligned} \epsilon_{rr} &= \frac{\partial u_r}{\partial r} \\ \epsilon_{\theta\theta} &= \frac{1}{r}\frac{\partial u_\theta}{\partial \theta} + \frac{u_r}{r} \\ \gamma_{r\theta} &= \frac{1}{r}\frac{\partial u_r}{\partial \theta} + \frac{\partial u_\theta}{\partial r} - \frac{u_\theta}{r} \end{aligned} \tag{B.2}$$

where u_r and u_θ are radial and hoop displacements in polar coordinates. Since the displacements should be finite at $r = 0$, and the stresses must be bounded as $r \to \infty$, it follows that,

$$M_{N-1} = C_{N-1} = D_{N-1} = B_{N+1} = 0 \tag{B.3}$$

Using Airy's stress function in polar coordinates, the stresses for the layer '(N-1)' are,

$$\sigma_{rr}^{N-1} = H_{N-1} - A_{N-1}\cos 2\theta$$

$$\sigma_{\theta\theta}^{N-1} = H_{N-1} + \left[A_{N-1} + 6B_{N-1}\frac{r^2}{R_N^2}\right]\cos 2\theta \tag{B.4}$$
$$\sigma_{r\theta}^{N-1} = \left[A_{N-1} + 3B_{N-1}\frac{r^2}{R_N^2}\right]\sin 2\theta$$

the stresses for the layer 'N' are,

$$\sigma_{rr}^{N} = \frac{1}{2}M_N\frac{R_N^2}{r^2} + H_N + \left[-A_N - \frac{3}{2}C_N\frac{R_N^4}{r^4} - 2D_N\frac{R_N^2}{r^2}\right]\cos 2\theta$$
$$\sigma_{\theta\theta}^{N} = -\frac{1}{2}M_N\frac{R_N^2}{r^2} + H_N + \left[A_N + 6B_N\frac{r^2}{R_N^2} + \frac{3}{2}C_N\frac{R_N^4}{r^4}\right]\cos 2\theta \tag{B.5}$$
$$\sigma_{r\theta}^{N} = \left[A_N + 3B_N\frac{r^2}{R_N^2} - \frac{3}{2}C_N\frac{R_N^4}{r^4} - D_N\frac{R_N^2}{r^2}\right]\sin 2\theta$$

and the stresses for the layer '(N+1)' are,

$$\sigma_{rr}^{N+1} = \frac{1}{2}M_{N+1}\frac{R_N^2}{r^2} + H_{N+1} + \left[-A_{N+1} - \frac{3}{2}C_{N+1}\frac{R_N^4}{r^4} - 2D_{N+1}\frac{R_N^2}{r^2}\right]\cos 2\theta$$
$$\sigma_{\theta\theta}^{N+1} = -\frac{1}{2}M_{N+1}\frac{R_N^2}{r^2} + H_{N+1} + \left[A_{N+1} + \frac{3}{2}C_{N+1}\frac{R_N^4}{r^4}\right]\cos 2\theta \tag{B.6}$$
$$\sigma_{r\theta}^{N+1} = \left[A_{N+1} - \frac{3}{2}C_{N+1}\frac{R_N^4}{r^4} - D_{N+1}\frac{R_N^2}{r^2}\right]\sin 2\theta$$

According to the 2D plane-strain constitutive relations in Equation (2.24), the strains for the layer '(N-1)' are calculated as,

$$\epsilon_{rr}^{N-1} = \frac{1}{4G_{23}^{N-1}}\left\{2H_{N-1}\frac{G_{23}^{N-1}}{K_{23}^{N-1}} + \left[-2A_{N-1} + 6B_{N-1}\left(\frac{G_{23}^{N-1}}{K_{23}^{N-1}} - 1\right)\frac{r^2}{R_N^2}\right]\cos 2\theta\right\}$$
$$\epsilon_{\theta\theta}^{N-1} = \frac{1}{4G_{23}^{N-1}}\left\{2H_{N-1}\frac{G_{23}^{N-1}}{K_{23}^{N-1}} + \left[2A_{N-1} + 6B_{N-1}\left(\frac{G_{23}^{N-1}}{K_{23}^{N-1}} + 1\right)\frac{r^2}{R_N^2}\right]\cos 2\theta\right\} \tag{B.7}$$
$$\gamma_{r\theta}^{N-1} = \frac{1}{2G_{23}^{N-1}}\left[2A_{N-1} + 6B_{N-1}\frac{r^2}{R_N^2}\right]\sin 2\theta$$

the strains for the layer 'N' are,

$$\epsilon_{rr}^{N} = \frac{1}{4G^N}\left\{\left[M_N\frac{R_N^2}{r^2} + 2H_N\frac{G^N}{K_{23}^N}\right] + \left[-2A_N + 6B_N\left(\frac{G^N}{K_{23}^N} - 1\right)\frac{r^2}{R_N^2} - 3C_N\frac{R_N^4}{r^4}\right.\right.$$
$$\left.\left. - 2D_N\left(\frac{G^N}{K_{23}^N} + 1\right)\frac{R_N^2}{r^2}\right]\cos 2\theta\right\}$$

$$\epsilon_{\theta\theta}^{N} = \frac{1}{4G^{N}}\Bigg\{\Bigg[-M_N\frac{R_N^2}{r^2}+2H_N\frac{G^N}{K_{23}^N}\Bigg]+\Bigg[2A_N+6B_N\Big(\frac{G^N}{K_{23}^N}+1\Big)\frac{r^2}{R_N^2}+3C_N\frac{R_N^4}{r^4} - 2D_N\Big(\frac{G^N}{K_{23}^N}-1\Big)\frac{R_N^2}{r^2}\Bigg]\cos 2\theta\Bigg\} \tag{B.8}$$

$$\gamma_{r\theta}^{N} = \frac{1}{2G^{N}}\Bigg[2A_N+6B_N\frac{r^2}{R_N^2}-3C_N\frac{R_N^4}{r^4}-2D_N\frac{R_N^2}{r^2}\Bigg]\sin 2\theta$$

and the strains for the layer '(N+1)' are,

$$\epsilon_{rr}^{N+1} = \frac{1}{4G_{23}^{N+1}}\Bigg\{\Bigg[M_{N+1}\frac{R_N^2}{r^2}+2H_{N+1}\frac{G_{23}^{N+1}}{K_{23}^{N+1}}\Bigg]+\Bigg[-2A_{N+1}-3C_{N+1}\frac{R_N^4}{r^4} - 2D_{N+1}\Big(\frac{G_{23}^{N+1}}{K_{23}^{N+1}}+1\Big)\frac{R_N^2}{r^2}\Bigg]\cos 2\theta\Bigg\}$$

$$\epsilon_{\theta\theta}^{N+1} = \frac{1}{4G_{23}^{N+1}}\Bigg\{\Bigg[-M_{N+1}\frac{R_N^2}{r^2}+2H_{N+1}\frac{G_{23}^{N+1}}{K_{23}^{N+1}}\Bigg]+\Bigg[2A_{N+1}+3C_{N+1}\frac{R_N^4}{r^4} - 2D_{N+1}\Big(\frac{G_{23}^{N+1}}{K_{23}^{N+1}}-1\Big)\frac{R_N^2}{r^2}\Bigg]\cos 2\theta\Bigg\} \tag{B.9}$$

$$\gamma_{r\theta}^{N+1} = \frac{1}{2G_{23}^{N+1}}\Bigg[2A_{N+1}-3C_{N+1}\frac{R_N^4}{r^4}-2D_{N+1}\frac{R_N^2}{r^2}\Bigg]\sin 2\theta$$

Finally, the displacements can be calculated based upon the strain-displacement relations in Equation (A.1). The displacements for the layer '(N-1)' are,

$$U_r^{N-1} = \frac{R_N}{4G_{23}^{N-1}}\Bigg\{2H_{N-1}\frac{G_{23}^{N-1}}{K_{23}^{N-1}}\frac{r}{R_N}+\Bigg[-2A_{N-1}\frac{r}{R_N}+2B_{N-1}\Big(\frac{G_{23}^{N-1}}{K_{23}^{N-1}}-1\Big)\frac{r^3}{R_N^3}\Bigg]\cos 2\theta\Bigg\}$$

$$U_\theta^{N-1} = \frac{R_N}{4G_{23}^{N-1}}\Bigg[2A_{N-1}\frac{r}{R_N}+2B_{N-1}\Big(\frac{G_{23}^{N-1}}{K_{23}^{N-1}}+2\Big)\frac{r^3}{R_N^3}\Bigg]\sin 2\theta \tag{B.10}$$

the displacements for the layer 'N' are,

$$U_r^{N} = \frac{R_N}{4G^{N}}\Bigg\{\Bigg[-M_N\frac{R_N}{r}+2H_N\frac{G^N}{K_{23}^N}\frac{r}{R_N}\Bigg]+\Bigg[-2A_N\frac{r}{R_N}+2B_N\Big(\frac{G^N}{K_{23}^N}-1\Big)\frac{r^3}{R_N^3}+C_N\frac{R_N^3}{r^3} + 2D_N\Big(\frac{G^N}{K_{23}^N}+1\Big)\frac{R_N}{r}\Bigg]\cos 2\theta\Bigg\} \tag{B.11}$$

$$U_\theta^{N} = \frac{R_N}{4G^{N}}\Bigg[2A_N\frac{r}{R_N}+2B_N\Big(\frac{G^N}{K_{23}^N}+2\Big)\frac{r^3}{R_N^3}+C_N\frac{R_N^3}{r^3}-2D_N\frac{G^N}{K_{23}^N}\frac{R_N}{r}\Bigg]\sin 2\theta$$

and the displacements for the layer '(N+1)' are,

$$U_r^{N+1} = \frac{R_N}{4G_{23}^{N+1}}\Bigg\{\Bigg[-M_{N+1}\frac{R_N}{r} + 2H_{N+1}\frac{G_{23}^{N+1}}{K_{23}^{N+1}}\frac{r}{R_N}\Bigg] + \Bigg[-2A_{N+1}\frac{r}{R_N} + C_{N+1}\frac{R_N^3}{r^3} + 2D_{N+1}\Big(\frac{G_{23}^{N+1}}{K_{23}^{N+1}}+1\Big)\frac{R_N}{r}\Bigg]\cos 2\theta\Bigg\}$$

$$U_\theta^{N+1} = \frac{R_N}{4G_{23}^{N+1}}\Bigg[2A_{N+1}\frac{r}{R_N} + C_{N+1}\frac{R_N^3}{r^3} - 2D_{N+1}\frac{G_{23}^{N+1}}{K_{23}^{N+1}}\frac{R_N}{r}\Bigg]\sin 2\theta \qquad \text{(B.12)}$$

APPENDIX C

Flowchart of VUMAT for combined NCYL and SCA subroutines

The commercially available finite element software, ABAQUS (version 6.14), is used for the macroscale FEA, and the NCYL micromechanics model at the subscale is implemented at each integration point of the macro scale, using a user defined material subroutine, VUMAT. This subroutine is called at each integration point at each increment, and the material constitutive law is updated through user-defined options. At the start of each increment, the material state i.e. stress-strain and solution-dependent state variables from the previous equilibrium step and the strain increments in the current step are passed into the VUMAT through the ABAQUS solver. The algorithm of the main VUMAT subroutine is shown below in Figure C.1.

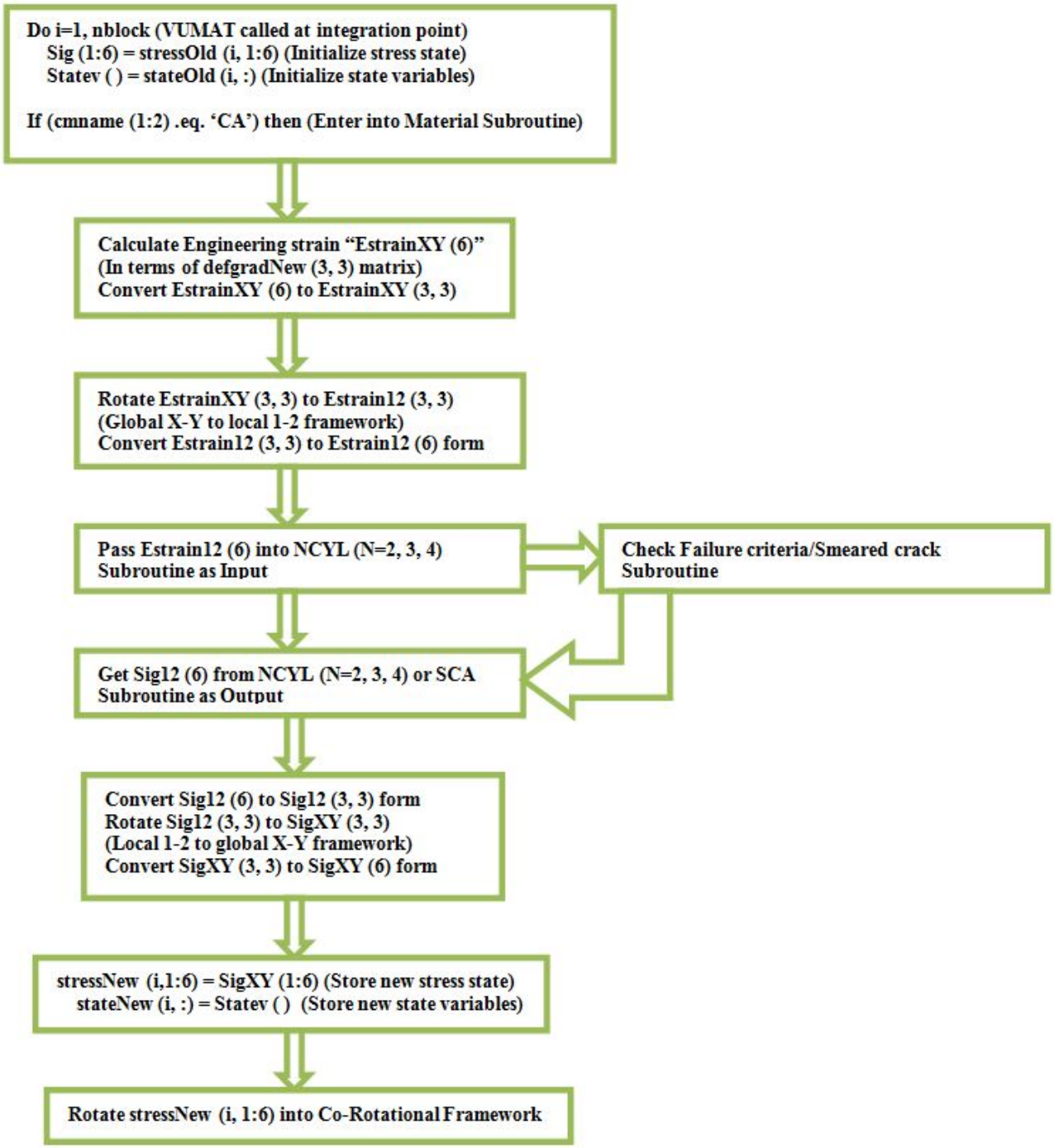

Figure C.1: Flowchart of main VUMAT.

APPENDIX D

Flowchart of NCYL (N=2, 3 and 4) subroutines

The detailed algorithm for NCYL (N=2, 3 and 4) subroutines are explained in the following flowcharts.

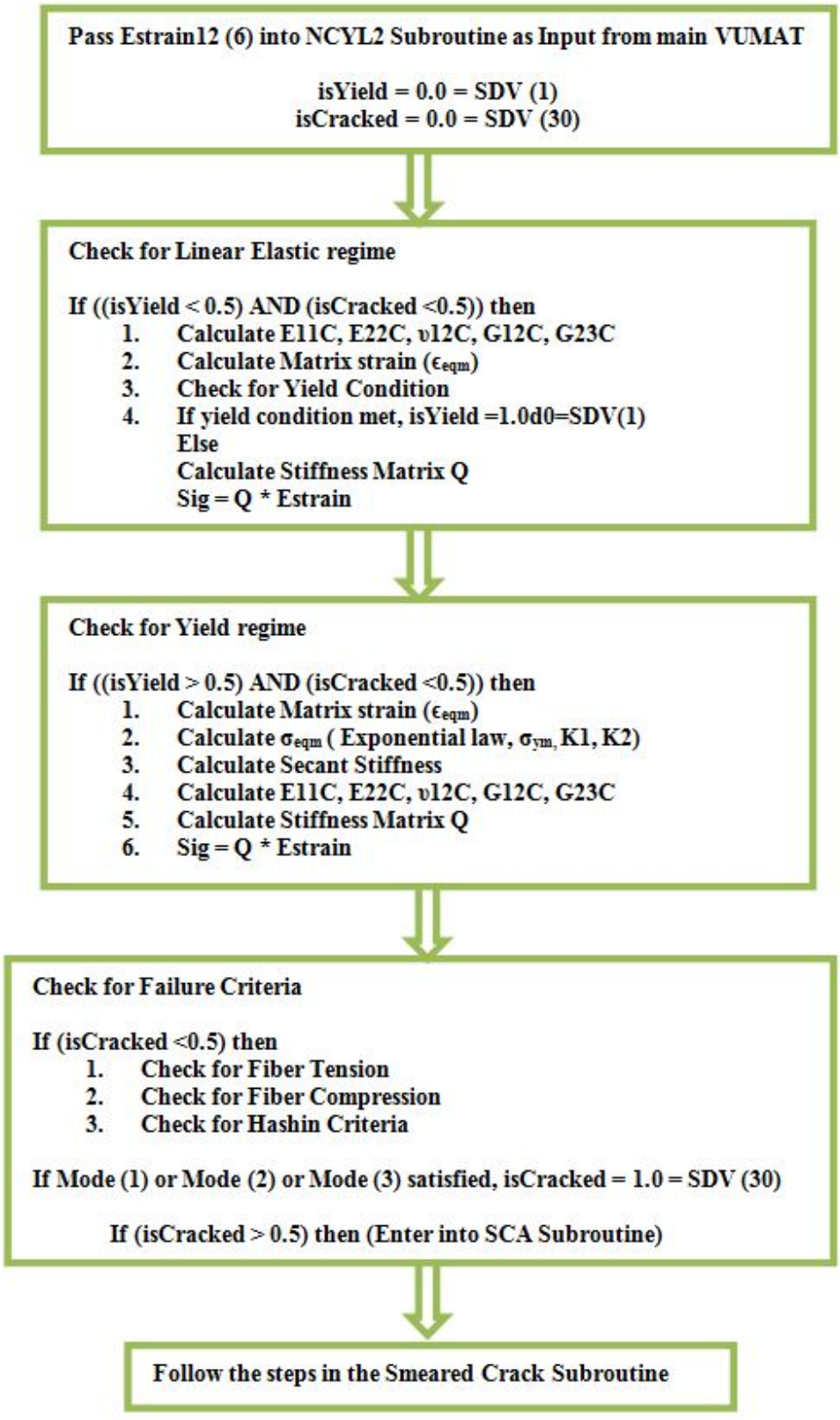

Figure D.1: Flowchart of NCYL2 subroutine.

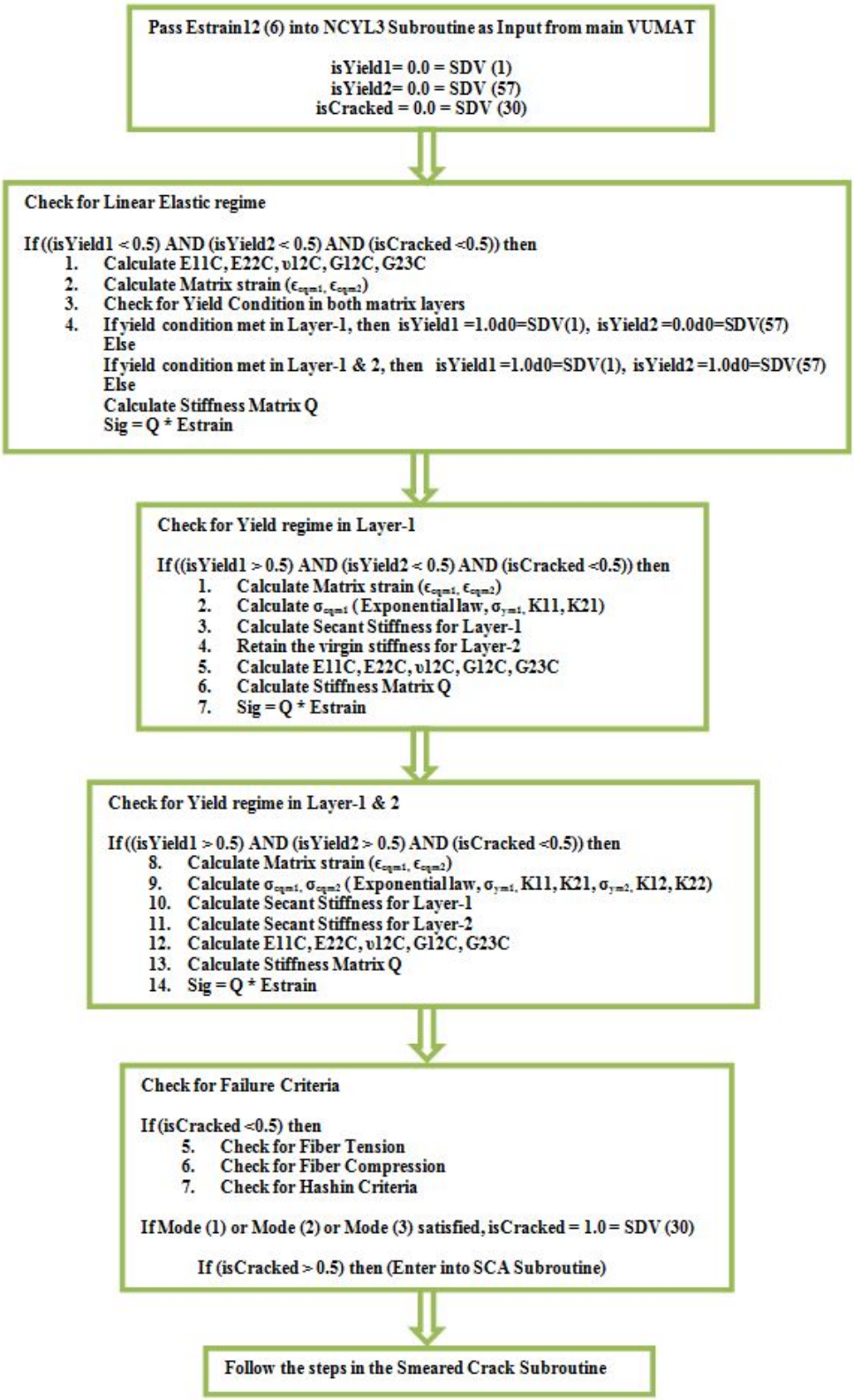

Figure D.2: Flowchart of NCYL3 subroutine.

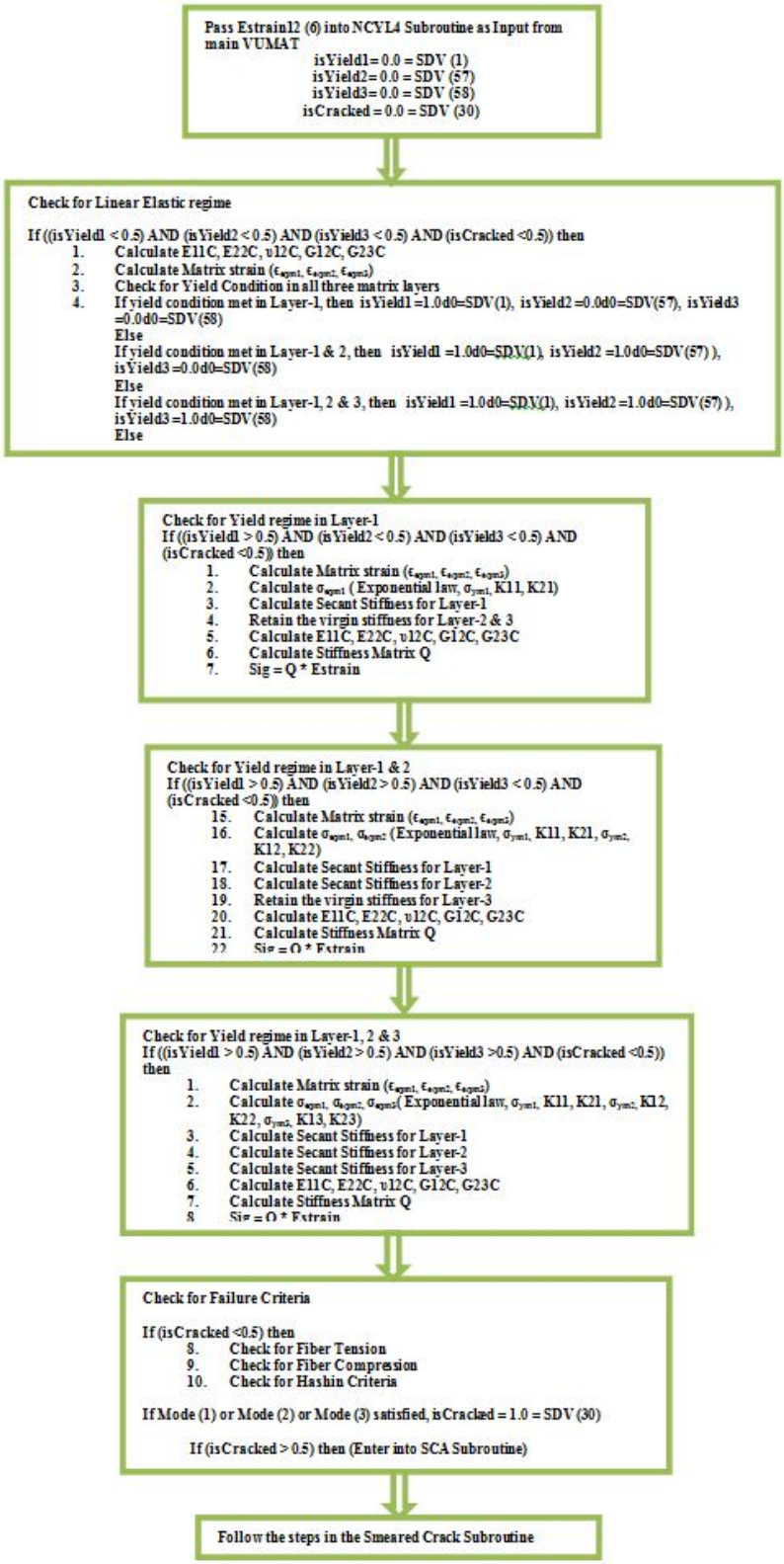

Figure D.3: Flowchart of NCYL4 subroutine.

APPENDIX E

Flowchart of 3D Orthotropic and Isotropic smeared crack subroutines

The detailed algorithm for SCA (3D Orthotropic and Isotropic) subroutines are explained in the following flowcharts.

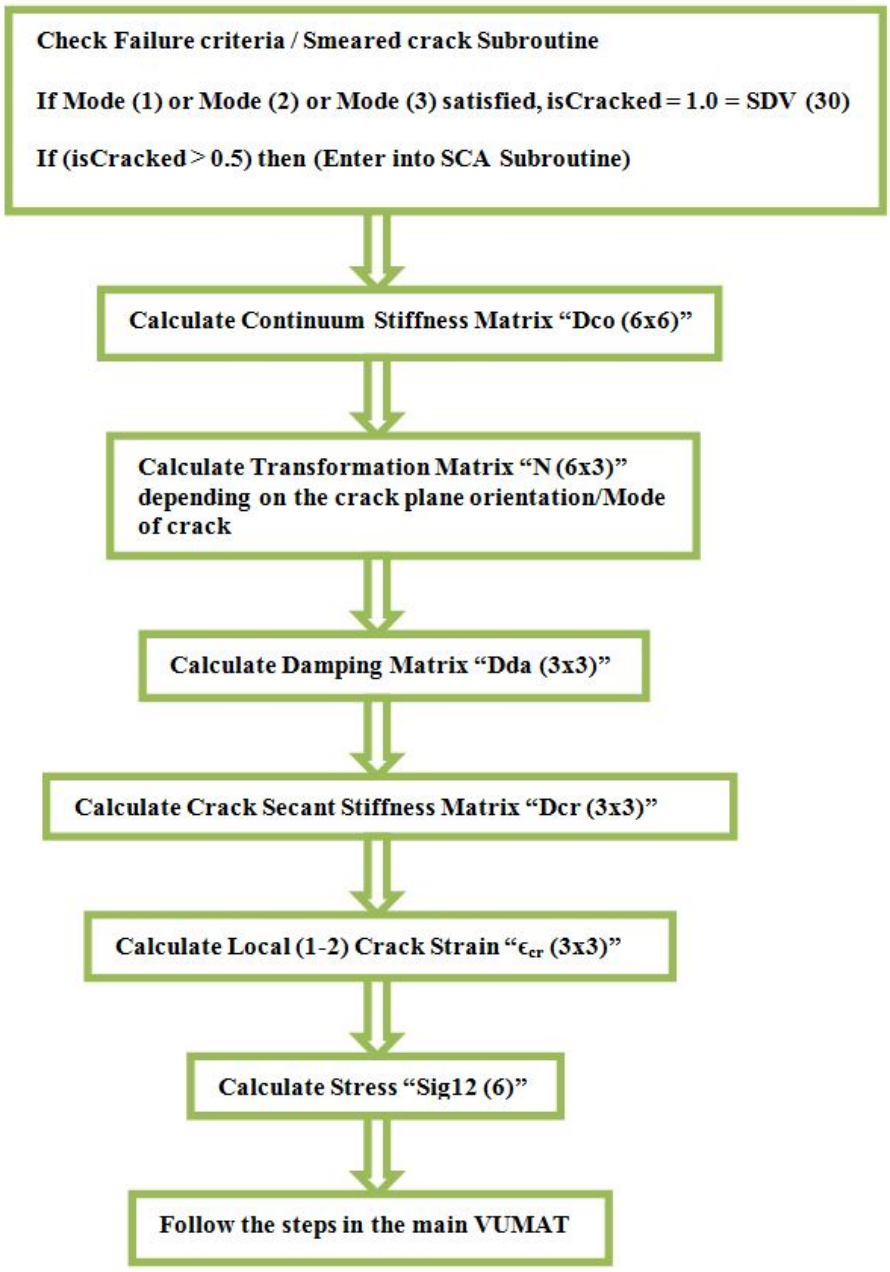

Figure E.1: Flowchart of 3D Orthotropic smeared crack subroutine.

APPENDIX F

Multiscale static analysis of notched laminates using NCYL and SCA models

This section visits the numerical simulations on predicting the progressive damage and failure response of three different multidirectioanl lay-ups from Tech Scout-1, conducted by AFRL, for uniaxial tension tests using the two-scale computational mechanics framework described earlier. The carbon fiber composite laminates of material system IM-7/977-3, including notched specimens are studied here. All the coupon laminates are modeled explicitely using 3D solid elements for individual lamina and the interlaminar failure due to delamination is modeled using discrete cohesive zone elements (DCZM) inserted in-between the layers. All the constituent level input parameters are obtained from standard unnotched [0], [90] and $[+45/-45]_{4s}$ coupon level experimental data, provided by AFRL through micromechanics analysis. The pre-peak nonlinearity, as caused by matrix microdamage is modeled using N-layers concentric cylinder model (NCYL) and the post-peak softening failure response is modeled using the mesh-objective smeared crack approach (SCA) in a multiscale framework. The proposed two-scale strategy with refined mesh and 3D Hashin failure modes implemented in the SCA code predicts the global stress-strain response and the detailed local complex failure mechanisms of the laminated composites. The coupon level simulation results are compared with experimental results to further validate the proposed model.

The tensile test simulations are carried out at the coupon level for all the three lay-ups including notched laminates. Figure F.1 shows the comparison of the global stress versus strain responses for the current model of open-hole tensile specimens with the experimental results. The failure evolution in each lamina is illustrated by the absolute index values of the failure flag. Figures F.2-F.4 compare the damage contour of each lamina with X-ray images at 90% of the ultimate strength. Generally, the current refined non-fiber aligned mesh model results are in better agreement with

the experiment in terms of strength, stiffness and mode of failures in each lamina with different fiber orientation.

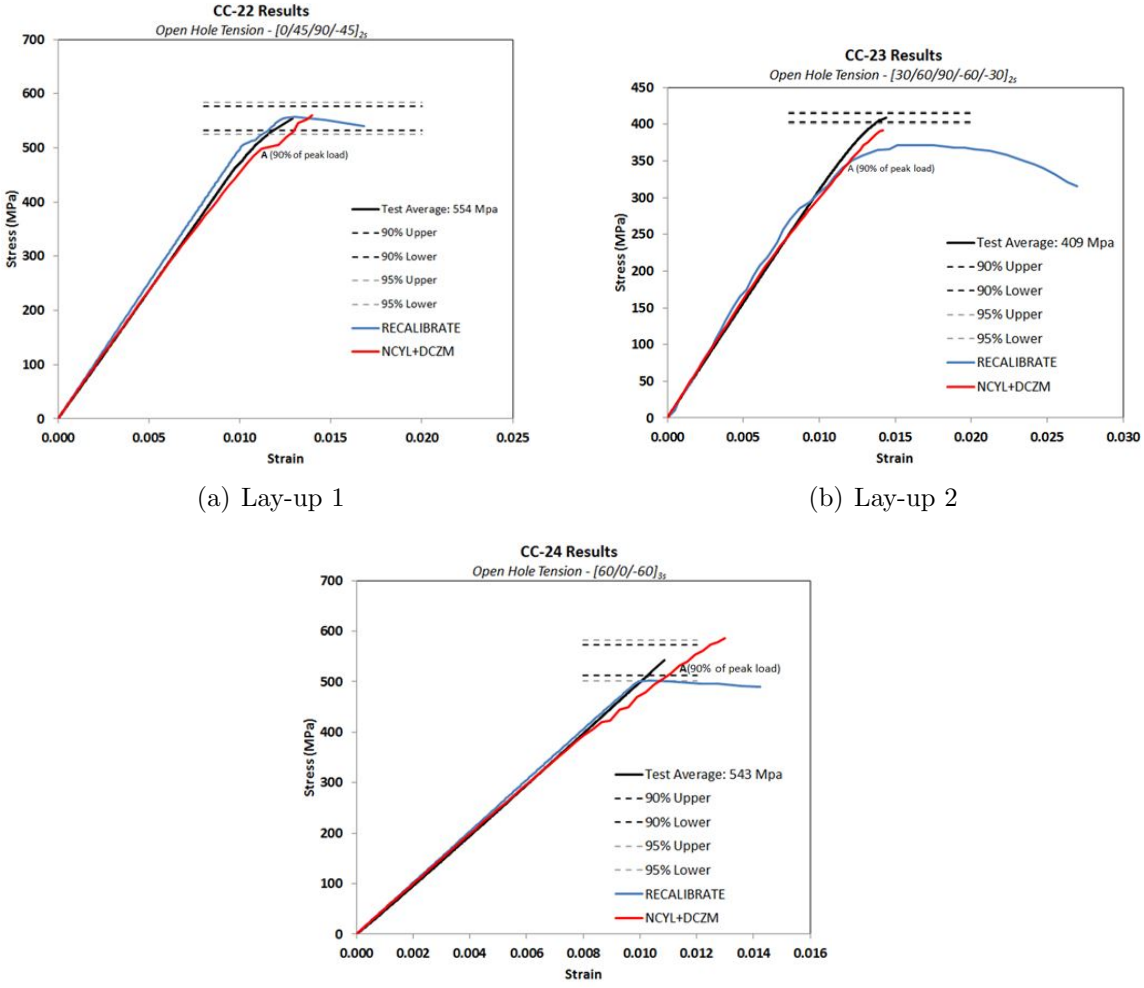

(a) Lay-up 1

(b) Lay-up 2

(c) Lay-up 3

Figure F.1: Comparison of stress vs. strain responses for OHT lay-ups.

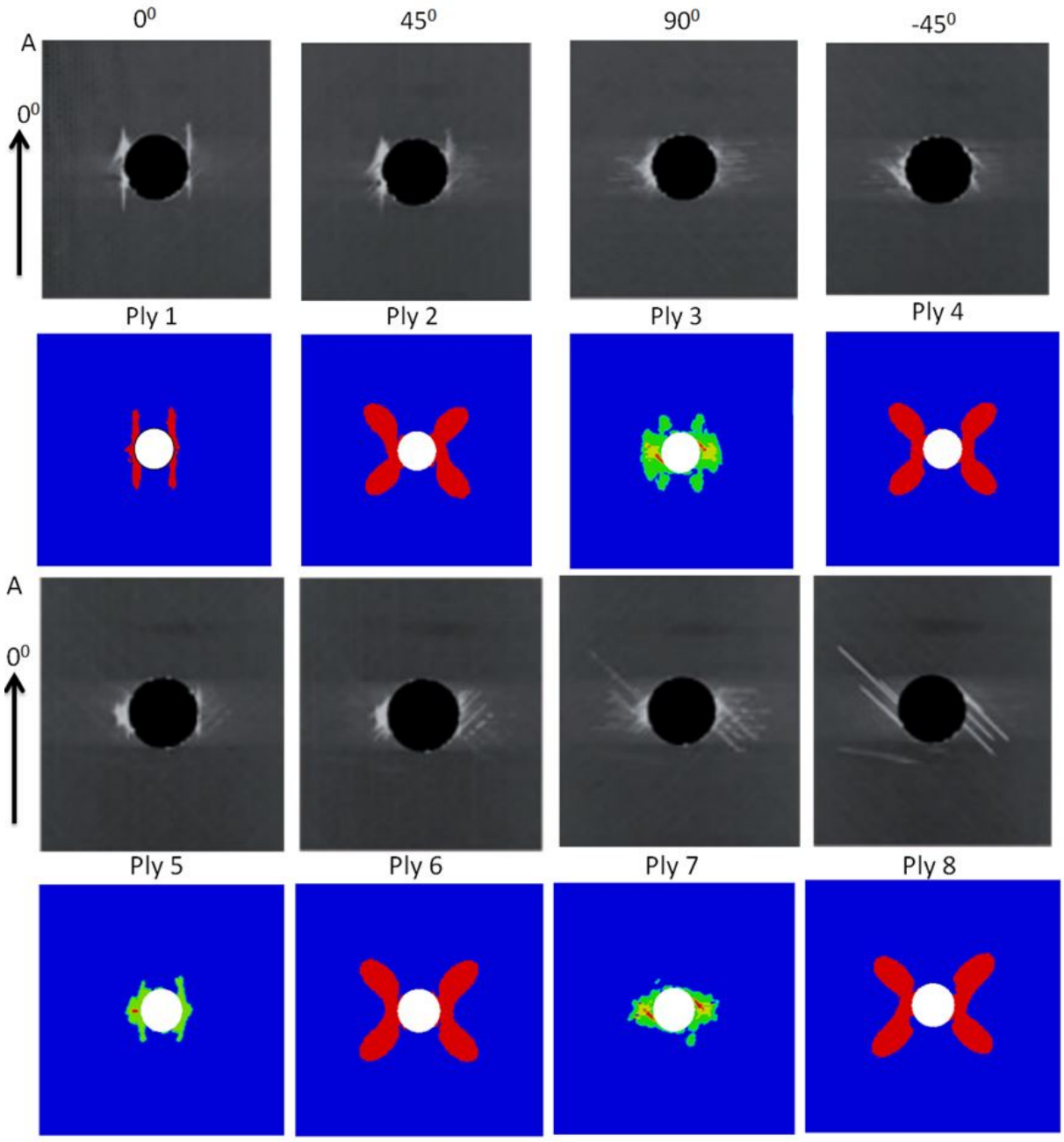

Figure F.2: Damage contours of each lamina for OHT Lay-up 1 $[0/45/90/-45]_{2s}$.

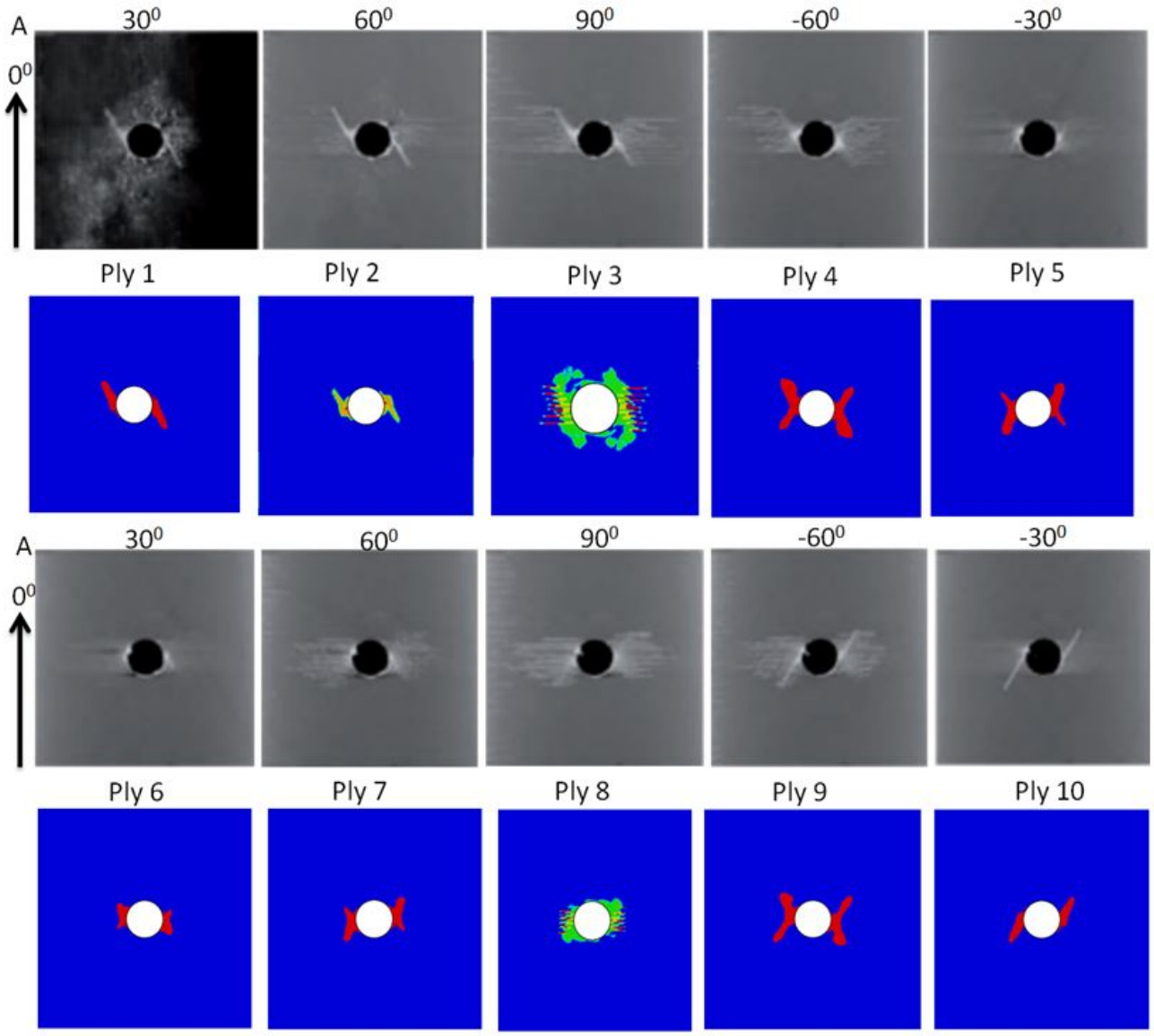

Figure F.3: Damage contours of each lamina for OHT Lay-up 2 $[30/60/90/-60/-30]_{2s}$.

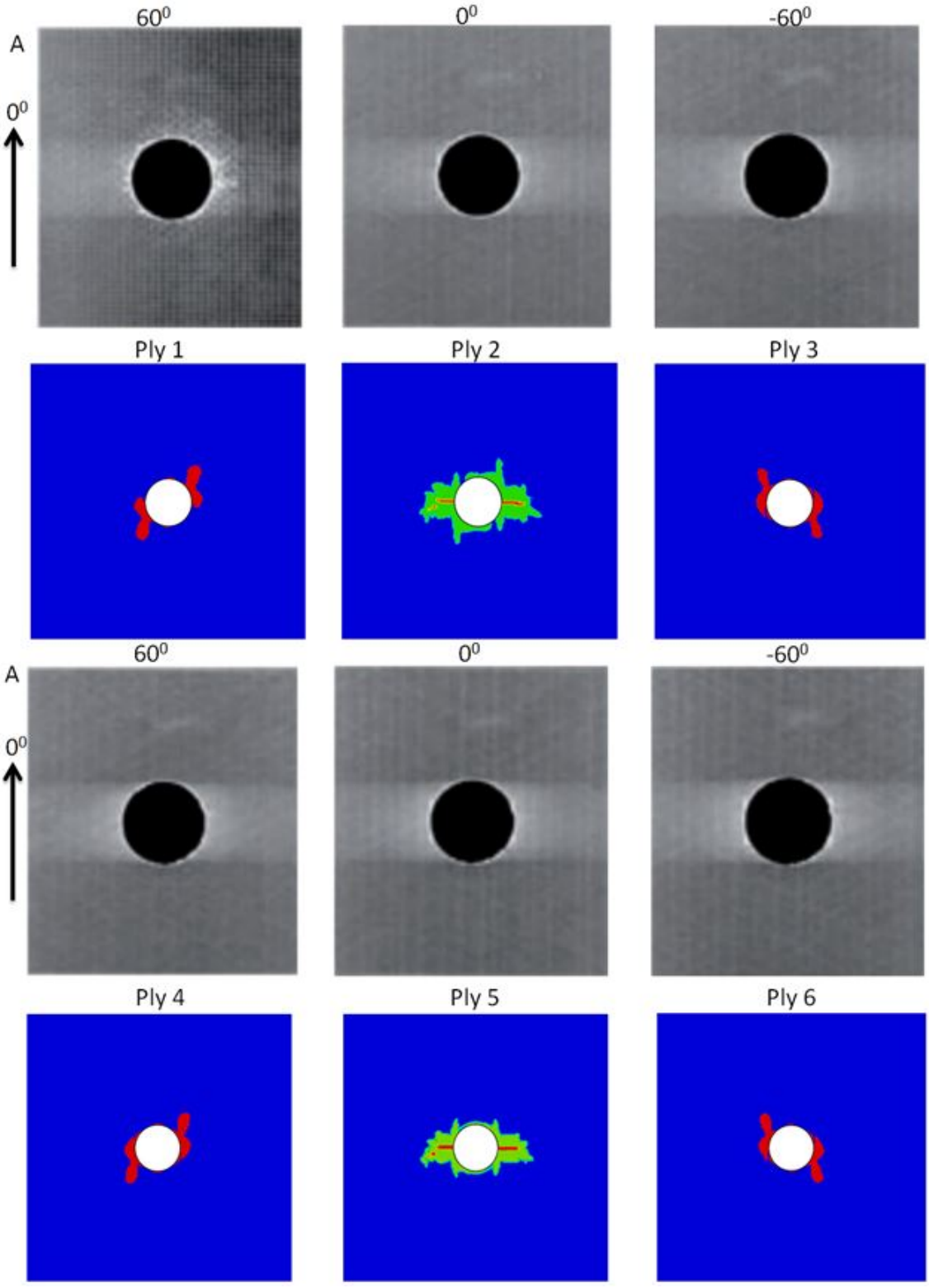

Figure F.4: Damage contours of each lamina for OHT Lay-up 3 $[60/0/-60]_{3s}$.

In this work, three different lay-ups are simulated for uniaxial tensile response to

compute the effective stiffness and strength for notched laminates. A more realistic finite element mesh is used to restore the mesh objectivity and capture the stress gradient around the notch area. The subscale micromechanics NCYL model is used to establish a multiscale computational framework to predict the effective nonlinear response of a homogenized lamina and the Smeared crack approach is revised to include all possible failure modes for the post-peak behavior. Overall, the main focus in this work is achieved by establishing a multiscale method, which is capable of predicting the complex failure mechanisms in each lamina and two-piece failure strength of all the configurations.

APPENDIX G

Imperfection characterization using Micro-CT data

This section studies the tow imperfections in more details using the Micro-CT data and image analysis using the tool, 'Simpleware'. A single RVE of Thick Symmetric architecture at mesoscale level is considered here to characterize the imperfections in each component level, as shown in Figure G.1. This 'hybrid' textile configuration consist of fibers, including IM-7 carbon, S2 glass and Kevlar that are integrally woven into a single preform. A series of warp and weft fibers run in-plane throughout the panel. A set of Z-fibers run in the direction of warp fibers and are drawn from bottom to top to bind all the layers together. Z-fibers are usually inserted in-between the spaces of the warp fibers. This architecture contains the carbon layers for both outer surfaces (four layers of carbon on each side) and nine layers of glass in the middle. The carbon and glass tows (total 17 layers) are orthogonally oriented in-plane and symmetric with respect to the mid-plane. The Z-fibers run half the thickness in two layers to bind the in-plane layers together.

The hybrid architecture is examined under microscopy to identify unit cells and characterize the in-situ imperfections. The in-plane tows show high straightness and high uniformity of the geometry, compared to out-of-plane binder kevlar tows. For weft tows, the waviness is highest in certain layers, as caused by the Z-fibers, where the kevlar fibers change directions from top to bottom or vice-versa and clearly visible in the Figure G.2. The fiber tow waviness and the crookedness are further examined with a SkyScan 1173 Micro-CT machine set-up (with 70-80kV X-ray source and pixel size of 17μm) to characterize the textile architecture and geometric imperfections.

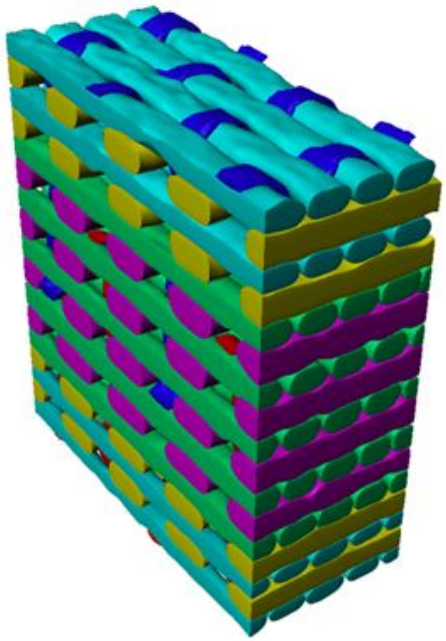

Figure G.1: Meso-scale RVE of Thick Symmetric configuration.

Here, all the tow imperfections from Micro-CT analysis are summarized as follows: (i) measurement of centerline position of fiber tow, (ii) measurement of tow curvature (iii) measurement of fiber tow cross-section area and (iii) measurement of tow ellipse major radius. All these measurements are conducted at multiple cross-sections along the length of a fiber tow and random sampling of fiber tows are chosen in the RVE for both carbon and glass tows in both warp and weft directions. Figures G.3 - G.6 show the contours of all these imperfection parameters in a range for all the four cases. A statistical average calculation is done with confidence interval of 95% to find the uncertainty bounds and mean for each imperfection parameter measured here.

The tow undulations are measured with reference to the center line of tow for both weft and warp directions carbon and glass tows, as shown in Figures G.7. The mean values of the tow centerline position with respect to a reference coordinate frame and the bounds are tabulated in Tables G.1 - G.4 for all the four cases. Therefore, if the 'bounds' are 'zero', it would imply that the tow is perfectly straight (zero undulation). Therefore, the bounds provide the magnitude of the imperfection in the tow straightness. The tow cross-sectional areas are measured and bounds are calculated as shown in Figure G.8 and tabulated in Table G.5.

In this work, different geometric imperfection parameters are measured for both warp and weft directions carbon and glass tows. Statistical bounds and variations are calculated to characterize the uncertainty in the material system, which is a signature

Table G.1: Weft Carbon tow bounds for undulation.

$Townumber$	$Mean(mm)$	$Bounds(mm)$
Tow1	7.6	±0.003
Tow2	7.64	±0.003
Tow3	7.73	±0.008
Tow4	7.65	±0.005
Tow5	7.57	±0.002

Table G.2: Weft Glass tow bounds for undulation.

$Townumber$	$Mean(mm)$	$Bounds(mm)$
Tow1	9.73	±0.003
Tow2	9.77	±0.004
Tow3	9.67	±0.004
Tow4	9.77	±0.003
Tow5	9.72	±0.004

Table G.3: Warp Carbon tow bounds for undulation.

$Townumber$	$Mean(mm)$	$Bounds(mm)$
Tow1	8.7	±0.014
Tow2	8.68	±0.016
Tow3	8.67	±0.015

Table G.4: Warp Glass tow bounds for undulation.

$Townumber$	$Mean(mm)$	$Bounds(mm)$
Tow1	10.82	±0.007
Tow2	10.87	±0.006

Table G.5: Tow area bounds.

$Townumber$	$Mean(mm)$	$Bounds(mm)$
Weft Glass	1.27	±0.024
Weft Carbon	1.04	±0.046
Warp Glass	2.46	±0.063
Warp Carbon	2.16	±0.04

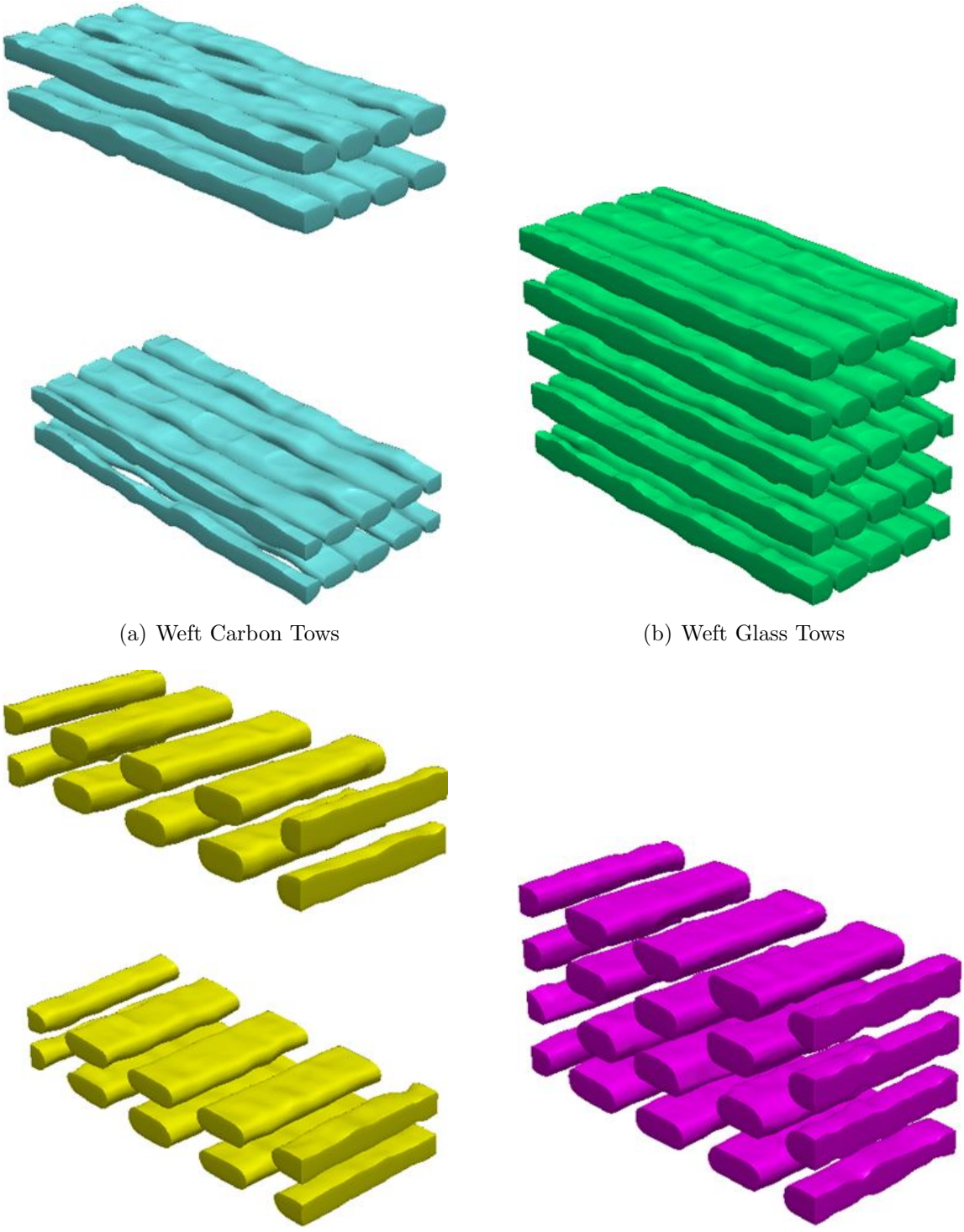

(a) Weft Carbon Tows

(b) Weft Glass Tows

(c) Warp Carbon Tows

(d) Warp Glass Tows

Figure G.2: Breakdown of components of 3D woven textile composite.

of the associated manufacturing process. These parameters can be referred as inputs for geometric modeling of the imperfection to include in the progressive damage and

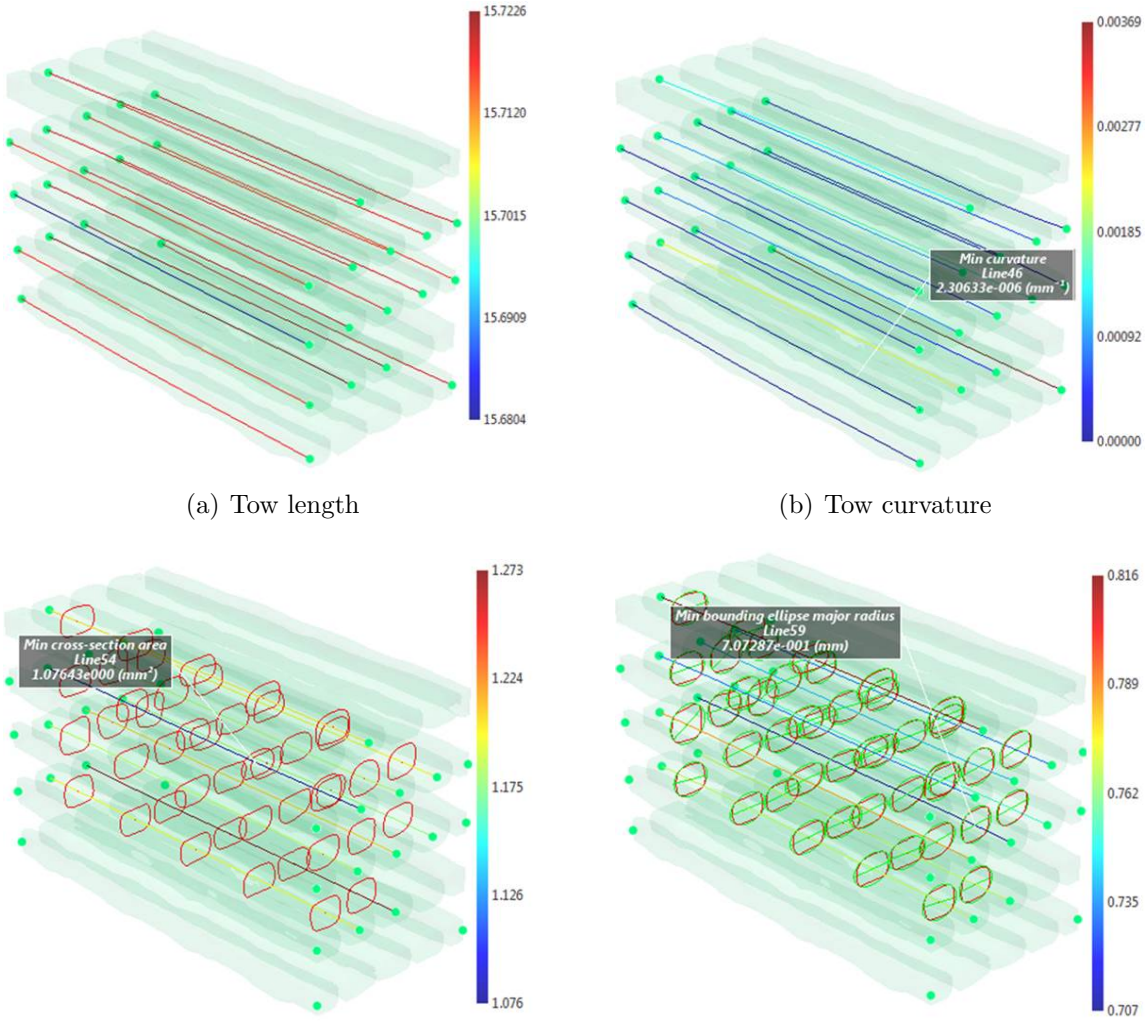

(a) Tow length

(b) Tow curvature

(c) Tow area

(d) Tow cross-section radius

Figure G.3: Weft Glass tows characterization.

failure analysis of textile composites, using the multiscale method established in this research.

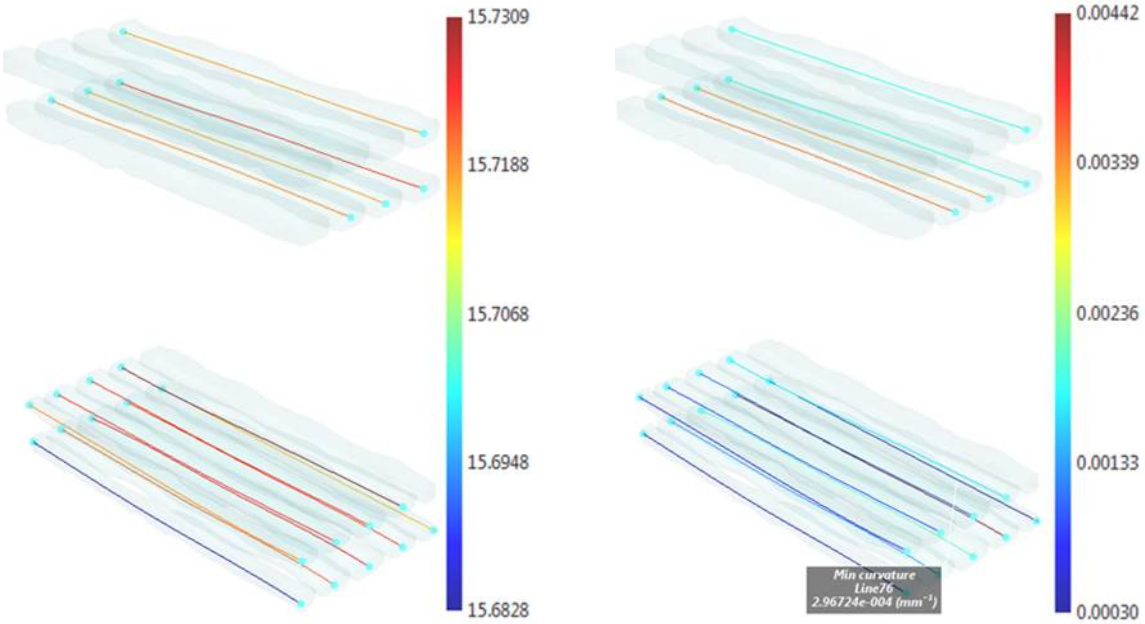

(a) Tow length

(b) Tow curvature

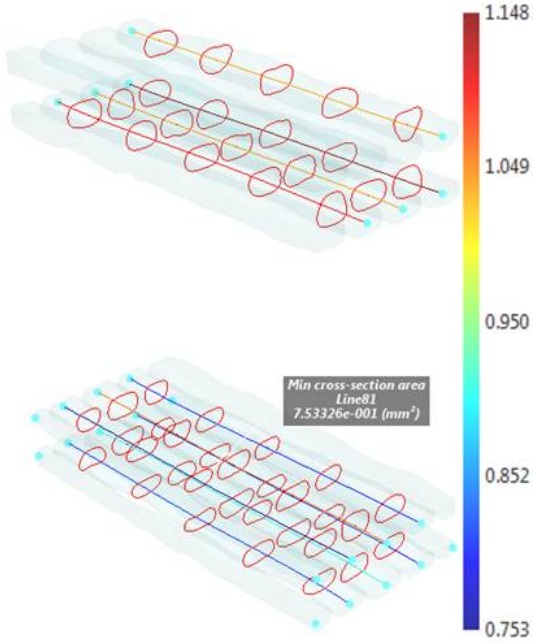

(c) Tow area

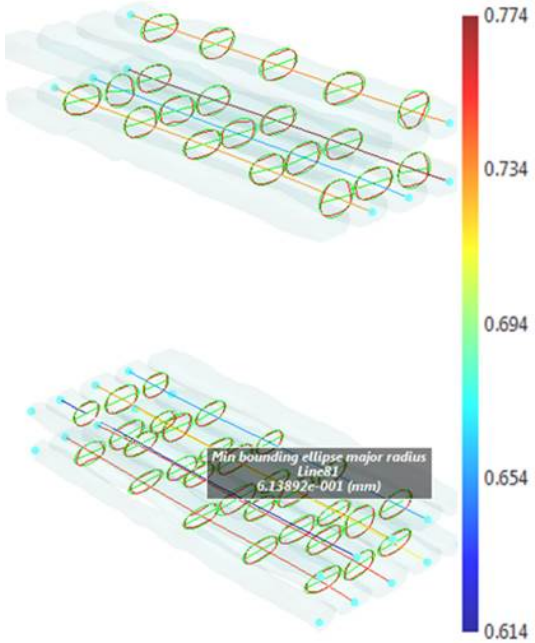

(d) Tow cross-section radius

Figure G.4: Weft Carbon tows characterization.

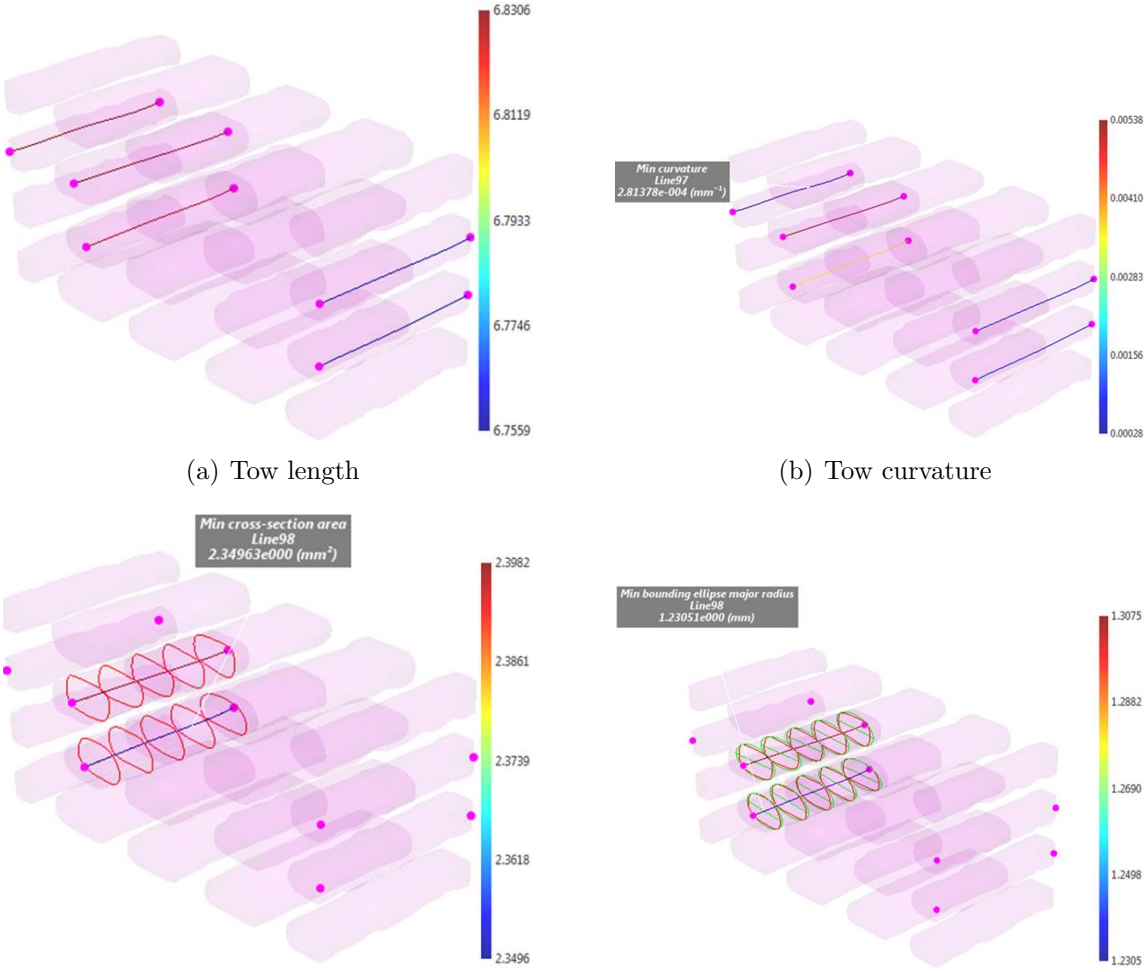

(a) Tow length

(b) Tow curvature

(c) Tow area

(d) Tow cross-section radius

Figure G.5: Warp Glass tows characterization.

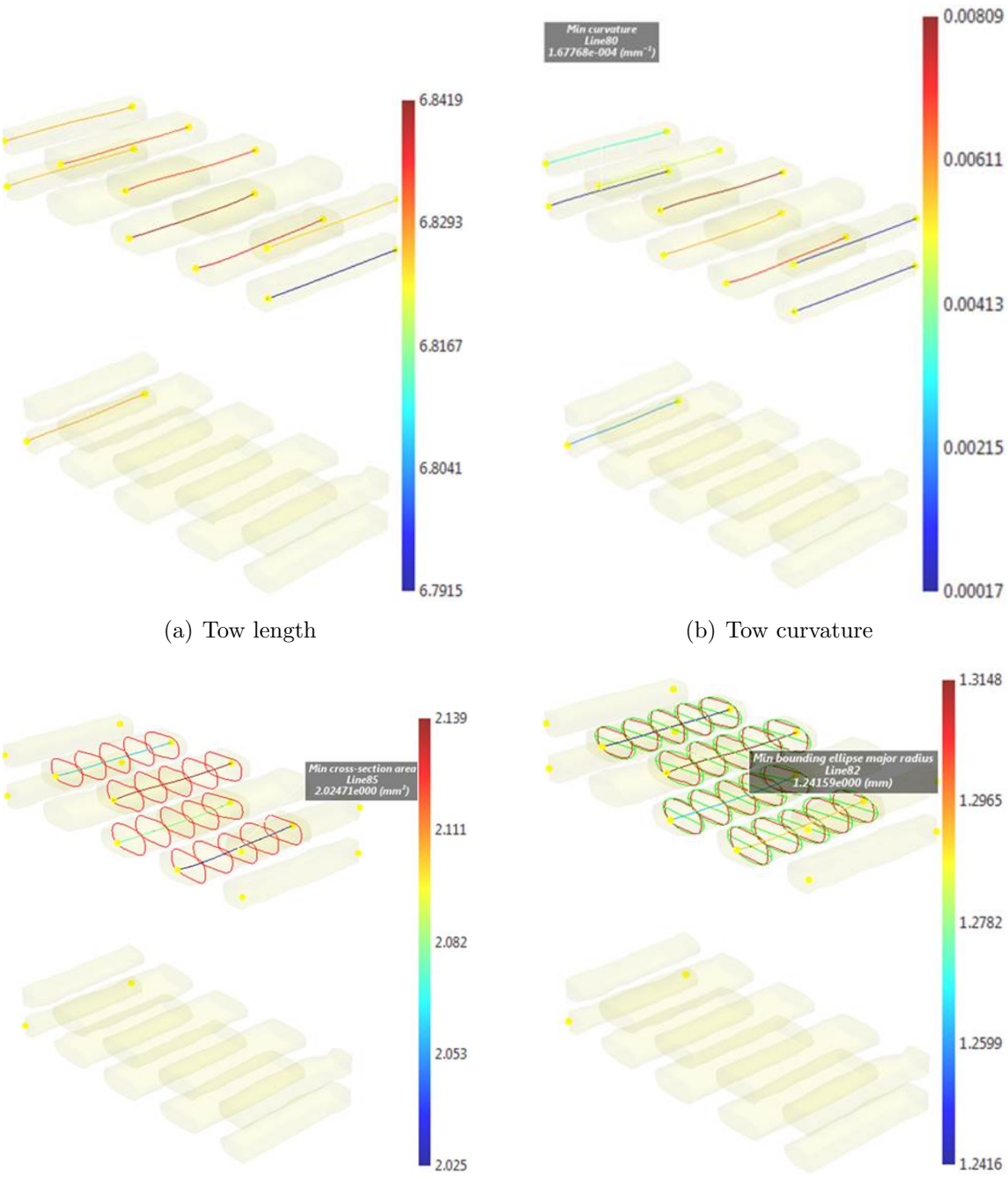

(a) Tow length

(b) Tow curvature

(c) Tow area

(d) Tow cross-section radius

Figure G.6: Warp Carbon tows characterization.

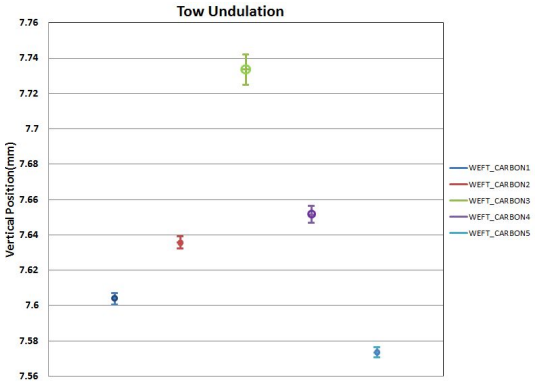

(a) Weft Carbon Tows: Circle indicates mean value

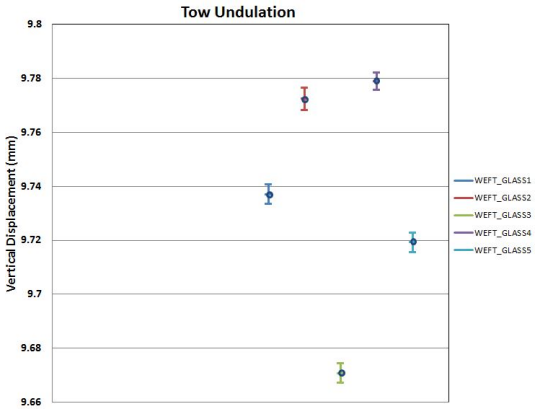

(b) Weft Glass Tows: Circle indicates mean value

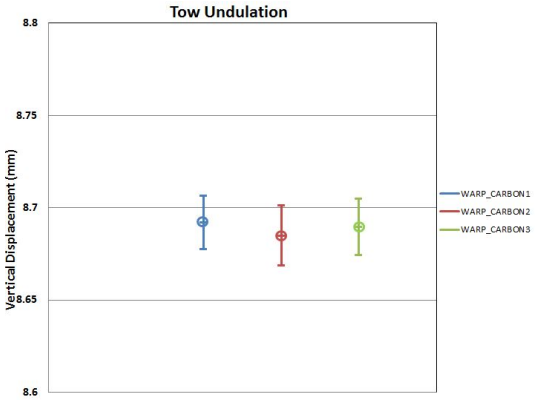

(c) Warp Carbon Tows: Circle indicates mean value

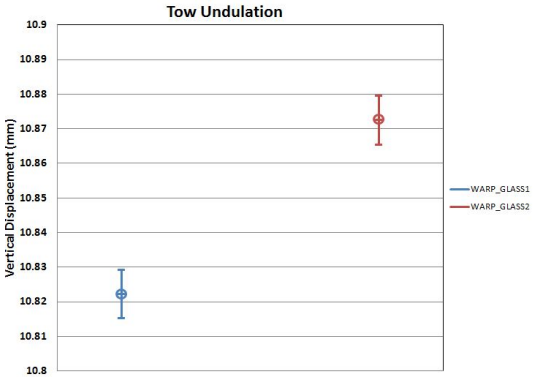

(d) Warp Glass Tows: Circle indicates mean value

Figure G.7: Uncertainty bounds for tow crookedness.

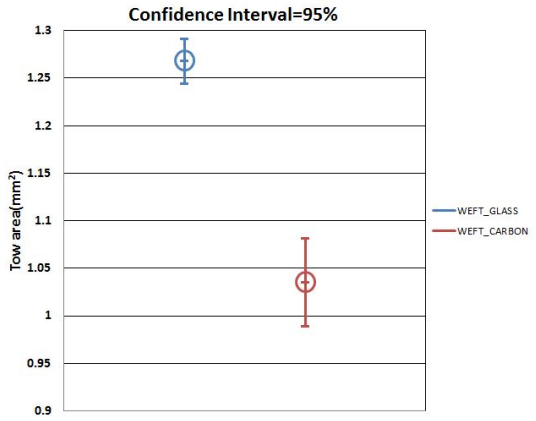

(a) Weft Tows: Circle indicates mean value

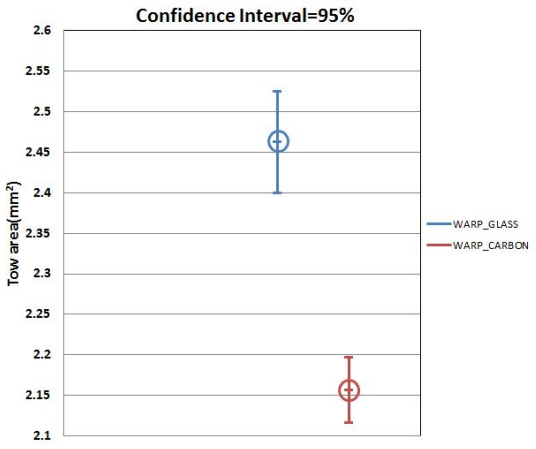

(b) Warp Tows: Circle indicates mean value

Figure G.8: Uncertainty bounds for tow cross-section area.

APPENDIX H

Imperfection sensitivity study on single RVE compression

The sensitivity of the initial geometric imperfection angle on the carbon tow compressive strength and load-displacement curve are studied in detail in Section 6.6, using a micro-mechanics model and Mohr-Coulomb's failure initiation criteria for matrix compression. Similar geometric models of the RVE are constructed with various glass fiber misalignment angles ranging from 0.1^0 to 2.5^0 and the corresponding axial stress-strain plots are shown in Figure H.1.

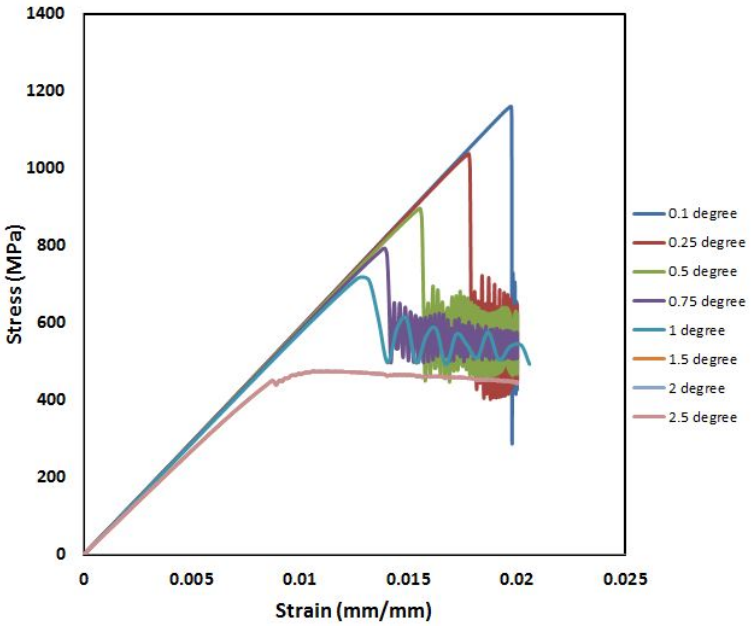

Figure H.1: Imperfection sensitivity of compressive strength.

For all the imperfection angles, the model behaves linearly at first in the pre-peak regime and the initial stiffnesses closely match, indicating that the range of imperfections considered here are small in magnitude. The matrix stiffness is degraded using

the secant stiffness approach and modeled using J2-deformation theory of pasticity, as described in Section 6.4. As observed in Figure H.1, the compressive strength of the RVE is sensitive to the tow strengths. It is noted that there is a gradual drop in tow strength with increase in imperfection angle within a tow. The post-peak compressive behavior is also affected by the tow strengths and the tow undulations within the RVE. The compressive strengths for both carbon and glass fiber tows are summarized in Figure H.2.

Angle of Imperfection	Tow Compressive Strength	
	Carbon Tow (MPa)	Glass Tow (MPa)
0.1^0	1610	1160
0.25^0	1435	1038
0.5^0	1247	896
0.75^0	1110	792
1.0^0	1004	718
1.5^0	767	475
2.0^0	767	475
2.5^0	767	475

Figure H.2: Carbon and glass tows compressive strength.

The tow compressive strength is governed by both material and geometric nonlinearity and the kinking failure mechanism is the culmination of a structural instability. As shown in Figure H.2, the tow strength is sensitive to the degree of imperfection for both the material systems. The crookedness of fiber tows in both warp and weft directions are characterized in Appendix G, which shows the statistical variations and uncertainties in the geometric imperfections, which play a crucial role in the geometric modeling of RVE for progressive failure analysis. The imperfections inherent in the structure must be included in the numerical modeling and analysis to study this effect. In this study, eigen buckling modes are extracted for the RVE and a linear superposition of first few critical modes are embedded in the ideal geometry to model the imperfection. At the same time, the imperfect RVE is modeled directly from Micro-CT data using 'Simpleware' as a reference solution. The fiber tow crookedness along warp and weft directions for both carbon and glass tows are measured directly from the Micro-CT data and used to scale the buckling modes to represent

the geometry of fiber tow close to the real ones. That is, the scale factors are chosen such that the undulated tows remain within the bounds of the measured undulation indicated in Appendix G, Tables G.1 - G.4. The scaling factors for various modes are chosen such that, the initial stiffness is always ±5% of the measured mean value. The sensitivity study is carried out on the perfect RVE model using the carbon and glass fiber tows compressive strength from Figure H.2, for a range of strength and for a range of undulations. Figure H.3 shows the computational runs that were carried out and the results are shown in Figure H.4.

Run	Tow Compressive Strength		Maximum amplitude of undulation	
	Carbon Tow (MPa)	Glass Tow (MPa)	Carbon Tow (mm)	Glass Tow (mm)
1	1610	1160	Weft: 0.008 Warp: 0.015	Weft: 0.003 Warp: 0.007
2	1435	1038	Weft: 0.008 Warp: 0.015	Weft: 0.003 Warp: 0.007
3	1110	792	Weft: 0.008 Warp: 0.015	Weft: 0.003 Warp: 0.007
4	1247	896	Weft: 0.008 Warp: 0.015	Weft: 0.003 Warp: 0.007
5	767	475	Weft: 0.008 Warp: 0.015	Weft: 0.003 Warp: 0.007
6	1435	718	Weft: 0.008 Warp: 0.015	Weft: 0.003 Warp: 0.007

Figure H.3: Summary chart for simulations results in Figure H.4.

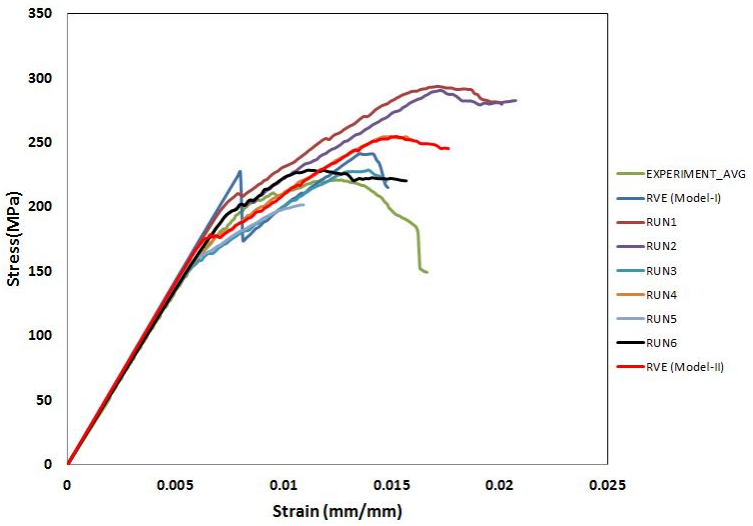

Figure H.4: Imperfection sensitivity of RVE simulations.

The results show the sensitivity of RVE strength to the tow strengths and fiber undulation amplitudes. The RVE compressive response matches closely with the imperfect model and the experiments after embedding the tow undulations within the bounds and choosing the carbon and glass tow strengths indicated as RUN6. The first load drop is dictated by carbon fiber tow compressive strength and the peak load is dictated by glass fiber tow compressive strength, as shown in Figure H.4. There is progressive kinking after initiation and a load rise between the first load drop and the peak load. It is cleat that the non-linearity in the stress-strain response of textile composites is driven by the tow undulation imperfections, whereas, carbon and glass fiber tow strengths are determined to be strength limiting mechanism for this type of textile composite materials.

BIBLIOGRAPHY

[1] Zhang, D. and Waas, A. M., "A micromechanics based multiscale model for nonlinear composites," *Acta Mechanica, 225(4-5), 1391-1417*, 2014.

[2] Voigt, W., "Uber die Beziehung zwischen den beiden Elastizitatskonstanten Isotroper Korper," *Wied. Ann., 38, 573-587*, 1889.

[3] Reuss, A., "Berechnung der," *Zeitschrift Angewandte Mathematik und Mechanik, 9, 49-58*, 1929.

[4] Halpin, J. C. and Kardos, J. L., "The Halpin-Tsai equations: A review," *Polymer Engineering and Science, Vol. 16, No. 5*, 1976.

[5] Hashin, Z. and Rosen, B. W., "The elastic moduli of fiber reinforced materials," *Journal of Applied Mechanics, 31, 223-228*, 1964.

[6] Christensen, R. M. and Lo, K. H., "Solutions for effective shear properties in three phase sphere and cylinder models," *J. Mech. Phys. Solids, 27, 315-330*, 1979.

[7] Mori, T. and Tanaka, K., "Average stress in matrix and average elastic energy of materials with misfitting inclusions," *Acta Mettallica, 21, 571-574*, 1973.

[8] Tandon, G. P. and Weng, G. J., "The effect of aspect ratio of inclusions on the elastic properties of unidirectionally aligned composites," *Polymer Composites, Vol. 5, No. 4*, 1984.

[9] Hill, R., "Theory of mechanical properties of fibre-strengthen materials-III, Self-consistent model," *Journal of Mechanics and Physics of Solids, 13, 189-198*, 1965.

[10] Budiansky, B., "On the elastic moduli of some heterogeneous materials," *J. Mech. Phys. Solids, 13, 223-227*, 1965.

[11] Huang, Z. M., "Simulation of the mechanical properties of fibrous composites by the bridging micromechanics model," *Composites: Part A, 32, 143-172*, 2001.

[12] Huang, Z. M., "Micromechanical prediction of ultimate strength of transversely isotropic fibrous composites," *International Journal of Solids and Structures, 38, 4147-4172*, 2001.

[13] Li, S., "Boundary conditions for unit cells from periodic microstructures and their implications," *Composites Science and Technology, 68, 1962-1974*, 2008.

[14] Sun, C. T. and Vaidya, R. S., "Prediction of composite properties from a representative volume element," *Composites Science and Technology, 56(2), 171-179*, 1996.

[15] Sicking, D. L., "Mechanical characterization of nonlinear laminated composites with transverse crack growth," *Ph.D. thesis, Texas AM University*, 1992.

[16] Lamborn, M. J. and Schapery, R. A., "An Investigation of the Existence of a Work Potential for Fiber-Reinforced Plastic," *Journal of Composite Materials, Vol. 27, 352-382*, 1993.

[17] Ng, W. H., Salvi, A. G., and Waas, A. M., "Characterization of the in-situ non-linear shear response of laminated fiber-reinforced composites," *Composites Science and Technology, 70, 1126-1134*, 2010.

[18] Herakovich, C. T., "Mechanics of Fibrous Composites," *John Wiley & Sons, Inc.*, 1998.

[19] Hyer, M. W. and Waas, A. M., "Micromechanics of linear elastic continuous fiber composites, Comprehensive Composite Materials," *Pergamon, Oxford, 345-375*, 2002.

[20] Hashin, Z., "The elastic moduli of heterogeneous materials," *Journal of Applied Mechanics, 29, 143-150*, 1962.

[21] Hashin, Z. and Shtrikman, S., "A variational approach to the theory of the elastic behavior of multiphase materials," *J. Mech. Phys. Solids, 11, 127-140*, 1963.

[22] Huang, Y., Hu, K. X., Wei, X., and Chandra, A., "A Generalized Self-Consistent Mechanics Method for Composite Materials with Multiphase Inclusions," *J. Mech. Phys. Solids, 42, 491-504*, 1994.

[23] Hill, R., "A Self-Consistent Mechanics of Composite Materials," *J. Mech. Phys. Solids, 13, 213-222*, 1995.

[24] Li, G., Zhao, Y., and Pang, S. S., "Four-Phase Sphere Modeling of Effective Bulk Modulus of Concrete," *Cement and Concrete Research, Vol. 29, 839-845*, 1999.

[25] Eshelby, J. D., "The Determination of the elastic field of an ellipsoidal inclusion, and related problems," *Proceedings of the Royal Society A: Mathematical, Physical and Engineering Sciences, 241(1226), 376396*, 1957.

[26] Pankow, M., Yen, C. F., Rudolph, M., Justusson, B., Zhang, D., and Waas, A. M., "Experimental investigation on the deformation response of hybrid 3D woven composites," *53rd AIAA/ASME/ASCE/AHS/ASC Structures, Structural Dynamics and Materials Conference, Honolulu, Hawaii, USA, AIAA 2012-1572*, 2012.

[27] Heinrich, C., Aldridge, M., Wineman, A. S., Kieffer, J., Waas, A. M., and Shahwan, K., "The influence of the representative volume element (RVE) size on the homogenized response of cured fiber composites," *Modeling and Simulation in Materials Science and Engineering, 20, 075007*, 2012.

[28] Rots, G., Nauta, P., Kusters, G. M. A., and Blaauwendraad, J., "Smeared crack approach and fracture localization in concrete," *HERON, 1-48*, 1985.

[29] Heinrich, C. and Waas, A. M., "Investigation of progressive damage and fracture in laminated composites using the smeared crack approach," *53rd AIAA/ASME/ASCE/AHS/ASC Structures, Structural Dynamics and Materials Conference, Honolulu, Hawaii, USA, AIAA 2012-1537*, 2012.

[30] Zhang, D., Waas, A., and Yen, C., "Progressive failure analysis on textile composites," *55th AIAA/ASME/ASCE/AHS/ASC Structures, Sturctural Dynamics and Materials Conference, National Harbor, Maryland, USA, AIAA 2014-0157*, 2014.

[31] Zhang, D., "Progressive Damage and Failure Analysis of 3D Textile Composites Subjected to Flexural Loading," *Ph.D. thesis, University of Michigan*, 2014.

[32] Zhang, D., Waas, A. M., and Yen, C. F., "Progressive damage and failure response of hybrid 3D textile composites subjected to flexural loading, Part I: Experimental studies," *Int. J. Solids Struct., Vol. 75-76, 309-320*, 2015.

[33] M., P., Salvi, A., Waas, A. M., C., Y., and Ghiorse, S., "Split Hopkinson pressure bar testing of 3D woven composites," *ICompos. Sci. Technol., Vol. 71, 1196-1208*, 2011.

[34] Pankow, M. R., "The Deformation Response of 3D Woven Composites Subjected to High Rates of Loading," *Ph.D. thesis, University of Michigan*, 2010.

[35] Hashin, Z., "Analysis of Composite Materials-A Survey," *Journal of Applied Mechanics, Vol. 50, 481-505*, 1983.

[36] Camanho, P. P., Davila, C. G., Pinho, S. T., Lannucci, L., and Robinson, P., "Prediction of in situ strengths and matrix cracking in composites under transverse tension and in-plane shear," *Compos. Part A: Appl. Sci. Manuf., Vol. 37, 165 – 176*, 2006.

[37] Potluri, P., Sharif, T., and Jetavat, D., "Robotic Approach to Textile Preforming for Composites," *Journal of Fibre and Textile Research, Vol. 33, 333-338*, 2008.

[38] Lomov, S. V., Bogdanovich, A. E., Ivanov, D. S., Mungalov, D., Karahan, M., and Verpoest, I., "A compartive study of tensile properties of non-crimp 3D orthogonal weave and multi-layer plain weave E-glass composites. Part 1: Materials, methods and principal results," *Composites Part A, Vol. 40, 1134-1143*, 2009.

[39] Ivanov, D. S., Lomov, S. V., Bogdanovich, A. E., Karahan, M., and Verpoest, I., "A compartive study of tensile properties of non-crimp 3D orthogonal weave and multi-layer plain weave E-glass composites. Part 2: Comprehensive experimental results," *Composites Part A, Vol. 40, 1144-1157*, 2009.

[40] Carvelli, V., Gramellini, G., Lomov, S. V., Bogdanovich, A. E., Mungalov, D., and Verpoest, I., "Fatigue behaviour of non-crimp 3D orthogonal weave and multi-layer plain weave E-glass reinforced composites," *Composites Science and Technology, Vol. 70, 2068-2076*, 2010.

[41] Karahan, M., Lomov, S. V., Bogdanovich, A. E., Mungalov, D., and Verpoest, I., "Internal geometry evaluation of non-crimp 3D orthogonal woven carbon fabric composite," *Composites Part A, Vol. 41, 1301-1311*, 2010.

[42] Bogdanovich, A. E., Lomov, S. V., Karahan, M., Mungalov, D., and Verpoest, I., "Quasi-static and fatigue tensile behaviour of carbon/epoxy composite reinforced with 3D non-crimp orthogonal woven fabric. Part 1: Stiffness and strength," *Composites Part A, Submitted*, 2010.

[43] Karahan, M., Lomov, S. V., Bogdanovich, A. E., and Verpoest, I., "Quasi-static and fatigue tensile behaviour of carbon/epoxy composite reinforced with 3D non-crimp orthogonal woven fabric. Part 2: Damage monitoring and analysis," *Composites Part A, Submitted*, 2010.

[44] Karahan, M., Lomov, S. V., Bogdanovich, A. E., and Verpoest, I., "Quasi-static and fatigue tensile behaviour of carbon/epoxy composite reinforced with 3D non-crimp orthogonal woven fabric. Part 3: Fatigue," *Composites Part A, Submitted*, 2010.

[45] Long, A. C., "Design and manufacturing of textile composites," *Woodhead Publishing Limited in association with The Textile Institute, Cambridge, England, 1st ed.*, 2005.

[46] Song, X., "Vacuum Assisted Resin Transfer Molding (VARTM): Model Development and Verification," *Ph.D. thesis, Cambridge, Virginia Polytechnic Institute and State University*, 2003.

[47] Chen, R., Dong, C., Liang, Z., Zhang, C., and Wang, B., "Flow modeling and simulation for vacuum assisted resin transfer molding process with the equivalent permeability method," *Polymer Composites, Vol. 25, 146-164*, 2004.

[48] Song, S., Waas, A. M., Shahwan, K. W., Xiao, X., and Faruque, O., "Braided textile composites under compressive loads: Modeling the response, strength and degradation," *Composites Science and Technology, Vol. 67, 3059-3070*, 2007.

[49] Cox, B. N., Dadkhah, M. S., and Morris, W., "On the tensile failure of 3D woven composites," *Composites part A: Applied Science and Manufacturing, Vol. 27, 447-458*, 1996.

[50] Huang, H. J. and Waas, A. M., "Modeling and predicting the compression strength limiting mechanisms in Z-pinned textile composites," *Composites Part B: Engineering, Vol. 40, 530-539*, 2009.

[51] Rao, M., Sankar, B., and Subhash, G., "Effect of Z-yarns on the stiffness and strength of three-dimensional woven composites," *Composites Part B: Engineering, Vol. 40, 540-551*, 2009.

[52] M., P., Waas, A. M., F., Y. C., and Ghiorse, S., "A new lamination theory for layered textile composites that account for manufacturing induced effects," *Compos. Part A: Appl. Sci. Manuf., Vol. 40, 1991-2003*, 2009.

[53] M., P., Waas, A. M., F., Y. C., and Ghiorse, S., "Modeling the response, strength and degradation of 3D woven composites subjected to high rate loading," *Compos. Struct., Vol. 94, 1590-1604*, 2012.

[54] Song, S., Waas, A. M., Shahwan, K. W., Faruque, O., and Xiao, X. S., "Compression response, strength and post-peak response of an axial fiber reinforced tow," *Int. J. Mech. Sci., Vol. 51, 491-499*, 2009.

[55] Zhang, D., Waas, A. M., and Yen, C. F., "Progressive damage and failure response of hybrid 3D textile composites subjected to flexural loading, Part II: Mechanics based multiscale computational modeling of progressive damage and failure," *Int. J. Solids Struct., Vol. 75-76, 321-335*, 2015.

[56] Potluri, P., Parlak, I., Ramgulam, R., and Sagar, T. V., "Analysis of tow deformations in textile preforms subjected to forming forces," *Composites Science and Technology, Vol. 66, 297-305*, 2006.

[57] Zhang, D., Waas, A. M., Pankow, M., Yen, C. F., and Ghiorse, S., "Flexural Behavior of a Layer-to-Layer Orthogonal Interlocked Three-Dimensional Textile Composite," *Journal of Engineering Materials and Technology, Vol. 134, 031009-1-8*, 2012.

[58] Green, S. D., Matveev, M. Y., Long, A. C., Ivanov, D., and Hallett, S. R., "Mechanical modelling of 3D woven composites considering realistic unit cell geometry," *Composite Structures, Vol. 118, 284-293*, 2014.

[59] Kyriakides, S., Arseculeratne, R., Perry, E. J., and Liechti, K. M., "On the compressive failure of fiber reinforced composites," *Int. J. Solids Struct., Vol. 32, 689-738*, 1995.

[60] Ahn, J. and Waas, A. M., "Prediction of Compressive Failure in Laminated Composites at Room and Elevated Temperature," *AIAA Journal., Vol. 40, 93-122, DOI: 10.1007/s10704-013-9860-1*, 2002.

[61] Pineda, E. J. and Waas, A. M., "Numerical implementation of a multiple-ISV thermodynamically-based work potential theory for modeling progressive damage and failure in fiber-reinforced laminates," *Int. J. Fract., Vol. 182, 93-122*, 2013.

[62] Bazant, Z. P. and Gambarova, P. G., "Rough cracks in reinforced concrete," *J. Struct. Div., Vol. 106, 819-842*, 1980.

[63] Walraven, J. C., "Aggregate interlock: a theoritical and experimental analysis," *Ph.D. thesis, Delft university of Technology*, 1980.

[64] Walraven, J. C. and Reinhardt, H. W., "Theory and experiments on the mechanical behaviour of cracks in plain and reinforced concrete subjected to shear loading," *HERON, Vol. 26*, 1981.

[65] Gambarova, P. G. and Karakoc, C., "A new approach to the analysis of the confinement role in regularly cracked concrete elements," *In: Transactions 7th SMIRT Conference H (Paper H5/7), Chicago, 251 – 261*, 1983.

[66] "Hexcel, 2010 Hextow im7 carbon fiber," *http://www.hexcel.com/Resources-DataSheets/Carbon-Fiber*, 2010.

[67] "AGY, 2006 High strength glass fibers," *http://www.agy.com/technical-info/graphics-PDFs/HighStrengthTechPaperEng.pdf*, 2010.

[68] Lomov, S. V., Bogdanovich, A. E., Karahan, M., Mungalov, D., Verpoest, I., and Leuven, K. U., "Mechanical behaviour of non-crimp 3D woven carbon/epoxy composite under in-plane tensile loading," *18th International Conference on Composite Materials, 1-5*, 2011.

[69] Yu, B., Bradley, R. S., Soutis, C., Hogg, P. J., and Withers, P. J., "2D and 3D imaging of fatigue failure mechanisms of 3D woven composites," *Compos. Part A: Appl. Sci. Manuf., Vol. 77, 37-49*, 2015.

[70] Saleh, M. N., Lubineau, G., Potluri, P., Withers, P., and Soutis, C., "Micromechanics based damage mechanics for 3D orthogonal woven composites: Experiment and numerical modelling," *Composite Structures, Article in press*, 2016.

[71] Obert, E., Daghia, F., Ladeveze, P., and Ballere, L., "Micro and meso modelling of woven composites: Transverse cracking kinetics and homogenization," *Composite Structures, Vol. 117, 212-221*, 2014.

[72] Pankow, M., Waas, A. M., and Yen, C. F., "Modeling the Response of 3D Textile Composites under Compressive Loads to Predict Compressive Strength," *CMC, Vol: 32, no.2, 81-106*, 2012.

[73] Prabhakar, P. and Waas, A. M., "Interaction between kinking and splitting in the compressive failure of unidirectional fiber reinforced laminated composites," *Composite Structures, Vol: 98, 85-92*, 2013.

[74] Song, S., Waas, A. M., Shahwan, K. W., Faruque, O., and Xiao, X., "Compression response, strength and post-peak response of an axial fiber reinforced tow," *International Journal of Mechanical Sciences, Vol: 51, Issue 7, 491-499*, 2009.

[75] Lee, S. H. and Waas, A. M., "Compressive response and failure of fiber reinforced unidirectional composites," *International Journal of Fracture, Vol: 100, Issue 3, 275-306*, 1999.

[76] Yerramalli, C. S. and Waas, A. M., "The Effect of Fiber Diameter on the Compressive Strength of Composites - A 3D Finite Element Based Study," *cmes, Vol: 6, no.1, 1-16*, 2004.

[77] Puck, A., "Calculating the strength of glass fibre/plastic laminates under combined load," *Kunststoffe, German Plastics, Vol. 55, 18-19*, 1969.

[78] Puck, A. and Schneider, W., "On failure mechanisms and failure criteria of filamentwound glass-fibre/resin composites," *Plastics and Polymers, 33-44*, 1969.

[79] Puck, A. and Schurmann, H., "Failure analysis of FRP laminates by means of physically based phenomenological models," *Composites Science and Technology, Vol: 58, 1045-1067*, 1998.

[80] Puck, A. and Schurmann, H., "Failure analysis of FRP laminates by means of physically based phenomenological models," *Composites Science and Technology, Vol: 62, 1633-1662*, 2002.

[81] Patel, D. K., Hasanyan, A. D., and Waas, A. M., "N-Layer concentric cylinder model (NCYL): an extended micromechanics-based multiscale model for nonlinear composites," *Acta Mechanica, doi:10.1007/s00707-016-1696-0*, 2016.

[82] Schultheisz, C. R. and Waas, A. M., "Compressive failure of composites, part I: Testing and micromechanical theories," *Progress in Aerospace Sciences, Vol: 32, 1-42*, 1996.

[83] Rosen, V. W., "Mechanics of composite strengthening," *Fiber Composite Materials American Society of Metals, Metals Park, Ohio, 37-75*, 1965.

[84] Argon, A. S., "Fracture of composites," *Treatise on Materials Science and Technology, Academic Press, New York, 79-114*, 1972.